REPORT DOCUMENTATION PAGE

Form Approved
OMB NO. 0704-0188

Public reporting burden for this collection of information is estimated to average 1 hour per response, including the time for reviewing instructions, searching existing data sources, gathering and maintaining the data needed, and completing and reviewing the collection of information. Send comment regarding this burden estimates or any other aspect of this collection of information, including suggestions for reducing this burden, to Washington Headquarters Services, Directorate for information Operations and Reports, 1215 Jefferson Davis Highway, Suite 1204, Arlington, VA 22202-4302, and to the Office of Management and Budget, Paperwork Reduction Project (0704-0188), Washington, DC 20503.

1. AGENCY USE ONLY *(Leave blank)*

2. REPORT DATE
March 1998

3. REPORT TYPE AND DATES COVERED
Final

4. TITLE AND SUBTITLE
Vortex Surface Collisions

5. FUNDING NUMBERS
DAAH04-93-G-0048

6. AUTHOR(S)
A. T. Conlisk and N. M. Komerath

7. PERFORMING ORGANIZATION NAMES(S) AND ADDRESS(ES)
Ohio State University Research Foundation

8. PERFORMING ORGANIZATION REPORT NUMBER
760601/727272

9. SPONSORING / MONITORING AGENCY NAME(S) AND ADDRESS(ES)
U.S. Army Research Office
P.O. Box 12211
Research Triangle Park,, NC 27709-2211

10. SPONSORING / MONITORING AGENCY REPORT NUMBER
ARO 30707.4-EG

11. SUPPLEMENTARY NOTES
The views, opinions and/or findings contained in this report are those of the author(s) and should not be construed as an official Department of the Army position, policy or decision, unless so designated by other documentation.

12a. DISTRIBUTION / AVAILABILITY STATEMENT
Approved for public release; distribution unlimited.

12 b. DISTRIBUTION CODE

13. ABSTRACT *(Maximum 200 words)*

Many flows of practical interest contain discrete vortices. These include tornadoes, propeller wakes, and flows over swept wings and missile forebodies. The encounter of a vortex with a solid body is always a complex event involving very large gradients of pressure and velocity. We consider the problem in which a rotor-tip vortex collides with a helicopter airframe. The primary objective of this work is to describe both experimentally and computationally the interaction when the vortex "collides" directly with the airframe in the sense that at some point the flow in the vortex core must be altered to accomodate the presence of the airframe. The pressure field caused by the collision is also described. The dominant physics of the collision process may be described by inviscid flow theory and it is the component directed along the tip-vortex axis, termed the axial flow, which is the major cause of the collision.

14. SUBJECT TERMS
Fluid Dynamics, Tip-vortex, Boundary layers, Axial flow

15. NUMBER IF PAGES
270

16. PRICE CODE

17. SECURITY CLASSIFICATION OR REPORT
UNCLASSIFIED

18. SECURITY CLASSIFICATION OF THIS PAGE
UNCLASSIFIED

19. SECURITY CLASSIFICATION OF ABSTRACT
UNCLASSIFIED

20. LIMITATION OF ABSTRACT
UL

NSN 7540-01-280-5500

Standard Form 298 (Rev. 2-89)
Prescribed by ANSI Std. 239-18
298-102

Vortex Surface Collisions

Final Report

By

A.T. Conlisk, P. I.
and
N. M. Komerath, Co-PI[1]

Department of Mechanical Engineering
The Ohio State University
Columbus, Ohio 43210-1107

The U. S. Army Research Office

Contract DAAH04-93-G0048

March 1998

Approved for Public Release;

Distribution Unlimited.

---

[1] School of Aerospace Engineering, Georgia Institute of Technology, Atlanta, Georgia, 30332.

DTIC QUALITY INSPECTED 2

19980519 060

The views, opinions, and/or findings contained in this report are those of the author(s) and should not be construed as an official Department of the Army position, policy, or decision, unless so designated by other documentation.

ACKNOWLEDGEMENTS

The authors wish to express their appreciation to the contract monitor Dr. Thomas L. Doligalski for his support and guidance during the course of this research. Dr. Robert Funk(GT) was instrumental in setting up the data acquisition systems for the experiments. Professor Odus R. Burggraf has also been an integral part of this effort and is responsible for many of the ideas discussed in Chapter 6. Dr. Thomas D. Radcliff performed the computations presented in Chapter 6. In addition, the co-authors acknowledge the student personnel who have contributed significantly to the production of this document; these include John Lynn (GT), Zhenhua Xiao (OSU), Jeff Lee (OSU), and Raghav Mahalingam (GT). In addition Rohit Jain (OSU) generated the results for the 2D box vortex discussed in Chapter 6. Professor Odus R. Burggraf has also been an integral part of this effort and is responsible for many of the ideas discussed in Chapter 6. Sean Brown(OSU) performed many of the editorial tasks required to refine the document. The Ohio Supercomputer Center has provided computer time for which the authors are also grateful.

COMMENTS ON NOTATION

In the current report, we have defined all variables as they appear. However, it should be noted that two different variables may have the same meaning. Thus the unsteady pressure denoted by p in the calculations is the same quantity as the instantaneous pressure denoted by *Cpinst*. The variable z measures distance along the airframe in the calculations and X_B/R measures distance from the nose of the airframe in the same direction. The definition of each variable should be clear from the context.

Contents

List of Tables

List of Figures

EXECUTIVE SUMMARY

Many flows of practical interest contain discrete vortices. These include tornadoes, propeller wakes, and flows over swept wings and missile forebodies. Often, other parts of a system must operate within such flows and thus encounter these vortices. The encounter of a vortex with a solid body is always a complex event involving very large gradients of pressure and velocity. Moreover, the encounter is also transient, causing large and rapid changes in local conditions. Examples are numerous, from tornado touchdowns to blade-vortex interactions (BVI), to secondary flows in turbomachinery and rotor-tip vortex interactions with a helicopter airframe. It is the last problem that is the subject of this work.

Specifically, we consider the impingement of a tip-vortex on a cylindrical airframe. A tip-vortex shed from a wing is known to possess a significant velocity directed along the axis (Batchelor 1964) and we show that it is this component which has a major effect on the interaction of the vortex with a downstream body. The primary objective of this work is to describe both experimentally and computationally the interaction when the vortex "collides" directly with the airframe in the sense that at some point the flow in the vortex core must be altered to accomodate the presence of the airframe. The pressure field caused by the collision will also be described. In the present work we consider the case where the scale of the vortex is much smaller than the body scale although this is not essential. The more general situation where a patch of high vorticity of any shape may be affected by the presence of a body, we define the collision process as follows. A vortex-surface "collision" is defined as the physical process in which the core structure of the vortex defined as a specified region of large vorticity surrounded by irrotational fluid is substantially and most often permanently altered. The primary cause of the collision is the axial flow in the core of the vortex; when the axial flow is directed toward the surface as on the advancing side of the helicopter, the flow is "blocked" and the vorticity originally in the core is redistributed outward forming a shell of concentrated vorticity surrounding the central portion of the vortex which is no longer distinguishable from boundary layer fluid. When the axial velocity is directed away from the wall as on the retreating side of the helicopter, the flow is also "blocked" but the vorticity in the core is redistributed inward toward the central portion of the vortex.

The primary results and major accomplishments of this work are of this work are:

- The dominant physics of the collision process may be described by inviscid flow theory because the vorticity associated with the vortex is much larger than that associated with the surrounding fluid which includes the boundary layer.
- The collision is induced in large part by the presence of a significant velocity component oriented along the vortex centerline and directed back toward the blade tip at which the vortex is formed.
- Experiments indicate that this "axial flow" component can exceed the local swirl velocity component.
- The presence of axial flow causes the vortex core to bulge on the advancing side and to thin on the retreating side of the airframe. This phenomenon has been seen in the experiments and is predicted in the computations.
- The presence of axial flow along with entrainment of boundary layer fluid is responsible for the persistence of a suction peak on the retreating side of the airframe seen in previous experiments and as predicted in the analysis and computations.
- The experiments indicate and the analysis and computations also predict that the suction peak on the advancing side of the airframe is reduced substantially in a very short period of time, due primarily to the stagnation of the axial velocity in the core of the vortex.
- Just prior to the completion of the collision process, the vortex core flattens enabling the vorticity level to be reduced to the level of the surrounding boundary layer.
- The final stages of the collision may be modeled using a "box" vortex which allows the suction peak to decrease as seen in the experiments.

During the course of this work a new model for the tip-vortex which includes the presence of axial flow has been developed. This model views the vortex as a superposition of a set of axially-oriented line vortices along a cylinder simulating the finite-radius core of the vortex (i.e. the vortex cylinder) and vortex rings with the major radius coinciding with the radius of the vortex cylinder. The vortex rings induce axial flow along the centerline of the vortex automatically. In addition it has been shown that a box vortex configuration in which vorticity may not cross the airframe allows the reduction of the suction peak seen in experiments.

Chapter 1

Introduction

1.1 Overview

Many flows of practical interest contain discrete vortices. These include tornadoes, propeller wakes, flows over swept wings and missile forebodies, turbomachinery flows, blade-vortex interactions (BVI) and tip vortex-airframe interactions on helicopters. Often, other parts of a system must operate within such flows and thus encounter these vortices. The encounter of a vortex with a solid body is always a complex event involving very large gradients of pressure and velocity. Moreover, the encounter is also transient, causing large and rapid changes in local conditions. It is the interaction between a tip-vortex shed from a rotor blade and the helicopter airframe that is the subject of this work.

Indeed, the flow field around a helicopter in flight is very complex; the calculation of the flow field has been a great challenge today even with the availability of present day supercomputers. Unlike a fixed wing aircraft, the flow around a helicopter is strongly three-dimensional, highly unsteady, and often involves strong aerodynamic interactions among various components of the helicopter (Sheridan and Smith 1980). Some commonly observed aerodynamic phenomena in helicopter flight are depicted in Figure 1.1 from Caradonna (1992). The flow near the rapidly rotating blade is generally compressible, whereas the flow in the wake of the helicopter is usually not. On the advancing blade side (i.e, the side where the blade is moving in the direction of forward flight), the flow can be transonic near the tip of the blade and a shock can be present. This transonic region is the predominant source of blade drag at high advance ratios. On the retreating side blade, dynamic stall can arise, and thus may induce very high drag, pitching moments and flutter (Caradonna 1992).

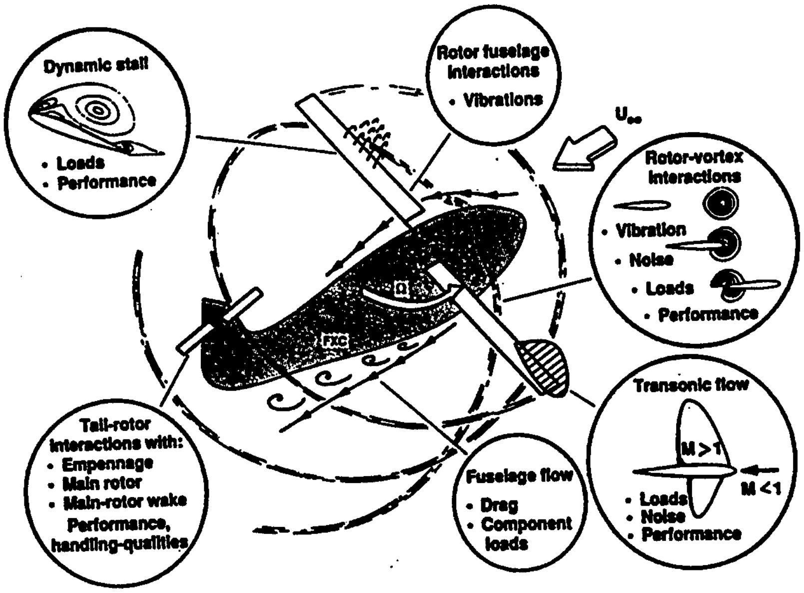

Figure 1.1: Rotorcraft problems, adopted from Caradonna (1992).

At the same time, the rotating blades shed concentrated tip-vortices and inboard vortex sheets. The tip-vortex and the inboard vortex sheet have a very complicated helical structure as shown in Figure 1.2 for a single blade. This complicated vortex wake is responsible for many peculiar aerodynamic features of a helicopter in flight. First, the tip-vortex will interact with the rotor blades and this phenomenon is referred to as "blade/vortex interaction"(BVI). This interaction causes vibration of the rotor blades and noise radiated to the far field. BVI noise is responsible for the familiar sound of an approaching helicopter. Second, the vortical wake interacts with the fuselage of the vehicle, producing a large-amplitude short-scale pressure load on the airframe. Third, the main rotor wake interacts with the tail rotor and can greatly affect the handling qualities of the helicopter. As pointed out by Landgrebe (1994), "despite the recent advances in rotorcraft methodology through improved technology and high speed computers, many of those phenomena remain poorly understood."

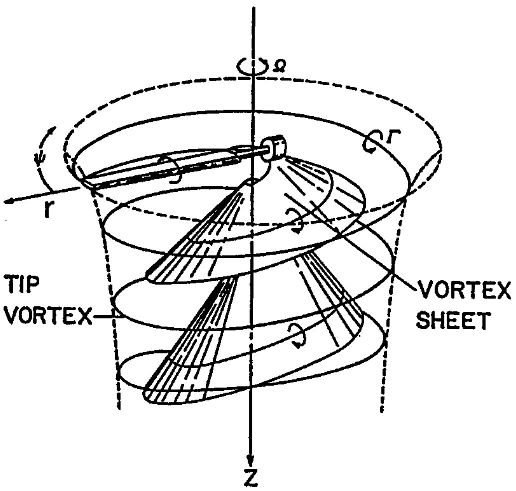

Figure 1.2: Rotor wake as described by Gray (1956).

It is sometimes mentioned that the objective of any analysis of the flow field around a helicopter is to compute the entire flow field around a full configuration including the main rotor, tail rotor and airframe by the full Navier-Stokes equations with sufficient resolution in space and time. However, given the computer speed and memory capacity available today, this goal has yet to be achieved and with the complexity and range of the length and time scales in helicopter flows, in the opinion of the present authors, this goal will likely not be reached in the forseeable future.

The purpose of this work is to describe quantitatively the nature of the local flow as a vortex collides with a body. The focus for this work is the analysis and computation of the interaction between the tip-vortex and a model airframe which is only one of the many interaction phenomena; however the results are intended to have much wider application. This problem is of special interest due to the fact that significant pressure loads are generated on the body which increase in intensity as the vortex approaches. These short-time and short-length-scale suction peaks result from the development of an adverse pressure gradient due to the vortex above the surface and previous work by Affes *et al.* (1993b) has shown that the suction peak reaches a maximum before reducing in amplitude to its effectively steady value in a very short period of time. These pressure loads may result in radiated noise and fatigue loading on the airframe.

This work is timely because in a modern high-performance helicopter design, the clearance between the main rotor and the airframe is getting smaller to enable greater maneuverability; this leads to a strong interaction between the tip-vortex and the airframe. In particular, the unsteady pressure airload due to the impingement of the tip-vortex is very large and can adversely affect the performance of the helicopter, especially in maneuver situations.

Specifically, we consider the impingement of a tip-vortex on a cylindrical airframe. Tip-vortices shed from wings are known to possess a significant velocity directed along its axis (Batchelor 1964) and we show that it is this component which has a major effect on the interaction of the vortex with a downstream body. The primary objective of this work is to describe the interaction when the vortex "collides" directly with the airframe in the sense that at some point the flow in the vortex core must be altered to accomodate the presence of the airframe. The pressure field caused by the collision will also be described. In the present work we consider the case where the scale of the vortex is much smaller than the body scale although this is not essential. To consider the more general situation where a patch of high vorticity of any shape may be affected by the presence of a body, we define the collision process as follows. A vortex-surface "collision" is defined as the physical process in which the core structure of the vortex defined as a specified region of large vorticity surrounded by irrotational fluid is substantially and most often permanently altered. The primary cause of the collision is the axial flow in the core of the vortex; when the axial flow is directed toward the surface as on the advancing side of the helicopter, the flow is "blocked" and the vorticity originally in the core is redistributed outward forming a shell of concentrated vorticity surrounding the central portion of the vortex which is no longer distinguishable from boundary layer fluid. When the axial velocity is directed away from the wall as on the retreating side of the helicopter, the flow is also "blocked" but the vorticity in the core is redistributed inward toward the central portion of the vortex. Note that this definition of a "collision" excludes the situation where a vortex grazes the surface of a body and the vortex core flow is unaffected by the interaction.

The primary results and major accomplishments of this work are

- The dominant physics of the collision process may be described by inviscid flow theory because the vorticity associated with the vortex is much larger than that associated with the surrounding fluid which includes the boundary layer.

- The collision is induced in large part due to the presence of a significant velocity component oriented along the vortex centerline and directed back toward the blade tip at which the vortex is formed.

- Experiments indicate that this "axial flow" component can exceed the local swirl velocity component.

- The presence of axial flow causes the vortex core to bulge on the advancing side and to thin on the retreating side of the airframe. This phenomenon has been seen in the experiments and is predicted in the computations.

- The presence of axial flow along with entrainment of boundary layer fluid is responsible for the persistence of a suction peak on the retreating side of the airframe seen in previous experiments and as predicted in the analysis and computations.

- The experiments indicate and the analysis and computations also predict that the suction peak on the advancing side of the airframe is reduced substantially in a very short period time.

- Just prior to the completion of the collision process, the vortex core flattens enabling the vorticity level to be reduced to the level of the surrounding boundary layer.

- The final stages of the collision may be modeled using a "box" vortex which allows the suction peak to decrease as seen in the experiments.

The fact that the dominant physics of the present problem is inviscid is not as surprising as it may seem. As is well known, the induced pressure on the airframe is intimately related to the vorticity field through the local velocity field. Consider the situation where the ratio of the vortex core radius to the characteristic body length scale, denoted by a is small but finite. Consider also a strong vortex in the sense that the dimensionless circulation based on free-stream variables $\Gamma = \frac{\Gamma^*}{W_\infty a}$ is $O(1)$. Then the vortex Reynolds number, $Re_v = \frac{\Gamma^*}{\nu}$ is the same order of magnitude as the Reynolds number based on the body length scale and the external mean velocity, W_∞, $Re = \frac{W_\infty a}{\nu}$. Assuming that the scaled vortex radius in laminar flow is $O(Re^{-1/2})$, then from a simple Rankine vortex model the swirl velocity is $O(Re^{1/2})$. Since the axial vorticity is essentially the radial derivative of the swirl, it is easily seen that the axial vorticity within the vortex core is of magnitude $\xi \sim Re$ (see equation 5.6). If the axial velocity within the vortex is of the same order as the swirl, then similarly, the azimuthal vorticity is $\omega \sim O(Re)$. The vorticity magnitude within a classical laminar boundary layer on the body is $O(Re^{1/2})$ and so the vorticity within the vortex is much larger than that in the boundary layer. In particular, it is expected that in the collision process the magnitude of the vorticity field within the vortex will be reduced to the order of magnitude of the boundary layer vorticity, in which case distinguishing between boundary layer and vortex vorticity becomes impossible. Thus, the vorticity in the vortex is not destroyed in the collision process but merely redistributed inviscidly. As is well known, this is a major computational simplification: the dominant features of the collision process need not be calculated using the full Navier-Stokes equations. Coinciding with this redistribution of vorticity is the relaxation or focusing of the pressure suction peak associated with the original vortex. In this regard, it is useful to note that for small circulation when the boundary layer and vortex vorticity are of the same order (i.e. a weak vortex) the interaction between the vortex and the boundary layer is very weak. The same ideas may be applied to three-dimensional vortex sheets which in the present application are much weaker and thus much more benign in terms of impulsive loading on the airframe. However, viscous effects must eventually become important on the retreating side of the airframe where the axial velocity in the vortex is directed away from the airframe and the vortex core is fed by boundary layer fluid.

During the course of this work a new model for the tip-vortex which includes the presence of axial flow has been developed. This model views the vortex as a superposition of a set of axially-oriented line vortices along a cylinder simulating the finite-radius core of the vortex (the vortex cylinder) and vortex rings with the major radius coinciding with the radius of the vortex cylinder. The vortex rings induce axial flow along the centerline of the vortex automatically.

The geometry of the present problem is depicted on Figure 1.3. The experiments are conducted in the John J. Harper Wind Tunnel at Georgia Institute of Technology. Here the airframe is represented by a solid circular cylinder and the problem is to predict the trajectory of the tip-vortex as it approaches the airframe. Since the interaction is an oblique one, the vortex will eventually "collide" with the airframe. The flows are described by detailed and structured experiments the results of which are supported

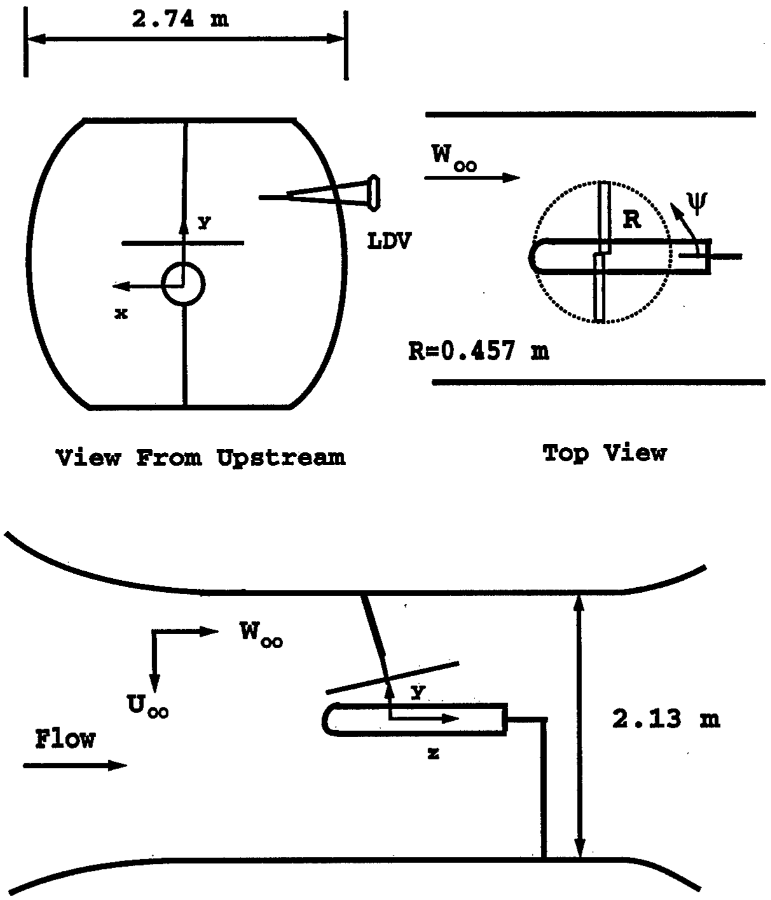

View From Upstream

Top View

Figure 1.3: Geometry of the present work and the coordinate system employed in the computations.

by carefully targeted computations. The computations fall within the class of methods termed vortex methods by those in the helicopter aerodynamics community (Conlisk 1997).

1.2 The Importance of Axial Flow

We have mentioned that the suction peak on the advancing side of the airframe is reduced significantly on the advancing side of the rotor and persists on the retreating side. Coinciding with the reduction of amplitude of the suction peak, it is believed that the axial flow in the vortex stagnates in the sense that it must be brought to zero at the airframe boundary. In the case where the axial velocity in the vortex is directed towards the solid boundary (coinciding with the advancing side of the rotor), the stagnation is manifest in an apparent bulging of the vortex core. In the case where the axial velocity in the vortex is directed away from the solid boundary (coinciding with the retreating side of the rotor), the vortex core is seen to thin locally. This phenomenon of vortex bulging and thinning has been observed in experiments at Georgia Tech by Liou *et al.* (1990).

Figure 1.4(a) depicts the measured pressure distribution around a model airframe at a rotor phase angle of $\psi = 180^o + 90^o = 270^o$. These results are for an advance ratio of 0.1 on the two-bladed model rotor at Georgia Institute of Technology. The rotor phase angle is a time-like variable which measures the angle between the rotor and the generators of the airframe. For example, a rotor angular speed of $1050rpm$ corresponds to a physical time of about $0.16ms$ per degree rotor phase angle, hence $\psi = 90^o$ corresponds to $t \sim 14ms$. It can be seen from Figure 1.4(a) that the vortex has apparently "broken" into two pieces which is indicated by the fact that there are two suction peaks on the airframe as indicated by the very dark spots signifying a negative pressure coefficient located at about $\phi = 0^o$; here ϕ is an angle measuring distance from the top of the airframe. It is believed that at this point, the vortex has split into two pieces, each containing a strong suction peak. Later we will define this as being characteristic of the end of the vortex-airframe collision process. Figure 1.4 will be discussed in more detail in Chapter 4. Figure 1.4(b) shows the pressure distribution at a much larger rotor phase angle of $\psi = 180^o + 150^o = 330^o$. This figure clearly shows that the suction peak on the advancing blade side ($\phi > 0$) is effectively gone, while the suction peak on the retreating blade side persists. Figure 1.5 depicts a

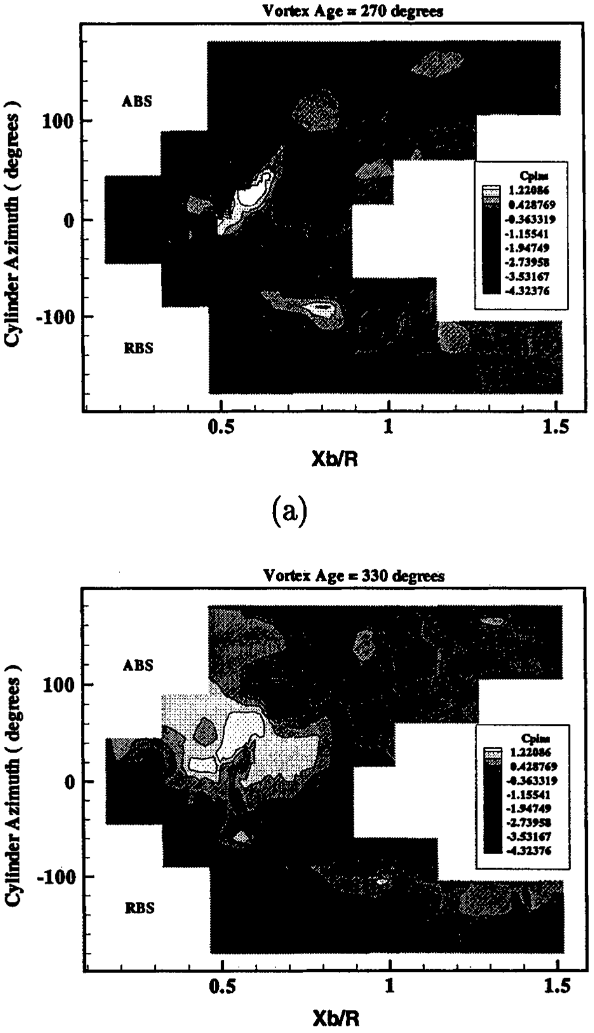

(a)

(b)

Figure 1.4: Pressure distribution around a model airframe showing the differences exhibited on the advancing and retreating sides of the airframe. The azimuthal angle is measured from the top of the cylinder. $\frac{X_b}{R}$ measures distance along the airframe in the forward flight direction. (a) $\psi = 270^o$. (b) $\psi = 330^o$. The dark spots indicate the presence of a large suction peak.

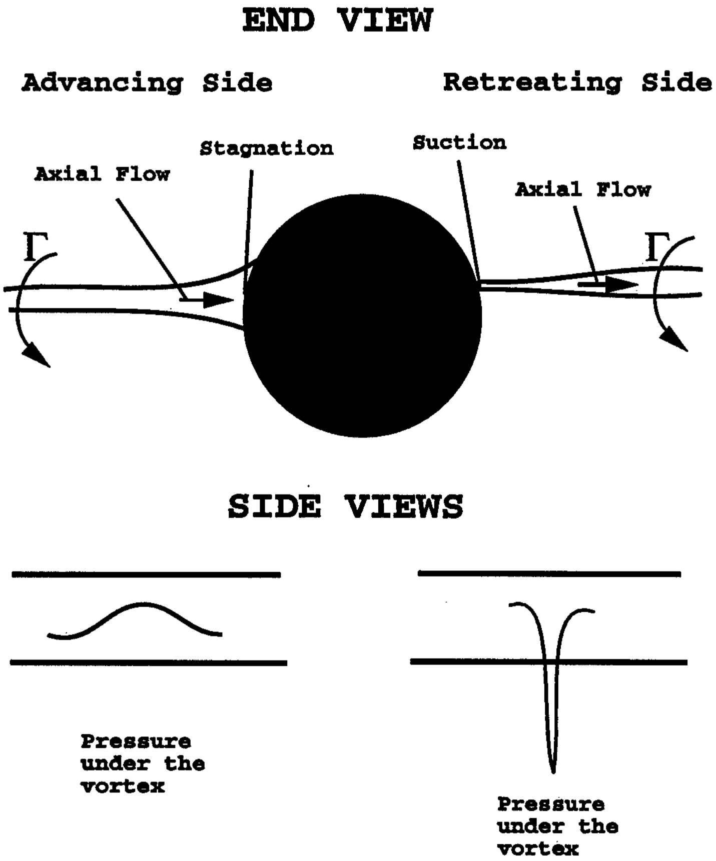

Figure 1.5: A sketch of the tip-vortex structure along the sides of the airframe as described by Kim and Komerath (1995) and Lee *et al.* (1995). The vortex core radius is greatly enlarged for clarity. Arrows denote direction of axial flow within the vortex.

schematic of the phenomenon depicted in Figure 1.4 based on the experiments of Kim and Komerath (1995). On the advancing side of the rotor where the velocity within the vortex core is directed toward the airframe (this velocity we term the axial velocity), the core bulges to reflect the fact that the axial velocity must be brought to rest on the airframe. On the retreating side of the rotor where the axial velocity is directed away from the airframe, the core must thin since it is no longer supplied with fluid from upstream within the vortex.

Another view of the same phenomenon is provided in previous work done in this area by Affes *et al.* (1993b) in which experimental data is compared to a simplified model for the interaction between a vortex and a model airframe. Figures 1.6(a) and 1.6(b) show the numerical versus computational values for the pressure along the top of the airframe for $\psi = 48^o$ and $\psi = 54^o$ respectively. Note that the crosses (+) are the experimental values. The rotor speed is 2100 rpm. It can be seen from this figure that the experimental pressure on the top of the airframe relaxes from $\psi = 228^o$ to $\psi = 234^o$. This is another indication that the vortex core flow has been modified as depicted in Figure 1.5. Note that the computational model used in the work of Affes *et al.*(1993b) does not predict the relaxation of the pressure because the model does not account for axial flow within the vortex.

It will be shown in Chapter 6 that in the absence of axial flow in the core of the vortex, the vortex core radius will decrease indefinitely, thereby increasing the vorticity in the core at fixed circulation and hence the suction peak. Only with the inclusion of axial flow will the suction peak be reduced as seen in Figure 1.6.

1.3 Review of Vortex/Surface Interactions

The interaction of regions of concentrated and large vorticity with solid boundaries is a problem which has received much attention in the past 10-15 years. Problems of this nature occur when a well-defined vortex structure approaches a solid surface. In two-dimensions there is an extensive literature on the subject of vortex flows and extensive reviews have been published on various aspects of vortex motions (Rockwell and Naudascher 1979, Rockwell 1983, Saffman and Baker 1979, and Sarpkaya 1989, Rockwell 1998). Most of the work described in these reviews investigate the situation where the path of the vortex is nearly parallel to the solid surface (Tucker and Conlisk 1992).

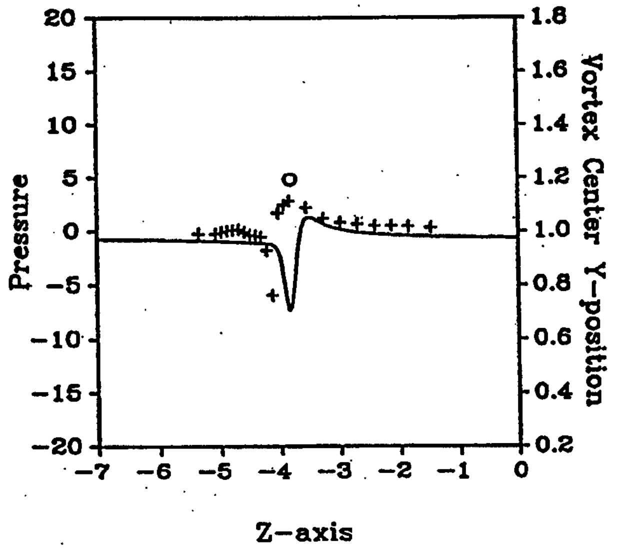

(a)

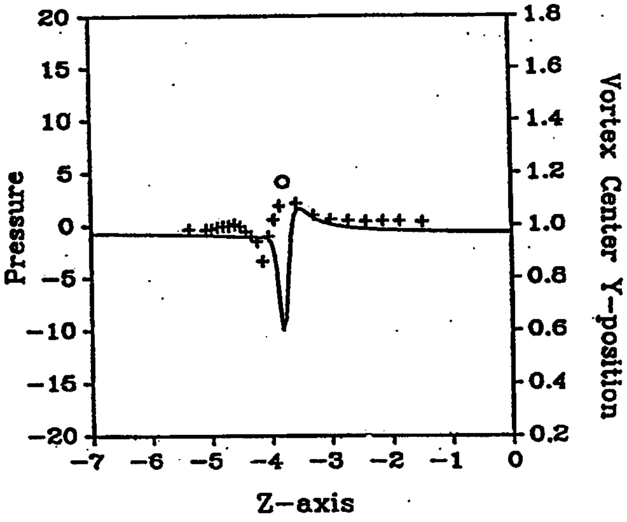

(b)

Figure 1.6: Pressure distribution along top of airframe for (a) $\psi = 228^o$ and (b) $\psi = 234^o$. From Affes *et al.*(1993b).

Considerably less work of an analytical and computational nature has been devoted to the three-dimensional interaction which occurs when a vortex impacts or collides with a surface at an oblique angle; in the present work we consider the situation where the collision angle is 90^o. Much of the work on this problem in recent years has been done in the context of helicopter interactional aerodynamics (Affes *et al.* 1993a,b,c, Kim and Komerath 1995, Liou *et al.* 1990 among many others) and in the area of blade-vortex interactions (Marshall 1994, and Marshall and Yalamanchilli 1994; see the reviews of McCroskey (1995), Conlisk (1997), and Yu (1995) for current references to the BVI problem). In what follows, we review the body of significant work on vortex-surface interactions associated with helicopter aerodynamics applications which has had an influence on the solution of the present problem.

The vortex wake generated by the rotor blades inevitably interacts with other non-rotating components of the rotorcraft and the interaction is fully three-dimensional and unsteady. The most prominent example is the vortex wake/fuselage interaction. This interaction process is the strongest in hover and low speed forward flight since, in these two flight regimes, the wake is transported almost vertically downward toward the fuselage. An immediate consequence is that the vortex wake may directly impinge on the surface of the fuselage. As a result, it may adversely influence the handling qualities of the aircraft. Landgrebe *et al.* (1977) are among the earliest to use experimental and analytical tools to study the wake/airframe interaction. Wilson and Mineck (1975) conducted an experimental study of the effect of vortex wake on three different helicopter fuselages. They show that small clearance between the rotor and the airframe may lead to higher induced airload and vibration levels on the airframe due to the strong vortex/surface interaction.

Smith (1979) found that the presence of the fuselage will distort the wake geometry. This wake distortion in return enhances blade/wake interactions and even triggers a torsional aeroelastic response of the rotor, resulting in a premature retreating blade stall. Freeman (1980) studied the wake/airframe interaction using an inviscid panel code. However, in his study, the interaction process was not fully coupled and the rotor was not affected by the presence of the airframe. Sheridan and Smith (1980) summarized some common characteristics of interactional process among wake and other rotorcraft components based on their experimental study of Boeing Vertol UTTAS program.

A subsequent experimental study by Betzina and Smith (1983) revealed that the longitudinal aerodynamic characteristics of the airframe are influenced by the rotor and hub. Johnson and Yamauchi (1984) confirmed that the distortion of the rotor wake due to the presence of a fuselage will result in harmonic excitations at the rotor. Egolf and Lorber (1987) and Lorber and Egolf (1990) investigated the interaction between a rotor and a fuselage in forward flight. They used the combination of a lifting line, panel representation of the airframe and a prescribed wake model to predict the unsteady airload on the airframe. Their results agreed well with the experimental results obtained by Brand *et al.* (1989) on a circular cylinder with a hemispherical nose, suspended under a two-bladed teetering rotor. However, the mean pressure on the airframe exhibited some discrepancy due to the quasi-steady approach they used to simulate the vortex wake.

In the same study, Brand *et al.* (1989) also noticed a very interesting phenomenon: the blade passage effects are the most dominant and are responsible for the large periodic pressure pulsations on the airframe. In addition, they found that the interaction of the vortex wake with the airframe is characterized by a large-amplitude, short-scale, periodic suction spike on the airframe. This suction peak coincides with the time frame in which the tip-vortex is one core radius from the airframe. They also suggested that the intensity of the interaction between the inboard vortex sheet and the airframe is much weaker than the tip-vortex/airframe interaction. When the distance between the rotor disk and the airframe is large, the unsteady pressure load on the airframe will mainly depend on the tip-vortex.

In a similar investigation, Liou, Komerath and McMahon (1990) used the same model as Brand to study the transient interaction between the airframe and the vortical wake. In their experimental model, a round headed circular cylinder is placed under a two-bladed rotor to simulate the helicopter. By using Laser Doppler Velocimetry, they were able to trace the tip-vortex trajectory and measure the velocity field in a vertical plane on top of the airframe. They also measured the pressure distribution on the surface of the airframe. Their results show the same type of short-scale, large-amplitude suction peak on the airframe as observed by Brand *et al.* (1989). Affes *et al.* (1993a,b) performed a numerical study of the vortex/airframe interaction based on the Georgia Tech model. They employed a Fourier transform method to solve the potential flow field due to the tip-vortex. A mean flow field, which was generated from experimental data taken from Georgia Tech, was added to the flow to simulate the downwash due to the rotor. The Biot-Savart law is used to compute the induced velocity by the vortex. The calculated vortex trajectory and the pressure distribution on the airframe agreed well with the experimental data of Komerath (1993).

Bi *et al.* (1993) conducted an experiment to study the interaction of rotor tip-vortex with an airframe. By using the wide-field shadowgraph method to visualize the flow field, they obtained considerable information about the interaction process of the tip-vortex with the airframe. Similar to the findings of Brand *et al.* (1989) and Liou, Komerath and McMahon (1990), Bi *et al.* (1993) also found that the pressure on the airframe is very sensitive to the tip-vortex trajectory.

Instantaneous pressure measurements all around the cylindrical airframe surface at Georgia Tech by Kim and Komerath (1995) and other unpublished work at Georgia Tech showed that as the vortex impinges on the airframe it breaks into two pieces. One piece stagnates on the advancing blade side of the airframe surface in an almost 90^o angle with the surface and the another piece attaches to the retreating blade side of the airframe surface and extends outward as shown on Figure 1.5. The piece which stagnates on the advancing blade side of airframe bulges near the end of the vortex. The piece which attaches to the retreating blade side of the airframe attenuates near the airframe surface and boundary-layer fluid erupts away from the surface along the vortex. This process is similar to the phenomenon observed in the study by Burggraf *et al.* (1971), who investigated the problem of a potential vortex attached to a coaxial disc. They showed that the boundary layer induced by the vortex will erupt from the wall at $r = 0$. A simplified inviscid model used to simulate the process of a vortex stagnating on a surface is developed in Chapter 5 (Lee *et al.* 1995, 1997) and shows the same trends as in the experiments. In this model, a vortex with axial flow is suddenly cut by a plane wall. The axial velocity in the vortex can be directed toward or away from the wall. Subsequently, the vortex shows bulging near the wall when the axial velocity is directed toward the wall (i.e. the advancing side of the rotor) and thinning when the axial velocity in the vortex is directed away from the wall (i.e. the retreating side of the rotor).

1.4 Outline of the Present Work

The vortical wake shed from the rotor blade interacts with the airframe and is the main source of the impulsive airload on the airframe in hover and in low speed forward flight. The accurate prediction of this unsteady pressure force has significant importance for the design of modern high performance helicopters. Furthermore, the accuracy of the predicted wake trajectory is directly related to that of the predicted rotor power. Thus far, as pointed out by Caradonna (1992), the ability of any code to predict this wake with acceptable accuracy is a subject of great debate.

Another consequence of this unsteady wake/airframe interaction is the viscous boundary-layer separation above the surface of an airframe. This boundary-layer separation had been observed in rotorcraft experiments conducted at Georgia Tech in 1993. In the experiment, although difficult to find, it was found that a secondary eddy develops at the top of the helicopter airframe (Affes *et al* (1993c). This second eddy grows rapidly with time and eventually erupts into the inviscid flow region. However, it needs to be pointed out that the influence of this secondary-flow eruption on the vortex/airframe interaction is probably not significant.

The current problem is approached from a fundamental point of view with targeted computations supported by appropriately directed experiments. This is a modular approach designed to illuminate features of the collision process which occur on the scale of the vortex core. A purely computational approach has been avoided for the following reason. Consider, for example, in Figure 1.3, a Navier-Stokes computation in which there are 200 points in each of the three coordinate directions; for simplicity, consider a cartesian coordinate system. Suppose that the total computational domain is based on the lengths $L_x = L_z = 2R + \Delta R$ where R is the rotor radius; $R = .457m$ and $L_y = 2H + H + D_{airframe} + 2H = .82m$, where H is the rotor to airframe gap and is about $0.14m$, and the diameter of the airframe is $0.134m$. Note that this is a rather limited domain for a computational approach. Then the grid sizes are $\Delta x = \Delta z = 6.25mm$ and $\Delta y = 4mm$. A typical vortex radius (Kim and Komerath 1995) is about $.3in = 7.6mm$ and the boundary layer thickness is about $2mm$ based on the airframe radius and axial speed W_∞.

In the present hypothetical computation based on a uniform grid, there would be *no* points within the boundary layer, and only *one* grid point to represent the vortex core. Moreover, since the three velocity components and the pressure need to be computed, for the present number of grid points, 32Mwords of memory are required for a single time step. This is about the size of the typically available memory in a standard supercomputer (say Cray YMP) calculation. Clearly, this situation is not tenable and suggests that some procedure for placing more points in the regions where the flow varies rapidly (i.e. in the vortex and near the wall) is necessary in order to resolve the local flow field around the vortex. There are two ways to do this. First, as many additional grid points as necessary can be added to resolve the small scales; in the present computational environment, this does not appear to be possible. Second, along with solving the three-dimensional Navier-Stokes equations, a two-dimensional adaptive gridding procedure could be developed in which the grid spacing is tied in some way to the behavior of the solution, say one of the velocity components which is large in the region of large vorticity. In the present computational environment this approach is very difficult and time-consuming and a matter for future research. In summary, the present computational environment does not support an approach in which the Navier-Stokes equations are solved over the entire domain because the small length and time scales which naturally arise cannot be resolved. In this spirit, a modular approach to the vortex-surface collision problem is warranted.

In Chapter 2 we discuss the interaction between a tip-vortex and a downstream airfoil as a prelude to the much more complex vortex-airframe interaction. This was done since the length and time scales in this problem are not as small as in the vortex-airframe problem. The tip-vortex airfoil interaction is a quasi-steady interaction which has some similarity with the rotor-airframe intearaction until the vortex collides head-on with the airfoil. The most important factor affecting the interaction is the vertical standoff distance between the vortex and the airfoil. The interaction adhered to image-vortex theory until the vortex was in the plane of the airfoil. Vortex trajectories for this part of the interaction have been obtained from flow-visualization. In a head-on interaction whether the vortex split along its axis or not is dictated by the thickness of the airfoil. For a thick interacting airfoil the vortex bulges ahead of the LE. For a thin interacting airfoil, however the vortex splits into two vortices of the same sign. These vortices do not recombine behind the trailing edge of the airfoil. While the interaction is primarily steady the switching process of the vortex from above the airfoil to below it is sudden. One unresolved issue is the asymmetry in the vortex trajectories above and below the airfoil.

In Chapter 3 we discuss the behavior of the viscous flow on the airframe from the point of interacting boundary layer theory. Initially, it was anticipated that it would be possible to capture the full range of the viscous flow phenomena with the interacting boundary layer approach, thus avoiding the need to solve the full Navier-Stokes equations. However, this proved not to be the case since a singularity of the same type as in two-dimensions arises;

moreover, simple scaling arguments which appear in the summary section of Chapter 3 clearly show that for a sufficiently strong vortex, the collision process is dominated by inviscid phenomena. Thus, further work on the viscous flow problem does not seem to be necessary.

In Chapter 4, the results of the experiments are presented. Results of earlier work by Thompson (1985) show that the axial velocity in the tip-vortex core could be substantial. Pressure measurements by Kim and Komerath (1995) show an asymmetry in the pressure distribution on the sides of the airframe. In particular, strong suction peaks on the RBS and weak stagnation on the ABS indicated that the axial velocity component in the tip-vortex core could not be neglected. This chapter describes in detail the experiments performed to quantify the core axial velocity along with the lateral component of wake velocity on top of the airframe. It is shown that the core axial velocity can be larger than the core circumferential velocity. The inboard sheet velocities are shown to be about half the magnitude of the core axial velocities. Both are directed towards the blade from which they were generated. Flow-visualization was performed to identify other aspects of the interaction as suggested by the computations. The behavior of the vortex in the post-collision phase is described using flow-visualization and the velocity measurements.

To illustrate the results of Chapter 4, a simple model problem was formulated. Here a Lamb vortex (Lamb 1945) having a specified velocity distribution oriented along the centerline of the vortex is assumed to be split instantaneously by a wall at a 90^o angle to the axis of the rotation of the vortex. For axial flow in the vortex directed toward the wall, the vortex core is seen to "bulge". The swirl velocity decreases rapidly in the core of the vortex allowing the pressure distribution to return to its steady-state, mean value as observed in experiments. The time scale associated with the reduction of the pressure spike depends on the magnitude of the axial velocity in the core of the vortex and on the nominal vortex core radius. At the same time the axial vorticity near the axis decreases by an order of magnitude with a consequent increase at larger radii as the vorticity is carried outward by the induced radial velocity. A similar comment applies to the azimuthal vorticity.

For the case where the axial flow is directed away from the wall, the axial vorticity is redistributed inward and the vortex core radius shrinks. At the same time the suction peak increases in amplitude and focuses. The essential features of the process described here have been observed on the advancing side of the helicopter rotor in experiments (Kim and Komerath 1995) and in the results of the experiments described above.

The ideas set out in the previous chapter were used to construct a new model for the tip-vortex which automatically incorporates axial flow. Here the effect of a variable vortex core radius is also incorporated. The new model consists of the superposition of vortex rings and a modified line vortex. The combination of the variable vortex core radius and the presence of axial flow lowers the suction peak somewhat in comparison with past work. Bulging on the advancing side and thinning on the retreating side are obtained as seen in the experiments. Results are presented for a stagnant medium, as well as for symmetric mean flow and asymmetric mean flow cases. We then compare these results with the experiments conducted at Georgia Tech. The primary deficiency of the circular vortex model which is associated with vorticity penetrating the airframe is then discussed and we address this issue by introducing the "box" vortex which allows the core of the vortex to change shape; an argument based on theoretical grounds supporting this concept is also given. Discussion of the passage of the vortex along the sides of the airframe and possible reconnection of the vortex complete the last chapter.

A number of papers have been published as a result of this work and these papers are listed in Appendix A. The students who have been awarded degrees are also listed there. Important technology transfer events are described in Appendix B.

Chapter 2

Vortex-Airfoil Interaction

2.1 Introduction

In this chapter, we seek to understand the quasi-steady interaction between a wing tip vortex and a downstream airfoil. The original motivation for studying this problem was as a test case of a slow vortex-surface interaction. Until the vortex collides head-on with the interacting airfoil, the dominant body scale is the chord of the interacting airfoil and some similarities can be drawn with the rotor-airframe interaction. However, the time-scales involved in the rotor-airframe interaction are orders of magnitude smaller. In a head-on interaction this problem is similar to the blade-vortex interaction (BVI) problem. Thus the vortex-airfoil interaction falls somewhere between the rotor-airframe collision (obstacle size $\gg$ vortex core), and the BVI problem (obstacle size $\leq$ core size). This interaction is quasi-steady, but three-dimensional. The axial velocity in the vortex core is small relative to the swirl velocity, unlike the rotor case. The vortex filament has little curvature prior to the interaction. The Mach number is close to zero. The behavior of the vortex when cut by the airfoil is also different from the rotor-airframe interaction case due to the orientation of the tip vortex to the mean flow.

The previous work by other researchers in this area has been motivated by a variety of reasons. Lombardi (1995) reports the problem where the vortex from a canard interacts with the main wing. This is primarily a quasi-steady interaction, but can also involve sudden loads and moments during maneuvers such as landing and pitch-up, due to vortex switching across the surface of the interacting wing. Vortex switching can also reduce control surface effectiveness and produce control reversal over short periods of time. Computational simulation of the flow with small stand-off distances between the vortex and the airfoil is complicated and expensive because of the viscous effects involving both the vortex and boundary layer on the interacting airfoil. A similar problem is the interaction of flap vortices with horizontal tails and with the ground during landing and take-off. Yu (1995) summarizes the large body of research conducted on the problem of BVI encountered by rotorcraft during descent. This occurs on a short time scale and causes sharp pressure pulses which propagate. This is a source of noise and therefore a limiting factor in the community acceptance of helicopters. Tung *et al.* (1996) review the aerodynamic aspects of BVI. Other applications are in the interaction of vortices from different wings of a micro air vehicle, or between the main-rotor tip vortex with a downstream stabilator and/or tail-rotor. Understanding the fluid-dynamics of vortex surface interactions is also very important for wake-avoidance issues for small aircraft tailing larger aircraft.

Patel and Hancock (1974) conducted visualization and pressure measurements on the interaction of a tip vortex with a wing. They concluded that while the overall trends of the loads induced on a wing by a streamwise vortex can be determined by classical wing theory, detailed load distributions, especially for close interactions, are too complex for theoretical treatment. Low-speed studies by Seath and Wilson (1986) documented a significant change in the pressure distribution of the interacting airfoil and noticed a spanwise drift. Kalkhoran *et al.* (1992) studied the interaction details at transonic Mach numbers and concluded that there is an unsteadiness associated with the location of the vortex core and that the closeness of the vortex to the airfoil was an important parameter in the interaction while the Reynolds number was not. They noticed the formation of two vortical regions during close interactions which they associated with the formation of a secondary vortex. Cutler and Bradshaw (1993) studied the interaction between a longitudinal vortex pair and a turbulent boundary layer on a plate. Wittmer and Devenport (1994, 1995, 1996) did a series of experiments on a wing-vortex/airfoil configuration. They concluded that negative vorticity is shed in the airfoil wake due to the vortex load and this imparts an unstable circulation distribution to the vortex. They also found that the blade wake is distorted considerably. There is also a large body of research dealing with the general interaction of vortices with walls. A complete review of past work on this problem is presented by Doligalski *et al.* (1994).

The initial attempt at this problem was with a NACA0021 interacting airfoil. During the course of preliminary investigations with this airfoil, several interesting aspects of the problem presented themselves and this prompted the investigation of other airfoils and configurations. Thus, we followed our initial tests with experiments directed at specific features of the problem. We are now able to describe the entire interaction process as the vortex comes close to the top surface of the interacting airfoil and then switches across to the bottom surface. The changes in the vortex structure during the time in which it switches are captured. Differences in the interaction for the different airfoils are noted. Vortex trajectories obtained from digitizing flow-visualization images are presented. These are also available in electronic form for computational comparisions. The interaction can be divided into three phases. When the vortex is more than one core radius away from the surface of the airfoil the interaction behaves according to potential flow expectations and hence this phase is called the potential phase. When the vortex is less than one core radius from the airfoil the interaction is termed a close-interaction phase. When the vortex is in the plane of the airfoil the interaction is termed the head-on interaction phase.

2.2 Issues

Issues raised prior to the experiments were:

- What is the effect of the vortex stand-off distance on the interaction?
- During the close-interaction phase, will secondary structures be formed by vortex-boundary-layer interaction? Will these cause unsteady behavior?
- Will the vortex split when it interacts head-on with the airfoil? Or will it stay entirely on the top or bottom of the airfoil and jump from one side to the other?
- If a split occurs, how will the split vortices move over the airfoil surface?
- Will the split filaments roll around each other downstream of the airfoil and rejoin?

As the tests progressed other issues came up, including:

- Asymmetry in vortex trajectories above and below the interacting airfoil.
- Effects of pressure gradient on the vortex trajectories.
- Effect of interacting airfoil thickness on the vortex behavior in the head-on interaction.

2.3 Experimental Setup and Diagnostics

Three different tests were performed as part of this study. Two of them were performed in the J. J. Harper closed-circuit, low speed wind-tunnel at Georgia Tech. The test section has a $2.13m \times 2.74m$ cross-section and freestream turbulence levels $\leq 0.5\%$. The vortex generator (VG) was placed upstream of the interacting airfoil and positioned so that the vortex would nominally pass over the mid-span of the downstream airfoil. Two airfoils almost spanning the wind tunnel test section were tested; one a 21% thick airfoil, and the other a thin flat plate with a rounded leading edge and a sharp trailing edge. A third case was tested in the 1.07m square test-section of the blow down, Low Turbulence Wind Tunnel at Georgia Tech as an undergraduate class project with a 12% thick full-span airfoil to provide answers to some of the issues unresolved in the first two cases. The experimental setup and coordinate system are shown in Figure 2.1.

The velocity profile of the tip vortex prior to the interaction was measured using a laser velocimeter. A TSI fiber-optic probe transmitted the dual-beam with the unshifted beam at 514nm (green). The scattered light was collected in back-scatter by the same probe and conveyed to the photomultiplier. The photomultiplier signal was downmixed and processed by a TSI 1990 counter. A TSI 1998 interface was used to transfer the data to a Gateway2000 486/66 computer. The flow was seeded using atomized mineral oil placed downstream of the test-section. An approximate location for the vortex core was established from flow visualization in vertical, spanwise planes at 7.6 ($\frac{x}{c} = -0.293$) and 6.5 ($\frac{x}{c} = -0.585$) vortex generator chord lengths behind the trailing edge of the VG. The vertical velocity component was measured along a spanwise line passing through the center of the core. The velocity profile of the vortex was used to estimate the core circulation. The location of the peak velocities in the velocity profile were used to deter-

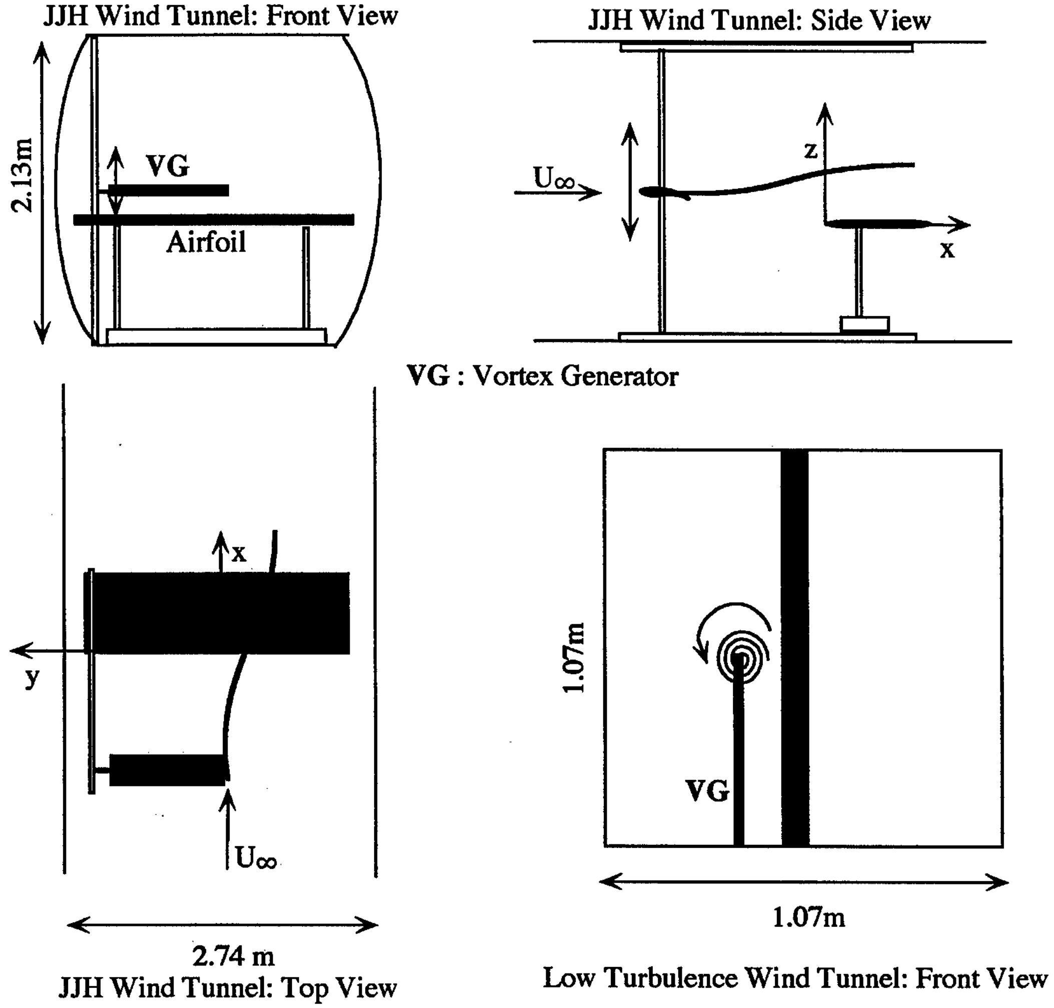
JJH Wind Tunnel: Front View

JJH Wind Tunnel: Side View

VG : Vortex Generator

JJH Wind Tunnel: Top View

Low Turbulence Wind Tunnel: Front View

Figure 2.1: Tip-Vortex airfoil interaction setup.

mine the core radius. Knowing the peak velocities and the core radius, the circulation was obtained.

2.3.1 Flow Visualization

The flow was illuminated in spanwise, vertical planes using a thin light sheet from a 30W Copper Vapor laser operating at 6000, 25-ns pulses per second (5 mJ per pulse). Flow images in the light sheet were recorded with an intensified CCD video-camera. The camera was initially aligned by focussing on a grid board with scale markings, placed in the plane of the laser sheet. The grid-board also provided the scaling factor for transferring vortex locations from screen-coordinates to physical coordinates. Wax decomposing from heated Nichrome wires provided the seeding. The video signal from the camera was recorded on standard VHS half-inch videotapes. Instantaneous flow images were digitized from the video throughout the interaction period at several locations along the chord. These images had to be enhanced for contrast and brightness. Selected stills from the sequence are presented here to describe different phases of the collision process along the top and bottom surface of the interacting surface. The three-dimensional vortex trajectories were derived from these frames by locating the vortex core position on the screen coordinates and transforming that location to physical coordinates. Figure 2.2 shows a schematic of the flow visualization technique.

2.3.2 Pressure Measurements

Since the flow was expected to be primarily steady, upper-surface pressure measurements on the interacting airfoil were used as a criterion to quantify the effect of the vertical vortex stand-off distance from the airfoil. This was achieved by static pressure ports on the airfoil surface multiplexed through a scanivalve to a Barocel pressure transducer mounted outside the test-section. The data acquisition program sampled both the tunnel dynamic and model surface pressure transducers 50,000 times at 2000 Hz.

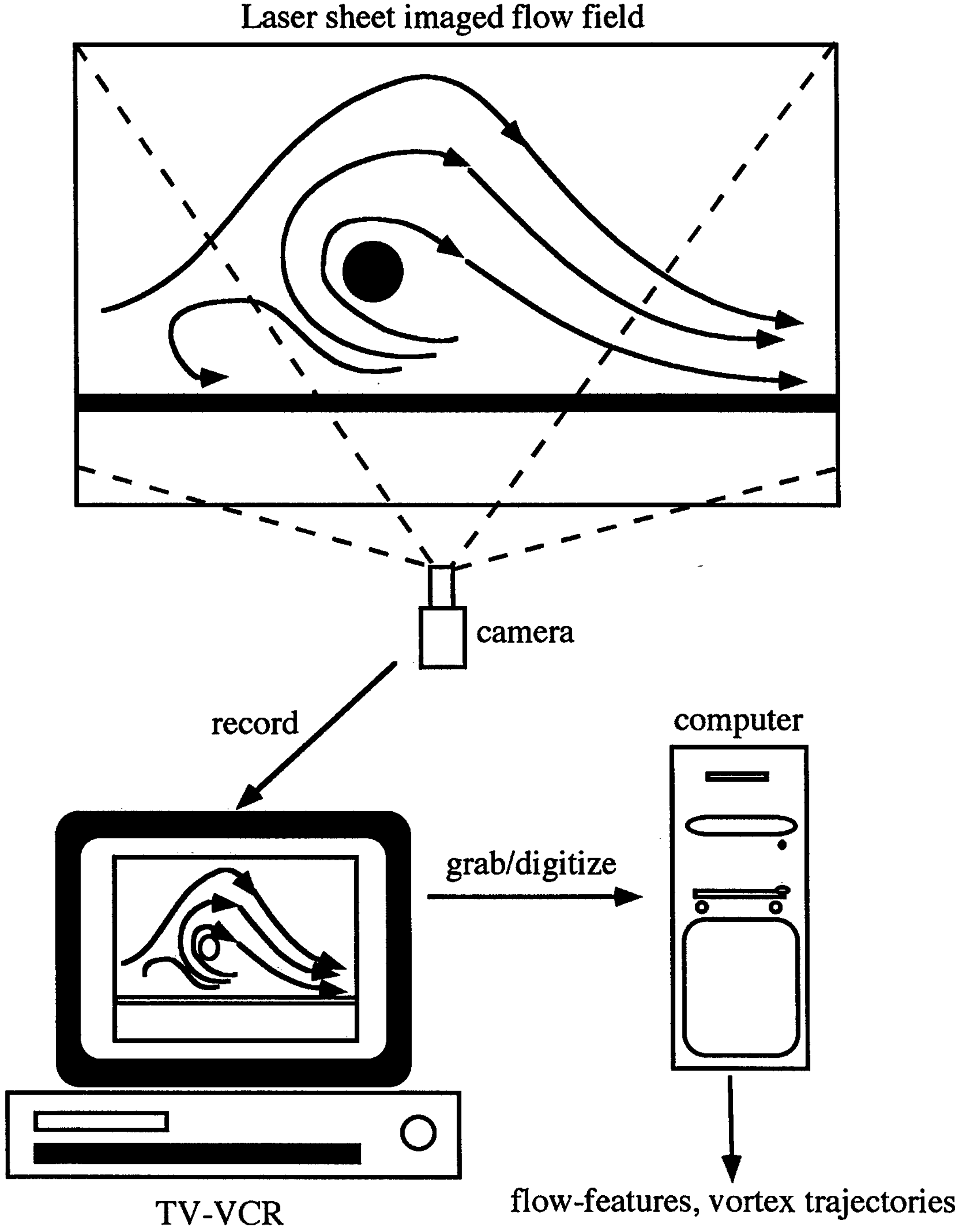

Figure 2.2: Schematic of flow-visualization system.

2.4 Test Cases

2.4.1 NACA0021 airfoil

A series of preliminary experiments were performed with the 21% thick airfoil to identify the various factors that play a role in the interaction. The airfoil had a span of 2.23m and a chord of 0.4m. Though this airfoil was not full span and did not have end-plates, its aspect ratio of 5.6 was large enough so that the end effects were negligible. It was held at an angle of attack of 1.1^o for all the test cases. The vortex generator was a NACA0016 semi-span wing of aspect ratio 4.26 and 0.14m chord. Initial pressure measurements with this airfoil were performed at a freestream speed of $15.24\frac{m}{s}$ with fixed vortex generator locations and 5^o angle of attack. This provided a basic understanding of loads on the airfoil due to the vortex. Then the following variations were tested during the flow-visualization at $3.048\frac{m}{s}$.

- Variation of streamwise separation between VG and interacting airfoil
- Variation of VG angle of attack
- Variation of vertical separation between VG and interacting airfoil

These tests provided valuable insight into the problem until the end of the close-interaction.

2.4.2 Flat plate airfoil

When the vortex interacted head-on with the airfoil, the thickness of the NACA0021 airfoil prevented visualization on both surfaces simultaneously. To correlate the effects on the top and bottom, we decided to perform flow-visualization tests on a flat-plate airfoil. The flat-plate airfoil had chord 0.52m and thickness 1.3cm and an aspect ratio of 4.62, which was large enough to neglect end-effects. The leading edge of the flat-plate was rounded, so that there was a favorable pressure gradient until $\frac{x}{c} = 0.037$. The sharp trailing edge resulted in an adverse pressure gradient on the surface for $0.9 \leq \frac{x}{c} \leq 1.0$. Ten spanwise, vertical planes along the chord of the airfoil were visualized. Effects that gradients might introduce in the vortex trajectories were expected to be seen around the leading and trailing edges. The vortex generator was a NACA0016 semi-span wing of aspect ratio 4.26 and 0.14m chord. The only variable in this test was the vertical separation between the vortex generator and the airfoil. The vortex generator angle of attack was held fixed at 5^o for all the experiments and the free-stream velocity at $3.048\frac{m}{s}$. The VG was moved vertically through $-0.146 \leq VG_{\frac{z}{c}} \leq 0.146$ at a vertical speed of $2.496\frac{mm}{s}$.

2.4.3 12% Thick Airfoil

A third test case was performed to study the lack of symmetry in the vortex trajectories above and below the airfoil. The airfoil was a full-span NACA0012, set at 0^o angle of attack. Flow visualization was performed in planes perpendicular to the plane of the airfoil. Two angles of attack of the vortex generator, $\pm 10^o$ were studied.

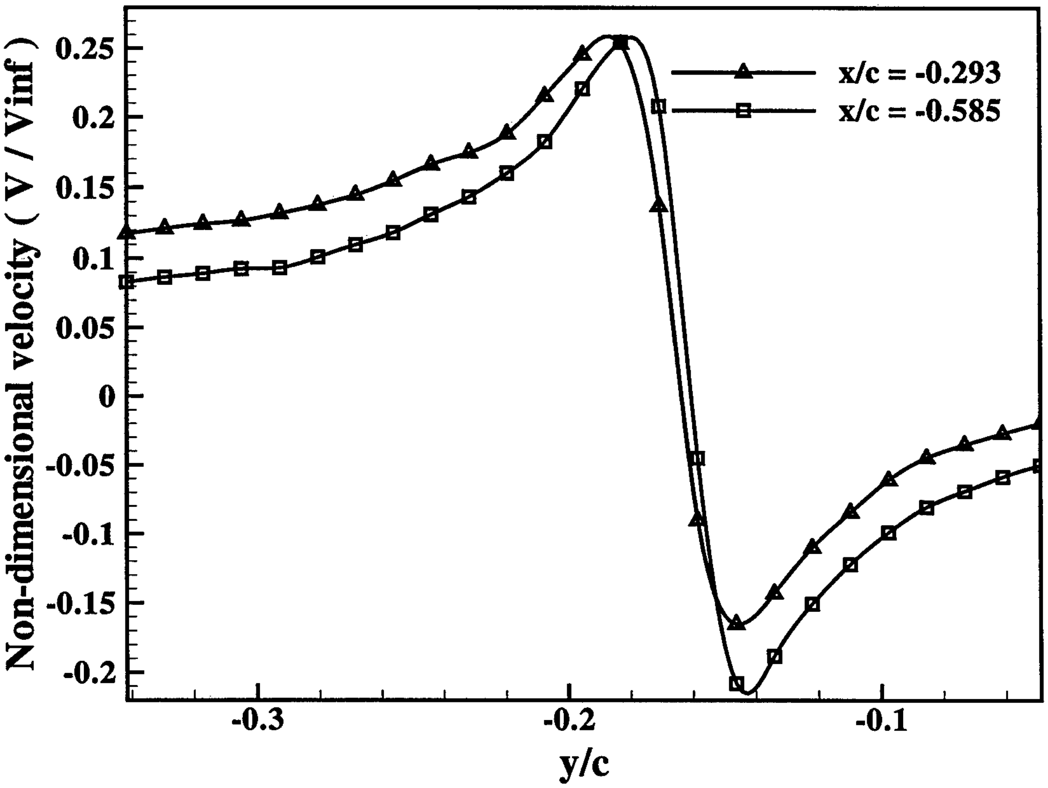

Figure 2.3: Vortex characteristics prior to interaction.

2.5 Results

2.5.1 Vortex Characteristics Before Interaction

Figure 2.3 shows the vertical component of the velocity across the center of the vortex at two streamwise locations. The tip vortices have almost completely rolled up by $\frac{x}{c} = -0.585$ and the value of circulation obtained is $0.094\frac{m^2}{s}$. Further roll-up is achieved by $\frac{x}{c} = -0.293$ and the circulation has increased to $0.098\frac{m^2}{s}$. These values are close to the peak circulation value obtained using a lifting-line calculation. The vortex core diameter has not changed from $\frac{x}{c} = -0.585$ to $\frac{x}{c} = -0.293$. Thus, it was ensured that by the time the vortex interacted with the airfoil it is a well-developed, rectilinear vortex of constant core diameter. The vortex core diameter at the LE of the airfoil is 2.0cm (14% of vortex generator chord length).

2.5.2 Results for the NACA0021 Airfoil

Increasing the vortex generator angle of attack increased the vortex strength and therefore the strength of the interaction in a predictable fashion. This resulted in a greater spanwise movement of the vortex above the interacting airfoil. Varying the streamwise separation had no significant effect, since the wing-wake rolls up fairly rapidly. Thus, the dominant non-linearities in the interaction are due to the stand-off distance between the interacting airfoil and the vortex.

Pressure Measurements

Pressure measurements on the upper surface of the interacting airfoil were performed at three vortex generator stand-off distances. Figure 2.4 shows the effect of vortex closeness to the airfoil at two stand-off distances. Both the standoff distances ($VG_{\frac{z}{c}} = 0$ and -0.0136) shown are such that the vortex is still above the upper surface of the airfoil. The pressure traces show a suction which increases in magnitude as the vortex moves closer. Also note the difference in the pressure signature caused at different streamwise locations. The downstream traces show a pressure to the left of the primary suction. This is an indication of the beginning of boundary layer separation.

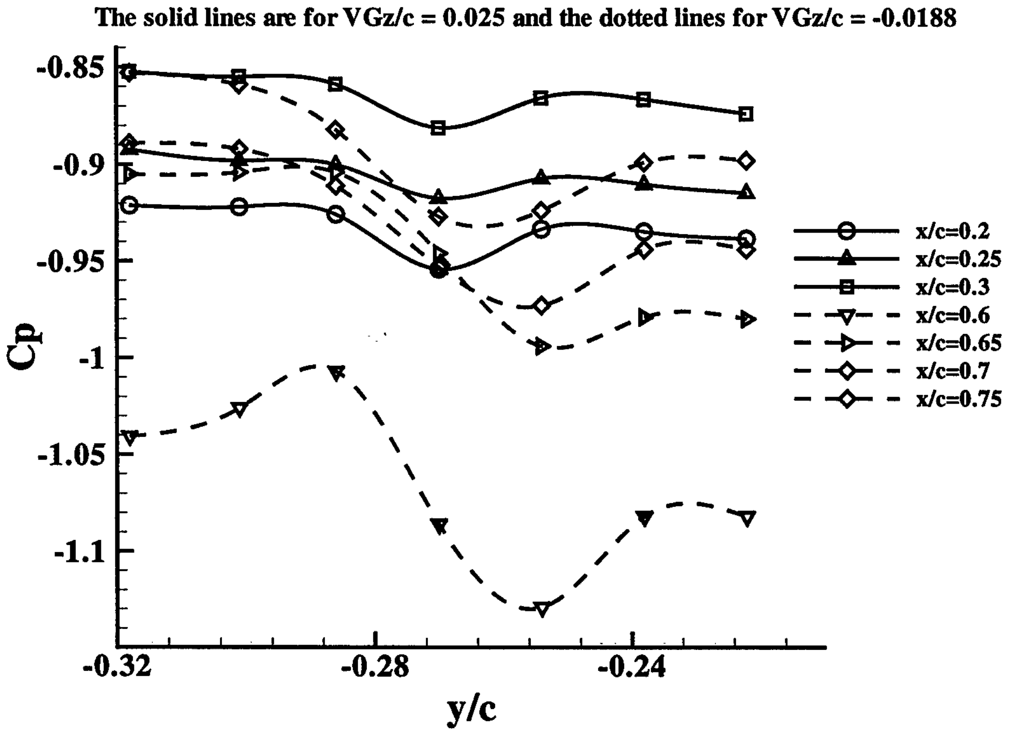

Figure 2.4: Pressure distribution induced by the tip-vortex on the upper surface of the interacting airfoil.

Vortex Trajectories

Figure 2.5 shows the vortex motion over the top surface of the airfoil as the vortex generator is moved vertically. The thickness of the airfoil prevented simultaneous visualization on the bottom surface. The results show spanwise movement of the vortex according to potential theory. All the planes shown in the figure are ahead of the maximum thickness point and are in a region of favorable pressure gradient. The spanwise movement is highest near the leading edge. This implies that in a region of favorable pressure gradient the spanwise motion induced by the image vortex is inhibited.

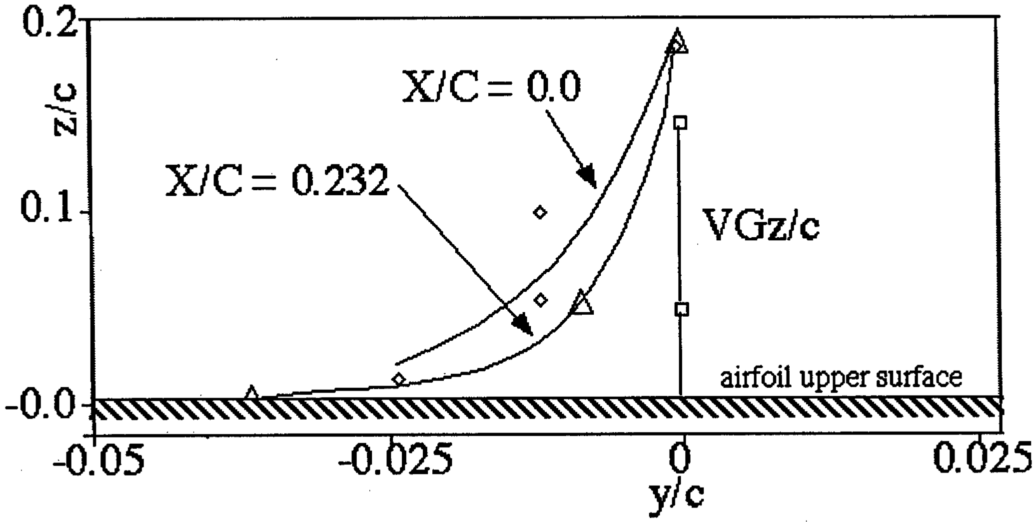

Figure 2.5: Vortex trajectories over a NACA0021 airfoil.

2.5.3 Vortex Stretching at the Leading Edge

An interesting feature noted on this airfoil was the stretching of the vortex core at the leading edge in a head-on interaction, as seen in Figure 2.6. The airfoil is much thicker (8.4cm) than the vortex core and the airfoil was not expected to cut the vortex. The core dilation has specific significance to vorticity redistribution as has been seen in the rotor/cylinder experiments and predicted by computations.

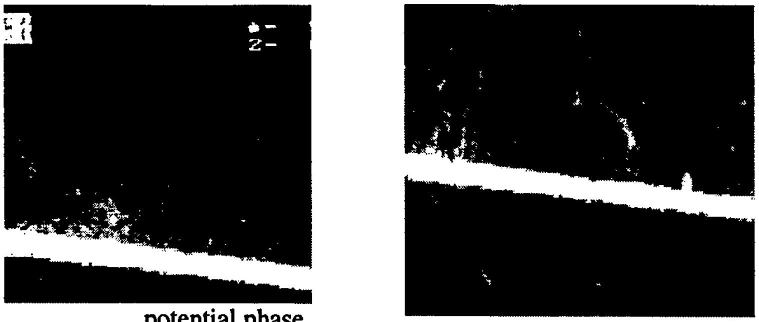

potential phase

headon interaction phase

The bright strip is the reflection from the LE of the NACA0021 airfoil

Figure 2.6: Vortex stretching at the leading edge of the NACA0021 airfoil; the camera is located upstream of the leading edge. Note the elongated features in the image on the right.

2.5.4 Results for the Flat-plate Airfoil

Flow Visualization

Figure 2.7 shows instantaneous cross-flow patterns at one spanwise location and three vortex generator (VG) heights. Three distinct phases of the interaction can be seen. In the top figure, $VG_{\frac{z}{c}} = 0$ and the vortex is more than one core radius above the top surface. This is the potential phase of the interaction and the vortex behaves according to potential flow expectations, i.e., the image-vortex theory. When the VG was taken lower such that $VG_{\frac{z}{c}} = -0.068$, the vortex core appeared flattened beyond $\frac{x}{c} = 0.66$. The core also appeared to become more diffuse for closer interactions with the surface. The location of core diffusion moved upstream as the vortex came closer to the surface. This is the close-interaction phase as seen in the middle figure. The bottom figure shows the head-on interaction phase. The vortex begins to split at a VG position of $VG_{\frac{z}{c}} = -0.083$. At $\frac{x}{c} = 0.171$ the vortex appears cut in two equal parts. Further downstream the individual split-up parts roll up to form two distinct circulatory regions above and below the airfoil. These regions diffuse out and break down by $\frac{x}{c} = 0.9$. The sense of circulation of the split-up vortices is the same as the parent vortex. The flow-visualization suggests that in the head-on interaction phase, the vortex does not breakdown ahead of the airfoil, but is split-up into secondary vortices. For a vortex of core size larger than the airfoil thickness, the vortex is cut by the airfoil. This is different from what was seen in the thick airfoil case where the vortex stretched at the leading edge but did not split.

Vortex Trajectories

Figures 2.8 , 2.9 , 2.10 , 2.11 show the planar trajectories of the vortex during interaction with the flat-plate. The vortex behaves according to potential flow expectations, i.e., the image vortex theory, as shown by its spanwise movement above and below the wing surface. At closer interactions, the spanwise movement is greater. As a result of this interaction the vortex bends as it goes over the surface of the airfoil. There is a spanwise displacement of the vortex beyond $\frac{x}{c} = 1.0$ and it increases as the vortex gets closer to the airfoil. We directed attention to the leading and trailing edges of the interacting airfoil to understand the effects of pressure gradients. Near the leading edge, the vortex tends to move in the positive spanwise direction relative to the centerline of the wing but by $\frac{x}{c} = 0.1$, the spanwise movement changes direction towards the port side. At the trailing edge, where there is an adverse pressure gradient the spanwise motion is accelerated towards the port side over the part of the airfoil.

The vortex stays above the airfoil even after the vortex generator has gone much below the airfoil. While the vortex filament is predominantly level on the top surface, on the bottom surface it gets further away from the surface as we go along the chord-length. The last figure shows the vortex motion in conjunction with the motion of the vortex generator. Downstream points on the vortex experience a bigger vertical jump from the top to the bottom surface. An interesting aspect is the hysteresis in vortex motion as it goes from the top to the bottom surface.

2.5.5 Results for the NACA0012 Airfoil

A last test case was conducted to resolve the issue of vortex trajectory asymmetries as discussed above. Figure 2.12 shows the vortex trajectories for VG angles of attack of $\pm 10^{o}$. A hysteresis is clearly seen in the vortex motion. The trajectory is not anti-symmetric for opposite angles of attack, implying that the asymmetry has to do with the vortex flow itself and not ground effects. Our present conjecture is that it might be due to the curvature of the inboard sheet of the vortex-generator.

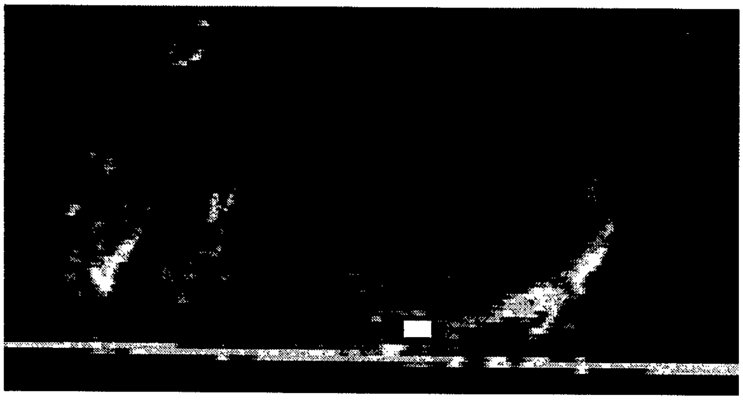

Potential Phase VGz/c = 0.0

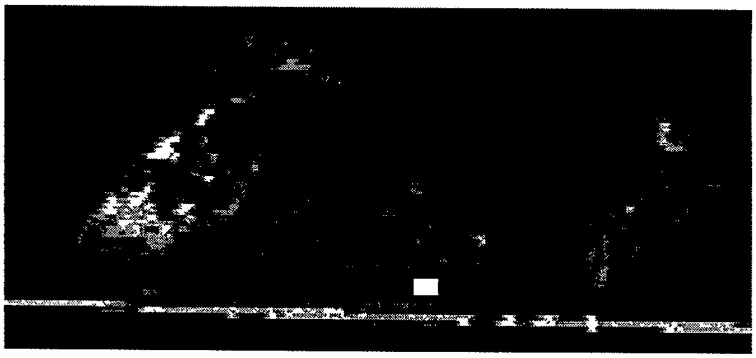

Close Interaction Phase VGz/c = -0.0683

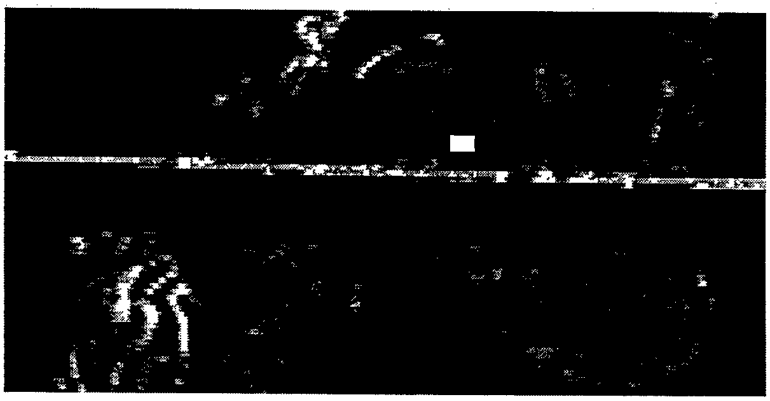

Head-on Interaction Phase VG z/c = -0.083

Figure 2.7: Growth in core size over the flat-plate airfoil; the rectangular box corresponds to bad pixels in the camera.

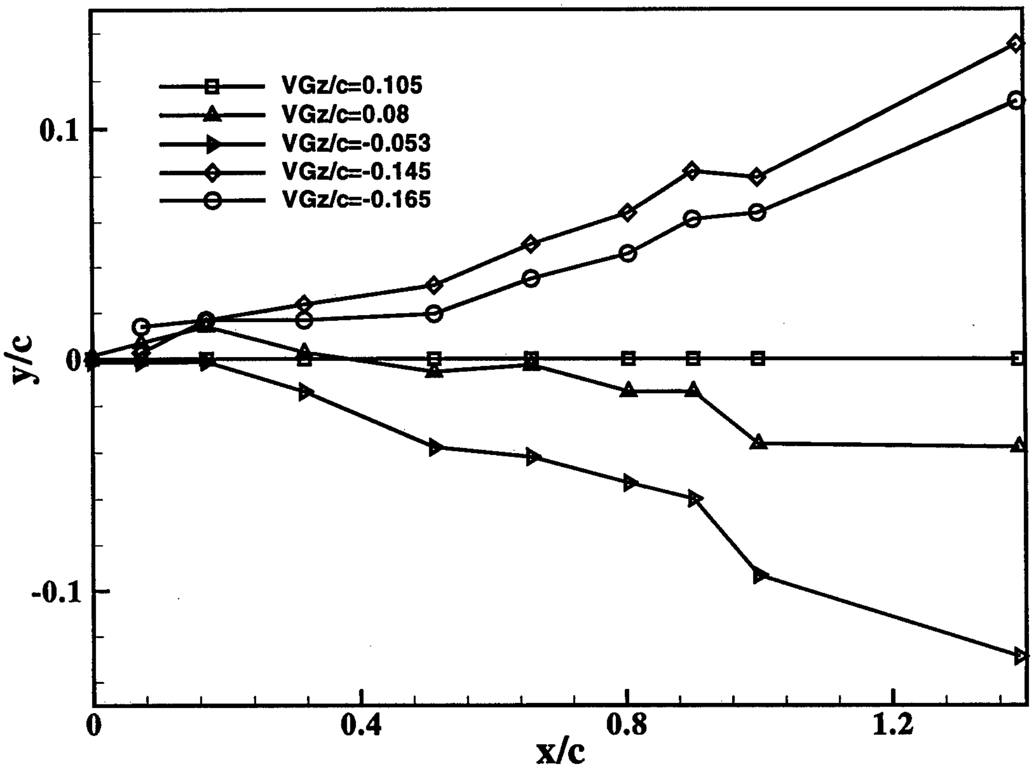

Figure 2.8: Trajectories of the tip vortex projected on the x-y plane for various vortex generator heights.

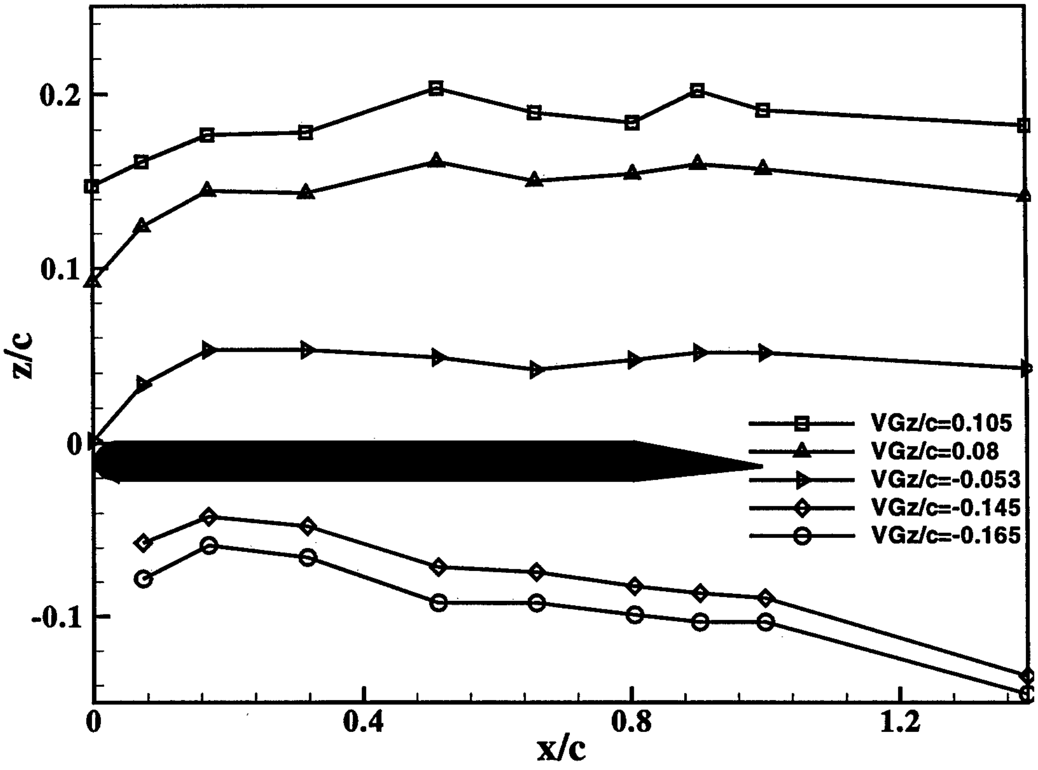

Figure 2.9: Trajectories of the tip vortex projected on the x-z plane for various vortex generator heights.

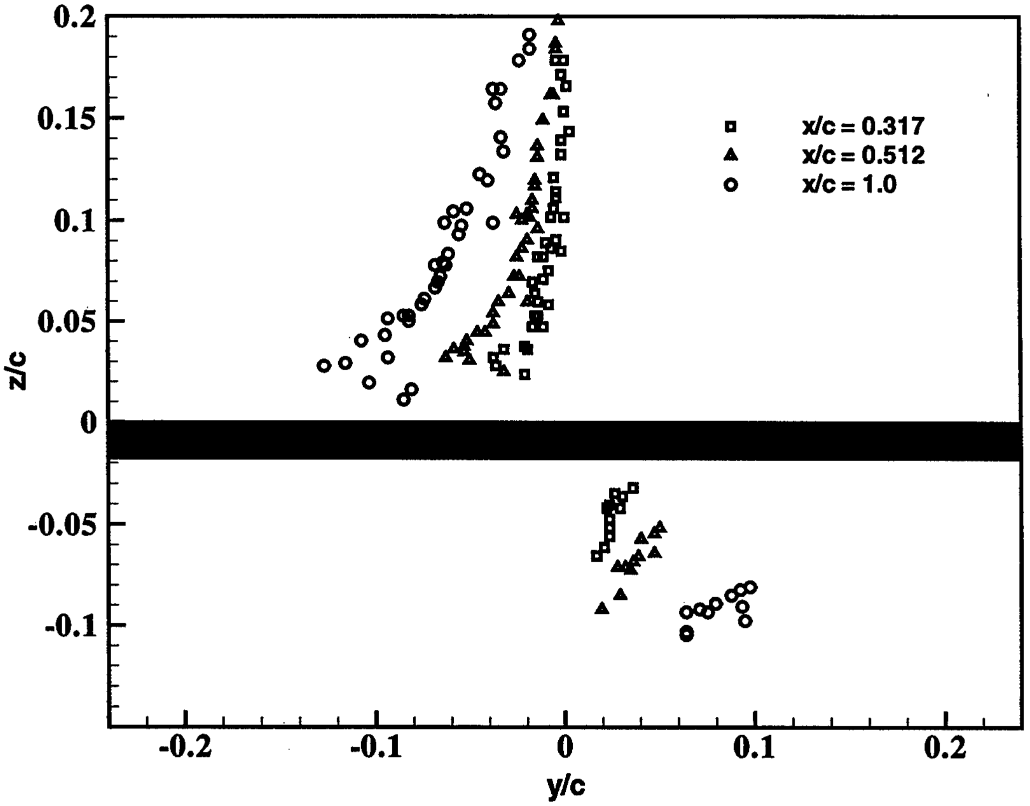

Figure 2.10: Trajectories of the tip vortex projected on the y-z plane for various chordwise locations.

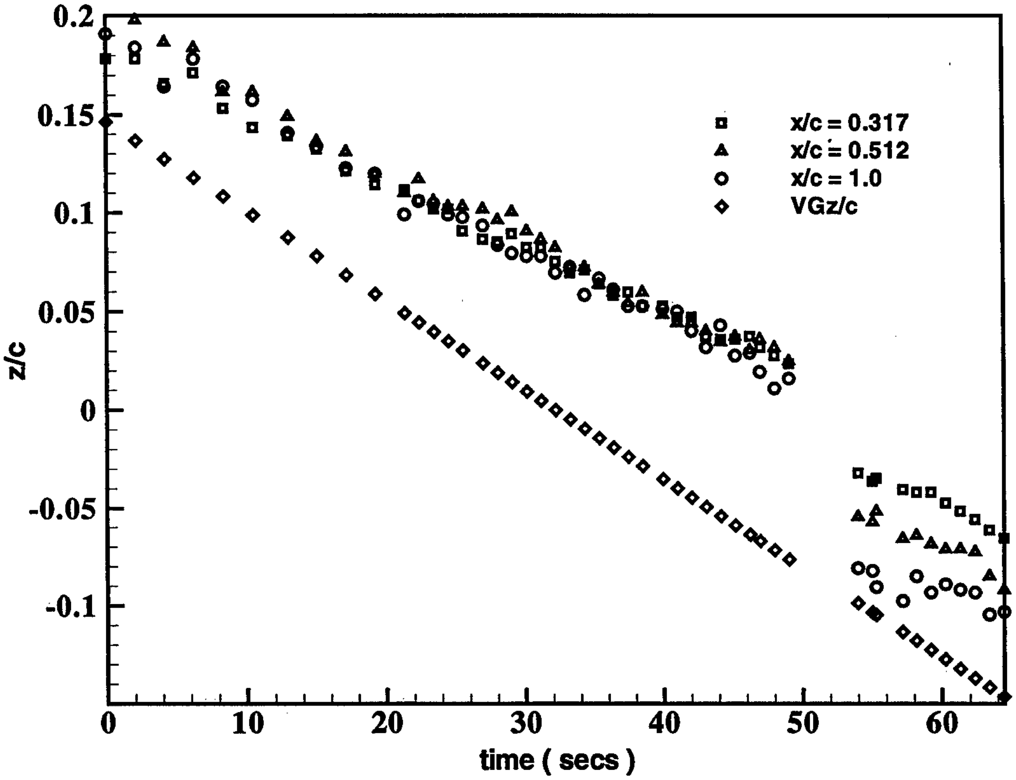

Figure 2.11: Vortex motion as a function of generating wing motion with time.

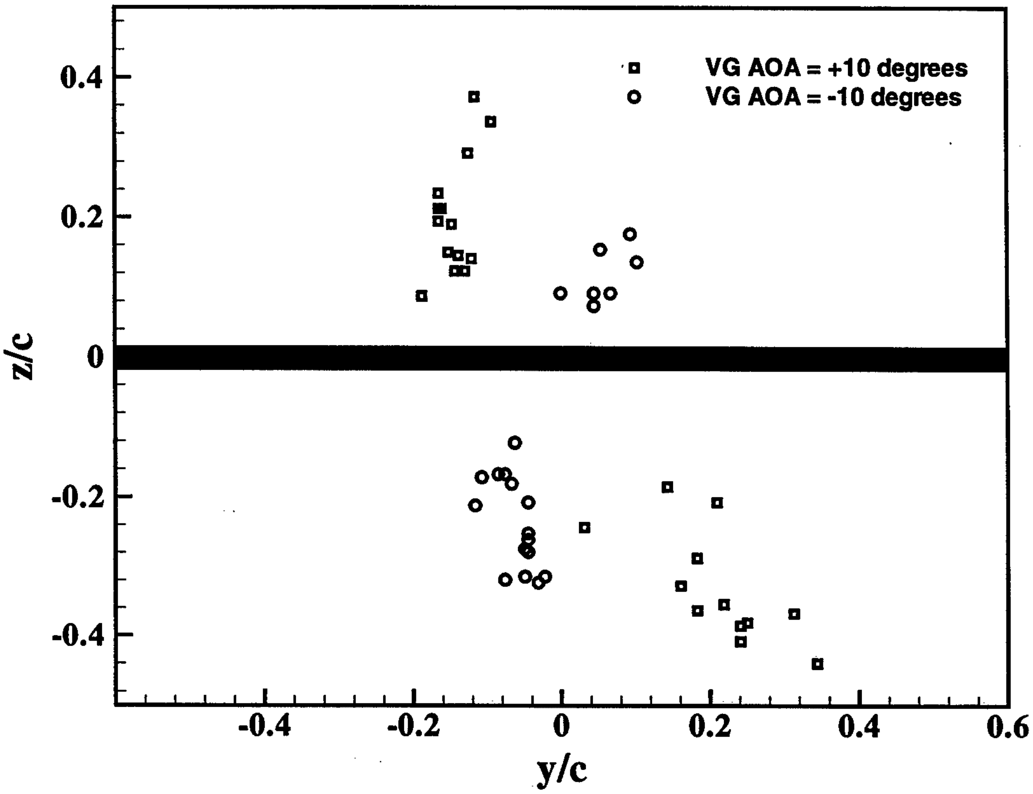

Figure 2.12: Asymmetry in vortex trajectories for the NACA0012 airfoil.

2.6 Conclusions

- The pressure signature of the vortex on the top-surface of the interacting airfoil increases as the vortex stand-off distance from the airfoil decreases.

- There is a spanwise movement of the vortex over the interacting airfoil, in agreement with the image vortex theory. The spanwise movement gets accentuated when the vortex moves closer to the interacting airfoil.

- The vortex vertical motion is steady, but lags behind the vortex-generator and stays on top of the interacting airfoil even after the vortex generator has gone below the plane of the interacting airfoil.

- For head-on collisions the tip-vortex core undergoes a sudden switching from the top to the bottom surface of the interacting airfoil. This switching is initiated by splitting of the vortex core into two vortices of the same sense of rotation, one staying above the airfoil while the other goes below the airfoil.

- The vortex does not straighten out behind the trailing edge of the interacting airfoil but continues to move spanwise.

- There is no reconnection of the two split vortices behind the trailing edge of the interacting airfoil.

- An adverse pressure gradient tends to favor the spanwise motion of the vortex over the interacting airfoil.

- There is an asymmetry in vortex motion above and below the airfoil; the vortex does not reach the same spanwise position when it is far above and below the airfoil. This is proposed to be due to the inboard wake of the vortex-generator.

Chapter 3

The Interacting Boundary Layer

3.1 Introduction

The three-dimensional unsteady interacting boundary-layer flow on an infinitely long circular cylinder placed near a three-dimensional vortex is considered in this Chapter. The primary motivation of this work is to determine whether the interacting boundary layer equations can describe a significant portion of the interaction between the tip-vortex and the airframe. In this regard, unfortunately, we show that a singularity in the equations is present and of a nature similar to that found in the classical boundary layer equations(Affes *et al.* (1994) and so much of the interaction cannot be described. Moreover, as pointed out by van Dommelen(1991), the interaction problem is numerically awkward. The difficulties are associated with the short length and time scales arising in the region where strong viscous/inviscid interaction takes place. Any serious attempt to solve this asymptotic interaction problem must include a solution procedure which is able to resolve the small scales.

In this Chapter we show that, as in the two-dimensional case (Peridier, Smith and Walker 1991; Xiao, Adams and Conlisk 1996), interaction cannot eliminate or delay the emergence of singularity in the unsteady boundary-layer equations; in fact, as in two dimensions, the singularity occurs sooner than in the classical case. A secondary motivation of the present work is that in the experiments at Georgia Tech a second suction peak in the pressure caused by separation had been observed when the tip vortex impinges the airframe (Affes *et al.* 1993c). This feature of the pressure distribution, although difficult to detect, cannot be calculated in the context of inviscid fluid dynamics (Affes and Conlisk 1993) or classical boundary-layer theory (Affes *et al.* 1994). The two dimensional results of Conlisk (1989) and Peridier, Smith and Walker (1991) for a vortex-driven boundary layer suggest that this influence may be simulated by allowing interaction between the inviscid outer flow and the viscous boundary-layer flow.

The extension of the interacting boundary-layer procedure to three dimensional flows has received only limited attention in recent years. Cebeci *et al.* (1986) used the approach to solve the steady transonic flow problem around a wing. In their study, two separate approaches are adopted to compute the viscous-inviscid interaction. The first one is the displacement thickness approach in which the surface coordinates are modified by the displacement thickness before carrying out the inviscid calculation. The second approach is the transpiration, or blowing approach in which the no-flux surface-boundary condition in the inviscid calculation is modified to allow a prescribed surface blowing condition, accounting for the addition or subtraction of mass flux through the displacement surface to maintain the growth or decay of the displacement thickness. Chen and Wu (1984) have developed an interacting boundary-layer procedure which uses an integral inverse boundary-layer method and an integral representation of the incompressible inviscid flow to investigate the separated flow over a flat plate with a protuberance. Edwards (1986) employs a quasi-simultaneous technique to couple a finite-difference representation of the viscous boundary-layer flow to an integral representation of the inviscid outer flow for the same geometry studied by Chen and Wu (1984). Smith (1986) has formulated the problem within the framework of triple-deck theory.

In the work mentioned above, the focus is on the steady flow. Indeed, computational results for the unsteady three-dimensional interacting boundary layer are rare. This is in part due to the extensive computer power required to compute accurate solutions to the three-dimensional unsteady problem. Recently, Yahiaoui (1993) studied the three-dimensional impulsive localized disturbance in a boundary layer on a flat plate using interacting boundary-layer theory. Triple-deck solutions involving the flow past an unsteady surface-mounted obstacle have recently been obtained by Duck (1990) and a discussion of the progress to date in unsteady interactive flows is given in that paper and in the subsequent papers by Smith (1991) and Hoyle and

Smith (1994).

The physical problem of interest is depicted in Figure 3.1; in general, the initial position of the vortex may be specified arbitrarily. In the present work we consider the case where the vortex is initially parallel to the x-axis; the initial position of the vortex is specified by the dashed line on Figure 3.1. We assume that the vortex is embedded in a stagnant medium and compute the solution to the interacting boundary-layer flow generated on the cylinder so that $U_\infty = V_\infty = W_\infty = 0$ on Figure 3.1. This assumption will not alter the basic results; only the time at which the singularity occurs will be affected. This assertion is based on several computations of the corresponding two-dimensional problems(Adams *et al.* 1995, Xiao *et al.* 1996) and on the classical boundary layer in three dimensions(Affes *et al.* 1994). The fluid is assumed to be incompressible, inviscid and irrotational outside the core of the vortex and away from the airframe boundary. To resolve the singular behavior, an adaptive grid is employed in the solution of the boundary-layer equations using Eulerian coordinates. This is sufficient to demonstrate the presence of the singularity; at the same time a second pressure spike does begin to emerge, although its amplitude is small during the time frame of the calculation. Despite the small amplitude of the second pressure spike in the computations, its emergence is suggestive of the origin of the second pressure spike in the rotorcraft experiments.

3.2 The Inviscid Flow

The inviscid flow in this geometry is calculated using a panel technique originally due to Hess and Smith (1967) and is thus somewhat different from the approach taken by Affes *et al.* (1994). The details of the panel method are standard and are presented in a previous version of this paper (Xiao *et al.* 1994); only a summary of the main features of the method are described here.

The infinitely long circular cylinder is first approximated by $M \times N$ rectangular constant source panels, where M is the number of panels along the cylinder and N is the number of panels around the cylinder. Similarly the vortex is broken into M+1 straight line segments of varying length. Figure 3.2 shows a three-dimensional oblique view of the cylinder panels and vortex segments. Here x, y and z are the global cartesian coordinates with origin at the cylinder center (Figures 3.1 and 3.2). Note that the panel size is not

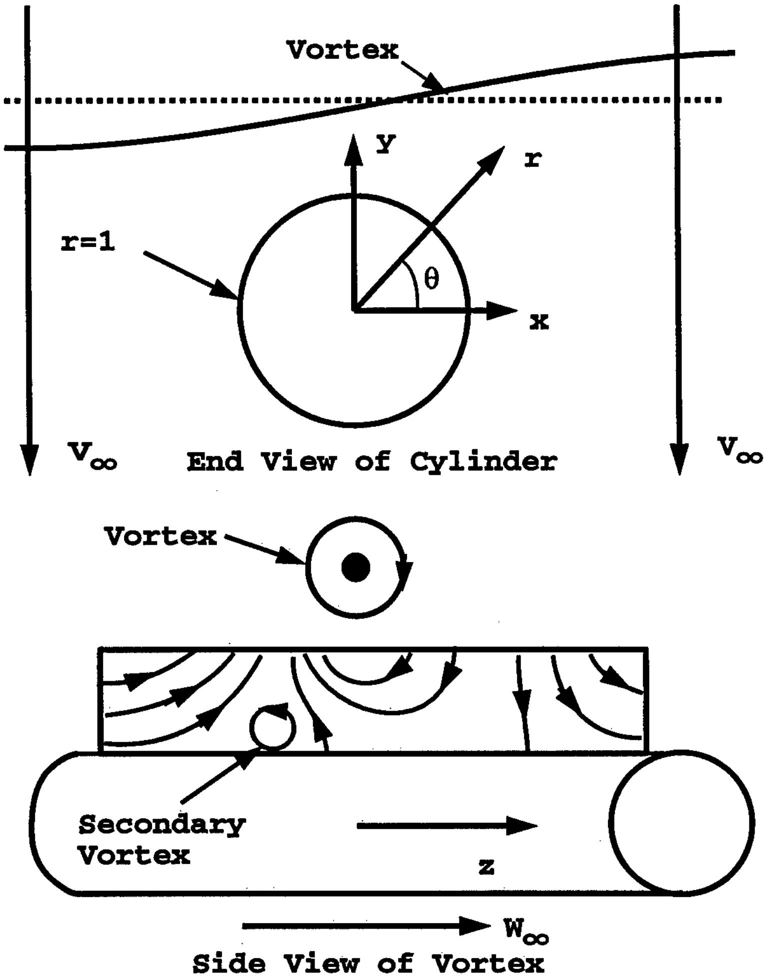

Figure 3.1: Geometry for the viscous flow problem. The solid line is the representation of a tip-vortex shed from a helicopter blade. The dashed line represents the initial condition for a vortex imbedded in a stagnant medium for which $W_\infty = U_\infty = 0$ as considered in this work. The origin of the z-coordinate follows the point on the vortex nearest the cylinder(see text).

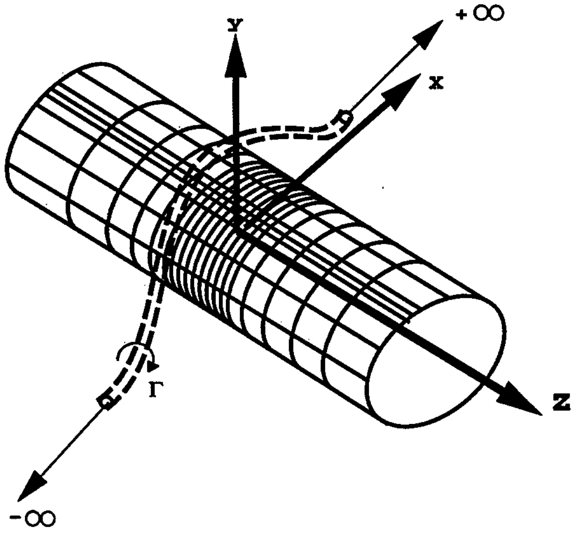

Figure 3.2: Three-dimensional oblique view of cylinder panels and vortex segments.

uniform and is designed to be the smallest in the region immediately under the vortex at the top of the cylinder.

To determine the velocity induced by a given panel on other neighboring panels, the local velocity field, assumed to be given by a uniform source distribution, is integrated over the rectangular panel. The influence exerted by the given panel on any other panel is obtained by evaluating the integrated velocity field at the midpoint of that panel. Let q_k denote the source density of panel k and v_j denote the velocity due to external sources normal to the true cylinder surface at the jth panel. Then the source strengths, q_k which are unknown, are obtained by solving the matrix equation

$$[A][Q] = [B], \tag{3.1}$$

where $[A]$ is an MN by MN matrix of influence coefficients; the element A_{jk} is the normal velocity at point j on the true cylinder surface above the midpoint of panel j due to the source panel k of unit source density. $[Q]$ is the column vector of source densities q_k, and $[B]$ is the column vector of normal velocities $-v_j$. From the above equation the source density vector $[Q]$ is given by

$$[Q] = [A]^{-1}[B], \tag{3.2}$$

where $[A]^{-1}$ is the inverse of $[A]$; it is important to note that for a fixed panel system, the matrix of influence coefficients $[A]$ is independent of time and its inverse $[A]^{-1}$ only needs to be calculated once. A LINPACK routine is employed to solve the system of equations defined by equation (3.1).

To numerically march the tip vortex in time, the vortex filament is broken into $M + 1$ segments. At any field point the velocity field induced by the vortex line is calculated by the Biot-Savart law with a smoothing parameter (Moore 1972, Affes *et al.* 1993a) which is given by

$$\vec{U}_V\left(\vec{X}, t\right) = -\frac{\Gamma}{4\pi}\int_C \frac{\left(\vec{X} - \vec{X}'\right) \times d\vec{X}'}{\left\{\mid \vec{X} - \vec{X}' \mid^2 + \mu^2\right\}^{3/2}} \tag{3.3}$$

where Γ is the circulation, and $\vec{X} = (x, y, z)$ is the field point and $\vec{X}' = (x', y', z')$ the position vector of the vortex. In the computational procedure, equation (3.3) is taken in dimensionless form, setting $\Gamma = 1$; all lengths are normalized by the cylinder radius a_c, and the velocity components are normalized by $\frac{\Gamma}{a_c}$. The flow in the vortex is similar to a Rankine vortex with radius a_v. The smoothing parameter is defined by $\mu = a_v e^{-3/4}$ where a_v is the dimensionless vortex core radius. Here we take $a_v = 0.11$ which is typical of the experiments (Affes *et al.* 1993a). For the time range of interest, in which the vortex is more than one core radius away from the cylinder, the effect of the smoothing parameter μ is negligible (Affes *et al.* 1993b).

In the actual computation, the panel geometry used to compute the inviscid flow corresponds to $M = 80$ panels in the z direction and $N = 40$ in the θ direction. The vortex is divided into 81 segments and the panel size and length of the vortex segments are not uniform. The lengths of the vortex segments vary according to

$$\Delta L_k = \Delta L_{min} + Bk^2, \quad for\ k = 1\ to\ K/2, \tag{3.4}$$

where

$$B = 6\frac{L_{max} - \frac{K}{2}\Delta L_{min}}{\frac{K}{2}(\frac{K^2}{2} + 1)}, \tag{3.5}$$

and ΔL_k is the length of the kth vortex segment. K is the total number of vortex segments which is taken to be $K = 81$, $\Delta L_{min} = 0.005$ is the minimum size of the vortex segments. L_{max} is the half length of the vortex filament, which is taken to be 5.0. The panel distribution in the θ direction also is not uniform and is clustered near the symmetry plane at the top of the cylinder. The minimum panel size employed is 2^o. The panel distribution in the z direction satisfies

$$\Delta L_{pk} = a_1 e^{[a_2(k-M/2-1)^2]}, \tag{3.6}$$

where ΔL_{pk} is the panel width of the kth panel. a_1 and a_2 are constants and a_1 specifies the minimum panel size and a_2 is used to cluster more panels underneath the main vortex. The clustering of panels is necessary since the flow varies rapidly right underneath the tip vortex.

The vortex is advanced by solving the differential equation in the Lagrangian frame using a simple Euler forward difference method; this first-order scheme has been compared to the fourth-order Adams-Moulton method and the results agree well for the time period used in the calculation. It should be noted that the vortex is advanced using the viscous time step, which is much smaller than that required for accuracy of the inviscid flow. In the computation, the $z-$coordinate is defined relative to the vortex head on the symmetry plane in the *fixed global* coordinates: $z = \bar{z} - Z_{vc}$; here Z_{vc} is the instantaneous vortex position on the top of the cylinder. The advantage of this definition is that the panels are always clustered right underneath the vortex head in the axial direction. It is also consistent with the coordinate definition in the boundary-layer calculation, as will be described below.

3.3 The Viscous Flow

The advance of the vortex toward the cylinder induces a three-dimensional unsteady boundary layer on the cylinder surface. To define the unsteady boundary-layer response, we write the boundary-layer equations in cylindrical coordinates as

$$\frac{\partial u_r}{\partial y} + \frac{\partial u_\theta}{\partial \theta} + \frac{\partial u_z}{\partial z} = 0, \tag{3.7}$$

$$\frac{\partial u_\theta}{\partial t} + u_r \frac{\partial u_\theta}{\partial y} + u_\theta \frac{\partial u_\theta}{\partial \theta} + (u_z - U_c) \frac{\partial u_\theta}{\partial z} = -\frac{\partial p}{\partial \theta} + \frac{\partial^2 u_\theta}{\partial y^2}, \tag{3.8}$$

$$\frac{\partial u_z}{\partial t} + u_r \frac{\partial u_z}{\partial y} + u_\theta \frac{\partial u_z}{\partial \theta} + (u_z - U_c) \frac{\partial u_z}{\partial z} = -\frac{\partial p}{\partial z} + \frac{\partial^2 u_z}{\partial y^2}, \tag{3.9}$$

where y is the boundary layer coordinate normal to the cylinder surface, θ is the coordinate in the azimuthal direction and z is the axial coordinate defined relative the axial position of vortex head on the symmetry plane defined just above. (u_r, u_θ, u_z) are the velocity components in the (r, θ, z) directions respectively and measured in the laboratory reference frame which is fixed in space. p is the pressure and U_c is the convection speed of the head of the vortex in the z direction. The dimensionless variables in equations (3.7), (3.8) and (3.9) are defined by

$$\theta = \theta^*, \; z = \frac{z^*}{a_c}, \; y = (\frac{r^*}{a_c} - 1) Re^{1/2}, \quad t = \frac{W_0}{a_c} t^*,$$

$$u_r = \frac{u_r^*}{W_0} Re^{1/2}, u_\theta = \frac{u_\theta^*}{W_\infty}, \quad u_z = \frac{u_z^*}{W_0}, \quad p = \frac{p^*}{\rho W_0^2} \tag{3.10}$$

where the superscript $*$ denotes corresponding dimensional variables. a_c is the radius of the cylinder, and W_0 is the velocity scale defined by $W_0 = \Gamma^*/a_c$. Hence $Re = W_0 a_c/\nu = \Gamma^*/\nu$ is the Reynolds number for a stagnant medium; using this nondimensionalization, $\Gamma = 1$ in equation (3.3). Equations (3.7-3.9) are subject to the following boundary conditions

$$u_\theta, u_z \text{ specified at } t = 0,$$

$$\frac{\partial u_\theta}{\partial z} = \frac{\partial u_z}{\partial z} = 0 \quad \text{as} \quad z \to \pm\infty,$$
$$u_r = u_\theta = u_z = 0 \quad \text{at} \quad y = 0,$$
$$u_\theta \to U_\theta \quad \text{as} \quad y \to \infty,$$
$$u_z \to U_z \quad \text{as} \quad y \to \infty,$$

where U_θ and U_z are the inviscid velocity components in the θ and z-directions respectively. Note that the streamwise derivatives of the velocity field are assumed to vanish far from the vortex. This is consistent with the decay of the influence of the vortex and this condition has been used successfully in past work (Affes *et al.* 1994).

It is convenient to use the Rayleigh variable defined by

$$\eta = \frac{y}{2\sqrt{t}}. \tag{3.11}$$

Also, it is necessary to cluster the points near the wall since the flow is expected to vary rapidly there with the clustering defined by

$$\eta = b_1(e^{b_2\xi} - 1), \tag{3.12}$$

where ξ is the new normal coordinate and has a range of [0,1]; b_1 and b_2 are constants used to cluster more points near the wall. With these transformations, the governing equations (3.7), (3.8) and (3.9) become

$$\xi_y \frac{\partial u_r}{\partial \xi} + \frac{\partial u_\theta}{\partial \theta} + \frac{\partial u_z}{\partial z} = 0, \tag{3.13}$$

$$\frac{\partial \vec{F}}{\partial t} + (\xi_t + u_r\xi_y - \xi_{yy})\frac{\partial \vec{F}}{\partial \xi} + \frac{\partial \vec{F}}{\partial \theta} + (u_z - U_c)\frac{\partial \vec{F}}{\partial z} - \xi_y^2 \frac{\partial^2 \vec{F}}{\partial \xi^2} = -\vec{P}, \tag{3.14}$$

where $\xi_t = \frac{\partial \xi}{\partial t}$, $\xi_y = \frac{\partial \xi}{\partial y}$ and $\xi_{yy} = \frac{\partial^2 \xi}{\partial y^2}$, $\vec{F} = (u_\theta, u_z)$, $\vec{P} = (\partial p/\partial\theta, \partial p/\partial z)$. The pressure gradient vector $\vec{P}$ is calculated using the inviscid surface speeds obtained from the panel code. The problem is started artificially by suddenly turning on the vortex at time $t = 0$. The immediate viscous response is a Stokes layer in the close vicinity of the cylinder surface, and we use this Stokes layer solution as our numerical initial conditions. This procedure is standard (Walker 1978) and the initial conditions are

$$u_\theta^0 = U_\theta^0 \operatorname{erf}\eta, \tag{3.15}$$

and

$$u_z^0 = U_z^0 \mathrm{erf}\eta, \tag{3.16}$$

where the superscript 0 indicates solutions at initial time.

Using the boundary-layer variables defined above and dropping the terms of $O(Re^{-1/2})$ the scaled vorticity field is given by

$$Re^{-1/2}\vec{\omega} = \omega_\theta \hat{i}_\theta + \omega_z \hat{i}_z, \tag{3.17}$$

where ω_θ and ω_z are respectively the azimuthal and the axial scaled vorticity components given by

$$\omega_\theta = -\xi_y \frac{\partial u_z}{\partial \xi}, \tag{3.18}$$

and

$$\omega_z = \xi_y \frac{\partial u_\theta}{\partial \xi}. \tag{3.19}$$

The scaled wall shear components may be written as

$$Re^{1/2}\tau_{r\theta} = \omega_z\Big|_{\xi=0} = \xi_y \frac{\partial u_\theta}{\partial \xi}\Big|_{\xi=0}, \tag{3.20}$$

$$Re^{1/2}\tau_{rz} = -\omega_\theta\Big|_{\eta=0} = \xi_y \frac{\partial u_z}{\partial \xi}\Big|_{\xi=0}, \tag{3.21}$$

where it is noted that $\tau_{\theta z}$ is small and $O(Re^{-1/2})$.

3.4 The Interacting Boundary-Layer Procedure

In the interacting boundary-layer approach employed in this study, the viscous flow inside the boundary layer is coupled with the external potential flow at each time step. The boundary-layer equations are solved with the external potential flow used to calculate the pressure gradient and the velocities on the cylinder surface. Within the iteration scheme during each time step, the inviscid surface speeds and the pressure gradients are updated based on the solution of the viscous flow. The influence of the viscous boundary-layer flow on the external potential flow is imposed by the introduction of the $O(Re^{-1/2})$ correction to the inviscid surface speeds. From the point of view of the inviscid flow, the presence of the boundary layer induces a displacement velocity normal to the surface (Moore 1952) according to

$$\sqrt{Re}V_d = \frac{\partial}{\partial z}(U_z\Delta_z) + \frac{\partial}{\partial\theta}(U_\theta\Delta_\theta), \tag{3.22}$$

where

$$\Delta_z = \int_0^{y_{max}} (1 - \frac{u_z}{U_z})dy = \int_0^1 (1 - \frac{u_z}{U_z})\frac{d\xi}{\xi_y} \tag{3.23}$$

$$\Delta_\theta = \int_0^{y_{max}} (1 - \frac{u_\theta}{U_\theta})dy = \int_0^1 (1 - \frac{u_\theta}{U_\theta})\frac{d\xi}{\xi_y} \tag{3.24}$$

The presence of the displacement velocity adds an additional component to the right side of the matrix equation for the source densities given by equation (3.1). The individual components of the right side vector are

$$B_j = -v_j + V_{d,j} \tag{3.25}$$

where v_j is the velocity normal to the cylinder surface induced by the vortex at the control point of the jth panel, $V_{d,j}$ is the displacement velocity calculated at the control point of the jth panel on the cylinder surface. Thus, through the displacement velocity term, the inviscid flow feels the growth of the boundary layer as an augmented panel source strength. Using this expression for B_j the panel source densities are updated at each iteration during each time step. In a previous unpublished version of this paper (Xiao, Burggraf and Conlisk, 1994) there is a sign error for the displacement velocity term, but it turns out that the pressure gradients are still large and the interaction has a similar effect on the flow.

3.5 The Adaptive Grid

It is well known that a small streamwise length scale (Elliott, *et al.* 1983 and Smith 1988) arises in the solution of unsteady boundary-layer equations in two dimensions. In the present three-dimensional problem, this is the case as well. Furthermore, since the location where this small length scale emerges moves with time, it is very difficult to numerically resolve the small scale structure locally on a fixed grid. Thus an adaptive grid is natural for resolving the 3D singular structure as required in the classical case.

If the z coordinate in the boundary-layer equations is allowed to move in time, then the time derivative of any quantity $\vec{F}$ on this moving grid becomes

$$\left.\frac{\partial \vec{F}}{\partial t}\right|_m = \left.\frac{\partial \vec{F}}{\partial t}\right|_f + \left.\frac{\partial \vec{F}}{\partial z}\right|_t \dot{z}, \tag{3.26}$$

where the subscript m denotes the moving frame and the subscript f the fixed frame. Here $\dot{z} = \frac{dz}{dt}$ is a Lagrangian derivative which describes the motion of the grid points and is termed the grid speed. Substituting the above equation into equation (3.14), we have,

$$\frac{\partial \vec{F}}{\partial t} + (\xi_t + u_r \xi_y - \xi_{yy})\frac{\partial \vec{F}}{\partial \xi} + \frac{\partial \vec{F}}{\partial \theta} + (u_z - U_c - \frac{dz}{dt})\frac{\partial \vec{F}}{\partial z} - \xi_y^2 \frac{\partial^2 \vec{F}}{\partial \xi^2} = -\vec{P}. \tag{3.27}$$

The grid movement is governed by a distribution law which states that

$$c d\zeta = W(z,t)dz, \tag{3.28}$$

where c is a constant. ζ is a uniformly distributed coordinate on the transformed plane on which the variation of solution is smooth. $W(z,t)$ is a weight function which is always positive. The simplest and most commonly used form for the weight function is

$$W(z,t) = 1 + \sum_1^m c_i M_i, \tag{3.29}$$

where the M_i are functions that are chosen to be appropriate to the solution and the c_i are constant coefficients. In the present calculation we take $m = 1$ and similar to Xiao, Adams and Conlisk (1996), we use a Gaussian function of the form:

$$M_1 = t \times \left(\left.\frac{d\Delta_z}{dz}\right|_{max} \right)^{\alpha_1} exp[-\beta_1 (z_c(t) - z)^2], \tag{3.30}$$

where t is time and α_1, β_1 are free parameters to be determined. $d\Delta_z/dz$ is the slope of the streamwise displacement thickness defined by equation (3.23). z_c is the location where the maximum slope of the displacement thickness occurs.

The constant c in the grid equation (3.28) can be eliminated by noting that on the transformed plane ζ is uniformly distributed and therefore we have

$$\int_{z_{i-1}}^{z_i} W(z,t)dz = \int_{z_i}^{z_{i+1}} W(z,t)dz. \tag{3.31}$$

In the present study, the trapezoidal rule is used to integrate the equation (3.31) to obtain the grid point z_i, which leads to

$$[W(z_i) + W(z_{i-1})]z_{i-1} - [W(z_{i-1}) + 2W(z_i) + W(z_{i+1})]z_i$$
$$+[W(z_i) + W(z_{i+1})]z_{i+1} = 0. \tag{3.32}$$

The above nonlinear system is solved by an iterative procedure with a relative convergence criteria of less than 10^{-4}. Note that the constant c and the actual range of values of ζ need never be calculated.

3.6 Numerical Methods

We solve the governing equations at each step by marching in time from an initial flow condition with appropriate boundary conditions. The second-order Crank-Nicolson scheme is employed in the present work to treat the time derivatives in the governing equations. In space, an implicit approximate factorization method similar to the Beam and Warming (1978) scheme is used to speed up the convergence rate at each time step. A second-order central difference is used for the space derivatives in the azimuthal direction and in the direction normal to the wall. A third-order upwind-differencing for arbitary grid spacing in the axial direction is employed for the convection terms.

The Crank-Nicolson finite difference representation of the time derivative in equation (3.27) centered at time level $(t + \Delta t/2)$ leads to

$$\left[1 + \frac{\Delta t}{2}(\xi_t + u_r\xi_y - \xi_{yy})^{n+\frac{1}{2}}\delta_\xi + \frac{\Delta t}{2}u_\theta^{n+\frac{1}{2}}\delta_\theta\right.$$
$$\left.+\frac{\Delta t}{2}(u_z - U_c - \dot{z})^{n+\frac{1}{2}}\delta_{z^{n+1}} - \frac{\Delta t}{2}(\xi_y^2)^{n+\frac{1}{2}}\delta_{\xi\xi}\right]\vec{F}^{n+1} = \vec{R}, \tag{3.33}$$

where Δt is the step size in time, $t = n\Delta t$ and n represents the time level t. The right hand side vector function $\vec{R}$ is defined by

$$\vec{R} = \left[1 - \frac{\Delta t}{2}(\xi_t + u_r\xi_y - \xi_{yy})^{n+\frac{1}{2}}\delta_{z^n} - \frac{\Delta t}{2}u_\theta^{n+\frac{1}{2}}\delta_\theta - \frac{\Delta t}{2}(u_z - U_c - \dot{z})^{n+\frac{1}{2}}\delta_{z^n}\right]\vec{F}^n$$

$$+\frac{\Delta t}{2}(\xi_y^2)^{n+\frac{1}{2}}\delta_{\xi\xi}(\vec{U}^{n+1} - \vec{U}^n) + \frac{\Delta t}{2}\vec{U}^{n+\frac{1}{2}}\delta_\theta(\vec{U}^{n+1} + \vec{U}^n)$$

$$+\frac{\Delta t}{2}(U_z - U_c - \dot{z})^{n+\frac{1}{2}}(\delta_{z^{n+1}}\vec{U}^{n+1} + \delta_{z^n}\vec{U}^n), \tag{3.34}$$

where $\vec{U} = (U_\theta, U_z)$. Here z^n denotes the streamwise grid at time step n and δ_{z^n} is defined just below. The operators δ_θ, δ_ξ and $\delta_{\xi\xi}$ are standard central difference operators in space. If the subscript i is used to denote the grid point in the θ direction, j the ξ direction and k the z direction, then the operators δ_θ,δ_ξ and $\delta_{\xi\xi}$ are defined by

$$\delta_\theta(.) = \frac{(.)_{i+1,j,k} - (.)_{i-1,j,k}}{2\Delta\theta}, \tag{3.35}$$

$$\delta_\xi(.) = \frac{(.)_{i,j+1,k} - (.)_{i,j-1,k}}{2\Delta\xi}, \tag{3.36}$$

$$\delta_{\xi\xi}(.) = \frac{(.)_{i,j+1,k} - 2(.)_{i,j,k} + (.)_{i,j-1,k}}{\Delta\xi^2}, \tag{3.37}$$

where (.) represents any one of the components of $\vec{F}$ or $\vec{U}$. The grid speed $(\dot{z})^{n+1/2}$ is calculated by the central difference

$$\dot{z}^{n+1/2} = \frac{z_k^{n+1} - z_k^n}{\Delta t}. \tag{3.38}$$

The velocities $u_r^{n+1/2}$ and $u_\theta^{n+1/2}$ occuring in the coefficients of the above difference equations are evaluated by a time average at n and $n+1$.

Third-order upwind-differencing is employed in the z direction. A general formulation of the third-order upwind-differencing for the finite-difference operator $C\delta_{z^n}$ can be written as,

$$\begin{aligned} C\delta_{z^n}(.) = {} & \frac{C-|C|}{2} d_k^n (.)_{i,j,k+2} + \left(\frac{C-|C|}{2} e_k^n + \frac{C+|C|}{2} f_k^n\right)(.)_{i,j,k+1} \\ & + \left(\frac{C-|C|}{2} g_k^n + \frac{C+|C|}{2} q_k^n\right)(.)_{i,j,k} + \left(\frac{C-|C|}{2} h_k^n + \frac{C+|C|}{2} l_k^n\right)(.)_{i,j,k-1} \\ & + \frac{C+|C|}{2} s_k^n (.)_{i,j,k-2}, \end{aligned} \tag{3.39}$$

where

$$d_k^n = -\frac{(z_k^n - z_{k-1}^n)(z_{k+1}^n - z_k^n)}{(z_{k+2}^n - z_k^n)(z_{k+2}^n - z_{k-1}^n)(z_{k+2}^n - z_{k+1}^n)}, \tag{3.40}$$

$$e_k^n = \frac{(z_{k+2}^n - z_k^n)(z_k^n - z_{k-1}^n)}{(z_{k+1}^n - z_k^n)(z_{k+1}^n - z_{k-1}^n)(z_{k+2}^n - z_{k+1}^n)}, \tag{3.41}$$

$$g_k^n = -\frac{(z_{k+1}^n + z_{k+2}^n - 2z_k^n)(z_k^n - z_{k-1}^n) - (z_{k+1}^n - z_k^n)(z_{k+2}^n - z_k^n)}{(z_{k+1}^n - z_k^n)(z_k^n - z_{k-1}^n)(z_{k+2}^n - z_k^n)}, \tag{3.42}$$

$$h_k^n = -\frac{(z_{k+1}^n - z_k^n)(z_{k+2}^n - z_k^n)}{(z_k^n - z_{k-1}^n)(z_{k+2}^n - z_{k-1}^n)(z_{k+1}^n - z_{k-1}^n)}, \tag{3.43}$$

$$f_k^n = \frac{(z_k^n - z_{k-1}^n)(z_k^n - z_{k-2}^n)}{(z_{k+1}^n - z_k^n)(z_{k+1}^n - z_{k-1}^n)(z_{k+1}^n - z_{k-2}^n)}, \tag{3.44}$$

$$q_k^n = \frac{(2z_k^n - z_{k-1}^n - z_{k-2}^n)(z_{k+1}^n - z_k^n) - (z_k^n - z_{k-1}^n)(z_k^n - z_{k-2}^n)}{(z_k^n - z_{k-1}^n)(z_k^n - z_{k-2}^n)(z_{k+1}^n - z_k^n)}, \tag{3.45}$$

$$l_k^n = -\frac{(z_{k+1}^n - z_k^n)(z_k^n - z_{k-2}^n)}{(z_k^n - z_{k-1}^n)(z_{k+1}^n - z_{k-1}^n)(z_{k-1}^n - z_{k-2}^n)}, \tag{3.46}$$

$$s_k^n = \frac{(z_{k+1}^n - z_k^n)(z_k^n - z_{k-1}^n)}{(z_k^n - z_{k-2}^n)(z_{k+1}^n - z_{k-2}^n)(z_{k-1}^n - z_{k-2}^n)}, \tag{3.47}$$

$C = (u_z - U_c - \dot{z})$ for $(.) = \vec{F}$ or $C = (U_z - U_c - \dot{z})$ for $(.) = \vec{U}$ is the convective speed in the moving frame. For the operator $C\delta_{z^{n+1}}$, replace the superindex n by $n+1$ in the above expressions.

The implicit factorization of the finite-difference equation (3.33) (Beam and Warming 1978) is

$$(EGH)\vec{F}^{n+1} = \vec{R}, \tag{3.48}$$

where E, G and H are finite difference operators expressed by

$$E = [1 + \frac{\Delta t}{2}(\xi_t + u_r\xi_y - \xi_{yy})^{n+\frac{1}{2}}\delta_\xi - \frac{\Delta t}{2}(\xi_y^2)^{n+\frac{1}{2}}\delta_{\xi\xi}], \tag{3.49}$$

$$G = [1 + \frac{\Delta t}{2}u_\theta^{n+\frac{1}{2}}\delta_\theta], \tag{3.50}$$

$$H = [1 + \frac{\Delta t}{2}(u_z - U_c - \dot{z})^{n+\frac{1}{2}}\delta_{z^{n+1}}]. \tag{3.51}$$

The implicit factorization (3.48) is an approximation to the original finite-difference equation (3.33) and the truncation error is $O(\Delta t^2)$; this is the same as the truncation error of the finite-difference approximation to the time derivatives of the boundary-layer equations employed in the present study. To solve equation (3.48), we define two intermediate variables $\vec{F}^{**} = H\vec{F}^{n+1}$ and $\vec{F}^{*} = G\vec{F}^{**}$. Three steps are needed to obtain the solution $\vec{F}^{n+1}$, as described below. These correspond to successive sweeps of the mesh in ξ, θ and then z.

The three steps required are :

step 1:

$$E\vec{F}^{*} = \vec{R}, \tag{3.52}$$

step 2:

$$G\vec{F}^{**} = \vec{F}^{*}, \tag{3.53}$$

step 3:

$$H\vec{F}^{n+1} = \vec{F}^{**}. \tag{3.54}$$

Equation (3.52) describes a tridiagonal system in the ξ direction and equation (3.53) is tridiagonal in θ. Because of the third order upwinding scheme used in the z-direction, equation (3.54) is pentadiagonal and is solved by a Gaussian elimination procedure.

At the beginning of the iterative procedure at each time level, the terms u_r^{n+1} and u_θ^{n+1} occuring in the above equation are not known at time level $n+1$. To obtain a time accurate solution, an iteration procedure is employed and at each iteration the values u_r^{n+1} and u_θ^{n+1} are approximated by the mth iterate u_r^m and u_θ^m respectively. The converged solutions are obtained when the following relative-criterion test is satisfied:

$$\left| \frac{\vec{F}^{m} - \vec{F}^{m-1}}{\vec{F}^{m-1}} \right| < 10^{-5}. \tag{3.55}$$

The iteration process at each time step is given below. First, we assume that solutions for the boundary-layer flow and the inviscid outer flow are known at time level n; from this solution we calculate the displacement velocity V_d on the cylinder surface according to equation (3.22). This displacement velocity then is applied to the source panel as a boundary condition for the external flow. After solving the matrix equation for the source panel density given by equation (3.1), the velocity at each of the vortex nodes is calculated and the locus of the vortex at the time level $n+1$ is obtained by advancing each point on the vortex forward in time using the simple first-order Euler formula. After obtaining the new vortex nodes, the surface speeds and the pressure gradients are predicted at the new time level. Equations (3.27) then are solved to obtain a predicted boundary-layer solution at time level $n+1$. Next, an updated displacement velocity is obtained from (3.22). This displacement velocity again is added to the right hand side of the matrix equation (3.1) to obtain updated inviscid surface speeds and pressure gradients. An updated boundary-layer solution at time level $n+1$ then is obtained by solving equation (3.27). This iteration process continues until convergence. For a relative convergence criteria of 10^{-5}, it usually requires four to seven iterations for both the boundary-layer solution and the inviscid surface speeds to converge.

The boundary condition in the y-direction is imposed at a large but finite value of η, say $\eta = \eta_{max}$. In general, $\eta_{max} = 6$ is used in the present calculation which corresponds to $b_1 = 0.01$ and $b_2 = 6.40$ in equation (3.12).

3.7 Results

The results to be discussed here are for $Re \to \infty$, 10^8, 10^7 and 10^6. The initial configuration of the vortex corresponds to a straight filament oriented at a right angle to the generators of the cylinder at $t = 0$. This initial position is represented by $x = s$, $y = 1.3$ and $z = 0$, and this is depicted on Figure 3.1 by the dashed line. In the current calculation, $a_1 = 0.0005$ and $a_2 = 0.0051$ are used in equation (3.6). With this choice of a_1 and a_2, the half length of the cylinder is equal to 5.5615. All the parameters chosen above have been numerically tested and they give at least two digit accurate solutions for the inviscid surface speeds and vortex positions.

Figure 3.3 shows the results for the vortex position corresponding to $t = 0.3$, $t = 0.6$ and $t = 0.85$ respectively when the influence of the boundary layer is not taken into consideration. The time step used to advance the vortex varies from 0.005 to 0.0001. Although a simple forward Euler scheme is used to advance the vortex in the present calculation, the inviscid flow results agree very well with a fourth-order Adams-Moulton method up to $t = 1.0$ for a purely inviscid calculation. The time step used to march the vortex is the same as the time step used in the boundary-layer calculations.

The boundary-layer grid extends from $z = -1.5$ to $z = 1.5$. Experience

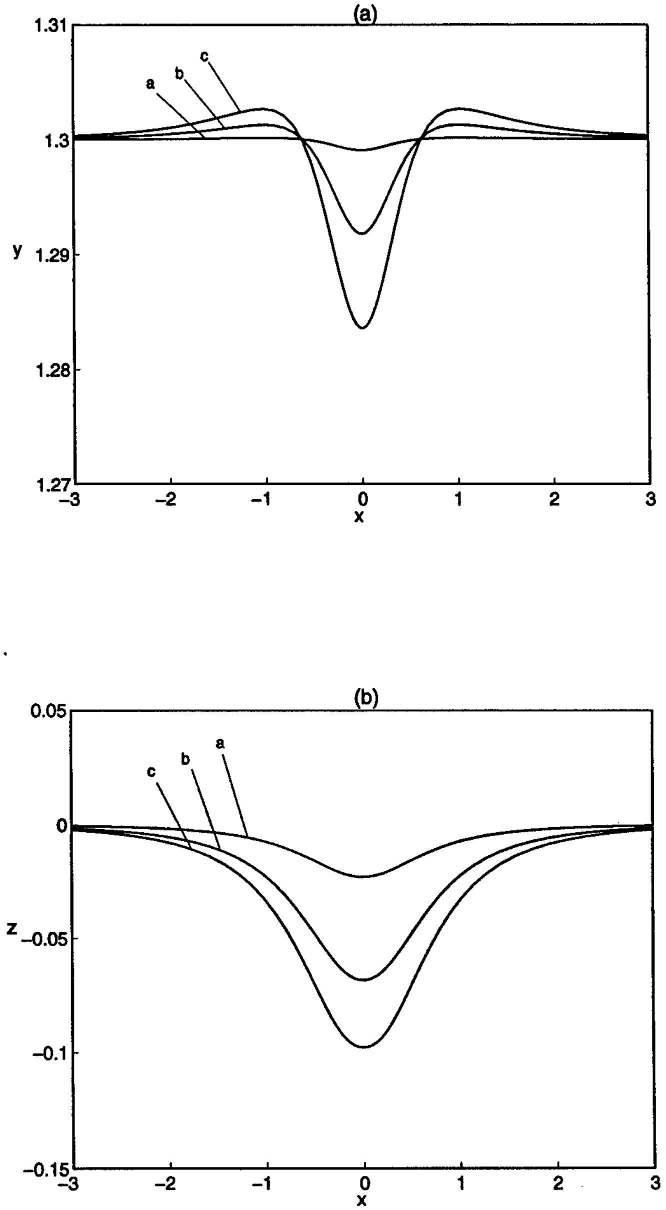

Figure 3.3: Vortex trajectory at several times. a: $t = 0.3$, b: $t = 0.6$, c: $t = 0.87$. (a) End view, (b) top view.

with the classical boundary-layer flow (Affes *et al.* 1994) has suggested that this length is sufficient due to the rapid decay of the vortex flow upstream and downstream. Since the grid size used in the boundary-layer calculation is varying with time and therefore differs from the panel size which is fixed in the potential-flow calculation, cubic-spline interpolation is used to transfer data between these two systems. Two grid sizes in (z, θ, η) have been tested corresponding to $(121, 64, 61)$ and $(241, 96, 61)$ in the solution of the boundary-layer equations. The solutions are most sensitive to the grid size in the z direction. To determine the accuracy of the solution, results were produced for each streamwise grid; the pressure gradient results were compared since this quantity provides the most stringent test of accuracy. The results indicate that an overall two digit accuracy has been achieved for these two grids. Similarly different grid spacings in the other two directions and time steps were tested for accuracy as well. It should be noted that for all of the grids tested the singular time can be predicted within two digits. The results presented below are for the grid $(241, 96, 61)$. The time step used for both the inviscid and viscous flows is the same and decreases when the solution approaches its terminal stages. For the finest mesh corresponding to over 700,000 grid points the classical boundary layer flow takes about 8 CPU hours on a single Cray YMP processor, with the interacting boundary-layer flow taking about twice as long.

In the following three sections, the viscous flow results for $Re \to \infty$ are presented first, followed by the results of interacting boundary-layer flow for $Re = 10^8$, 10^7 and 10^6.

3.7.1 Results for Classical Boundary-Layer Flow

The classical unsteady boundary-layer solutions corresponding to $Re \to \infty$ are presented in this section.

Figure 3.4 shows the trajectory of the moving z grid in the classical boundary-layer calculations. To clarify the view, only one fourth of the total 241 grid points are shown in this figure. It can be seen that the streamwise grid points are appropriately collapsed in the region where the flow is expected to vary rapidly. Based on a number of experiments, $\alpha_1 = 0.6$ and $\beta_1 = 500$ are used in the weight function (3.30) in all of the adaptive grid calculations. For the classical boundary layer, the minmum grid size is 0.00035 at t=0.87; this corresponds to about 127 grid points between $z = -0.1$ and $z = 0$. A uniform grid with this grid spacing requires about 8600 grid points

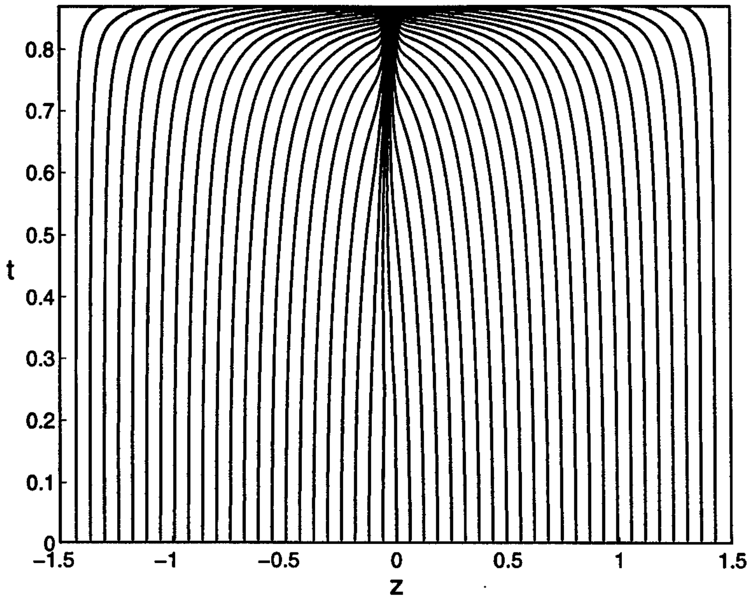

Figure 3.4: Trajectories of grid points; every 4th grid point trajectory of 241 is plotted for $Re \to \infty$.

for this value of Δz. The time step used is not fixed and is gradually reduced in the computation in order to obtain a time accurate solution. The time step used for the classical boundary-layer problem is shown in Table 3.1.

Table 3.1: Time step at different stages of the calculation for CBL.

t	0-0.6	0.6-0.7	0.7-0.8	0.8-0.85	0.85-0.87
dt	0.005	0.001	0.0005	0.00025	0.0001

The overall development of the flow on the symmetry plane is similar to that of the two-dimensional case. At some time after the impulsive start the flow begins to reverse in the boundary layer below the vortex and a closed eddy forms which is visible in the coordinate system travelling with the speed of the vortex head. This reversed-flow region had been observed experimently by Harvey and Perry (1971) and it was demonstrated that such a region will appear in computations in two dimensions by Walker (1978). The eddy grows in size as time goes on and this growth is accompanied by the

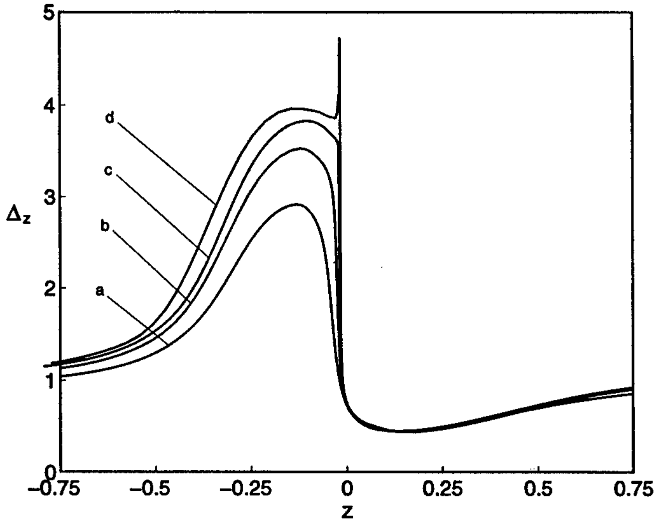

Figure 3.5: Displacement thickness on the symmetry plane for $Re \to \infty$. a: $t = 0.7$,b: $t = 0.8$, c: $t = 0.85$, d: $t = 0.87$.

rapid rise of the displacement thickness. The displacement thickness defined by (3.23) is shown in Figure 3.5 on the symmetry plane at $t = 0.7, 0.8, 0.85$ and 0.87. A spike starts to develop at $t = 0.85$ and grows rapidly with time thereafter. This phenomenon appears in two dimensional results of flow around a suddenly started circular cylinder calculated by van Dommelen and Shen (1981) using Lagrangian formulation. Physically, the spike reflects the fact that under the action of axial adverse pressure gradient, a fluid element located in the reversed flow region on the symmetry plane is squeezed and its dimension in the axial direction contracts, conservation of mass then forces it to expand in the normal direction, resulting in the ejection of fluid above it into the main stream. The growth rate of the spike depends on the rate at which the dimension of the fluid element shrinks in the axial direction. Indeed, our computational results show that the spike in the displacement thickness distribution becomes thinner and thinner as the magnitude of the spike gets larger and larger.

The wall shears, on the other hand, remain regular, as can be seen in Figure 3.6, which shows the axial wall shear on the symmetry plane for times corresponding to Figure 3.5. This is due to the fact that the normal derivatives of the wall shears are balanced by the surface pressure gradients calculated from the inviscid outer flow. Since the surface pressure gradients

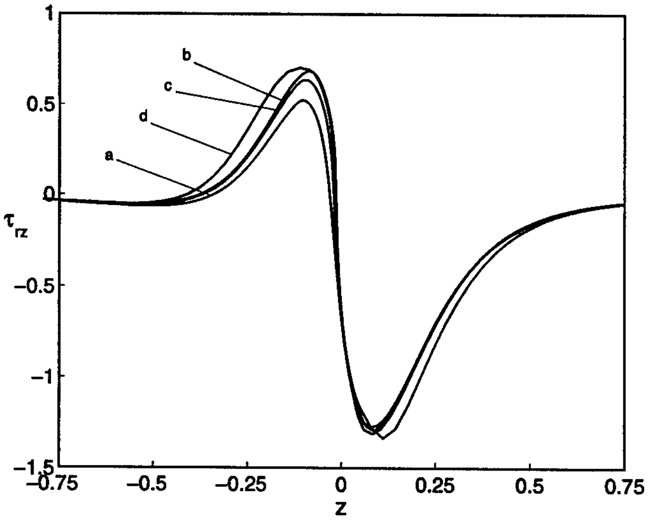

Figure 3.6: Wall shear stress on the symmetry plane for $Re \to \infty$. a: $t = 0.7$,b: $t = 0.8$, c: $t = 0.85$, d: $t = 0.87$.

remain smooth in the classical boundary-layer analysis, the wall shear stress does not develop a spike, even though the displacement thickness does.

The streamline patterns suggest that the flow is attached for times less than about $t = 0.3$. Near this time an eddy begins to form and is clearly visible by $t = 0.5$. The three-dimensional streamlines and surface streamlines at $t = 0.87$ are depicted in Figure 3.7. These three-dimensional streamlines have been produced by solving the system

$$\frac{d\theta}{u_\theta} = \frac{dr}{u_r} = \frac{dz}{u_z} = dS, \tag{3.56}$$

where S is a parameter that measures the distance along a given streamline. These equations are approximated using simple forward differences for the derivatives. Each streamline is traced by selecting a step ΔS and following Duck and Burggraf (1986)

$$(u_z^2 + u_\theta^2 + u_r^2)\Delta S = 0.005. \tag{3.57}$$

In general, points defining a streamline do not coincide with the mesh grid points and three-dimensional linear interpolation is used to compute the velocities u_z,u_θ, and u_r. To produce the streamline plots, the range $-0.75 \leq$

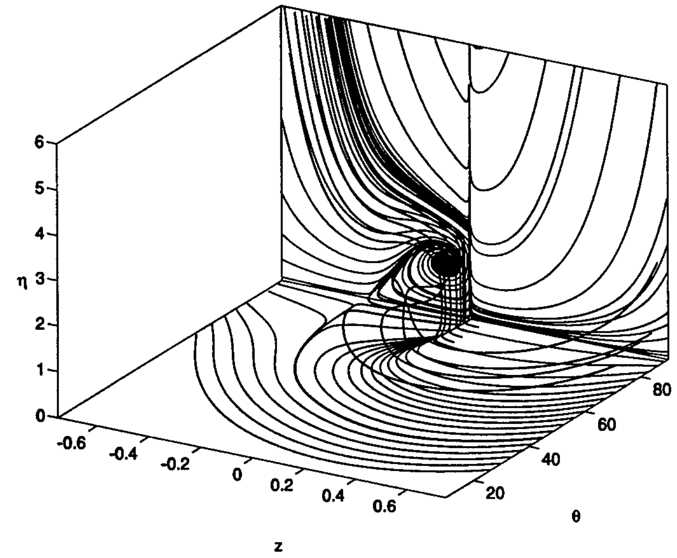

Figure 3.7: Instantaneous streamlines and surface streamlines for $Re \to \infty$ and $t = 0.87$.

$z \leq 0.75$ is considered and a limit of 3000 points along a streamline is imposed to reduce computer time. The initial starting point for a given streamline is a matter of choice and a number of different classes of initial positions were tested. The streamlines which seem to end in the flow field are actually initial starting points as discussed by Affes *et al.* (1994).

The flow patterns shown in Figure 3.7 indicate the presence of a thin spike in the streamlines on and near the symmetry plane at about $z = 0$. The z location of the spike coincides with the z location of the spike in the distribution of the displacement thickness shown in Figure 3.5. Clearly, the spikes in the streamlines convey an impression that the flow is in a process of ejection vertically into the inviscid free stream. The magnitude of the spike reaches a maximum on the symmetry plane and diminishes gradually in the cross flow direction and eventually disappears after about 10^o away from the symmetry plane. This is due to the fact that the axial adverse pressure gradient is largest on the symmetry plane. Therefore, flow separation will first occur on the symmetry plane. It should be noted that the total number of singular points in the surface streamlines obey the topological requirement which states that the number of saddle points equal the number of nodal points for an infinitely long cylinder(Flegg 1974). The vorticity distribution for this flow has characteristics which are similar to that described by Affes *et al.*(1994) and results are omitted for brevity.

For the grid of 241 points, the numerical results start to show oscillation slightly after $t = 0.87$ and the calculation fails to converge thereafter. These oscillations are numerical in character as evidenced that they could be eliminated by reducing the grid spacing; that is, at larger streamwise grid spacings corresponding to 121 points, the oscillations appear sooner. On a fixed grid, the same flow numerically fails after $t = 0.8$.

The primary purpose of this paper is to calculate the solution for the interacting boundary layer solution in three dimensions and the results for this case are discussed next.

3.7.2 Results for Interacting Boundary-Layer Flow

The results presented are for $Re = 10^8$, 10^7 and 10^6 respectively. The time steps used in these calculations are listed in Table 3.2. The interacting procedure is implemented from the start. As expected, at all three Reynolds numbers considered, the development of the viscous boundary-layer flow and the inviscid outer flow is not affected much by interaction until the later phases in the calculation. Thereafter, both the viscous boundary-layer flow and the inviscid outer flow start to deviate from the classical problem. The onset time of significant interaction depends on the Reynolds number. For the grid parameters $\alpha_1 = 0.6$, and $\beta_1 = 500$, for $Re = 10^8$, the mininum

Table 3.2: Time steps used in the calculations for the three Reynolds numbers.

$Re = 10^8$				
t	0-0.6	0.6-0.7	0.7-0.75	0.75-0.778
dt	0.005	0.001	0.00025	0.0001
$Re = 10^7$				
t	0-0.55	0.55-0.65	0.65-0.70	0.70-0.73
dt	0.005	0.001	0.0002	0.0001
$Re = 10^6$				
t	0-0.55	0.55-0.6	0.6-0.63	0.63-0.675
dt	0.005	0.0005	0.0001	0.00005

streamwise grid spacing at $t = 0.77$ is 0.001. There are about 69 grid points between $z = -0.1$ and $z = 0$. For $Re = 10^7$, the minimum grid size is 0.0013, there are about 56 grid points between $z = -0.1$ and $z = 0$ and for $Re = 10^6$, the minimum grid size is 0.0029, and there are about 27 grid points between $z = -0.1$ and $z = 0$. The minimum grid spacing increases with decreasing Reynolds number since the interaction region widens.

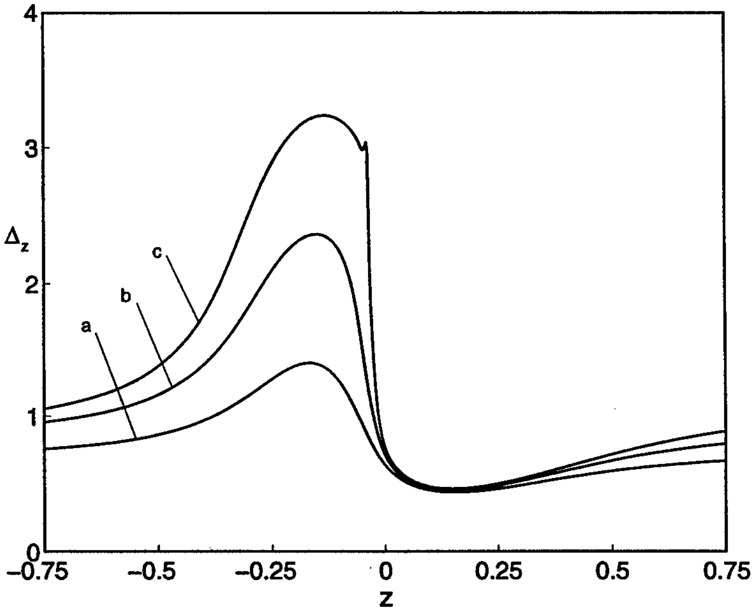

Figure 3.8: Streamwise displacement thickness on the symmetry plane for $Re = 10^8$ at a: t=0.4, b: t=0.6, c: t=0.77.

Figure 3.8 shows the streamwise displacement thickness on the symmetry plane for $t = 0.4$, 0.6 and 0.77. The results at $t = 0.4$ and $t = 0.6$ are virtually indistinguishable from the classical boundary-layer flow solution. But at $t = 0.77$, a spike, which is absent in the classical boundary-layer solution, develops in the displacement thickness. Slightly after $t = 0.77$, the calculation becomes numerically unstable and eventually fails to converge. This is evidence that the interacting boundary layer becomes singular sooner than the classical boundary layer. Figure 3.9 shows the shear stress on the symmetry plane for $Re = 10^8$ at two times. Note the appearance of the spike at $t = 0.77$. In the classical case, the wall shear is always smooth, even as the boundary layer solution breaks down, as can be seen by examining Figure

3.6. This clearly indicates that a different kind of flow structure is present in the interacting boundary-layer solution.

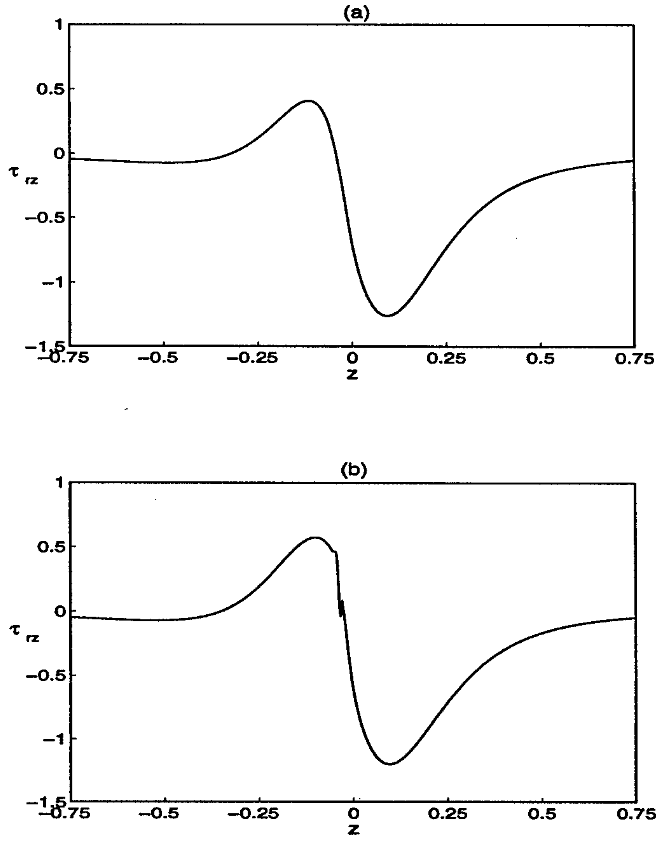

Figure 3.9: Wall shear stress for $Re = 10^8$ at (a) t=0.6, (b) t=0.77.

To see how the inviscid flow evolves when it is coupled with the boundary-layer solution, the streamwise pressure gradient on the symmetry plane is plotted in Figure 3.10 for $t = 0.6$ and 0.77. The pressure gradient is smooth for $t = 0.6$; however, at $t = 0.77$, it has developed a spike which has a much larger magnitude than the spike in the shear stress. This spike is closely related to the spike in the shear stress through the axial momentum equation evaluated on the cylinder. The pressure depicted in Figure 3.11 shows an irregularity late in the calculation at $t = 0.77$. While not large at this time, the result indicates that the pressure is likely to develop a singularity as well; this corresponds to the "severe breakup" scenario originally described

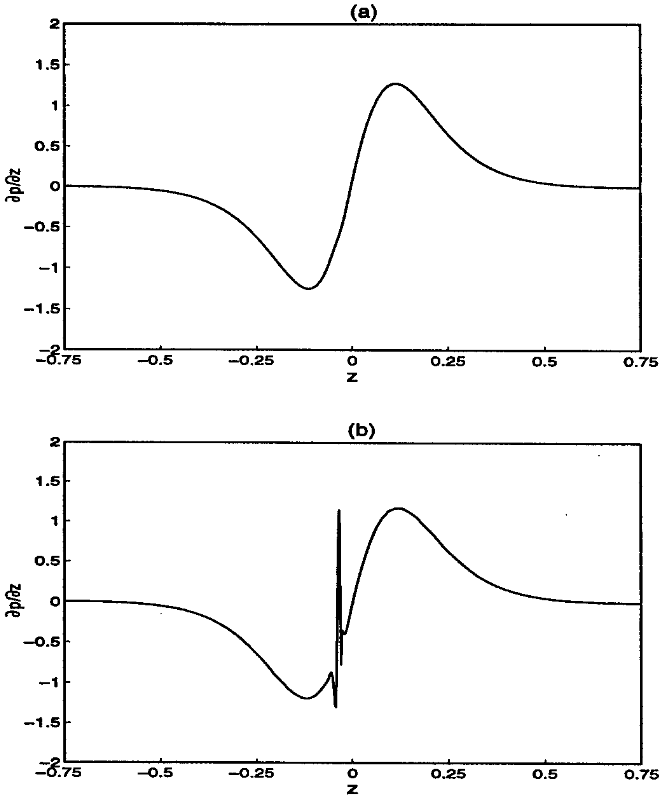

Figure 3.10: Streamwise pressure gradient on the symmetry plane for *Re* = 10^8 at (a) t=0.6, (b) t=0.77.

theoretically by Smith (1988) in two dimensions(See also Hoyle and Smith (1994) although "severe breakups" of the form described in the present results are not considered in that paper.)

Figure 3.12 shows the three-dimensional view of the streamwise pressure gradient at $t = 0.77$. From this figure we can see that the spike seen in Figure 3.10(b) diminishes in the azimuthal direction, and eventually disappears after about 20^o from the symmetry plane. The three dimensional view of the displacement velocity at $t = 0.77$ is depicted in Figure 3.13. This displacement velocity displays a crescent shape right under the main vortex. The crescent shape has a very thin length scale in the axial direction and extends about 20^o in the azimuthal direction from the symmetry plane. It is this displacement velocity that is added to the inviscid flow and causes the

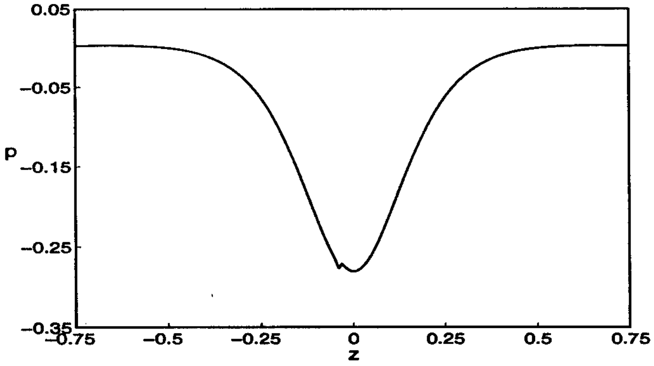

Figure 3.11: Pressure on the symmetry plane for $Re = 10^8$ at t=0.77.

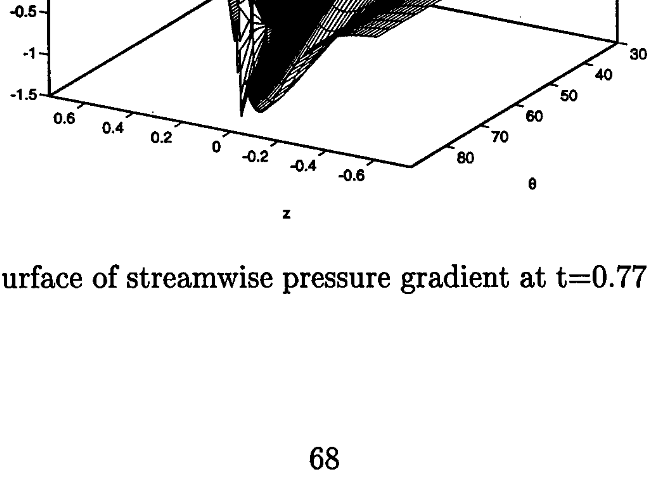

Figure 3.12: Surface of streamwise pressure gradient at t=0.77 for $Re = 10^8$.

streamwise pressure gradient to develop a spike.

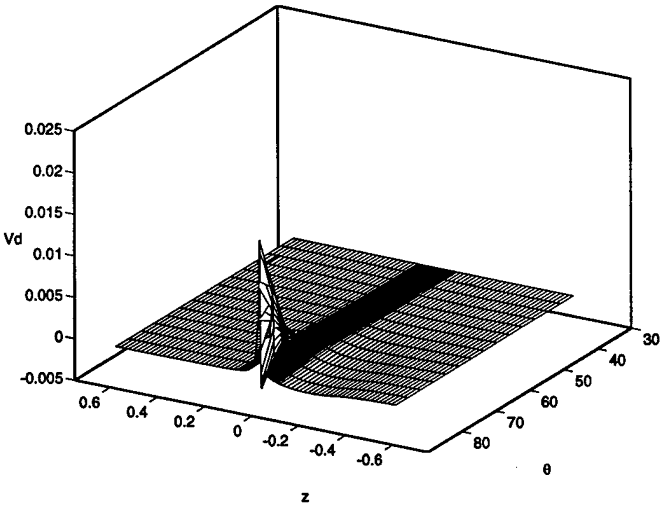

Figure 3.13: Surface of displacement velocity at t=0.77 for $Re = 10^8$.

As mentioned in Chapter 1, the interaction of the tip vortex shed from a helicopter blade interacts with the airframe and experimental measurement reveals that there are double pressure suction peaks (Affes *et al.* 1993a). The present calculation captures the initial stage of the development of the second suction peak (Figures 3.11, 3.15 and 3.16). Although the spike in the pressure is very small at this stage, it is believed that the development of the eddy will eventually lead to the emergence of the large second pressure spike seen in the experiment, although this can not be modeled in the context of the boundary-layer approximation. It is also worth mentioning that the effective interaction zone is confined to a very small region on the top of the cylinder; elsewhere the flow pattern of the interacting boundary layer differs little from the classical boundary-layer solution.

The instantaneous three-dimensional streamlines at $t = 0.77$ are shown in Figure 3.14(a). The flow pattern for the interactive boundary-layer flow differs from the classical flow solution in the region right under the head of the main vortex, where viscous-inviscid interaction takes effect. The spiky streamline patterns near $z = 0$ on the top of the cylinder indicates that the boundary-layer flow is about to erupt into the inviscid flow. For the classical boundary-layer solution, the flow pattern is still very smooth at this stage, as can be seen from Figure 3.14(b), which shows the streamline pattern at

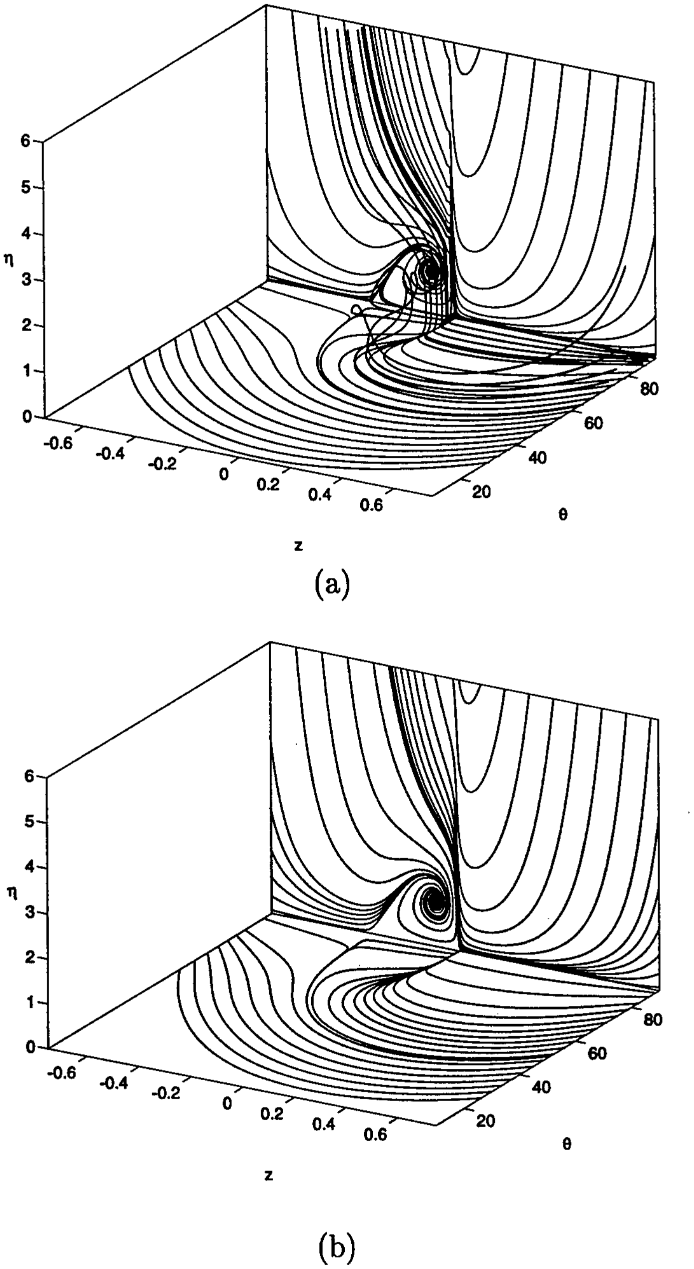

Figure 3.14: Instantaneous streamlines and surface streamlines for (a) $Re = 10^8$ and $t = 0.77$, (b) $Re \to \infty$ and $t = 0.78$.

$t = 0.78$ for classical boundary-layer flow.

Figure 3.15 shows the distribution of wall shear, displacement velocity, pressure gradient and pressure on the symmetry plane at $t = 0.73$ for $Re = 10^7$. The spike seen at $Re = 10^8$ also occurs here, but the spike occurs earlier at $Re = 10^7$. The corresponding results for $Re = 10^6$ is depicted in Figure 3.16 at $t = 0.675$. Comparing the results for these three Re numbers, we can see that not only does the spike occur earlier for smaller Reynolds numbers, but also the width of the spike is greater, which means that the length scale of the spike depends on the Reynolds number.

3.7.3 Singularity Development

The "spike" structures occuring in the classical and interacting boundary-layer results are associated with a finite time singularity in the classical and interacting boundary-layer solutions respectively.

According to the Lagrangian analysis of van Dommelen and Shen (1981), the two dimensional classical boundary-layer solution will terminate in a singularity. This singularity is characterized by a spike structure in the displacement thickness and vorticity distribution. Furthermore, Elliott *et al.* (1983) suggested that, to the leading order approximation, the displacement velocity in two dimensions exhibits a strong singularity at separation according to

$$V_d|_{max} \sim \frac{C_1}{(t_s - t)^{7/4}}, \tag{3.58}$$

where $V_d|_{max}$ is the maximum displacement velocity in two dimensions defined in Elliott *et al.* (1983); C_1 is a constant of order $O(1)$. As pointed out by van Dommelen and Cowley (1990), the singularity presented in two dimensions in fact is generic and thus the same type of singularity also arises in three dimensions.

A least-squares curve fit of $(V_d|_{max})^{-4/7}$ indicates a nearly linear variation with t for the classical boundary-layer solution, as shown in Figure 3.17, which suggests that the current numerical calculations support the asymptotic theory of singularity described by van Dommelen and Cowley (1990). The predicted singular time for the classical boundary layer is $t_s = 0.8890$.

Smith (1988) predicts that, as in the classical case, the two-dimensional interacting boundary-layer equations also break down at a finite time. Indeed, the present work supports his conclusion and Smith (1988) suggests

(a)

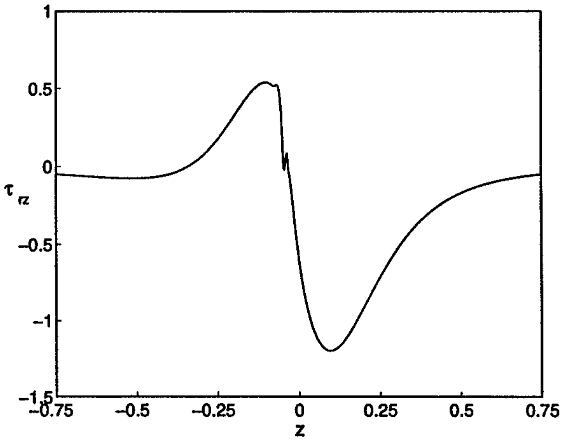

(b)

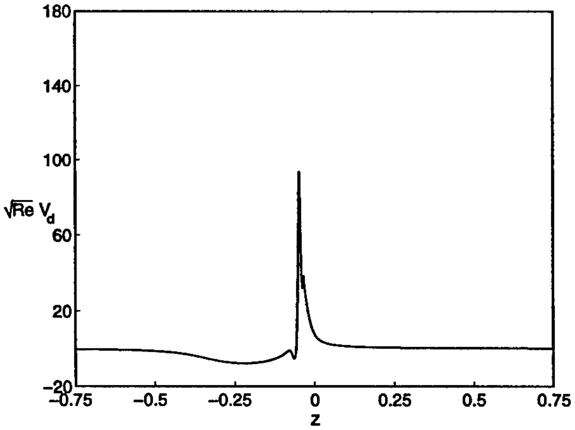

Figure 3.15(a,b)

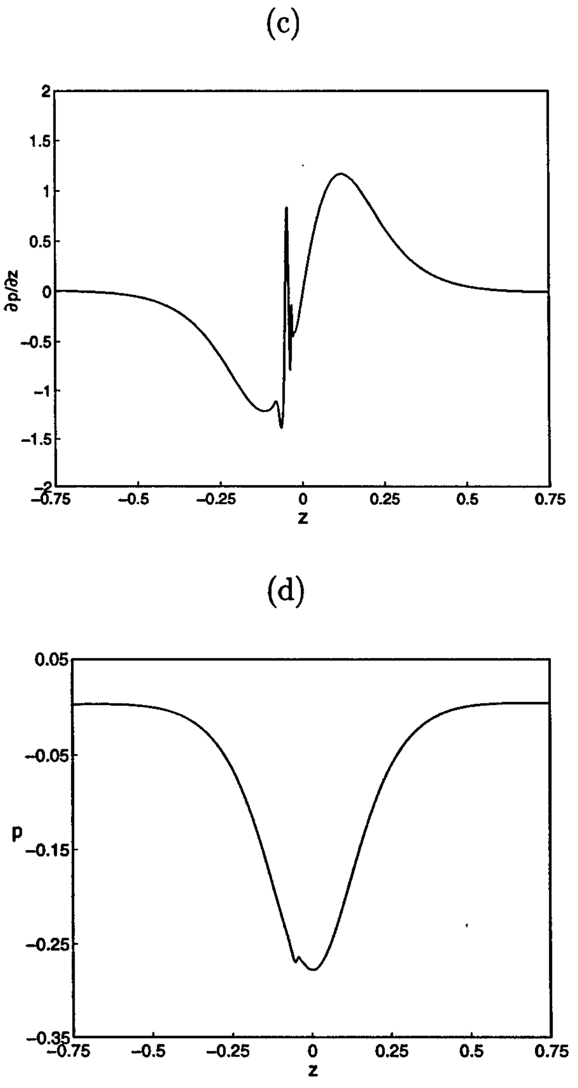

Figure 3.15: Results on the symmetry plane for $Re = 10^7$ at $t = 0.73$. (a) streamwise wall shear, (b) displacement velocity, (c) streamwise pressure gradient, (d) pressure.

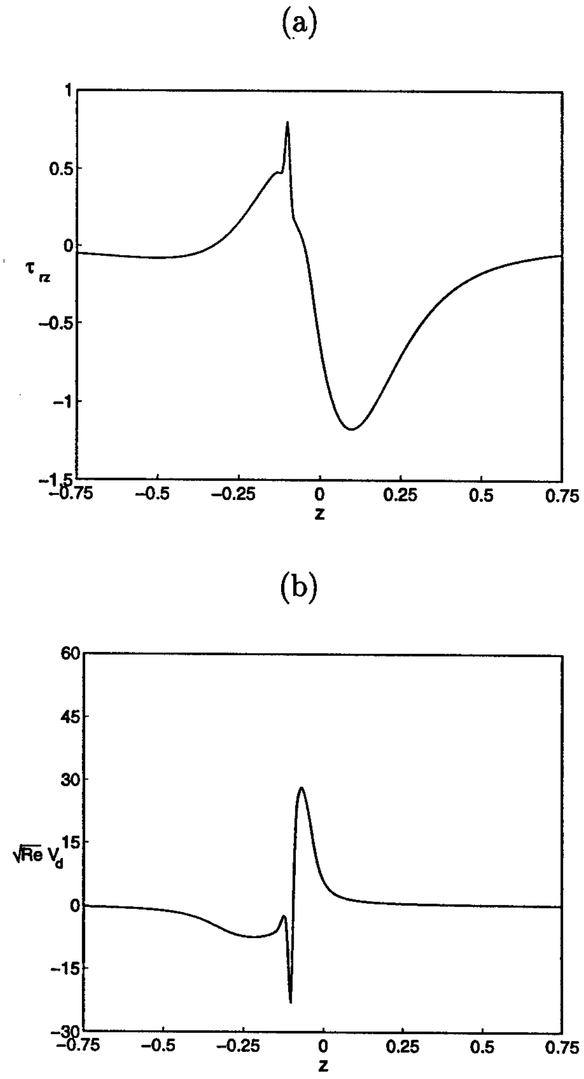

Figure 3.16(a,b)

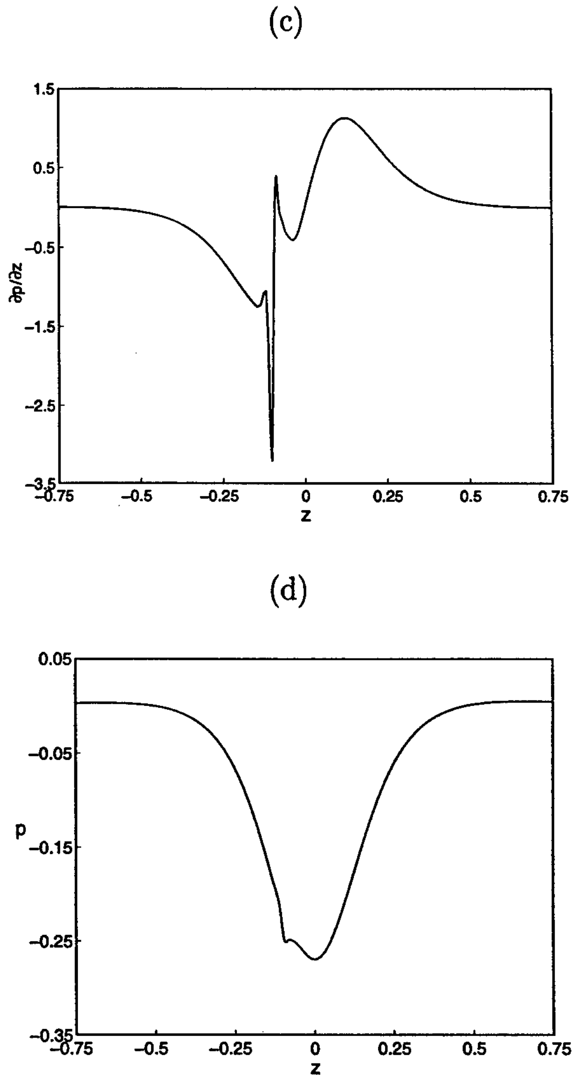

Figure 3.16: Results on the symmetry plane for $Re = 10^6$ at $t = 0.675$. (a) streamwise wall shear, (b) displacement velocity, (c) streamwise pressure gradient, (d) pressure.

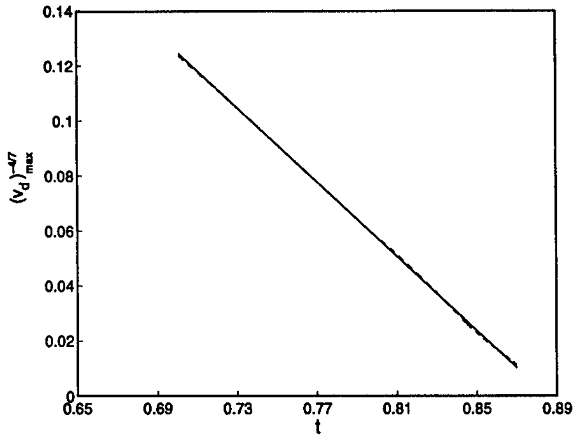

Figure 3.17: Least-squares curve fit of $V_d^{4/7}$ for $Re \to \infty$. The solid line is the curve-fitted result. The dashed line is the raw calculated result. The predicted $t_s = 0.8890$. Note that the results are almost indistinguishable.

that the streamwise pressure gradient approaches a singularity as

$$\left.\frac{dp}{dz}\right|_{max} \sim O(t_s - t)^{-1} \text{ as } t \to t_s. \tag{3.59}$$

By applying the z-momentum equation at the wall, Peridier, *et al.* (1991) showed that the local shear stress distribution on the wall will also develop a singularity according to

$$\tau_z|_{max} \sim O(t_s - t)^{-1/4} \text{ as } t \to t_s. \tag{3.60}$$

This prediction was qualitatively confirmed in the calculations of three-dimensional unsteady interacting boundary-layer flow using a uniformly distributed grid by Xiao, Burggraf and Conlisk (1994). In the present study, much better results are obtained due to the use of an adaptive grid procedure. Figure 3.18(a) shows the variation of $(dp/dz|_{max})^{-1}$ with time t for $Re = 10^8$. Results of the curve fit indicate a linear trend in the numerical data. Linear extrapolation of the result estimates the singular time t_s to be 0.7780. The variation of $(\tau_z|_{max})^{-4}$ with t for $Re = 10^8$ is shown in 3.18(b). Again, least-square fit of the data shows approximately a linear relationship between $(\tau_z|_{max})^{-4}$ and time t. The estimated singular time is about 0.7730, which agrees very well with the estimated time 0.7780 from the pressure gradient

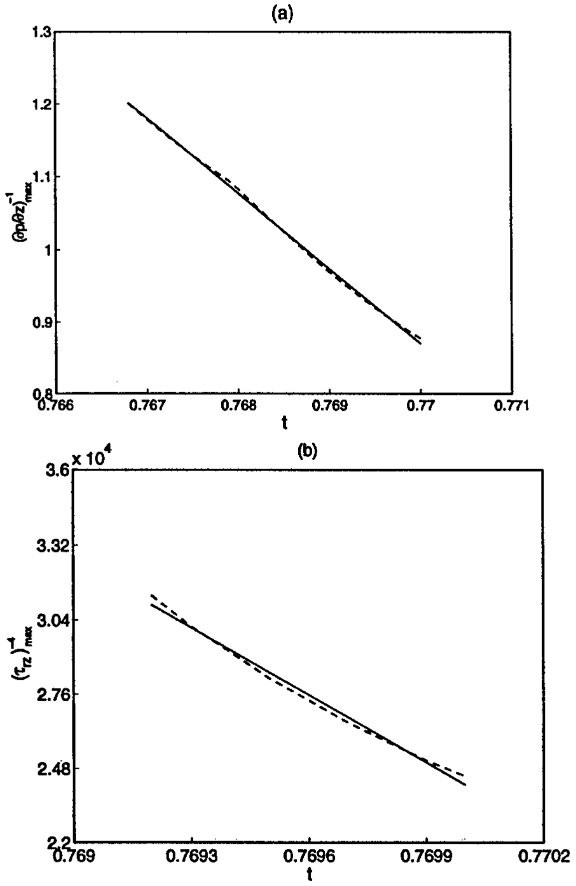

Figure 3.18: (a) Least-squares fit of $(dp/dz)^{-1}$ for $Re = 10^8$. (b) Least-squares fit of τ_z^{-4} for $Re = 10^8$.

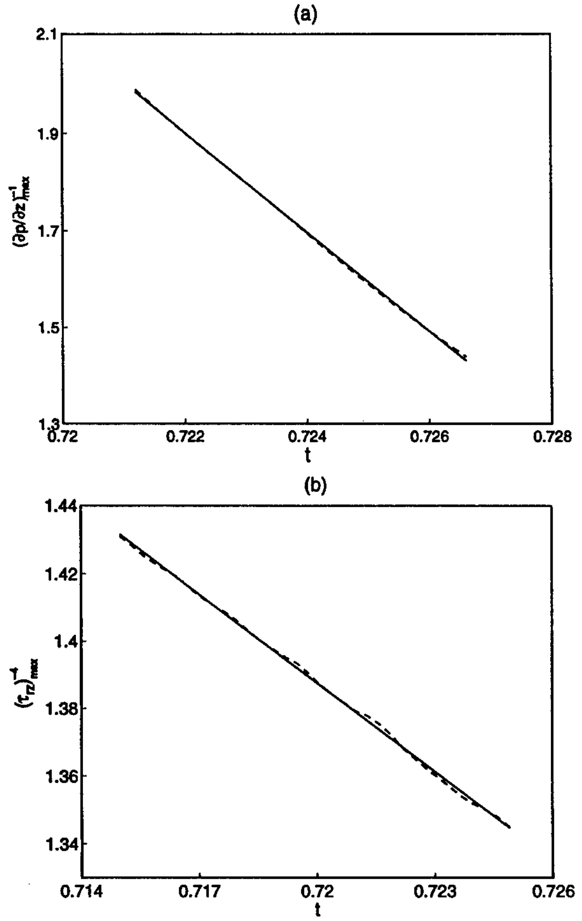

Figure 3.19: (a) Least-squares fit of $(dp/dz)^{-1}$ for $Re = 10^7$. (b) Least square fit of τ_z^{-4} for $Re = 10^7$.

data. Figure 3.19 shows the curve fitted results for $Re = 10^7$. The estimated singular time from the curve fitting of the pressure gradient is $t_s = 0.7398$ and the estimated singular time from the curve fitting of the wall shear is $t_s = 0.7316$. For $Re = 10^6$, the estimated singular time from the pressure gradient is $t_s = 0.6896$ and $t_s = 0.6872$ from the wall shear. The discrepancy between the predicted singular times is another indication of the two-figure accuracy of the numerical results.

Comparing with the estimated singular time for the classical boundary-layer solution, we can see that the interaction does not relieve or postpone the finite-time singularity, on the contrary, it hastens the emergence of this finite-time singularity.

The present computations are also consistent with the result of Smith (1988) in that the majority of the boundary layer responds inviscidly near the singular time. This had been shown in earlier work on the corresponding two-dimensional problem(Conlisk *et al.* 1996). In that work the viscous term corresponding to the second derivative of the streamwise velocity is about an order of magnitude less than the streamwise convective term late in the calculation. The ratio increases as the singular time is approached. This suggests that the local flow is inertially dominated. Upon further inspection of the present results, in particular for $Re = 10^6$, beyond about $\eta = 1$ the same trends are observed.

3.8 Discussion

Results have been obtained for the classical and interacting three-dimensional unsteady boundary-layer flows due to a vortex approaching a circular cylinder. The main objective of this work is to numerically resolve the extremely small length scales associated with the finite time singularity of the unsteady boundary-layer solution by using a moving adaptive grid procedure in Eulerian coordinates. Another motivation of this work is that recent experiments indicate (Affes *et al.* 1993a) that a second suction peak is present in the pressure on the top of the cylinder as the vortex approaches. In the present work it has been shown that this effect is beginning to emerge when the pressure and velocity field in the inviscid and viscous flows are coupled.

In general, the flow is more complex than in the classical case. The pressure gradient and shear stress on the top of the cylinder develop a spike-like character much as is the case in two dimensions. Moreover, in two-dimensions it has been shown that eventually a singularity will arise in interacting boundary-layer flow (Smith 1988) and the present results indicate that the same singularity will appear in the three-dimensional problem considered here. This is apparently due to the fact that the spanwise length scale of the flow is much longer than either of the streamwise and boundary layer length scales. In addition, interaction appears to hasten the development of the singularity, as is also true for the two-dimensional case. This fact leads to the conclusion that, when the large scale viscous boundary-layer flow starts to eject into the inviscid flow region, the boundary-layer approximation is no longer appropriate to calculate this eruption process.

These results are discouraging in the sense that the boundary-layer approximation is incapable of describing much of the inviscid-viscous interaction process. Moreover, since the rapid variation of the pressure gradient occurs on a very short streamwise length scale, and the singularity arises within this very narrow region, it is easy to integrate erroneously past the singularity if a sufficiently large grid spacing and time step are used.

However, simple scaling arguments suggest that the influence of the boundary layer on the main vortex is negligible, at least during the first interactive stage described by Elliott *et al.* (1983). In that theory of the subsequent stage in the interaction, the streamwise length scale is $O(Re^{-3/11})$ and the scale normal to the solid surface is $O(Re^{-5/11})$ which is slightly larger than the classical boundary layer thickness of $O(Re^{-1/2})$. The situation is depicted on Figure 3.20. Fluid is ejected from the boundary layer by the vertical velocity component which from continuity is

$$V \sim Y\frac{U}{X},$$

where U is the streamwise velocity component and X and Y are the streamwise and vertical length scales described just above. Thus

$$V \sim O(Re^{-5/11})\frac{O(Re^{-1/11})}{O(Re^{-3/11})} \sim O(Re^{-3/11}).$$

Thus, the flux in the eruptive region is $O(Re^{-6/11})$ which is only slightly greater than the mass flux through the boundary layer. On the other hand, the azimuthal velocity component in the vortex is $O(Re^{1/2})$ and since the area through which the swirl component of the vortex passes is $O(Re^{-1/2})$, the mass flux is $O(1)$. This may be illustrated by appeal to the Rankine

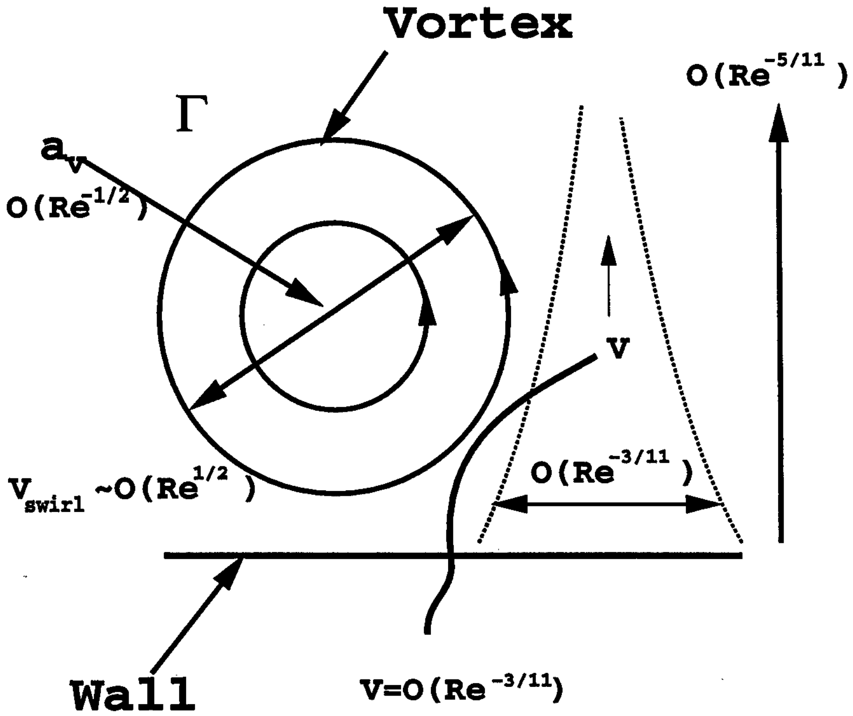

Figure 3.20: Sketch of the eruption process with the magnitudes of the boundary layer velocities and length scales from the first interactive stage according to Elliott *et al.* (1983).

vortex

$$v_\theta = \frac{\Gamma}{2\pi}\frac{r}{a_v^2} \; for \;\; r \leq a_v,$$

where Γ is the dimensionless circulation, a_v is the dimensionless core radius and r is the radial distance from the center of the vortex. Here $\Gamma = O(1)$. The mass flux is given by

$$\int_0^{a_v} v_\theta dr = O(1)$$

for $a_v = O(Re^{-1/2})$. Thus while the velocities in the erupting part of the boundary layer are large on the boundary layer scale, they are still small compared to the maximum velocity in the vortex core. For this reason we expect that the dominant aspects of the collision process may be described by inviscid (but rotational) flow theory. The present calculations assume that the dimensionless circulation $\Gamma = O(1)$, which means that the dimensional circulation $\Gamma^* \sim U_\infty L$ where U_∞ and L are the appropriate velocity and length scales. However if $\Gamma << 1$ and the vortex is weak, the collision with a solid boundary may be significantly affected by the eruption of the boundary layer.

This result, that the collision process is dominated by inviscid processes for a sufficiently strong vortex makes the computation of such collision flows much simpler since it implies that the Navier Stokes equations need not be solved. At this point we move to Chapter 4 which describes the experimental component of the vortex-airframe interaction process.

Chapter 4

Rotor-Airframe Experiments

4.1 Background

The interaction of the rotor tip vortex with a circular cylinder was studied experimentally at the John J. Harper Wind Tunnel at Georgia Institute of Technology. The test configuration, shown in Figure 4.1, consisted of a 2-bladed teetering rotor, suspended above a hemisphere-cylinder.

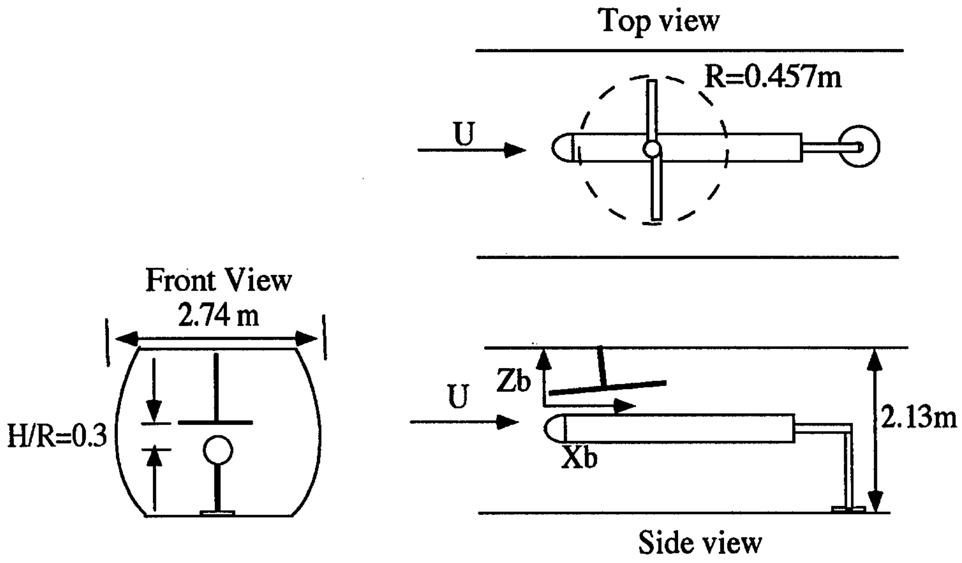

Figure 4.1: The rotor-airframe interaction test configuration in the $7' \times 9'$ Harper Wind Tunnel.

A review by Kim and Komerath(1995) summarizes the experimental work preceding the detailed studies of vortex-surface collision which were performed under the present project. A test case with rotor advance ratio of 0.1 was extensively documented, with the vortex trajectories (Brand 1989a), the inflow velocity variation above the rotor (Liou 1989a), the velocity field between the rotor and the cylinder (Liou 1989b), the surface pressure variation on the cylinder (Brand 1989b), and two components of the velocity field through the interaction of the tip vortex with the cylinder top (Liou *et al.* 1990) were documented. Figure 4.2 shows the vortex trajectories, measured using a strobed argon ion laser sheet and videography.

The figure was constructed as follows: a laser sheet, successively aligned in each of the many vertical and horizontal planes, was strobed at a frequency close to that of the rotor. The tunnel was seeded uniformly with mineral oil fog. The vortex core cross-section was visible in the sheet as a dark region devoid of seed particles. The motion of the core was thus seen in slow motion on video, with the frames corresponding to blade passage through the sheet also identifiable for phase reference. Frames were "frozen" in succession on a television monitor on which core positions were marked, and transferred manually to an overlaid graph paper. A skewed-cylinder rigid wake model would have given circular arcs matched to these trajectories away from the cylinder, as shown by the dashed lines. Distortion of the real trajectory is evident near the cylinder. The trajectory at the front of the wake appears decelerated. This corresponds to expectations based on the sense of rotation of the vortex and image plane models of vortex/surface interactions found in texts on potential flow. In these early experiments, it was impossible to discern the vortex core very near or below the cylinder. It did appear that there was a "broken end" under the retreating-blade side (RBS), which moved rapidly along the filament away from the cylinder. Beyond identifying the distortion, definite guidance could not be obtained regarding vortex behavior around the cylinder. Liou (1990) measured the azimuth-resolved velocity components in the vertical plane of symmetry above the cylinder in the region of vortex collision. Using contours of the lateral component of vorticity, and surface pressure data, he was able to observe distortion of the core, the occurrence of high stagnation pressures as well as the sharp pressure drop characteristic of vortex interaction.

Mavris (1989) was able to see the effects of the vortex interaction upon the performance of a prediction code. He tried two approaches. First, he modeled the energy addition to the flow through the rotor disk by dividing

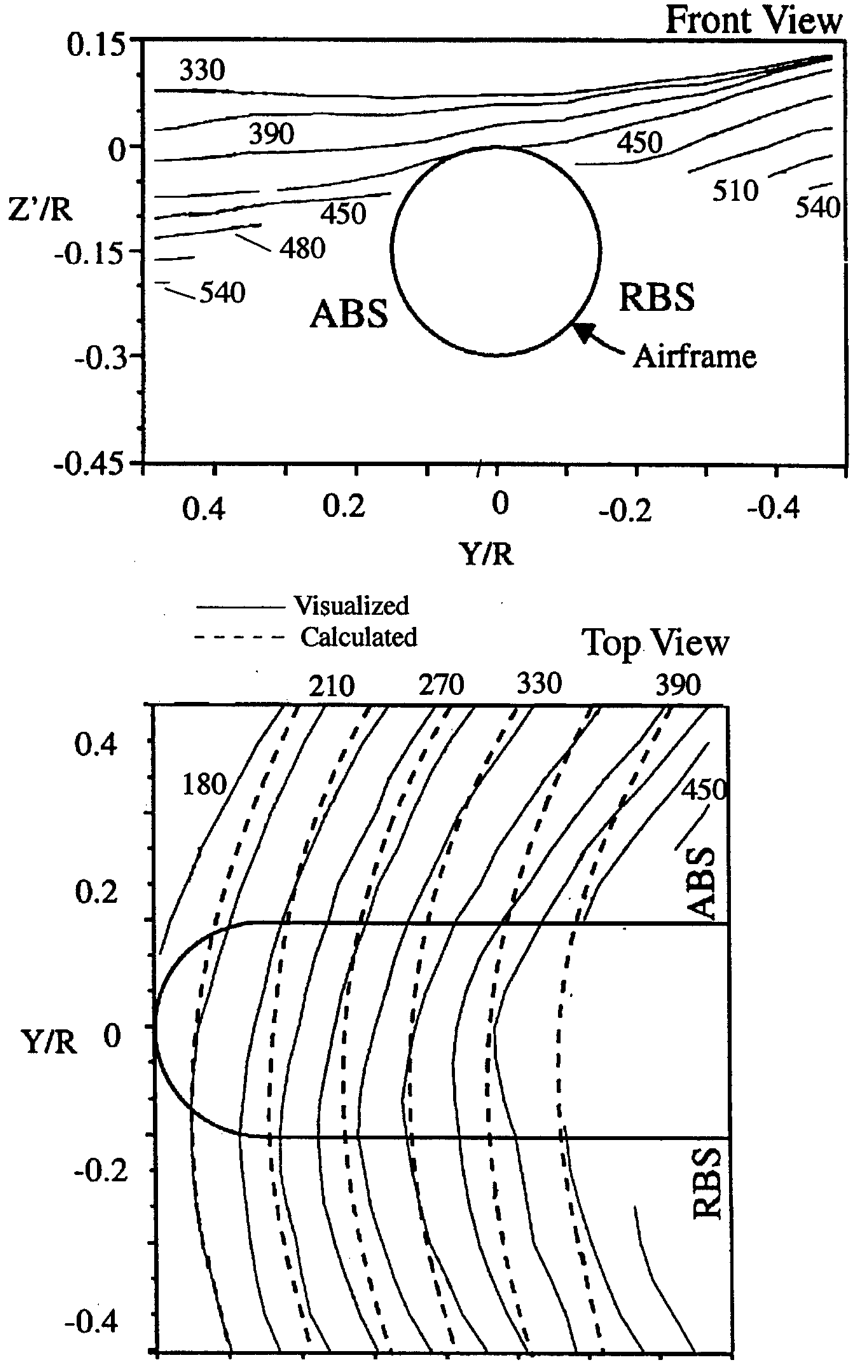

Figure 4.2: Vortex trajectories obtained from flow-visualization images obtained using a strobed argon ion laser sheet and videography, Brand (1989).

the disk into sectors of annular rings. This energy was then assumed to convect down the skewed wake. The resulting increase in stagnation pressure was superposed all around the cylinder as a time-averaged effect, after computing the rotor-airframe interaction using a combination of Scully's Free Wake (Scully 1975) and the VSAERO surface panel code (Clark 1983). This model, however rudimentary, proved successful in matching the measured pressure distribution over the top and sides of the cylinder. Encouraged by this success, he refined the computational scheme, including an unsteady potential term after the work of Lorber (1988). By this time, Liou's detailed velocity measurements over the top and RBS of the cylinder had become available, as had Brand's azimuth-resolved pressure measurements around the cylinder. The results were surprising. While agreement with experiment was excellent along the top of the cylinder, there were obvious problems along the sides. It was clear that the predictions from the potential flow calculation were generally valid until the vortex collided with the cylinder. After that, the predicted and measured trends of surface pressure were opposite, and this disagreement propagated down the sides of the cylinder on the RBS, following the vortex interaction trajectory. When the measured periodic velocity field from (Liou 1989b) was used in the computation instead of that computed from the singularity strengths, the agreement in surface pressure on the RBS improved substantially. It was clear that the velocity field after vortex-surface interaction could not be computed without more detailed knowledge.

In mid-1988, the state of knowledge was thus that the approach of the vortex system to the airframe could be modeled with confidence using potential-flow concepts. The distortion of the filaments in the vicinity of the airframe could be predicted, with accuracy limited by the knowledge of the vortex strength and structure. Once the collision with the surface began, uncertainties mounted, and nothing could be predicted about the behavior of the vortex system or the surface flowfield beyond this stage.

4.2 Approach

In the rest of this chapter, the measurement techniques are first described. The phase-resolved surface pressure on the airframe surface, measured by Kim (1993) are then presented. The pressure-time history through the collision phase of the interaction is correlated with flow visualization on the top of the airframe. Next, measurements of the lateral component of velocity above the cylinder are used to study the role of axial velocity during the collision phase. Note that the axial velocity in the tip vortex and in the inboard vortex sheet (which is the blade wake) are nominally parallel to the azimuthal component of wake velocity in the plane of measurement. Finally, flow visualization is used to answer the question of what happens under the cylinder after the vortex-surface interaction.

The test conditions for the data presented in this report are summarized below.

- Freestream Velocity : $5\frac{m}{s} \pm 0.0125\ \frac{m}{s}$ for present velocity measurements and $10\frac{m}{s} \pm 0.025\ \frac{m}{s}$ for previous velocity and pressure measurements
- Rotor rpm :1050 ± 1 for present flow-visualization and velocity measurements and 2100 ± 1 for previous velocity and pressure measurements
- Rotor collective pitch : 10^o
- Rotor diameter : 0.9144 m
- Tip path inclination from horizontal pitchdown : $4.2^o \pm 0.1^o$
- Vortex strength : $0.5\frac{m^2}{s} \pm .05\frac{m^2}{s}$ for 1050 rpm
- Cylinder diameter : 0.137 m
- Rotor tip height above cylinder : 0.137 m

4.2.1 Pressure Measurements

The pressure measurements described here were made by Kim (1993), and presented by Kim and Komerath (1995). The mean surface pressure was measured at a line of 72 pressure taps along the surface of the cylinder, multiplexed through Scanivalve pressure switches to a Barocel capacitance-type pressure transducer. The Pitot-static probe at the front of the tunnel test section was used for the reference pressure. The signal from the Barocel was digitized through a 16-bit A/D converter and sampled with a HP-1000 A700 minicomputer. The pressure at each station was averaged over 140 rotor revolutions. The line of pressure taps was rotated in 15-degree steps of cylinder azimuth in different runs to cover the entire cylinder surface. Pressure fluctuations on the airframe were measured using a set of four 6.35mm B&K condenser microphones. These microphones have flat frequency response from 1Hz to over 10Khz, and were mounted flush with the airframe surface. The periodicity of the rotor wake allowed ensemble averaged pressure measurements to be performed. The microphone signal sampling was triggered using a pulse from an encoder mounted on the rotor shaft. The data were sampled once per degree of blade rotation and averaged over an interval of 6^o. Therefore, 360 data points per revolution were sampled simultaneously from all 4 microphones and sorted into 6^o azimuth bins in each signal sample. This process was repeated 100 times and the results were averaged to get ensemble-averaged azimuth resolved data. Each microphone was calibrated using a Bruel and Kjaer Pistonphone. The interpolated value of the mean pressure, and the ensemble-averaged, phase-resolved fluctuating pressure were added at each measurement location.

4.2.2 Flow Visualization

Figure 4.3 shows the flow-visualization setup. The flow was seeded using wax smoke. For the experiments performed under this project, a 2-camera system was utilized, along with the light sheet from a copper vapor laser. The green 532nm laser beam, originally about 37mm in diameter was focused down to a fiber-optic receiver. The fiber-optic cable was directed into an optics box near the test-section. This box contained the optics for expanding the laser beam into a sheet about 12mm thick. The laser operated in a series of pulses, at a rate adjustable between 4000 and 8000 pulses per second. The duration of each laser pulse, as estimated from the measurements made using a photomultiplier, was between 25 and 50 nanoseconds. The cameras used were commercial grade security cameras with Gen I image intensifiers, and electronic shutters variable between 1/60 and 1/8000 seconds. Each shutter, as well as the laser pulses could be externally triggered within a narrow range of asynchronous operation. A Stanford Research Systems digital pulse generator was used to send TTL pulses to both the laser and the cameras. The timing accuracy of these trigger pulses was specified to be on the order of picoseconds.

By operating this system at the standard NTSC framing rate (29.97 full-frames, or 59.94 odd/even line fields per second), with the laser pulsing at a rate of 5994 per second, it was possible to capture just one laser pulse

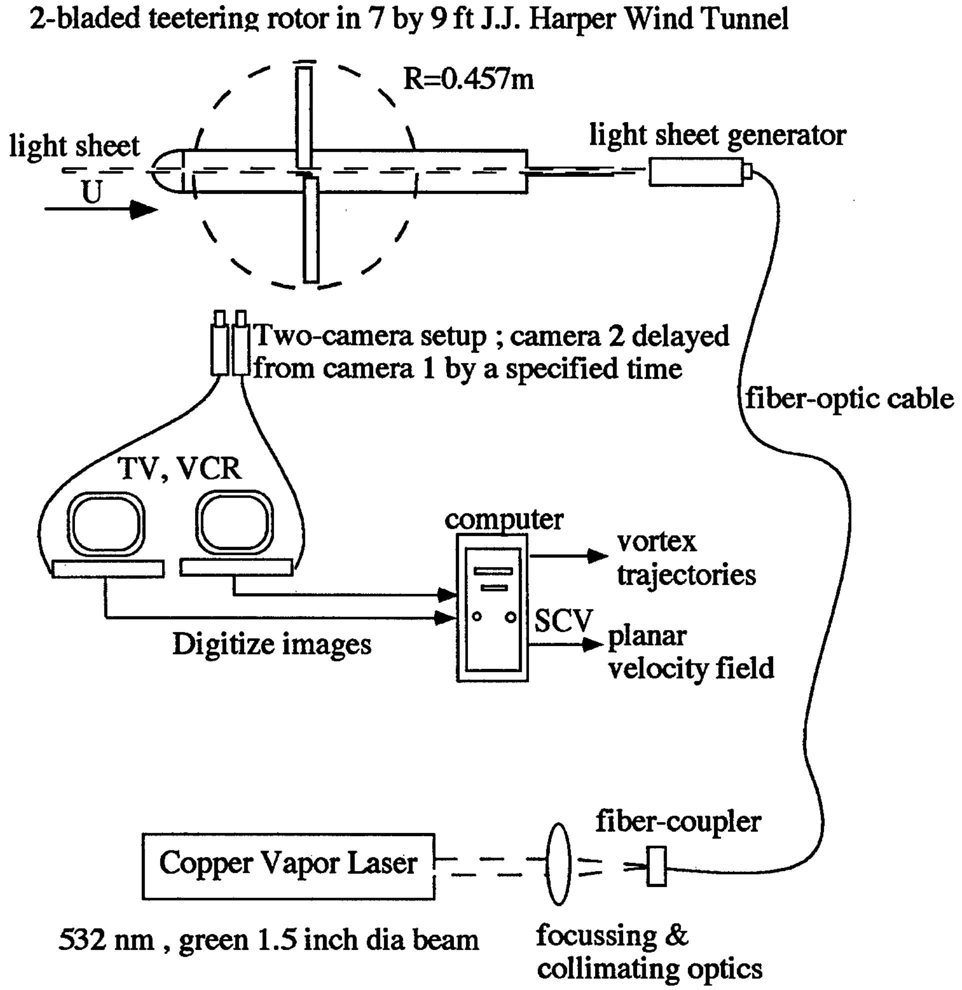

Figure 4.3: Flow-visualization setup used to capture the flow-field features on top of the airframe.

per 1/8000 second shutter opening. This means that the temporal precision of the resulting flow images is on the order of 25 to 50 nanoseconds, which essentially "freezes" all motion. The disadvantage was that there was no way to synchronize the rotor perfectly with the camera system to get desired rotor phases: the rotor system had dangerous levels of vibration near 1800 rpm, forcing the choice of an operating point well away from this frequency. To capture short time-scale events, the two cameras were focused on the same field of view: this alignment was shown to be accurate to 1 pixel when the resulting images were digitized onto a 640 x 480 screen. The shutter of the second camera was delayed with respect to the first by some time corresponding to an integer number of laser pulses, i.e, by multiples of 0.1667 milliseconds. The azimuth of the interaction captured in each image was known by recording simulataneously the image of a 360-degree protractor placed concentric with the rotor shaft. The flow-features and vortex trajectories were then obtained in the post-processing phase.

4.2.3 Laser Velocimetry

The streamwise and vertical components of velocity were measured by Liou (1989) above the airframe using an Argon-ion laser with the beams being projected from outside the test-section. Light was collected in the backscatter mode. To measure the lateral component of velocity, which is essentially along the axial direction of the tip vortex above the airframe, a fiber optic probe was embedded within the airframe and traversed over a range of a few mm. Figure 4.4 shows the embedded LV setup.

The fiber-optic probe was 15mm in diameter and had a 60mm focal length. To obtain adequate signal-to-noise ratio, the 12.5mm diameter quartz window installed flush with the airframe surface had to be removed. The presence of the resulting cavity prevents interpretation of lateral velocity data closer than 5mm to the surface. The probe also served to receive scattered light in the backscatter mode, and transmit it to a photmultiplier through a fiber. The photomultiplier signal was downmixed and analyzed with a TSI 1990 counter processor which timed the passage of 8 fringe crossings. The processor rejected all data values where the time for the first 5 fringes did not match the time for all 8 crossings to within 1% of the ratio 5/8. A TSI 1998 interface was used to transfer the data to a Gateway 2000 486/66MHz computer. The interface clocked the elapsed time since the last data point. The rotor trigger was used as an external pulse for the interface; this also

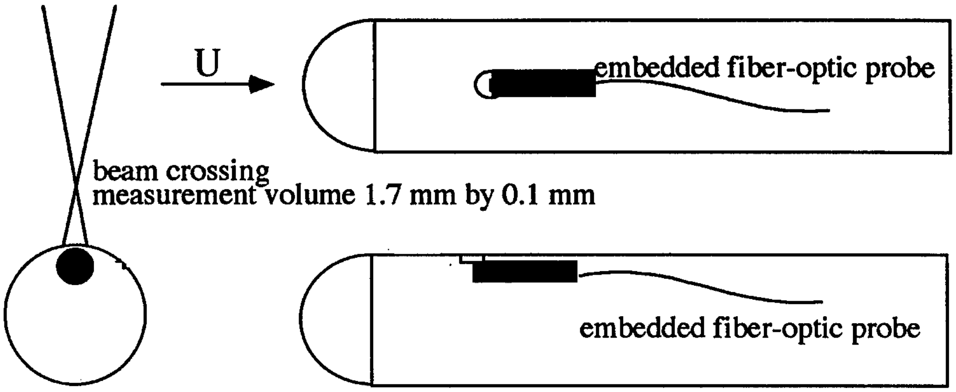

Figure 4.4: Laser velocimetry setup using a fiber-optic probe embedded within the airframe.

resent the elaspsed-time counter. The computer calculated the velocity and sorted the data into 1° azimuth bins. Each bin had an average of about 150 values for 50,000 total points taken.

With the fiber optic probe, the solid angle of light collection was substantially higher in the backscatter mode than it was in the earlier configuration (Liou's experiments) where the collection optics were placed outside the test section. Data at several locations were checked for repeatability. In most of the measuring grid shown, the data rate was high enough (several hundred per second) to enable collection of 100,000 individual points per measuring location, in order to sort out the ensemble-averaged periodic velocity with a resolution of 1° of rotor azimuth. Closer to the surface the data rates fell below a hundred per second, and the number of points was reduced to 50,000 and in some cases 30,000. The results shown below demonstrate that the flowfield was periodic enough to enable successful measurement of velocity profiles with such azimuth resolution. The flow was seeded with atomized mineral oil droplets which have a nominal diameter of the order of 4 microns. Incense seeding was tried out but the signal return from the particles was poor due to their sub-micron size.

4.2.4 Scaling Issues

The lateral velocities presented in this report were measured at 1050 rpm, (where flow visualization is clearer) while the streamwise and vertical velocity and surface pressure data were at 2100 rpm, for the same rotor advance ratio of 0.1. To confirm that the vortex characteristics at the two rpms could be properly scaled using advance ratio, the u-component was measured along a vertical line on top of the airframe at 1050 rpm. The core radius and maximum circumferential velocity were obtained from the u-velocity profile and used to compute the circulation. This gave a vortex core circulation of 0.5 $\frac{m^2}{s}$, which is half of what was measured at 2100 rpm. It has also been shown from LV measurements made by McAlister (1993) on a hovering 2-bladed rotor that the core axial velocity scales with rpm. So the core axial velocity was measured at 1050 rpm and scaled by a factor of 2 for input into the computations.

4.2.5 Pressure Distribution Around the Cylinder

This section begins with excerpts from Kim and Komerath (1995). Figure 4.5 shows the surface pressure distribution along the top of the airframe ($\phi = 360^o$) as a function of vortex age ψ, for the front portion of the airframe where the leading edge of the wake interacts. Note that previous papers on this topic and in this report, reference is made to both vortex age and rotor azimuth. While the rotor azimuth at interaction can be either between 0^o and 180^o or between 180^o and 360^o, the vortex age at the interaction is always greater than 180^o. This means a rotor azimuth of 60^o is equivalent to 240^o and correspond to a vortex age of 240^o.

Three dominant features are visible. The highest peaks correspond to the pressure pulse felt as the pressure distribution around the lifting rotor blade moves across the airframe above the microphones. The deep oblique valleys correspond to the tip vortex interacting with the surface. This starts at about $\frac{Xb}{R} = 0.16$, when the blade azimuth is at 90^o. The tip vortex age at this point is 270^o ,when the vortex is roughly 4 core diameters above the airframe. The vortex-induced suction is greatest at $\psi = 228^o$, when an instantaneous pressure coefficient of -7.57 is reached. At this stage, the core is very close to (less than one core diameter from) the surface. By $\psi = 348^o$, the suction peak disappears. At this stage, the filament can be considered to be broken into two. The shallower valley is caused by the secondary feature earlier observed by Liou *et al.* (1990). This has been shown by Kim (1994) to be caused by the interaction of the concentrated roll-up at the edge of the inboard vortex sheet, which forms a vortical structure rotating counter to the tip vortex. The suction peak corresponding to this structure moves faster downstream than the tip vortex due to the difference in the sense of

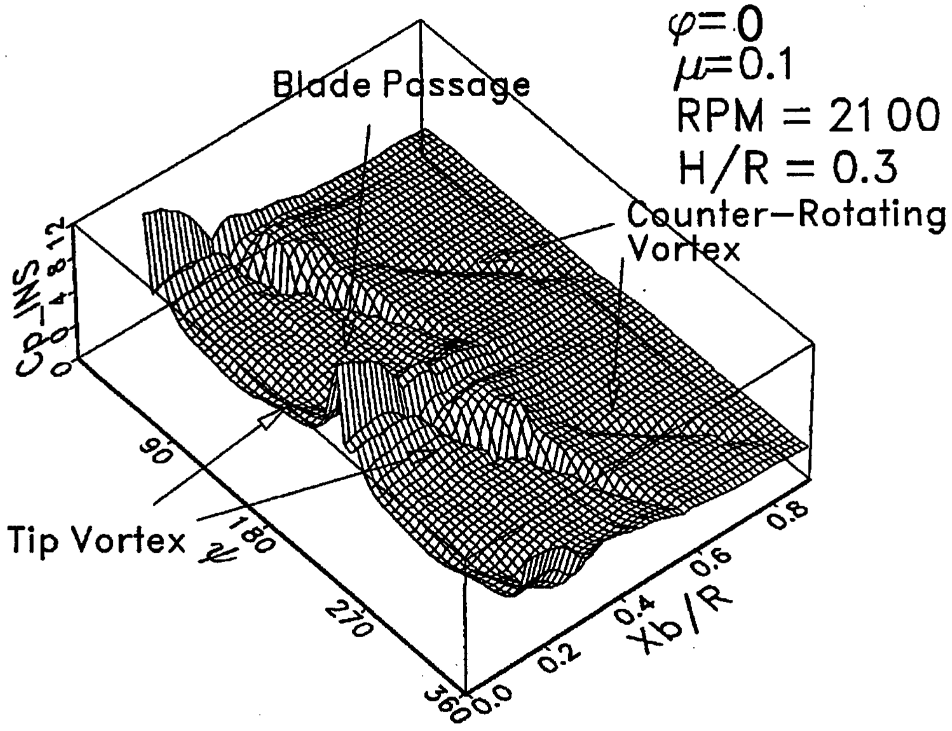

Figure 4.5: Pressure distribution on top of the airframe as a function of the vortex age, Kim and Komerath (1995).

rotation between these two features.

4.3 Results

4.3.1 Pressure Effects on the Sides of the Airframe

The substantial magnitude of core axial velocity and its effect on the rotor/airframe interaction are indicated by the pressure field on the sides of the airframe. Figure 4.6(a) shows the pressure distribution around the cylinder for a rotor azimuth of $\psi = 270^o$. Note that the age of the vortex interacting on the RBS of the airframe is close to $\psi = 300^o$. A strong suction is seen on the RBS and a weaker stagnation on the ABS. On both the sides the cut ends of the vortex core are aligned in a fashion resembling a column vortex on a flat plate or a tornado on the ground. The stagnation of the axial flow on the ABS causes a high-pressure region there in addition to the region of suction expected when the high-speed flow around the vortex approaches the surface. On Figure 4.6(b) is the same plot at a later rotor phase angle. Here we note the complete absence of the suction peak on the advancing side. Here, the stagnating end of the vortex slides down the ABS, and its effects slowly die out.

A key feature of the rotor tip vortex is the substantial axial velocity along the core. Unlike vortices over delta wings (prior to bursting), this core is wake-like i.e, the flow inside the core moves towards the blade that left the vortex behind. Thompson *et al.* (1987) reported axial velocities of the same order as the maximum tangential velocity in the core of a rotor tip vortex in hover within the first 180^o of vortex age. For the GT configuration, Liou (1986) reported axial velocities comparable to the rotor inflow velocity for vortex ages above 360^o. This velocity determines much of the interaction around the airframe. The vortex filament resembles a tube containing a helical flow, following the rotor blades across the cylinder from the ABS to the RBS. Thus, the axial flow should stagnate on the ABS, and cause suction on the RBS. In addition, under the cylinder, the axial component causes causes the remaining helical flow to cross the plane of symmetry to the RBS.

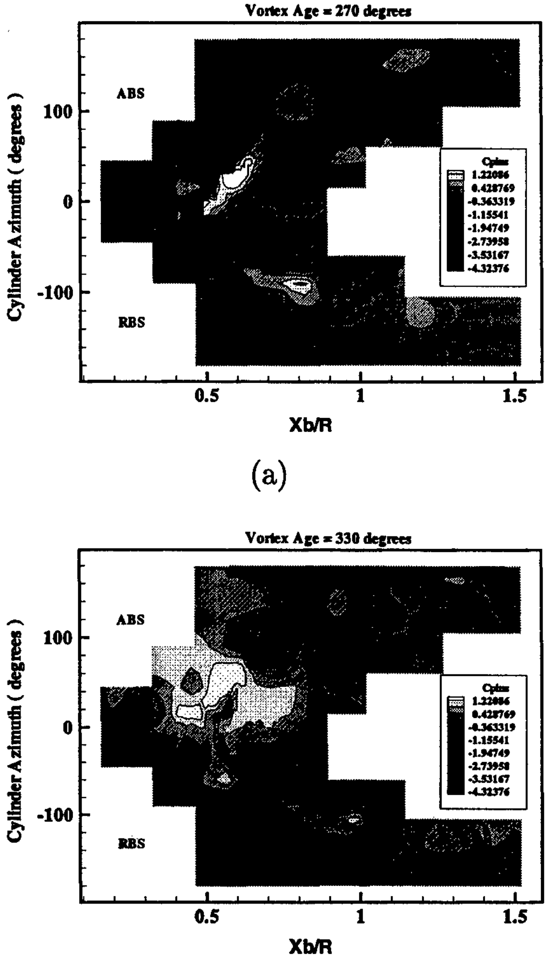

(a)

(b)

Figure 4.6: Surface pressure distribution around the airframe at rotor azimuths $\psi = 270^o, 330^o$. The vertical and horizontal axes in the plot represent circumferential and longitudinal coordinates on the cylinder surface respectively. Since the measurement grid was optimized to visualize the vortex interaction, there are no pressure data in the rectangular regions left blank. Otherwise, lighter regions indicate higher pressures.

4.3.2 Geometry of the Vortex Stagnation

As noted above, a positive pressure concentration is observed on the cylinder surface at a location close to a low pressure region on the ABS for rotor azimuth $210^o < \psi < 300^o$. In Figure 4.6 the pressures on the ABS show a region of stagnation downstream of a region of suction. This positive stagnation peak appears to be caused by the axial component of velocity in the tip vortex. Then a question is raised: why is the axial flow effect exhibited only downstream of the tip vortex suction peak? The asymmetry in the pressure distribution can be explained by combining the axial and circulatory motion of the tip vortex filament. The schematic diagram in Figure 4.7 shows the axial velocity component stagnating near the top of the airframe (based on flow visualization) and a vortical flow with an axial component of velocity interacting with the airframe surface. When the axial component and the downward motion of the tip vortex in the downstream region are combined, the local incidence angle between the resultant velocity and the airframe surface on the ABS becomes closer to a right angle. However, when the axial component in the core is combined with an upward velocity at the upstream edge of the core, the incidence angle becomes smaller. The local pressure maximum appears to correspond to the situation where the incidence is 90^o.

On the RBS, the axial flow is directed away from the surface. Thus, in the portion of the filament that never interacted with the surface, the flow goes along the filament, away from the cylinder. Visualized in a horizontal laser sheet, the region of seed particle deficit, which indicates the vortex core, appears to move along the filament, reminescent of the end of a train leaving a tunnel along a curved track. What happens in the region near the cylinder was again not quite clear; however, some of it could be postulated from the calculations described in the preceding chapters. Suction on the RBS would entrain seeded boundary layer fluid into the region previously occupied by the vortex core. Any rotation remaining from the destroyed vortex had to intensify in this region, and a strong core would form again. The suction region propagated down the RBS, but its pressure signature disappeared before reaching the bottom of the cylinder. The presence of a rotating core is seen on the RBS at a cylinder azimuth of $\phi = 90^o$. This is shown in Figure 4.8. Probably, interaction with the boundary layer dissipated the rotation of the core. The collision process and the phenomena at the bottom of the cylinder are discussed below from recent experiments.

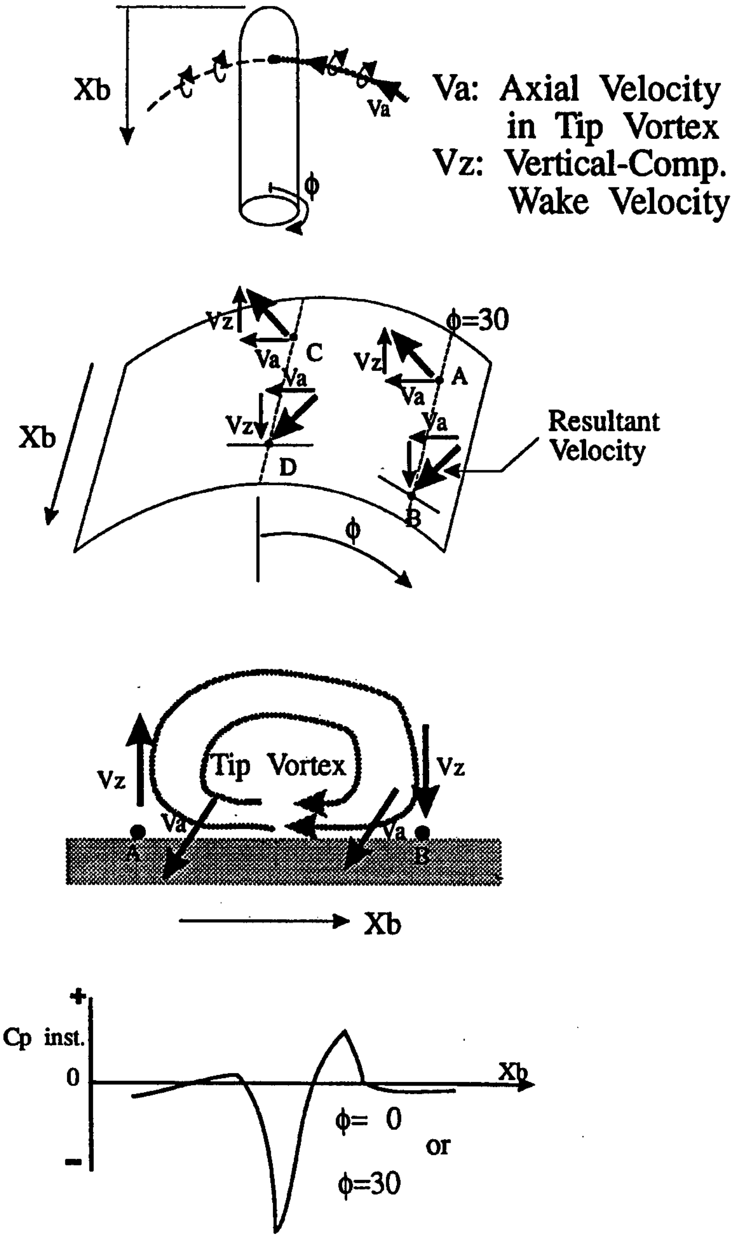

Figure 4.7: Schematic vectorial representation of the phenonmenon seen during the interaction of the tip-vortex on the ABS of the airframe.

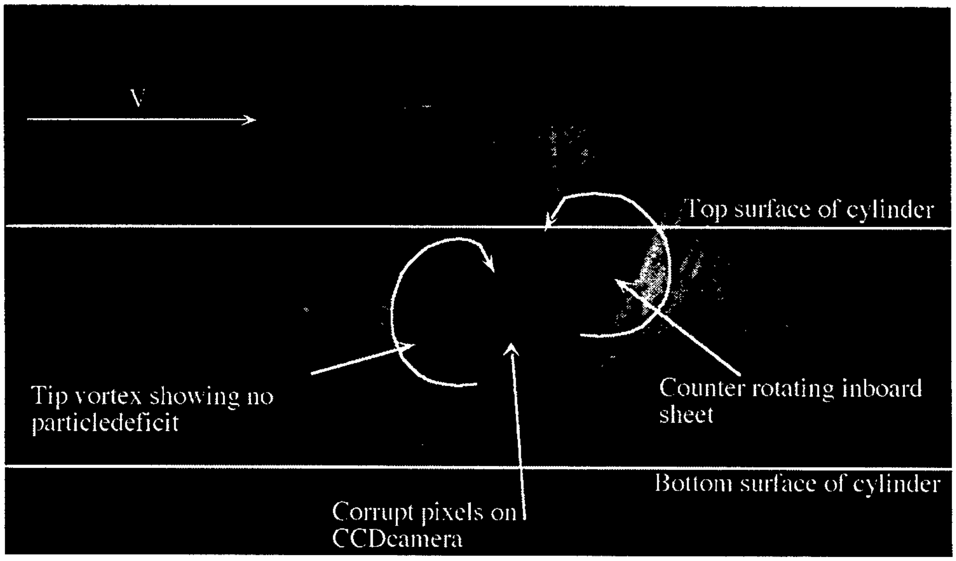

Figure 4.8: Flow visualization on the RBS shows a strong circulatory region devoid of particle deficit. This is presumably due to suction of the boundary layer fluid due to the core axial flow directed away from the surface of the cylinder on the RBS.

4.3.3 Pre-collision Features

Figure 4.9 shows two stages of the vortex prior to its collision with the top of the airframe. The age of the cross-section of the tip vortex, visible in each image, is used as the measure for sequencing the interaction process: it is noted that this vortex age is 180 degrees more than the rotor azimuth at the beginning, since the vortex cross-section seen in the image was generated from the previous blade. The vortex core is seen as a dark region (devoid of light-scattering particles) surrounded by a bright region of swirling fluid. At $\psi = 180^o$, the core is still about half the cylinder diameter away from the top surface. The slight flattening of the core is attributed to the blade passage, which imposes a sharp downward velocity, whose magnitude is higher on the upper part of the vortex than at the lower part. The instantaneous (i.e., ensemble-averaged with a resolution of 1 degree of rotor phase) pressure coefficient is plotted along the airframe surface, using data obtained by moving the set of 4 microphone sensors in steps along the x-axis, in different runs. The blade passage effect accounts for the high positive instantaneous pressure coefficient values (*Cpinst*) values. The dip at Xb/R = 0.3 indicates the effect of the vortex on the airframe. Up to an azimuth of 210^o, the primary clockwise-rotating vortex remains unchanged and its suction effect on the cylinder is the same. The image at 210^o shows that the core has recovered its circular shape after the passage of the blade pressure pulse. The *Cpinst* values stay near 1 upstream of the vortex, after the blade passage effect has died out, because there is a stagnation point upstream (left lower corner) of the vortex near the surface. Downstream of the vortex core, there is another stagnation region dividing the reverse-flow region below the vortex from the flow downstream: here the flow around the core turns around at the wall, accompanied by surface pressure coefficients of up to 2.5. Note that the stagnation pressure of the streamlines around the vortex is associated with the motion of the tip region of the rotor blade, and is hence much higher than the tunnel freestream stagnation pressure. In between these two stagnation regions, the suction on the surface becomes stronger as the core approaches. Past laser velocimeter data on the vortex core have shown that the highest seeding density is found in the region of highest tangential velocity, surrounding the core. This region is still intact above the surface. Core collision is just beginning, as the bright, heavily seeded region of highest tangential velocity at the outer edge of the core reaches the surface boundary layer.

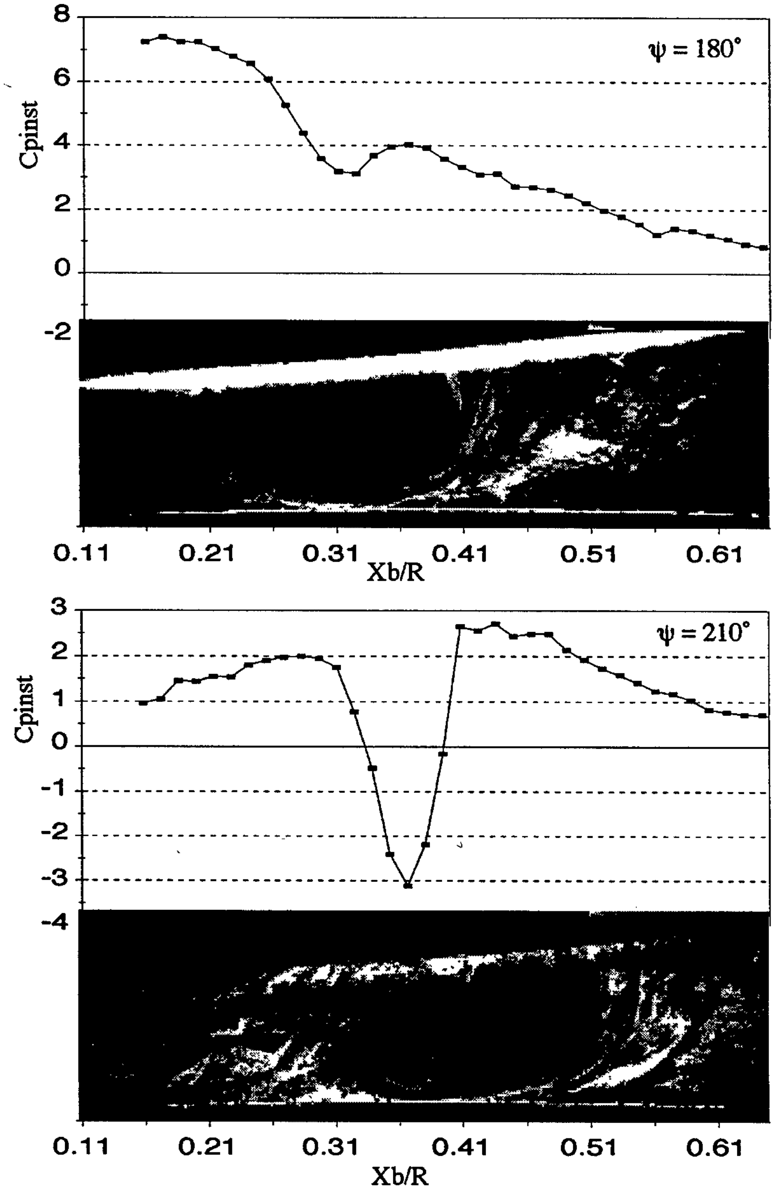

Figure 4.9: Correlation between flow-visualization and the pressure distribution on top of the airframe as the vortex approaches the airframe. This phase is prior to the beginning of collision on top of the airframe, $\mu = 0.1$.

4.3.4 Collision Phase

Initiation of Collision

Figures 4.10 shows the beginning of the collision of the tip-vortex with the airframe surface. The suction at the surface increases and reaches a maximum at $\psi = 222^o$. The core has not deformed and maintains its circular shape. The high-velocity region surrounding the tip-vortex is seen as a region of high particle density and this is seen to almost touch the cylinder surface. For $\psi > 222^o$, the flow visualization shows that the vortex core center is less than one core radius away from the airframe. This is the period when the rotor-airframe collision begins. At $\psi = 228^o$, in Figure 4.11, core distortion becomes evident, with the major axis being approximately vertical. The surface negative pressure peak has decreased slightly in magnitude from its value at 222^o. In addition, the pressure trace immediately upstream of the core shows a change in sense of curvature: this is the first evidence of a secondary structure developing upstream. There is little movement of the core along the X-direction from 222^o to 228^o.

Reduction of Primary Suction Spike

In the next 6^o, ($\psi = 234^o$ in Figure 4.10), the pressure spike has broadened greatly, and its amplitude has come down by almost a factor of two. This is indicated in the flow visualization by reduction in the sharpness of the core definition, and the reduction in its size. The pressure trace upstream appears to have smoothed out. In explaining the process in these figures, the reader is requested to return to the trajectories shown in Figure 4.2. The vortex first touches the surface on the Advancing Blade Side (ABS) of the airframe. The process observed in the vertical plane above the top of the airframe is consistent with a vortex whose axial flow has already begun to stagnate due to interaction at the ABS. At 240^o, in Figure 4.11 another discontinuity appears in the pressure trace upstream of the core. This discontinuity is presumably the first indication of formation of a secondary structure caused by the separation of the reverse-flow boundary layer. The region devoid of seeding is becoming smaller and smaller implying a weakening of the tip-vortex core. Thus the swirl component of the core is becoming smaller as we proceed further into the interaction.

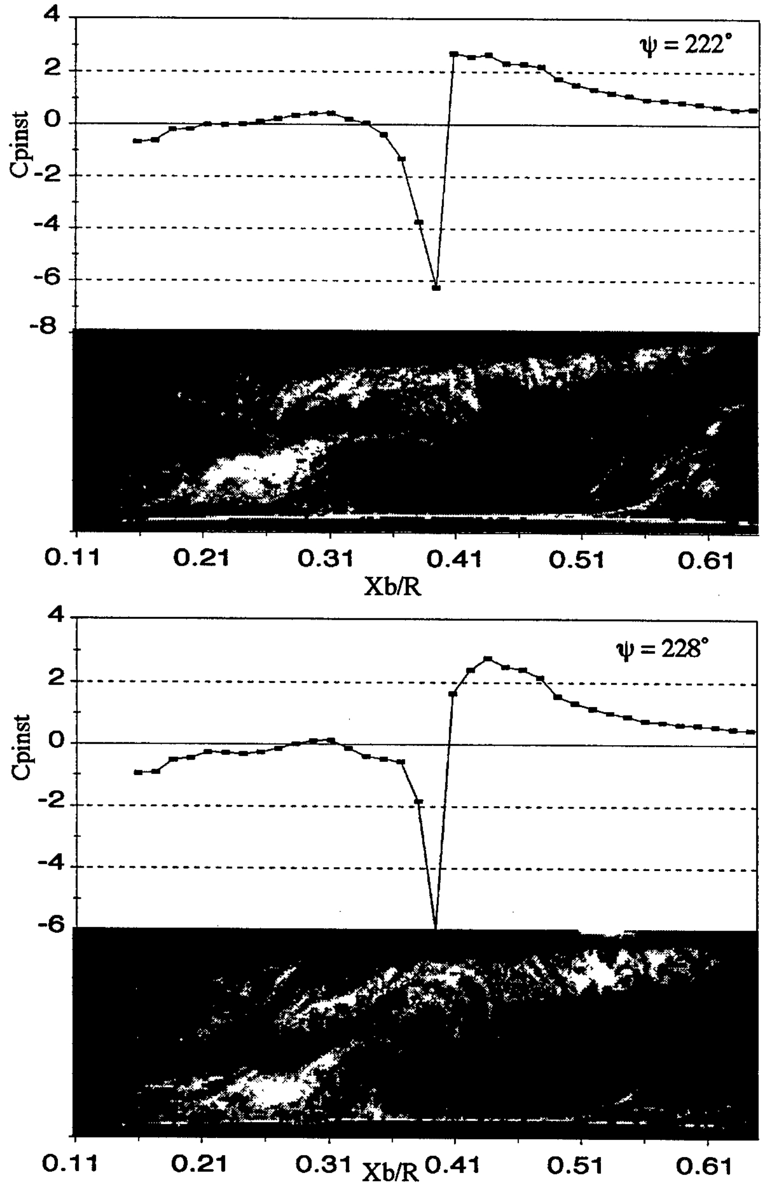

Figure 4.10: Correlation between flow-visualization and the pressure distribution on top of the airframe as the vortex enters the collision phase of the interaction, $\mu = 0.1$.

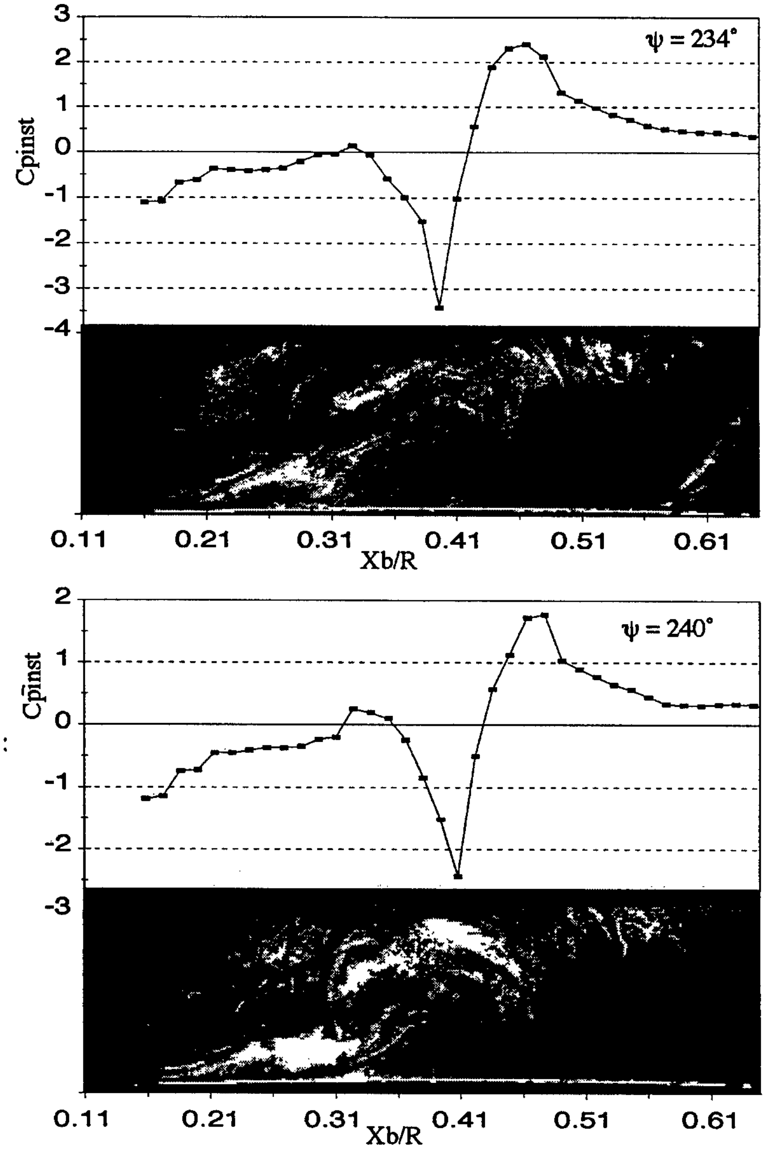

Figure 4.11: Correlation between flow-visualization and the pressure distribution on top of the airframe as the vortex collides with the airframe. This phase is the beginning of collision on top of the airframe, $\mu = 0.1$.

Secondary Suction Peaks and Collision Effects on the Tip-Vortex

Beyond 240 degrees, the vortex is not visible as a distinct entity in the flow visualization. The remainder of the collision phase will be described with the help of the lateral velocity and vorticity contours superposed with pressure traces on top of the airframe. Figures 4.12 (246^o), 4.13 (252^o), 4.14 (258^o), and 4.15 (270^o) show four stages of the tip-vortex undergoing a collision with the airframe. The three velocity components are individually measured and ensemble averaged over about 100 rotor revolutions. The periodicity of the flow, which makes this possible, is confirmed by the excellent correlation obtained between the lateral vorticity contours constructed from the data taken in 1986 by Liou, and the lateral velocity contours obtained in the present experiments in 1996. This obviates the need for simultaneous 3-component measurement in this flow. While the swirl velocities in the wake approach 2-3 $\frac{m}{s}$ (4-6 $\frac{m}{s}$ at 2100 rpm) in most parts, a predominant feature is the high core axial velocity, directed toward the blade. Note the persistence of the axial velocity even after the maximum vorticity has begun to reduce. A high magnitude of core axial velocity is seen throughout and beyond the interaction averaging about 12.5 $\frac{m}{s}$ (25 $\frac{m}{s}$ at 2100 rpm) prior to the beginning of the collision phase. This is the value that has been used in the computations. The vortex center matches up very well when seen as the point of maximum lateral velocity and vorticity.

In Figure 4.12 ($\psi = 246^o$), we see the discontinuity in the pressure traces upstream of the tip-vortex becoming steeper. The core axial velocity is directed out of the plane of the paper. The lateral velocity and vorticity contours match well. The core is still seen to retain an approximately circular shape. A region of very low swirl is seen upstream of the vortex. This is a separated region. The next figure (Figure 4.13) shows an increase in the separation region upstream of the vortex. At $\psi = 264^o$, we see a secondary spike begin to develop in the suction region, as the primary spike shrinks. Two points are noted here. First, Liou's vorticity contours were constructed from data which were averaged over 6 degrees of rotor revolution, during which the vortex core translates. This accounts for much of the apparent flattening of the vortex structure. The contours of lateral velocity were constructed from data averaged over 1 degree of rotor azimuth. The second point to note is the apparent mismatch between the suction spike in the pressure distribution, compared to the location of the center of the vorticity patterns and the lateral velocity contours. As Kim argued in Figures 4.6 and 4.7, the suction

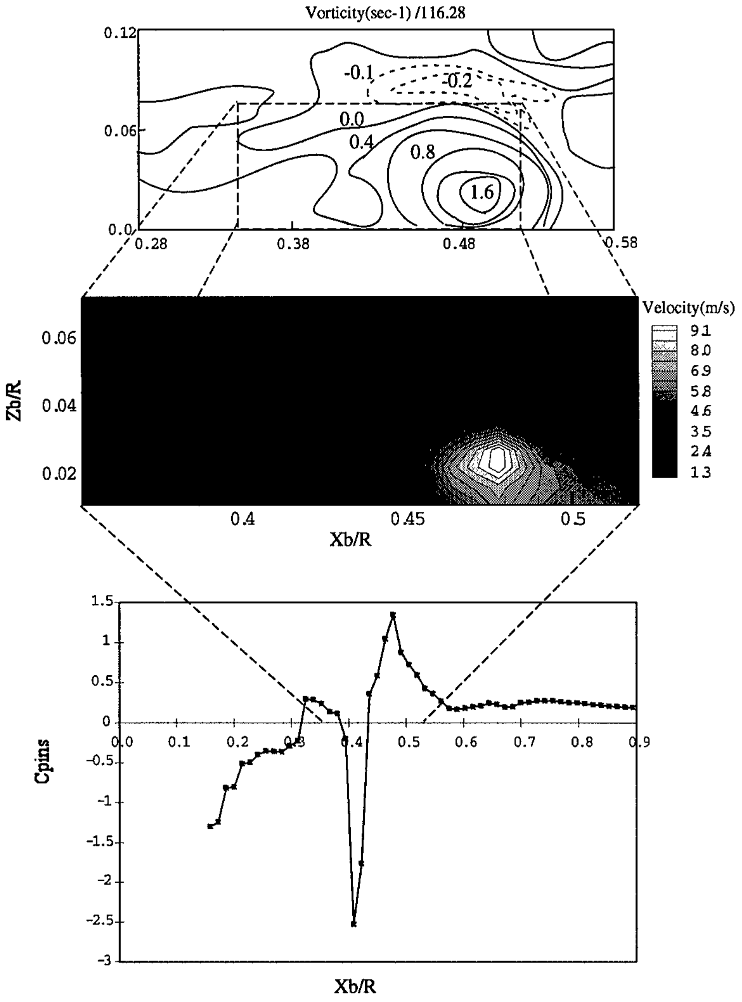

Figure 4.12: Correlation between lateral vorticity, velocity and surface pressure distribution on top of the airframe as the vortex collides with the airframe, $\mu = 0.1$, $\psi = 246^o$.

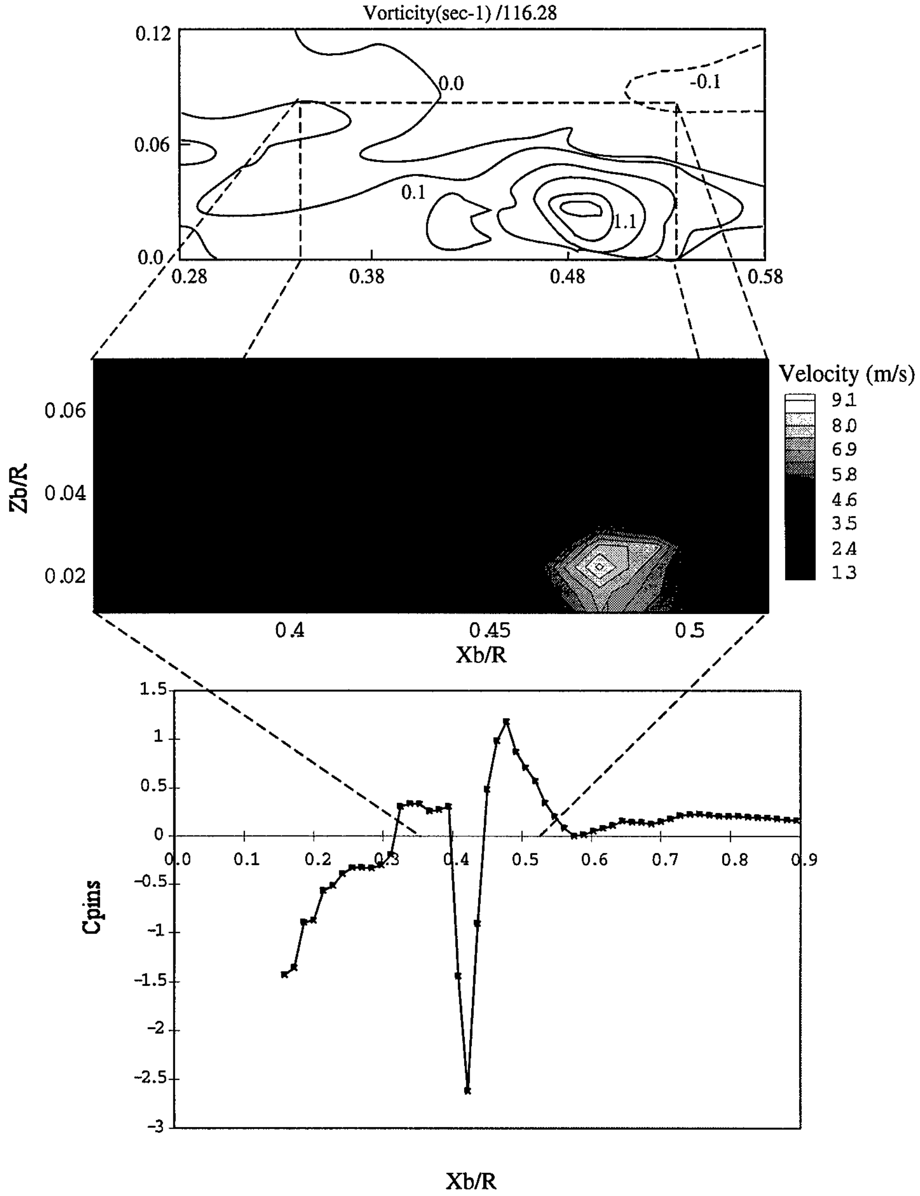

Figure 4.13: Correlation between lateral vorticity, velocity and surface pressure distribution on top of the airframe as the vortex collides with the airframe, $\mu = 0.1$, $\psi = 252^o$.

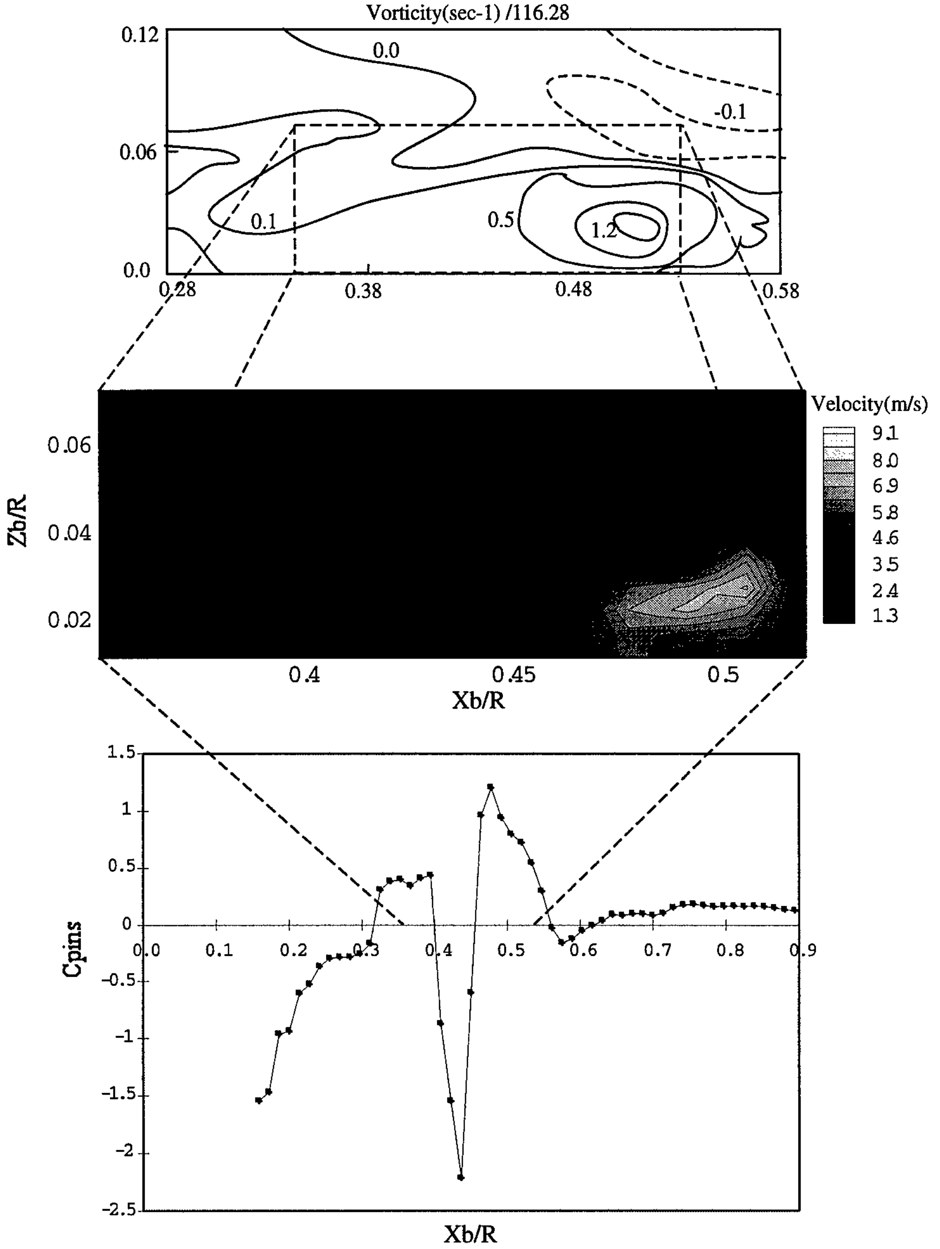

Figure 4.14: Correlation between lateral vorticity, velocity and surface pressure distribution on top of the airframe as the vortex collides with the airframe, $\mu = 0.1$, $\psi = 258^o$.

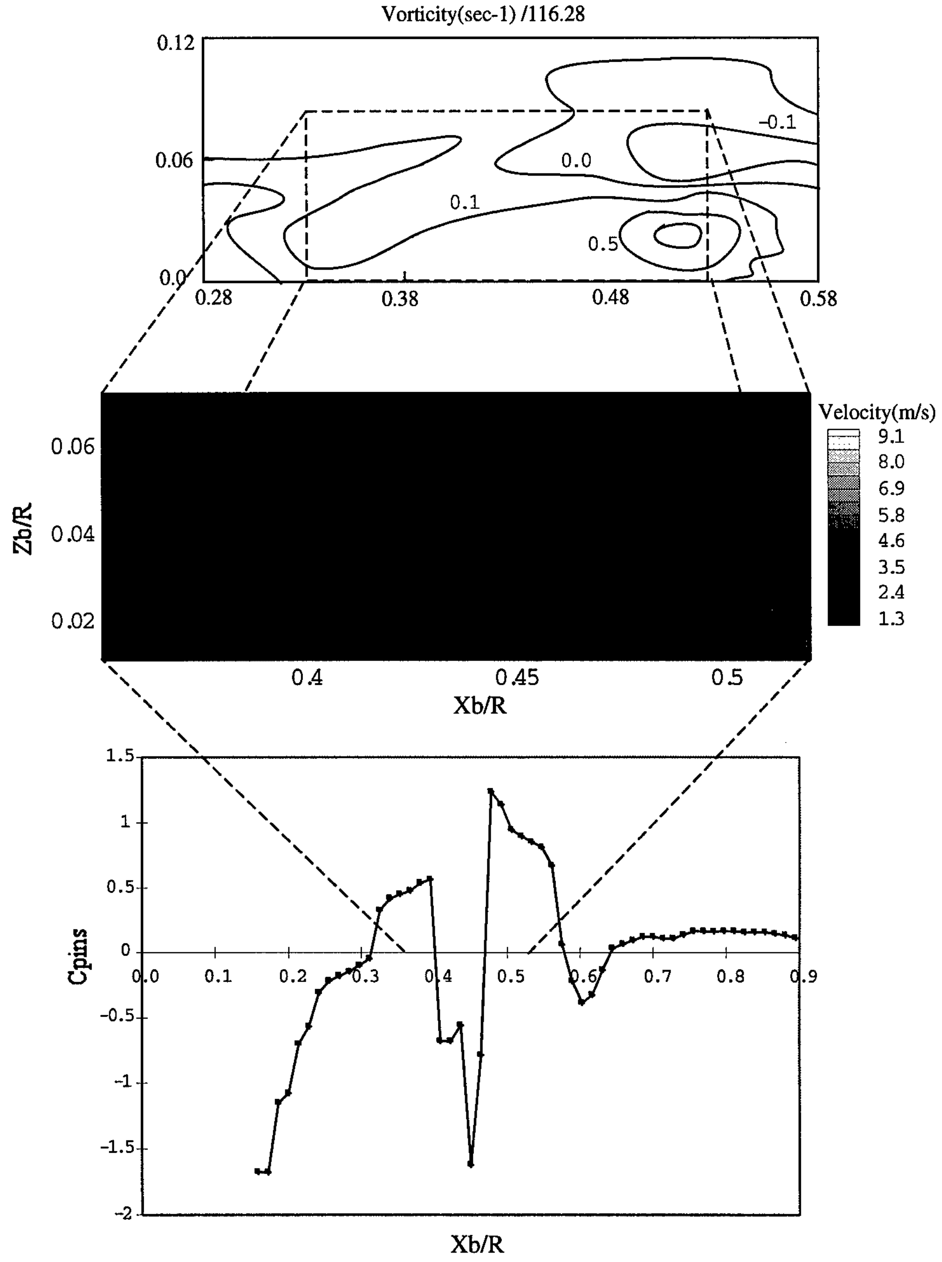

Figure 4.15: Correlation between lateral vorticity, velocity and surface pressure distribution on top of the airframe as the vortex collides with the airframe, $\mu = 0.1$, $\psi = 270^o$.

peak occurs upstream of the core on the ABS, whereas the stagnation occurs closer to the center of the vortex.

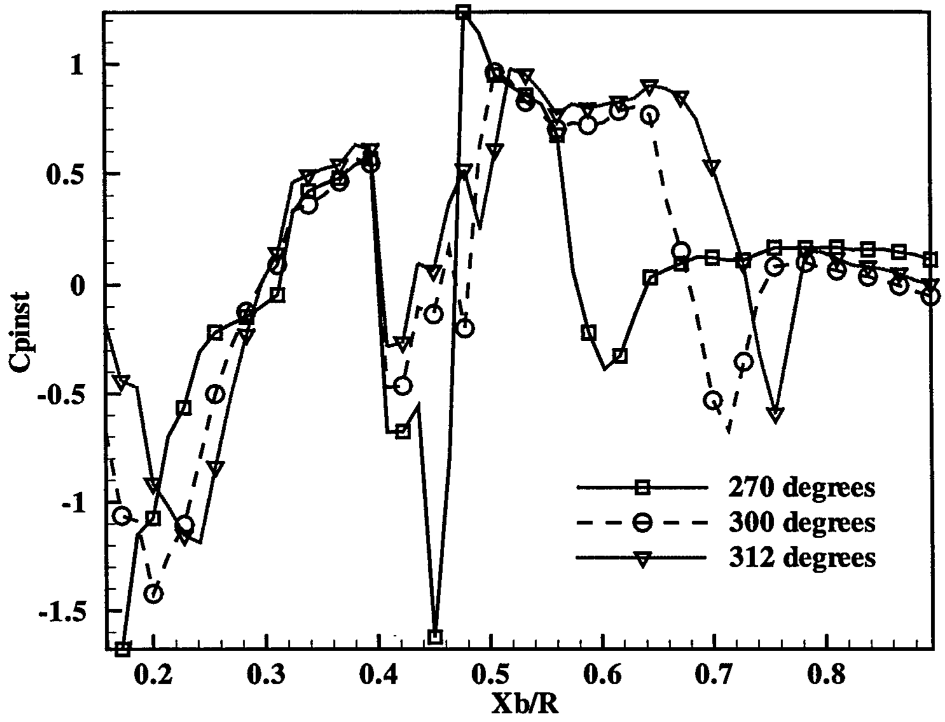

Figure 4.16: Instantaneous pressure on the top of the airframe at several vortex ages. The suction peaks downstream of the primary vortex around $\frac{Xb}{R} = 0.7$ are caused by the rolled-up inboard vortex sheet.

In Figure 4.15, the suction spike develops a secondary "ledge": an explanation for this is not evident from the velocity or vorticity contours. The contours of lateral velocity also show a break-up into two regions: this corresponds to an inflexion in the region of positive pressure coefficients (Xb/R of 0.51). The suction downstream (at Xb/R = 0.6) corresponds to the edge of the inboard vortex sheet from the current blade, as seen from the measurements made by Kim and Komerath (1995). Figure 4.16 emphasizes this. Here, pressure traces at several vortex ages are superposed, and show this downstream suction spike moving downstream rapidly, while increasing to a maximum of close to -1 at about $\psi = 300^o$. The edge of the inboard sheet convects much more rapidly than the tip-vortex itself.

Core Deformation on Top of the Airframe

The results from previous computations suggest that the core would flatten as the vortex approaches the cylinder. This is also seen in the lateral velocity contours seen in Figure 4.14. Figure 4.17 shows the ratio of the vertical to the streamwise dimension of the vortex (referred to here as the Vortex Aspect Ratio), as it goes through the final stages of the interaction. The core remains circular until the close interaction with the surface begins. At about $\psi = 270^o$ of vortex age the core abruptly flattens along the vertical dimension and forms into a sheet like region, with a persistence of axial velocity. The core flattening occurs over a rotor azimuth of about 4^o, which is much less than 1ms. This is not captured in the vorticity contours since the vertical and streamwise components of velocity were obtained at an azimuth resolution of 6^o, thus completely washing over the phenomenon.

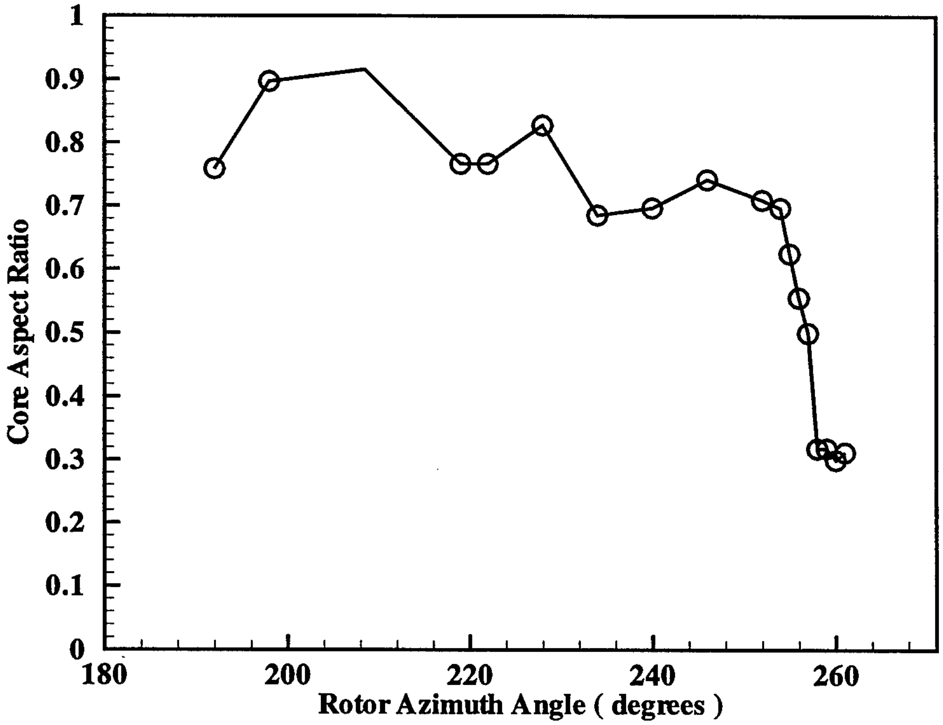

Figure 4.17: Time scale of vortex core flattening on top of the airframe. The core aspect ratio is defined as the ratio of the vertical to the horizontal dimension of the vortex.

4.3.5 Effect of Vortex Age on Core Axial Velocity

Figure 4.18 shows the maximum axial velocity measured in the core as a function of vortex age. Note the rapid variation and significant scatter in the axial velocity; some of this scatter may be in part due to the inablility to measure velocities in the exact center of the core. Much of the scatter in the figure up to $\psi = 200^o$ can be attriburted to the blade passage effect. Some of the scatter is also caused by vortex jitter during the collision on the top of the airframe. Axial velocities up to 16 $\frac{m}{s}$ (32 $\frac{m}{s}$ at 2100 rpm) are measured around $\psi = 222^o$, which is higher than the peak tangential velocity at that point (around 20 $\frac{m}{s}$ at 2100 rpm). Note that the axial velocity in the core even at $\psi = 270^o$ vortex age is of the order of 10 $\frac{m}{s}$ (20 $\frac{m}{s}$ at 2100 rpm). Even this late in the vortex age there is a persistence of the core axial velocity. While the axial velocity in the vortex tube on the RBS (still attached to the rotor blade, but growing older) is still very high, the velocity in the cut filament on the ABS goes down. These observations suggest that any dissipation/diffusion of the wake strength that are seen in meaurements are just artifacts of inadequate measurements in non-periodic flow-fields. Once a clean, periodic flow-field is established, the rotor-wake is seen to persist far beyond 300^o of vortex age.

4.4 Lateral Velocity Contours at $\mu = 0.09$

Figure 4.19 examines the magnitudes of the lateral velocity component in the wake of the rotor as the inboard vortex sheet sweeps by. Both the tip-vortex and the inboard wake are seen in the figure. The inboard wake rolls-up into a discrete region. Note that the inboard wake is from the current blade, while the tip-vortex is from the previous blade. There is a high lateral velocity in a broad region, directed towards the blade. This strengthens the hypothesis that both the tip-vortex core axial velocity and the inboard wake velocity stem from the viscous effects on blade. The large magnitudes of the inboard sheet velocity make it essential to be included in future prediction codes for aerodynamic interactions.

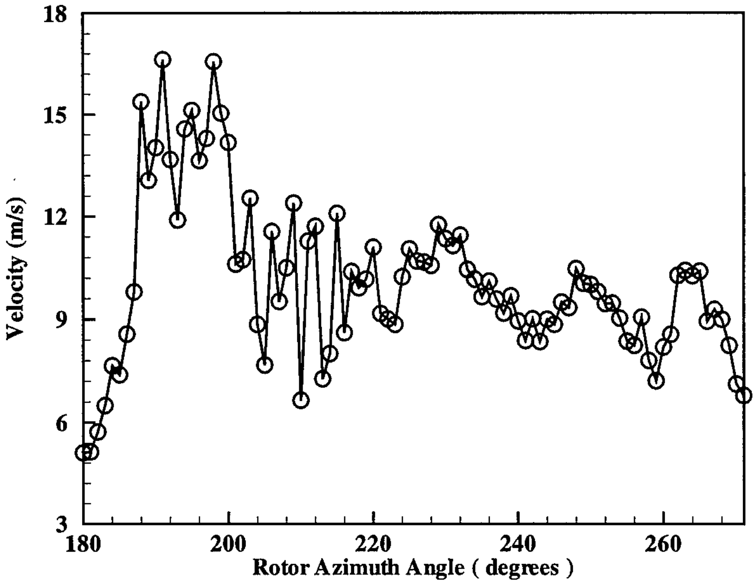

Figure 4.18: Variation of core axial velocity as measured in the collision region. Note that the core axial velocity is nominally in the direction of the swirl component of the wake in the plane of measurement. The blade passage effect appears to cause much of the fluctuation in the axial velocity up to $\psi = 200^o$. Other causes of the fluctuation of the axial velocity are discussed in the text.

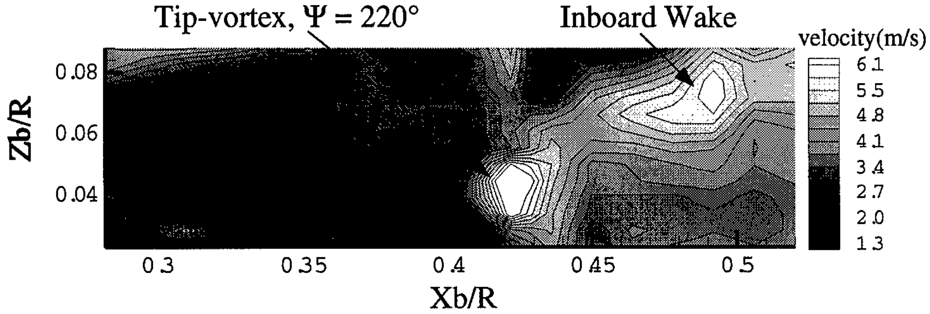

Figure 4.19: Lateral velocity field at $\mu = 0.09$ shows the development of the inboard sheet into a concentrated region of high wake-like axial velocity.

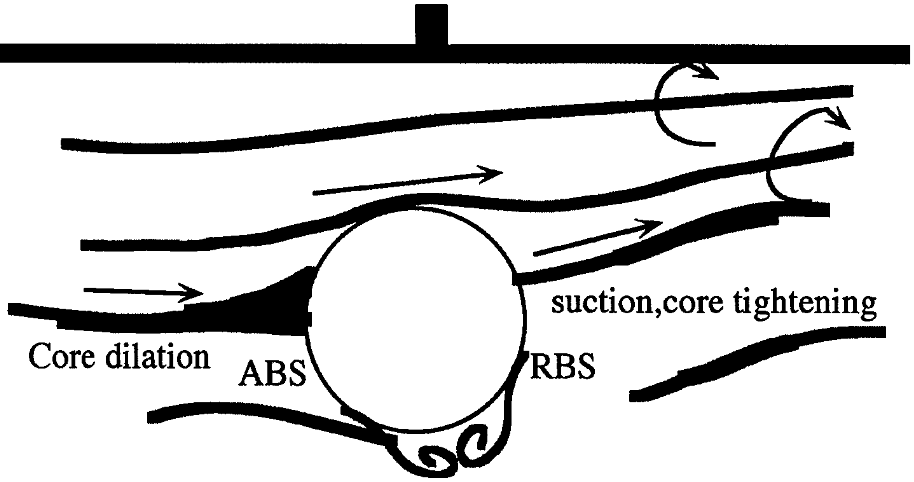

Figure 4.20: Schematic of the flow-field visualized under the cylinder.

4.5 Flow Features Under the Airframe

After the vortex gets cut on top of the airframe and convects down the sides of the cylinder, the question that arises is whether the cut ends of the vortex reconnect under the cylinder. With the enhanced pulse intensity and temporal resolution of the light sheet from a copper vapor laser, combined with an intensified camera, it was possible to examine the vortex behavior below the GT cylinder. Flow-visualization on the sides and under the cylinder was done to understand the flow behaviour after vortex collision on the top of the airframe. Figure 4.20 shows a composite schematic of the flow-features seen in the interaction on the sides and at the bottom of the airframe. On the ABS the cut vortex stays attached to the surface of the cyinder as it convects down. Thus vertical planes of illumination illustrate a rotating core all along the ABS. On the RBS, however, the core appears to detach from the cylinder surface after reaching 90^o on the side. Thus on the RBS the seed particle deficit, which indicates the vortex core, appears to move along the filament and away from the cylinder. At the bottom of the cylinder the combination of the downwash and the swirl cause flow-separation. The separation is not symmetric about the vertical plane through the center of the cylinder but is skewed to the RBS. This skew towards the RBS is due to the swirl component. A stable pair of vortices is seen to form in the wake. The cut end of the filament on the ABS is seen to end in this separated flow region.

4.6 Conclusions

- The collision phase of the rotor-airframe interaction is substantially influenced by the axial velocity in the tip-vortex core. The core axial velocity is primarily responsible for the asymmetric surface pressure distribution.
- The core axial velocity is of the order of core circumferential velocity and directed wake-like, i.e., towards the blade from which the vortex was generated. Core axial velocities approaching one-thirds the tip-speed of the rotor were measured just prior to the collision.
- Independent, phase-resolved and ensemble-averaged, three component velocity measurements of the rotor wake above the airframe were made feasible by the periodicity of the rotor wake, as well as the repeatability of test conditions, as shown by the successful correlation between the lateral velocity and vorticity contours measured 10 years apart.
- Instantaneous flow-image features, deduced from seed-particle distributions, correlate well with the pressure traces during the potential phase of the interaction.
- Several phenomena in the rotor airframe collision phase occur over a short time scale of the order of a 1^o rotor azimuth.
- Velocity deficits measured in the inboard blade wake approached half the core-axial velocities. The inboard wake was seen to concentrate into a region of high axial velocity. The effect of the rolled up inboard sheet is a suction spike rapidly convecting downstream of the tip vortex.

Chapter 5

The 90^o Collision Process

5.1 Introduction

As discussed in Chapter 1, the velocity component directed along the axis of the vortex has a major effect on the interaction of the vortex with a downstream body. We denote this type of vortex with axial flow a "vortex-jet" since it possesses characteristics typical of both vortices and jets. To illustrate the effect of axial flow in the core of the vortex described experimentally in the previous Chapter, we consider the case where a vortex is cut by a thin plate which is instantaneously inserted into the flow at a 90^o angle to the axis of rotation of the vortex. When the axial velocity in the vortex is directed towards the solid boundary, the condition that the axial flow in the vortex core must be brought to zero at the wall, causes the vortex to bulge in the sense that its core becomes larger. When the axial velocity in the vortex is directed away from the solid boundary, the vortex core is seen to thin locally.

To fix ideas, consider an already existing, infinitely-long vortex with core radius a_v, circulation Γ^*, and axial velocity w^*. At time $t^* = 0$, the vortex is instantaneously split by a plane wall normal to the axis of the vortex. The problem is to determine the fluid behavior for time $t^* > 0$, with particular interest in the behavior of the pressure, swirl velocity, and the axial vorticity. For convenience, the problem is formulated in cylindrical-polar coordinates (r^*, θ, z^*) with the axis of the vortex coincident with the z-axis. The physical problem of interest is depicted on Figure 5.1(a) for the case where the axial velocity in the vortex is directed toward the wall. This is the case which occurs on the advancing side of the helicopter rotor in which the rotor is

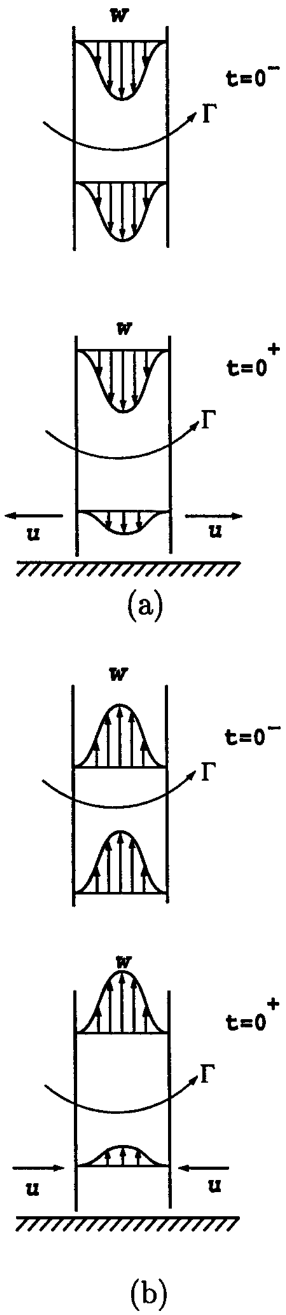

Figure 5.1: Vortex Normal to a Plane Wall; (a) axial inflow; (b) axial outflow.

travelling in the same direction as the airframe. Figure 5.1(b) shows the problem for the case where the axial velocity in the vortex is directed away from the wall, which occurs on the retreating side of the rotor in which the rotor is travelling in a direction opposite to the flight velocity.

As mentioned just above, the results presented in this chapter are meant to have much wider applications than to just the rotorcraft problem. For example, the present analysis should describe the qualitative features of the blade-vortex interaction problem as well as the vortex buffet problem with only minor adjustments to physical parameters and initial conditions. In addition, the qualitative features of the results in this work are not expected to depend substantially on the angle at which the vortex is cut.

In the next section, the formulation of the problem is given. This is followed by the derivation of an analytical solution for a vortex in which the axial and radial velocities are independent of time. This solution is compared with numerical results for the full problem which follows. In addition, analytical solutions for the initial and final flow conditions for a pure jet have been derived by the second author and are presented in Appendix A. These analytical solutions for the pure jet strongly confirm the accuracy of the numerical solution.

5.2 Formulation

The governing equations are taken to be the axisymmetric and incompressible Euler equations; these equations are sufficient to illustrate the basic physical phenomena. All length scales are non-dimensionalized by the initial vortex core radius a_v, and all velocities are non-dimensionalized by the vortex-jet velocity w_0. With a * denoting the dimensional variables, the non-dimensional variables are given as

$$t = \frac{t^* w_0}{a_v}, \quad r = \frac{r^*}{a_v}, \quad z = \frac{z^*}{a_v}, \quad \Gamma = \frac{\Gamma^*}{w_0 a_v},$$

$$u = \frac{u^*}{w_0}, \quad v = \frac{v^*}{w_0}, \quad w = \frac{w^*}{w_0},$$

with the non-dimensional pressure defined as

$$p = \frac{p^*}{\rho w_0^2}. \tag{5.1}$$

Here Γ^* is the circulation and ω^* is the azimuthal vorticity. In dimensionless form, the unsteady, axisymmetric Euler equations in cylindrical-polar coordinates (r, θ, z), with velocity components $(u, v, w) = (v_r, v_\theta, v_z)$, are given in dimensionless form as

$$\frac{\partial u}{\partial t} + u\frac{\partial u}{\partial r} + w\frac{\partial u}{\partial z} - \frac{v^2}{r} = -\frac{\partial p}{\partial r}, \tag{5.2}$$

$$\frac{\partial v}{\partial t} + u\frac{\partial v}{\partial r} + w\frac{\partial v}{\partial z} + \frac{uv}{r} = 0, \tag{5.3}$$

$$\frac{\partial w}{\partial t} + u\frac{\partial w}{\partial r} + w\frac{\partial w}{\partial z} = -\frac{\partial p}{\partial z}. \tag{5.4}$$

The continuity equation in cylindrical-polar coordinates for incompressible flow is given by

$$\frac{1}{r}\frac{\partial (ru)}{\partial r} + \frac{\partial w}{\partial z} = 0. \tag{5.5}$$

The numerical domain of solution is now $0 \le r \le R$ and $0 \le z \le L$.

The vorticity vector is defined as $\vec{\omega} = \nabla \times \vec{u}$ with the azimuthal and axial components denoted by ω and ξ. It should be noted that there exists a radial component of vorticity $-\frac{\partial v}{\partial z}$; however it is not required in this formulation. The azimuthal and axial components of vorticity are defined by

$$\omega = \frac{\partial u}{\partial z} - \frac{\partial w}{\partial r}, \;\; \xi = \frac{1}{r}\frac{\partial}{\partial r}(rv). \tag{5.6}$$

In the present work we assume that the flow is axisymmetric and in this situation, rather than solve equations (5.2) through (5.5) in their present forms, it is simpler to replace the velocity components (u, v, w) with the vorticity (ω), and the stream-function (Ψ). Equation 5.5 is satisfied by the existence of a stream function, Ψ, which is defined by the radial and axial velocity components as

$$u = -\frac{1}{r}\frac{\partial \Psi}{\partial z}, \tag{5.7}$$

$$w = \frac{1}{r}\frac{\partial \Psi}{\partial r}. \tag{5.8}$$

In terms of the stream function, equation (5.6) yields

$$\omega = -\frac{\partial}{\partial z}\left(\frac{1}{r}\frac{\partial \Psi}{\partial z}\right) - \frac{\partial}{\partial r}\left(\frac{1}{r}\frac{\partial \Psi}{\partial r}\right) = -\frac{1}{r}D^2\Psi, \tag{5.9}$$

and equation (5.3) for the circulation function ($\Omega = rv$) becomes

$$\frac{\partial \Omega}{\partial t} + u\frac{\partial \Omega}{\partial r} + w\frac{\partial \Omega}{\partial z} = 0. \tag{5.10}$$

The inviscid, axisymmetric azimuthal vorticity transport equation is found by combining the momentum equations (5.2) and (5.4) (thus eliminating pressure) and is given by

$$\frac{\partial \omega}{\partial t} + u\frac{\partial \omega}{\partial r} + w\frac{\partial \omega}{\partial z} - \frac{u\omega}{r} - 2\frac{v}{r}\frac{\partial v}{\partial z} = 0, \tag{5.11}$$

with u and w given by equations (5.7) and (5.8). Equations (5.9), (5.10) and (5.11) are solved simultaneously for the three unknowns Ψ, $v = \Omega/r$ and ω.

In the following we formulate the boundary conditions for the case where the axial velocity is directed toward the wall, assumed to be $z = 0$. Four boundary conditions are needed for the elliptic equation (5.9). It is expected that the influence of the wall is not felt at $z = L$ (precisely true only in the limit as L approaches infinity), and hence the following Dirichlet boundary condition may be used

$$\Psi = \int_0^R r w_I dr \ \ on \ \ z = L, \tag{5.12}$$

where w_I is a prescribed function of r. For time $t > 0$, the axial velocity w must be zero on the wall and hence

$$\Psi = 0 \ \ on \ \ z = 0; \tag{5.13}$$

similarly, on $r = 0$, u must be zero, yielding

$$\Psi = 0 \ \ on \ \ r = 0. \tag{5.14}$$

The axial velocity vanishes as $r \to \infty$ and so,

$$\frac{\partial \Psi}{\partial r} = 0 \ \ on \ \ r = R, \tag{5.15}$$

is the appropriate outer boundary condition provided R is sufficiently large.

The hyperbolic equations (5.11) and (5.10) also require boundary conditions specified on the inflow boundary $z = L$. For the vorticity transport equation (5.11), we assume that the vorticity at $z = L$ does not change from its initial condition for all time, which corresponds to a constant inflow (or outflow) of azimuthal vorticity. This is valid as long as the effects of the wall are not felt at $z = L$. In this case, the circulation function, equation (5.10), at $z = L$ also remains unchanged from its initial condition.

The pressure is obtained by integrating equations (5.2) and (5.4) with the reference pressure taken at $r = R$, $z = 0$. That is, equation (5.4) is solved on $r = R$, with the reference pressure being $p(R, 0, 0) = 0$. Equation (5.2) is used to solve the pressure elsewhere with the reference pressure being $p(R, z, t)$. For example, if equation (5.4) is expressed in conservative form, then the pressure on $r = R$ is given by

$$p(R,z,t) = -\int_0^z \left(\frac{\partial w}{\partial t} + \frac{1}{r}\frac{\partial}{\partial r}(ruw) + \frac{\partial}{\partial z}\left(w^2\right) \right) dz \tag{5.16}$$

and integrating equation (5.2) similarly yields

$$p(r,z,t) = \int_r^R \left(\frac{\partial u}{\partial t} + \frac{1}{r}\frac{\partial}{\partial r}\left(ru^2\right) + \frac{\partial}{\partial z}(uw) - \frac{v^2}{r} \right) dr + p(R,z,0), \tag{5.17}$$

where we have assumed that R is large enough so that $p(R, z, t) = p(R, z, 0)$.

5.3 Numerical Methods

The vorticity-stream function representation of the Euler equations given in the previous section actually contain two separate types of equations: equation (5.9) is a two-dimensional, second-order elliptic equation, whereas equations (5.10) and (5.11) are two-dimensional, unsteady, nonlinear first-order hyperbolic equations. This suggests that the implementation of at least two different numerical schemes are necessary to solve the system of equations. Equation (5.9) can be solved easily using the standard finite-difference methods and Gauss-Seidel iteration. The standard numerical method for solving the hyperbolic equations (5.10) and (5.11) is the method of characteristics. However, the programming of the method of characteristics is much more difficult than the programming of finite-difference methods, especially for problems involving a set of simultaneous two-dimensional nonlinear first-order equations. For this reason, numerical methods chosen for the solution of equations (5.10) and (5.11) utilize finite-difference methods. To significantly reduce the amount of computation time required, the multigrid method is employed in the solution of equation (5.9).

The numerical solution to equation (5.9) subject to boundary conditions (5.12) through (5.15) is calculated using a standard finite-difference scheme. The differential equation (5.9) is discretized in the (r, z) plane with uniform fixed grid spacing in both coordinates. Let i be the spatial index in the radial direction which varies from 0 to M and j be the spatial index in the axial direction which varies from 0 to N. The total number of gridpoints is $(N+1) \times (M+1)$. The grid spacings are $\Delta r = R/M$ and $\Delta z = L/N$, where R and L are the lengths of the computational domain in the r and z directions respectively.

Second order central differences are used for the spatial derivatives in equation (5.9) and these are

$$\left.\frac{\partial \Psi}{\partial r}\right|_{i,j} = \frac{\Psi_{i+1,j} - \Psi_{i-1,j}}{2\Delta r} + O\left(\Delta r\right)^2, \tag{5.18}$$

$$\left.\frac{\partial^2 \Psi}{\partial r^2}\right|_{i,j} = \frac{\Psi_{i+1,j} - 2\Psi_{i,j} + \Psi_{i-1,j}}{\left(\Delta r\right)^2} + O\left(\Delta r\right)^2, \tag{5.19}$$

with similar discretization in the $z-$direction. Accuracy is improved near $r = 0$ by using a fourth-order central difference approximation for $\frac{\partial \Psi}{\partial r}$ and is given by

$$\left.\frac{\partial \Psi}{\partial r}\right|_{i,j} = \frac{-\Psi_{i+2,j} + 8\Psi_{i+1,j} - 8\Psi_{i-1,j} + \Psi_{i-2,j}}{12\Delta r} + O\left(\Delta r\right)^4, \tag{5.20}$$

which yields truncation error $O\left(\Delta r\right)^3$ in equation (5.9) when $r \sim \Delta r$ and is valid for $i = 2, ..., M-2$, and $j = 0, ..., N$. Also for the points $i = 1$ and $i = M-1$ adjacent to the boundaries, fourth order sloping difference formulas for $\frac{\partial \Psi}{\partial r}$ are used.

The difference equation is solved using a standard Gauss-Seidel point-iterative scheme with successive over-relaxation (SOR) coupled with a multi-grid scheme to accelerate convergence. After each iteration of the system of equations is calculated, relaxation is applied with the relaxation parameter of 1.8 used in the present calculations. The process is repeated until the relative convergence test

$$max\left(\left|1 - \frac{\Psi^{n+1}_{i,j}}{\Psi^{n}_{i,j}}\right|\right) < \epsilon, \tag{5.21}$$

is satisfied for a criterion of $\epsilon = 10^{-7}$. If the convergence test given in equation (5.21) is satisfied, then the computed values of Ψ are used to calculate the velocities u and w as shown below, and the other two governing equations (5.10) and (5.11) are solved using a second-order predictor-corrector method in time, and second-order upwind differencing in space and all variables are saved at that time-level. Otherwise, the iteration is continued.

The meridional flow velocities u and w are calculated from equations (5.7) and (5.8) using standard fourth-order finite-differences. Fourth-order approximations are used in order to retain accuracy for $r \sim \Delta r$, and the equations are similar to those given above for $\frac{\partial \Psi}{\partial r}$.

The pressure is found through the numerical integration of equations (5.16) and (5.17) using a second-order accurate trapezoidal rule. The unsteady terms are calculated using a three-point second-order backward difference in time, and are given by

$$\left.\frac{\partial u}{\partial t}\right|_{i,j}^{n} = \frac{-3u_{i,j}^{n-2} + 4u_{i,j}^{n-1} - u_{i,j}^{n}}{2\Delta t} + O\left(\Delta t\right)^2, \tag{5.22}$$

$$\left.\frac{\partial w}{\partial t}\right|_{i,j}^{n} = \frac{-3w_{i,j}^{n-2} + 4w_{i,j}^{n-1} - w_{i,j}^{n}}{2\Delta t} + O\left(\Delta t\right)^2, \tag{5.23}$$

where $n \geq 2$ is the current time level. For $n = 1$ central differences are used. For $n = 0$, it can be seen from equations (5.16) and (5.17) and the initial conditions given in equations (5.42), (5.43) and (5.44) that the only contribution to the pressure is that from the swirl velocity. All spatial derivatives used in the calculation of the pressure are standard fourth-order central differences.

The axial vorticity as defined in equation (5.6) is calculated using standard fourth-order accurate finite-difference schemes such as given equation (5.20). Again, fourth-order accurate schemes are used to reduce the effect of the division by r in equation (5.6) which causes reduction in accuracy for $r \sim \Delta r$.

The computational procedure for solving the system of equations consisting of the stream-function, the vorticity-transport equation, and the circulation function is carried out in the following order:

1. Begin with initial distributions of u, v, w, ω, Ψ.

2. Calculate $\omega_{i,j}^{n+1/2}$, and $v_{i,j}^{n+1/2}$ from the predictor step of the discretization of equations (5.10) and (5.11).

3. Using the multigrid method, calculate $\Psi_{i,j}^{n+1/2}$ using $\omega_{i,j}^{n+1/2}$.
4. Calculate the meridional flow $u_{i,j}^{n+1/2}$ and $w_{i,j}^{n+1/2}$ from $\Psi_{i,j}^{n+1/2}$ from equations (5.7) and (5.8).
5. Calculate $\omega_{i,j}^{n+1}$, and $v_{i,j}^{n+1}$ from the corrector step.
6. Calculate $\Psi_{i,j}^{n+1}$ using $\omega_{i,j}^{n+1}$ using the multigrid scheme.
7. Calculate the meridional flow $u_{i,j}^{n+1}$ and $w_{i,j}^{n+1}$ from $\Psi_{i,j}^{n+1}$.
8. Solve for the axial vorticity from equation (5.6) and calculate the pressure as described above.
9. Transfer all the newly computed values to the previous time-level and go to the next time level. Repeat steps 2 – 9 until the desired time is reached.

The present computational scheme was tested on a model problem for which an analytical solution can be found. This problem exhibits many of the features of the full nonlinear problem and it is worthwhile to investigate this problem first.

5.4 Multigrid Methods

5.4.1 Background

The multigrid method can be a powerful tool in solving elliptic problems such as given in equation (5.9), however the extent of increase in computational efficiency is highly dependent on the problem. In this problem, it is of interest to solve the vorticity/stream-function equation (5.9) in a more efficient manner than the Gauss-Seidel method(Lee *et al.* 1995). When used independently, Gauss-Seidel and other relaxation methods become ineffective when numerous iterations are needed to solve a problem with many grid points or small convergence criteria. In the first few relaxation sweeps, the error decreases sharply because the error is oscillatory with well-defined amplitude peaks which are easily damped. As the iterations proceed, however, the peaks become rounded, or "smooth", reducing the ability of the relaxation method to decrease the error at an efficient rate. This is called the "smoothing" effect which slows solution convergence and increases computation time considerably.

Multigrid methods eliminate the smoothing effect and reduce computing time by combining a few techniques. First, multigrid uses only the first few iteration sweeps at the fine grid level to optimize the decreasing error, fully utilizing the effectiveness of the relaxation method. When transferring from a fine to coarse grid, the residual remains oscillatory with a smaller number of amplitude peaks. In effect, the interpolation decreases the number of error modes while maintaining the oscillating form. This enables the relaxation sweeps on the error-residual equation (Section 5.4.2) to efficiently converge on the error vector $\mathbf{e}$.

The following subsections give a general description of the multigrid method used in this work beginning with a discussion on the above mentioned concepts, and ending with the method of solution of the vorticity/streamfunction using multigrid techniques. The following formulation is from Briggs (1987).

5.4.2 The Residual

A system of equations in matrix form is given by

$$A\mathbf{u} = \mathbf{f} \tag{5.24}$$

or

$$\mathbf{f} - A\mathbf{u} = 0 \tag{5.25}$$

where A is the scalar (or coefficient) square matrix in equation (5.9) defined as

$$A = D^2 = \frac{\partial^2}{\partial r^2} - \frac{1}{r}\frac{\partial}{\partial r} + \frac{\partial^2}{\partial z^2}, \tag{5.26}$$

$\mathbf{u}$ is the exact solution vector in equation (5.9) defined as

$$\mathbf{u} = \Psi, \tag{5.27}$$

and $\mathbf{f}$ is the source term in equation (5.9) defined as

$$\mathbf{f} = -r\omega. \tag{5.28}$$

Vectors $\mathbf{u}$ and $\mathbf{f}$ are of equal size. Vector $\mathbf{v}$, which is an approximation for $\mathbf{u}$, satisfies the same set of equations and is defined as the difference between $\mathbf{u}$ and the error vector $\mathbf{e}$ where

$$\mathbf{v} = \mathbf{u} - \mathbf{e}. \tag{5.29}$$

When solving a system of equations numerically, the error between the approximate and exact solutions is critical in determining solution validity. Up to this point the error cannot be determined from equation (5.29) because $\mathbf{u}$ is unknown. When $\mathbf{v}$ is substituted for $\mathbf{u}$, the right side of equation (5.25) is no longer zero. This non-zero term creates a vector known as the residual vector $\mathbf{r}$ which is defined as

$$\mathbf{r} = \mathbf{f} - A\mathbf{v}. \tag{5.30}$$

Solving equation (5.29) for $\mathbf{u}$ and substituting into equation (5.24) gives

$$A(\mathbf{v} + \mathbf{e}) = \mathbf{f} \tag{5.31}$$

or

$$A\mathbf{e} = \mathbf{f} - A\mathbf{v}. \tag{5.32}$$

Replacing the right hand side with equation (5.30) yields

$$A\mathbf{e} = \mathbf{r}. \tag{5.33}$$

This is known as the error-residual equation. From a known approximate solution which is found at any relaxation sweep, the residual is calculated from equation (5.30) and inserted as the source term into equation (5.33) from which $\mathbf{e}$ is determined. The exact solution is then obtained from equation (5.29). The concept of the residual and its relationship to the error in equation (5.33) is a fundamental idea used in establishing the multigrid technique.

The boundary conditions for the error-residual equation can be obtained from the boundary conditions on the stream-function Ψ as defined in Section 5.2. Since the stream-function is known on three of the four boundaries, the error is zero there. On the boundary $r = R$, the appropriate boundary condition is $\frac{\partial e}{\partial r} = 0$. The initial condition for the error-residual equation is $e = 0$. Figure 5.2 shows the boundary conditions for the error-residual equation over the domain of the problem.

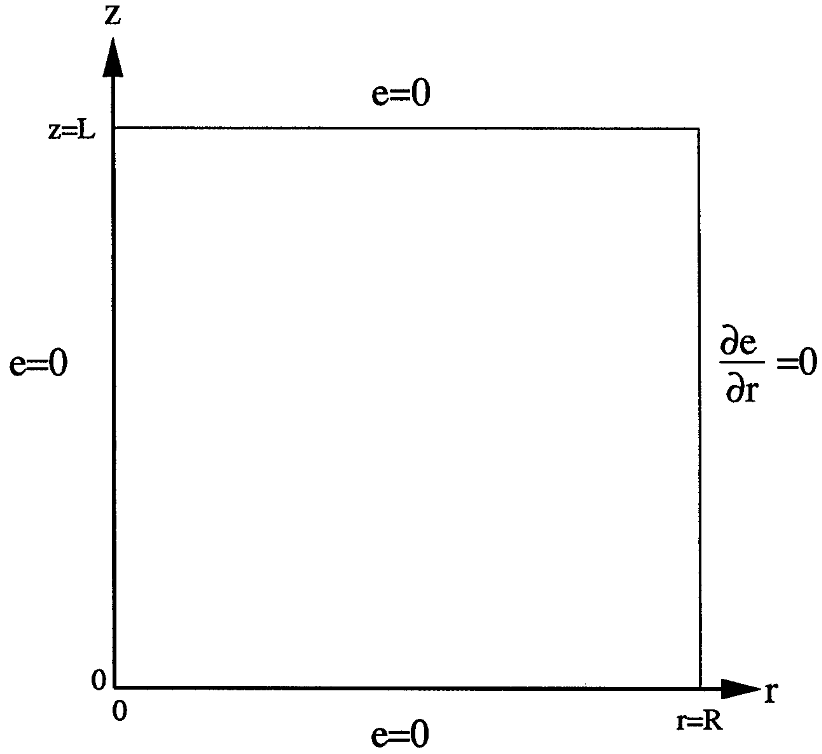

Figure 5.2: Boundary conditions for the error-residual equation.

5.4.3 Multilevel Grids

Multigrid methods do not alter the domain on which the problem is solved, hence the given physical boundaries remain unchanged. Within this domain, the multigrid scheme utilizes many different grid sizes, or "levels", moving from a fine grid to a coarse grid and vice versa. From one grid level to another, whether from fine-to-coarse or coarse-to-fine, the grid spacing differs by a factor of two. For example, a two dimensional fine grid with uniform spacing h and $M+1$ and $N+1$ grid points is transformed to a coarser grid with twice the spacing, $2h$, and $\frac{M}{2}+1$ and $\frac{N}{2}+1$ grid points, respectively. This process is reversible and repeatable allowing multigrid methods the freedom to move to any desired grid level one level at a time.

5.4.4 Elementary Multigrid Cycle

By combining the information discussed in the preceding sections, a working multigrid method can be formulated. From an initial guess, say $\mathbf{u} = 0$, an initial approximation $\mathbf{v}$ is found from a few relaxation sweeps on the fine grid. The residual $\mathbf{r}$ is then calculated from equation (5.30) and transferred to the coarse grid by a fine-to-coarse grid interpolation. Equation (5.33) is then solved to obtain $\mathbf{e}$ on the coarse grid. By a coarse-to-fine grid interpolation, $\mathbf{e}$ is transferred to the fine grid where it is added to $\mathbf{v}$ to obtain the exact solution $\mathbf{u}$. This process can be combined to form an elementary multigrid procedure outlined as

1. Set initial guess: $\mathbf{u}^f = 0$
2. Relax K times on fine grid: $A\mathbf{v}^f = \mathbf{f}^f$
3. Calculate the residual: $\mathbf{r}^f = \mathbf{f}^f - A\mathbf{v}^f$
4. Transfer residual to coarse grid: $\mathbf{r}^c = I_f^c \mathbf{r}^f$
5. Solve for error: $A\mathbf{e}^c = \mathbf{r}^c$
6. Transfer error to fine grid: $\mathbf{e}^f = I_c^f \mathbf{e}^c$
7. Calculate exact solution: $\mathbf{u}^f = \mathbf{v}^f + \mathbf{e}^f$

where the superscripts f and c represent the fine and coarse grid levels, respectively. The fine-to-coarse and coarse-to-fine grid interpolations are denoted by interpolation operators I_f^c and I_c^f, respectively. The letter K is a small integer usually from one to three. The above procedure describes a single fine-to-coarse-to-fine computation. In the next section, we show how to extend this concept to multiple grid levels.

5.4.5 The Multigrid Cycle

The elementary multigrid method in section 5.4.4 can be expanded to include numerous grid levels which minimize computation time without jeopardizing solution validity. This is done by further applying the multigrid technique to solve equation (5.33) since it takes the same form as equation (5.24). Being able to repeat this technique gives multigrid methods a recursive nature. In fact, repeated applications allow equation (5.33) to be solved on the coarsest grid possible where only a few grid points remain. Once the error is found on the coarsest grid, it is then transferred to successive finer grids where μ relaxations are performed at each level until the original fine grid is reached. This procedure, a revised version of the one in section 5.4.4, can be outlined as

1. Set $\mathbf{v}^h = 0$.
2. Relax K times on $A\mathbf{v}^h = \mathbf{f}^h$.
3. Calculate $\mathbf{r}^h = \mathbf{f}^h - A\mathbf{v}^h$.
4. Interpolate $\mathbf{f}^{2h} = I_h^{2h}\mathbf{r}^h$.
    (a) Set $\mathbf{v}^{2h} = 0$.
    (b) Relax K times on $A\mathbf{v}^{2h} = \mathbf{f}^{2h}$.
    (c) Calculate $\mathbf{r}^{2h} = \mathbf{f}^{2h} - A\mathbf{v}^{2h}$.
    (d) Interpolate $\mathbf{f}^{4h} = I_{2h}^{4h}\mathbf{r}^{2h}$.
    (e) ...

    (a) Correct $\mathbf{v}^{2h} = I_{4h}^{2h}\mathbf{v}^{4h}$.
    (b) Relax K times on $A\mathbf{v}^{2h} = \mathbf{f}^{2h}$.
5. Correct $\mathbf{v}^h = I_{2h}^h\mathbf{v}^{2h}$.

6. Relax K times on $A\mathbf{v}^h = \mathbf{f}^h$.

This is one type of multigrid cycle henceforth referred to as a V-cycle. The superscript h (superscript f in the previous section) represents the finest grid level whereas $2h$, $4h$, etc. identify successively coarser grid levels each with twice the grid spacing as the previous level. The initial guess for $\mathbf{v}^h$ is not restricted to zero. Relaxing a few times on the coarsest grid level and then extrapolating the results back to the original fine grid provides an excellent starting approximation while taking minimal time to compute.

Notice here the changes made to adapt a V-cycle from the simple multigrid method given in section 5.4.4. One solution vector $\mathbf{v}$ is used instead of three solution vectors: $\mathbf{u}$, $\mathbf{v}$ and $\mathbf{e}$. When interpolated, the residual $\mathbf{r}$ becomes the source vector $\mathbf{f}$ to be used in the next relaxation on the coarser grid level. The two-step procedure of interpolating the error and adding it to the original approximation on the fine grid is combined into one correction step by an interpolation operator. These changes allow relaxation on a consistent equation form, $A\mathbf{v} = \mathbf{f}$, simplifying the programming code by reducing all relaxation sweeps into a single subroutine. A subroutine can also be constructed for each of the other procedures. Calculation of the residual, interpolation of the residual, and correction of the approximation can each be handled in separate subroutines. In this research, these subroutines are used recursively where the subroutine arguments defined by the current grid level determine the subroutine outputs.

The vorticity/stream-function can now be solved by combining the contributions from the problem discretization, the Gauss-Seidel relaxation method, and the V-cycle multigrid method. To clarify notation, the stream-function solution $\Psi_{i,j}$ and the source term $(-r_i\omega_{i,j})$ from equation (5.9) are denoted by $v_{i,j}$ and $f_{i,j}$, respectively. As before, the superscripts h, $2h$, $4h$, etc. represent the grid level on which the variable is contained. For example, $f^h_{i,j}$ is the source variable values on a grid with spacing h, the finest grid level. A subroutine to perform the Gauss-Seidel relaxation on any grid level with known $f_{i,j}$ is constructed by using the discretized version of the vorticity-streamfunction, equation (5.9). For example, by sending f^h, Δr^h, Δz^h, N^h, and M^h as arguments to a subroutine, the solution for the streamfunction at grid level h, $v^h_{i,j}$ is calculated from the discretized form of equation (5.9).

The residual is calculated from equation (5.30) where $A\mathrm{v}$ is defined by the left side of equation (5.9) and the associated difference approximations.

Similarly, the two dimensional grid interpolation operator used to transfer the residual to a subsequent coarser grid level is defined differently for the interior and boundary points. The interpolation used here is known as a full weighting operator which calculates a weighted average of the grid points that are within a close proximity. Given a coarse grid point at a certain location, the fine grid point at that location and its immediately surrounding fine grid points are used to transfer the information to the coarse grid point. The full weighting operator for the interior points is

$$\begin{aligned} f_{i,j} &= \frac{1}{16}[r_{2i-1,2j-1} + r_{2i+1,2j+1} + r_{2i+1,2j-1} + \\ &\quad r_{2i-1,2j+1} + 2(r_{2i,2j-1} + r_{2i-1,2j} + \\ &\quad r_{2i+1,2j} + r_{2i,2j+1}) + 4r_{2i,2j}] \end{aligned} \tag{5.34}$$

where nine fine grid points, $r_{2i,2j}$ and its eight adjacent points, define the residual on the coarse grid $f_{i,j}$ for $i = 1, 2, ..., M - 1$ and $j = 1, 2, ..., N - 1$. On the boundaries, the full weighting operator is

$$f_{i,j} = r_{2i,2j} \tag{5.35}$$

where the fine grid point $r_{2i,2j}$ defines the residual on the coarse grid $f_{i,j}$ on the boundaries $i = 0$, $i = M$, $j = 0$, and $j = N$.

Equations (5.34) and (5.35) are included in a subroutine to transfer the known residual $r_{i,j}$ on any fine grid level to $f_{i,j}$ on a subsequent coarser grid level ($i = 0, 1, 2, ..., M - 1$ and $j = 0, 1, 2, ..., N - 1$). For example, $r_{i,j}^{2h}$ along with M^{4h} and N^{4h} are sent to a subroutine which interpolates $f_{i,j}^{4h}$ using equations (5.34) and (5.35).

The correction interpolation operator combines the coarse-to-fine grid interpolation of the error and the approximation correction into one step. The two dimensional correction interpolation operator used in this work is defined as

$$\begin{aligned} v_{2i,2j}^{f} &= v_{2i,2j}^{f} + v_{i,j}^{c} \\ v_{2i+1,2j}^{f} &= v_{2i+1,2j}^{f} + \frac{1}{2}(v_{i,j}^{c} + v_{i+1,j}^{c}) \\ v_{2i,2j+1}^{f} &= v_{2i,2j+1}^{f} + \frac{1}{2}(v_{i,j}^{c} + v_{i,j+1}^{c}) \\ v_{2i+1,2j+1}^{f} &= v_{2i+1,2j+1}^{f} + \frac{1}{4}(v_{i,j}^{c} + v_{i+1,j}^{c} + v_{i,j+1}^{c} + v_{i+1,j+1}^{c}) \end{aligned} \tag{5.36}$$

where $i = 0, 1, 2, ..., M-1$ and $j = 0, 1, 2, ..., N-1$. M and N are the number of points on the coarse grid in the i and j directions, respectively. As before, the superscripts f and c represent the fine and coarse grid levels, respectively.

The fine grid point at $(2i, 2j)$ corresponds to the coarse grid point at (i, j); therefore, in the first line of equation (5.36), $v^f_{2i,2j}$ on the right hand side is corrected by adding $v^c_{i,j}$ directly with no interpolation necessary. For the remaining corrections in equation (5.36), v_f is updated by interpolation of v_c from a simple linear average of the coarse grid points adjacent to the fine grid point. Equation (5.36) is included in a subroutine which transfers the known $v^c_{i,j}$ to the subsequent finer grid level and corrects the previous solution approximation $v^f_{2i,2j}$, $v^f_{2i+1,2j}$, $v^f_{2i,2j+1}$, and $v^f_{2i+1,2j+1}$ ($i = 0, 1, 2, ..., M-1$ and $j = 0, 1, 2, ..., N-1$). For example, $v^{4h}_{i,j}$ along with M^{4h} and N^{4h} are sent to a subroutine which determines updated values of $v^{2h}_{i,j}$ by using equation (5.36).

We now use the methods described in this chapter to numerically solve the governing equations. Before discussing the numerical results we discuss the solution of an illustrative model problem which has an analytical solution and contains many of the features of the full problem.

5.5 The Sinusoidal Model Problem

Consider the following initial conditions for the radial, swirl, and axial velocity components (u, v, w):

$$u = \frac{B}{r}\sin\frac{\pi r^2}{2}, \tag{5.37}$$

$$v = \frac{A}{r}\sin\frac{\pi r^2}{2}, \tag{5.38}$$

$$w = -Bz\pi\cos\frac{\pi r^2}{2}, \tag{5.39}$$

where $A = \frac{\Gamma}{2\pi}$, B is a constant which controls the magnitude and direction of the meridional flow and is related to the volume flow-rate Q through the plane $z = L$ by $B = -\frac{Q}{2\pi L}$. Thus for $B > 0$, the axial velocity w is directed toward the wall, and for $B < 0$, w is directed away from the wall.[1]

The domain of this problem is $0 \leq r \leq 1$ and $0 \leq z \leq L$ where L is the length of the domain in the axial direction. Note that an analytical solution exists for $r \geq 1$; however it is not presented here as the validity of the computational scheme can be evaluated strictly from the analytical solution generated within the vortex core. Also note that the boundary conditions in this problem are the same as those given in the previous section.

Burggraf (1996)[2] has shown that if we assume u and w to be independent of time, then the circulation function which satisfies equation (5.10) can be used to solve the time-dependent swirl flow and the swirl is given by

$$v = \frac{2A}{r} \cdot \frac{e^{\pi Bt} \tan(\pi r^2/4)}{e^{2\pi Bt} + \tan^2(\pi r^2/4)}. \tag{5.40}$$

From the swirl velocity, the axial vorticity ξ can be found from equation (5.6) and is given by

$$\xi = \pi A e^{\pi Bt} \frac{e^{2\pi Bt}\cos^2(\frac{\pi r^2}{4}) - \sin^2(\frac{\pi r^2}{4})}{[e^{2\pi Bt}\cos^2(\frac{\pi r^2}{4}) + \sin^2(\frac{\pi r^2}{4})]^2}. \tag{5.41}$$

Since the meridional flow is taken to be steady and the swirl velocity is independent of z for all time t, the azimuthal component of vorticity is also independent of time. This can be seen by substituting equations (5.37), (5.39), and (5.40) into the vorticity transport equation (5.11), where the result is $\frac{\partial \omega}{\partial t} = 0$.

The solution for the swirl velocity and the axial vorticity are illustrative of the corresponding solutions to the full nonlinear problem. Note that for $B > 0$ the swirl velocity decreases rapidly in time at a fixed value of r; simultaneously, the axial vorticity decreases as well. This means that at fixed $r < 1$, eventually there is no swirl and no axial vorticity; the axial vorticity has been convected across $r = 1$ and thus there is no vortex inside $r = 1$. This is precisely what is seen in the solution for the full nonlinear problem. On the other hand, for $B < 0$, both the swirl and the azimuthal vorticity *increase* exponentially with time at a fixed value of r; again this is precisely what is seen in the full nonlinear problem.

---

[1] The above solution actually holds throughout the region $0 \leq r \leq \sqrt{2}$, representing swirl flow in a tube, down the axis to the end wall at $z = 0$ and back up along the tube wall at $r = \sqrt{2}$.

[2] Burggraf, O. R., private communication.

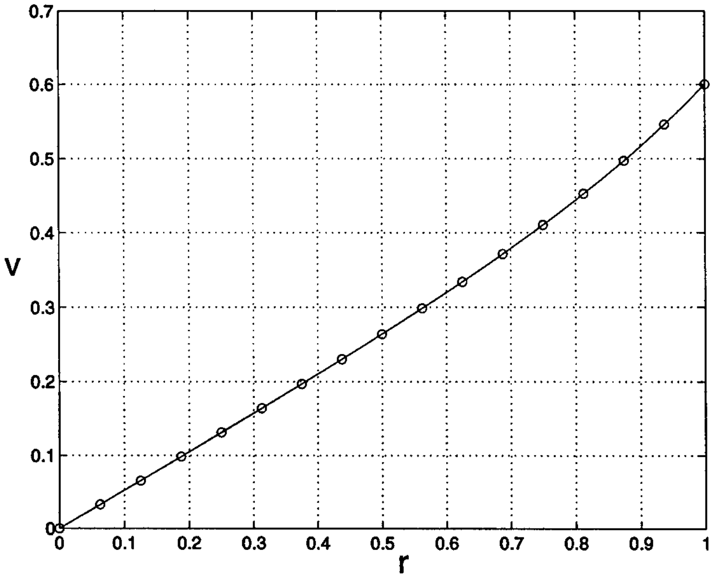

Figure 5.3: Swirl velocity distribution on the wall for the analytical case with $A = B = 1$. Numerical solution (o) with analytical solution (-) at time $t = 0.3495$.

To validate the full nonlinear algorithm, the numerical solution to this model problem is generated by using the velocities given in equations (5.37)-(5.39) as initial conditions to the computational procedure outlined in the previous section. Figure 5.3 shows the numerical solution for the swirl velocity on the wall after 700 time-steps as compared with the analytical solution. The numerical solution was obtained for $A = B = 1$, $\Delta t = 2.5e^{-4}$, $R = L = 1$, $M = N = 64$, $\lambda = 1.8$, and $\epsilon = 10^{-7}$ and is four-digit accurate in comparison with the analytical solution. Figure 5.4 shows the swirl velocity for this case for successive times; note the rapid decrease in the core. This feature is characteristic of the solution to the full problem as well; coincident with this decrease in the swirl is a substantial decrease in the axial vorticity(not shown). The results of Figure 5.4 describe the process of a vortex-surface collision as defined in Chapter 1. We now proceed to the results for the full nonlinear problem.

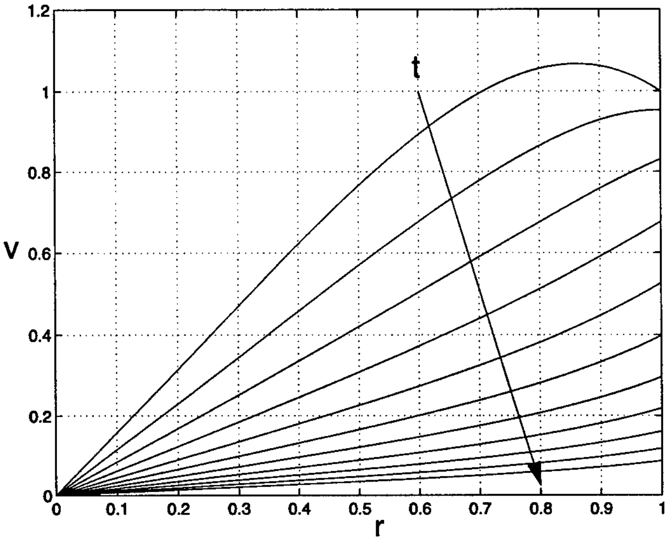

Figure 5.4: Swirl velocity distribution on the wall for the analytical case with $A = B = a = 1$. Time ranges from 0.0 to 1.0 in increments of 0.1 increasing in direction of arrow.

5.6 Results for the Full Nonlinear Problem

Based on the success of the computational scheme in reproducing the results for the analytical model problem, we now present results for the fully nonlinear and unsteady problem defined in Section 2. To provide a baseline for comparison of the results for the vortex flow, it is useful to consider the case where the swirl velocity is zero so that the flow is a jet. We present solutions first for the case of the axial flow toward the wall for both the case of the jet and the vortex-jet. Then we reverse the direction of the axial flow and consider the case where the axial flow is directed away from the wall.

To start the problem, we choose initial conditions corresponding to an undisturbed vortex with axial flow. The axial velocity distribution for this flow is taken as the simple form

$$w = w_I = -e^{-r^2}, \tag{5.42}$$

where the negative sign denotes that the axial velocity is toward the wall. Since the jet is undisturbed at time $t = 0^-$, we set the initial radial velocity as

$$u = u_I = 0. \tag{5.43}$$

The initial swirl velocity distribution that is assumed to exist up to time $t = 0^-$ is taken to be a Lamb-type vortex (Lamb 1945)

$$v = v_I = \frac{\Gamma}{2\pi r}\left(1 - e^{-r^2}\right), \tag{5.44}$$

corresponding to a decayed potential vortex with a linear swirl as $r \to 0$. Correspondingly, the initial circulation distribution is then

$$\Omega = \Omega_I = r v_I = \frac{\Gamma}{2\pi}\left(1 - e^{-r^2}\right). \tag{5.45}$$

The initial azimuthal vorticity distribution is defined by equation (5.6) as

$$\omega = \omega_I = -\frac{\partial w_I}{\partial r} = -2re^{-r^2}. \tag{5.46}$$

Numerical solutions have been computed for three sets of grids corresponding to $(64)^2$, $(128)^2$, and $(256)^2$ points, for $R = L = 4$ and the results for the velocities and the vorticity for each grid were compared. It was found that sufficient spatial resolution is achieved using 128 grid points in both r and z. This was measured by requiring two figure accuracy in the velocities; the vorticity values are slightly less accurate although two-figure accuracy was obtained at almost all points in the grid as well. Sufficient temporal accuracy is achieved using a time step of $\Delta t = 0.01$. In addition, the effects of the lengths of the computational domain in r and z on the numerical solution for the case of no swirl was tested, resulting in a 2.9% change in the azimuthal vorticity on the wall when R and L are doubled from 4 to 8. The grid spacing was held fixed at $\Delta r = \Delta z = 0.0312$ with $\Delta t = 0.01$ and the convergence criterion $\epsilon = 10^{-7}$ for these tests. All of the results presented here are for 128 points in both directions with $R = L = 4$, $\Delta t = 0.01$.

We have assumed that the vortex is instantaneously sliced; in reality we would expect a thin layer of vorticity to be wrapped around the leading edge of the plate. The time scale associated with the wrapping of vorticity around the leading edge is $t_w \sim a_v/U$ where a_v is the vortex core radius and U is the speed of the plate. The time scale associated with the simplified interaction is $t_v \sim a_v/W$ where W is the axial velocity scale. If these time scales are sufficiently different these two phenomena will not interact. Thus if $U \gg W$

then, the time scale of the wrapping is much shorter than the redistribution process. Moreover, the axial vortex lines which are deformed into the radial direction by the plate will ultimately lie parallel to the plate, and the portions on the top and bottom of the plate cancel each other since those portions have opposite-signed vorticity.

5.6.1 The Simple Jet: Axial Velocity Directed Toward the Wall

In this section, we consider the case where $\Gamma = 0$ in equation (5.44), or pure jet flow for the case of flow directed toward the wall. At time $t = 0$, a wall is instantaneously inserted into the flow at a right angle to the jet. In the case where the axial velocity is directed toward the wall, the resulting stagnation at the wall causes the fluid to flow radially outward locally near the wall.

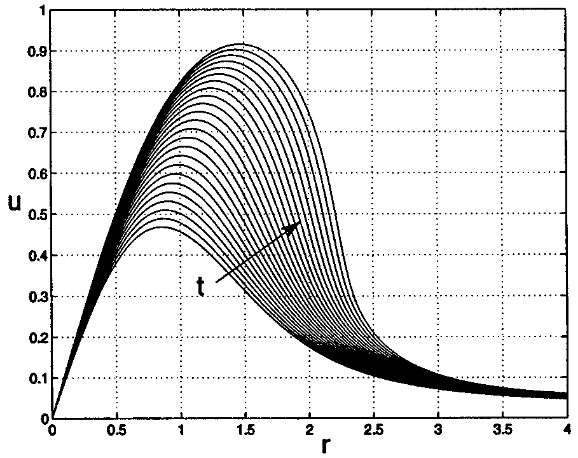

Figure 5.5: Radial velocity distribution on the wall for jet flow with axial flow in the jet directed toward the wall. Time ranges from 0.0 to 2.5 in increments of 0.1 increasing in direction of arrow.

The computed values for $t = 0^+$ compare very well with those predicted by the analytical solution presented in Figure .2 of the Appendix. As time increases, the radial velocity approaches the steady state for small r, as given in Section .1.2 of the Appendix (see Figure .2); indeed, the comparison is quite good up to $r \approx 1.2$ at $t = 2.5$. This indicates that for no swirl, the time scale a_v/w_0 determines the development of the steady jet flow. Outside this inner core of near steady flow, the radial velocity peaks and then falls off toward zero, with a large negative radial-velocity gradient developing as time increases. This reversal in the sign of the radial velocity gradient suggests that the axial velocity also reverses its sign, producing upwelling in this region of large radial-velocity decay. The analytical solution for $t = 0^+$ predicts upwelling for $r > r^*$, where $r^* = 1.256963\cdots$. As the radial velocity fall-off steepens, the upwelling also increases, possibly producing a local eruption of the fluid near the wall. This upwelling is coincident with the development of a region of high azimuthal vorticity, as seen in Figure 5.6(a). The peak wall azimuthal vorticity increases with time, in absolute value, while moving radially outward. Note that the vorticity curves, out to about $r = 2$, coalesce to the steady-flow limit $\omega = -2r$ (see Appendix A). This situation progresses until a near-discontinuity is formed and the numerical solution breaks down.

The development of this vorticity discontinuity is due to the outward propagation of the jet-core vorticity into the external region of zero vorticity. Note that in any flow with positive radial velocity that decays monotonically with increasing radius, the fluid particles must converge, since the inner particles move faster than the outer ones. Hence, any property carried by the particles will become more concentrated. In the present case, the azimuthal vorticity was initially confined inside the radius of the jet, and as it is carried radially outward, the rotational fluid develops into a shell of ever decreasing thickness. An adaptive-gridding numerical scheme would be better able to treat this situation. It should also be noted that the azimuthal vorticity varies most drastically near the wall. Farther out from the wall the azimuthal vorticity field changes very little from its initial distribution. To illustrate, a three-dimensional plot of the azimuthal vorticity field at time $t = 2.5$ is shown in Figure 5.6(b).

Figure 5.7 shows the pressure on the wall as a function of time. It can be seen that the pressure is moving toward a steady value near the axis $r = 0$ (evidenced by the clustering of curves near $r = 0$); however it has not yet reached a steady value. This is due to the fact that the pressure on the wall is only affected by the time-change of u and the change in u with respect to r as can be seen in equation (5.2). Also note the outward traveling wave in the pressure which increases in magnitude as time increases. This is caused by the large radial gradient of the radial velocity which also corresponds to the presence of large azimuthal vorticity in the region near the wall.

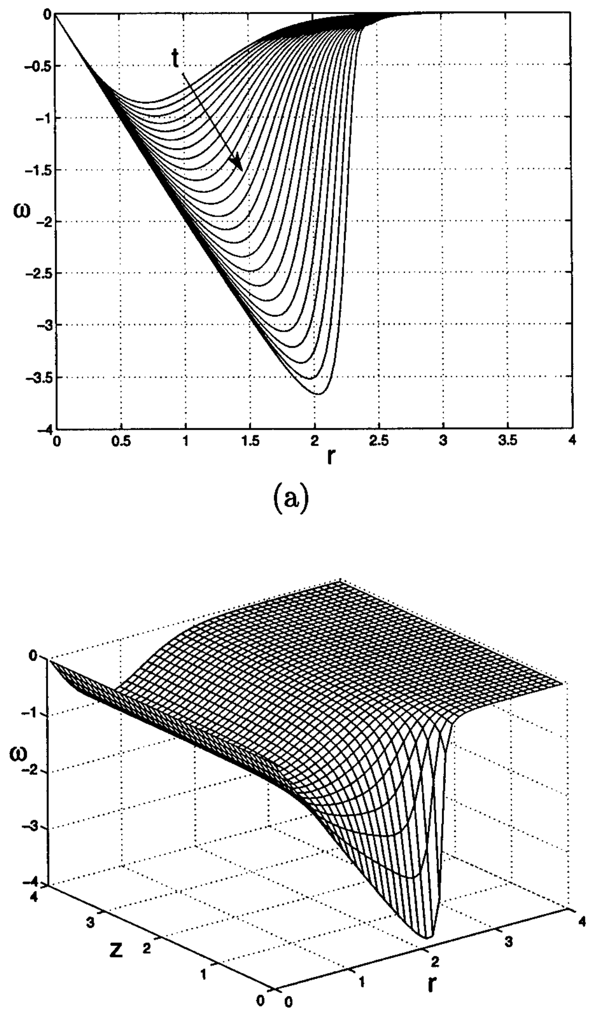

(b)

Figure 5.6: Azimuthal vorticity distribution; (a) on the wall for jet flow with axial flow directed toward the wall. Time ranges from 0.0 to 2.5 in increments of 0.1 increasing in direction of arrow. (b) Three-dimensional view at $t = 2.5$. Every third point is plotted.

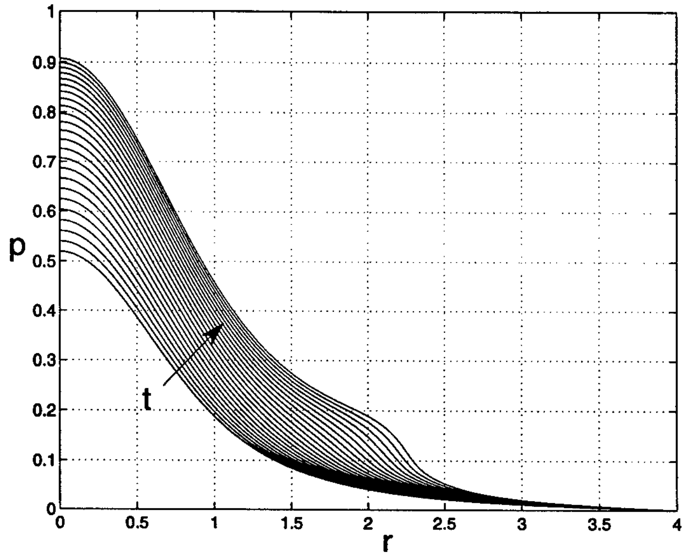

Figure 5.7: Pressure distribution on the wall for jet flow with axial flow directed toward the wall. Time ranges from 0.0 to 2.5 in increments of 0.1 increasing in direction of arrow.

5.6.2 Vortex-Jet: Axial Velocity Directed Toward the Wall

In this section, the effects of the addition of swirl velocity to the jet flow is investigated. Here we consider the case where the axial flow within the swirling jet is directed toward the wall. As previously stated, the only dimensionless parameter from the non-dimensionalization in Section 5.2 is the circulation associated with the complete vortex core, Γ. In this section, we focus on the value of $\Gamma = 5$ which will be shown to approximate the experimental situation to be discussed. The influence of the value of Γ is considered in the next section.

Figure 5.8(a) shows the swirl velocity on the wall as a function of time. The swirl velocity is reduced rapidly near $r = 0$, forming a growing inner-core of rotationally dead air. Outside this inner core, the swirl rapidly increases to the potential vortex level. The apparent bulging of the vortex core is evident here, as the location of the peak swirl velocity is carried radially outward by the radial velocity, shown later in Figure 5.10. Figure 5.8(b) shows the circulation on the wall as a function of time. As required by

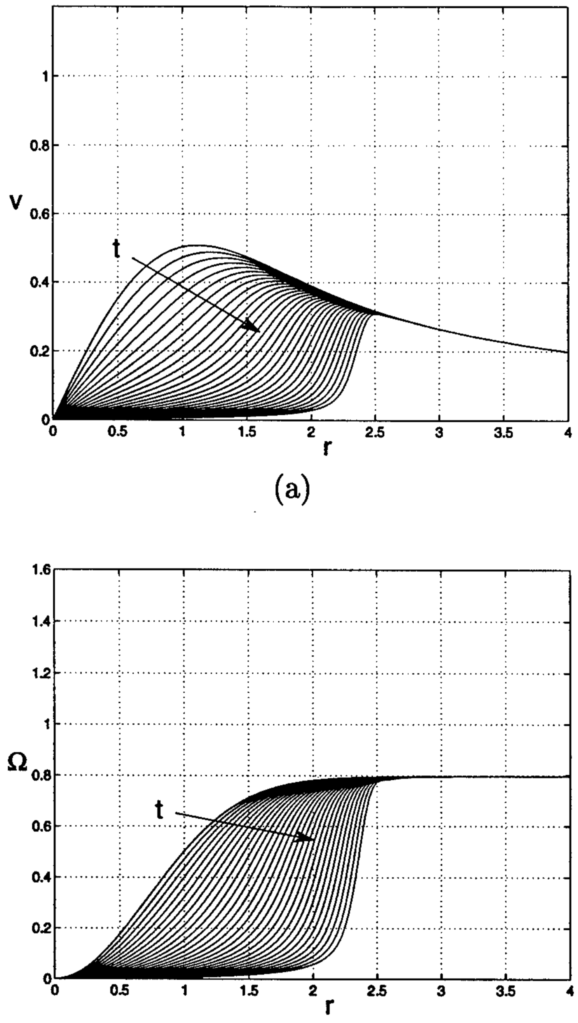

(a)

(b)

Figure 5.8: (a) Swirl velocity distribution on the wall for vortex-jet flow with axial flow directed toward the wall ($\Gamma = 5$). Time ranges from 0.0 to 3.1 in increments of 0.1 increasing in direction of arrow.(b) Circulation function Ω on the wall.

Kelvin's theorem, the circulation remains constant outside the vortex core, implying that the total vorticity is merely redistributed by convection, not destroyed. Also evident here is the rapid development of the stagnant inner-core, bounded by an annular shell of vorticity, corresponding to the rise of the circulation function Ω to its limiting value of $\frac{\Gamma}{2\pi}$. The evident steepening of the circulation distribution outside the inner core is caused by the decrease of radial velocity with r. It can be seen in Figure 5.10 that the radial velocity decreases somewhat faster than $\frac{1}{r}$ at the outer edge of the vortex, suggesting that the inner radius of the annulus of vortex filaments moves outward faster than the outer radius, thus producing a thinning of the shell with the result that the increase of circulation across the shell occurs over ever smaller radial distances. Correspondingly, the vortex filaments are squeezed together in this narrow annulus, producing an increase in the magnitude of the axial vorticity in the shell, as is evident in Figure 5.9.

Figure 5.9(a) shows the axial vorticity on the wall as a function of time. It can be seen in this figure that the axial vorticity on the wall decreases near $r = 0$ as time increases, and spreads radially outward with time. This behavior can be explained as follows. From the second of equations (5.6) the axial vorticity is $1/r$ times the radial derivative of the circulation. The circulation satisfies a first order wave-type equation so it is not surprising that the vorticity should be redistributed. Moreover, from Figure 5.8(b) the circulation is approaching zero rapidly for $r \leq 1$ so that the axial vorticity there is small but finite as $r \to 0$. This behavior is the main feature of the vortex-surface collision process. What was once a vortex (in the sense of a line vortex) is now locally rotationally dead, and the outer portion of the vortex which was once rotationally dead, now possesses significant axial vorticity. The original vortex has been transformed such that the high levels of axial vorticity become concentrated in an annular shell at ever increasing values of r.

The azimuthal vorticity on the wall as a function of time is depicted on Figure 5.9(b). Note here that the magnitude of the peak value of azimuthal vorticity on the wall first increases, then levels off, then continues to increase monotonically. In contrast, for the pure jet, the azimuthal vorticity on the wall increases in magnitude monotonically with no plateau, suggesting that this is a swirl-dominated effect. The maximum absolute value of the azimuthal vorticity in this case is only about 56% of that in the pure jet-flow case with axial inflow by time $t = 2.5$. This indicates that even though the azimuthal vorticity distribution on the wall has the same general trend as

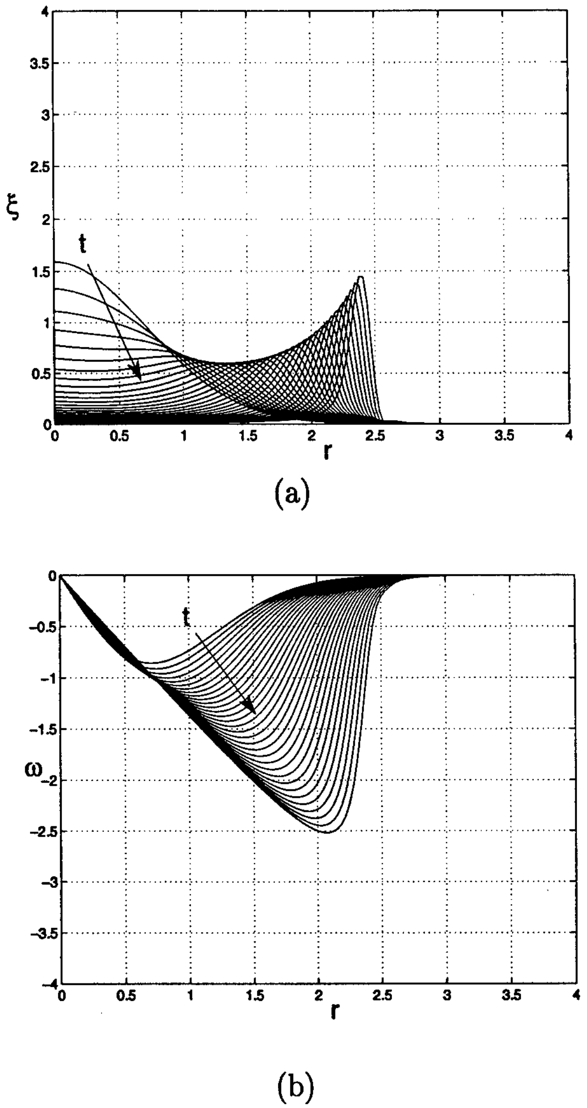

Figure 5.9: Vorticity distribution on the wall for vortex-jet flow with axial flow directed toward the wall and $\Gamma = 5$. Time ranges from 0.0 to 3.1 in increments of 0.1 increasing in direction of arrow. (a) Axial vorticity; note again the rapid decrease in the axial vorticity in the original core of the vortex. (b) Azimuthal vorticity distribution.

that of jet flow, the addition of swirl slows down the rate of outward travel of both the radial velocity and the azimuthal vorticity. As in the basic jet-flow case, the azimuthal vorticity varies most drastically near the wall. Farther out from the wall the azimuthal vorticity field changes very little from its initial distribution.

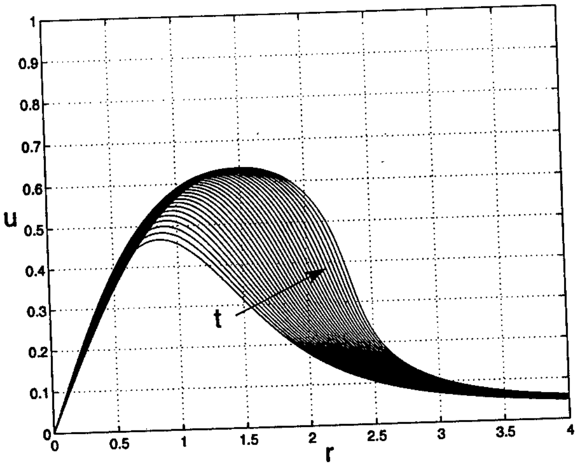

Figure 5.10: Radial velocity distribution on the wall for vortex-jet flow with axial flow directed toward the wall and $\Gamma = 5$. Time ranges from 0.0 to 3.1 in increments of 0.1 increasing in direction of arrow.

Figure 5.10 shows the radial velocity on the wall as a function of time. Here the peak radial velocity on the wall increases, then levels off as time increases. It is seen that the magnitude of the radial velocity at time $t = 5$ is only about 70% of that in the pure jet investigated in the previous subsection. The same steepening of the radial velocity curves occurs here. This fluid upwelling, as in the jet, is caused by the presence of a region of significant azimuthal vorticity as seen in Figure 5.9(b).

Figure 5.11 shows the pressure on the wall as a function of time. Note that the pressure at time $t = 0^-$, denoted by a (*), is due to the swirl flow only. It can be seen that the pressure jumps instantaneously at time $t = 0^+$ which is due to the insertion of the wall. Also note that the pressure is approaching a steady value especially near $r = 0$, as evidenced by the clustering of curves at later times. Recall that the given pressure is relative to the value at $(R, 0, 0)$. This apparent near steady behavior on the wall is due to the fact that the radial velocity is nearly steady in this region. In

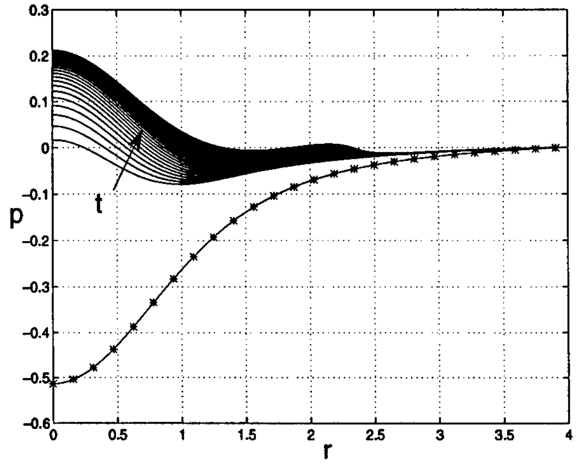

Figure 5.11: Pressure distribution on the wall for vortex-jet flow with axial flow directed toward the wall ($\Gamma = 5$). Time ranges from 0.0 to 3.1 in increments of 0.1 increasing in direction of arrow. The (*) indicates the initial condition, $t = 0^-$.

addition, the swirl velocity has nearly disappeared near the origin and thus its contribution to the radial momentum equation is negligible. It can also be seen that there is a secondary wave traveling radially outward. This outward traveling wave is a result of the steepening of the radial velocity profile on the wall which is indicative of a local fluid upwelling as for the pure jet. This region of adverse pressure is expected to be eventually convected outside the computational domain.

The major result of the present section is that the presence of the wall forces fluid out from the center of the core leaving behind a core devoid of swirl and axial vorticity. Recall that this is precisely the situation illustrated by the analytical solution presented in Section 5.5. Moreover, the pressure results provide an explanation for the reduction of the suction peak in the pressure seen on the advancing side of a helicopter as depicted on Figure 1(a) and on the top of the airframe as seen on Figure 2(b). In addition, it is clear that this reduction in pressure would not occur unless there is axial velocity in the core; that is, from an inviscid point of view, there is no collision unless there is axial flow in the core of the vortex. We now move on to the case where the axial flow in the vortex is directed away from the wall.

5.6.3 Vortex-Jet: Axial Velocity Directed Away From the Wall

Here we consider the case where the axial velocity is directed away from the wall. The boundary condition at the wall causes the fluid to be drawn radially inward toward the axis $r = 0$. To consider this problem using the current program, we merely reverse the sign in the axial velocity. The problem is then theoretically ill-posed since we apply a boundary condition on the circulation function and the azimuthal vorticity at $z = L$, which is now a downstream boundary. In addition, the derivatives in the hyperbolic equations (5.10) and (5.11) are evaluated using an upwinding scheme in which the solution downstream always depends upon the solution upstream. In order for the axial outflow problem to be theoretically well-posed, the azimuthal vorticity corresponding to a constant radial inflow would have to be specified at $t = 0$ on the boundary at $r = R$. Even though the axial outflow problem is ill-posed, the present time-marching scheme was successful over a considerable length of time for this case.

The swirl velocity on the wall for the case of axial outflow is shown in Figure 5.12(a). It can be seen in this figure that the swirl velocity on the wall focuses as time increases. This focusing of the swirl velocity is evidence of a contraction of the vortex. During this contraction, the peak swirl velocity moves radially inward as it is convected by the radial velocity. Figure 5.12(b) shows the circulation on the wall for the case of axial outflow. It can be seen in this figure that the circulation on the wall is convected radially inward by the radial velocity. This steepening corresponds to the fact that fluid particles are bunching up near $r = 0$, and hence the increase in circulation occurs over ever smaller radii.

Figure 5.13 shows the axial vorticity on the wall for the case of axial outflow. Note that the axial vorticity on the wall focuses as time increases. This focusing of the axial vorticity is caused by the contraction of the swirl velocity. Also, the axial vorticity seems to be approaching a steady value near $r = 0$, which is consistent with the behavior of the swirl velocity profile for later times near $r = 0$.

Figure 5.14 shows the pressure on the wall as a function of time. It can be seen that the pressure at the wall focuses with time, and is dominated by the swirl velocity for later times. This focusing of the pressure is precisely what is seen in experiments on the retreating side of a helicopter airframe (Kim and Komerath 1995; Figure 1(b)). Note that the (*) denotes the pressure at

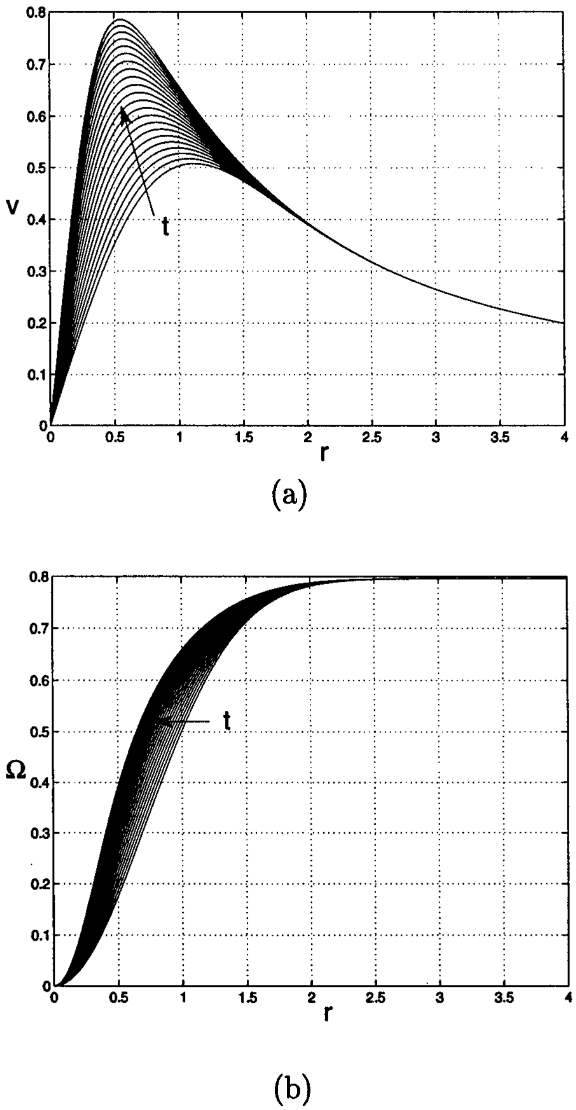

Figure 5.12: (a) Swirl velocity distribution on the wall for vortex-jet flow with axial flow directed away from the wall($\Gamma = 5$). Time ranges from 0.0 to 1.1 in increments of 0.05 increasing in direction of arrow. (b) Circulation function, $\Omega = rv$ on the wall.

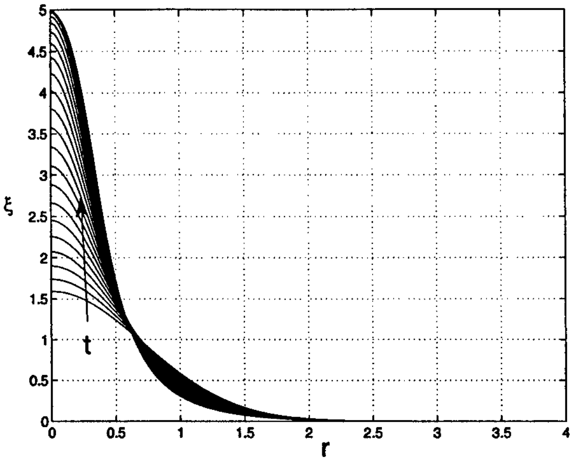

Figure 5.13: Axial vorticity distribution on the wall for vortex-jet flow with axial flow directed away from the wall($\Gamma = 5$). Time ranges from 0.0 to 1.1 in increments of 0.05 increasing in direction of arrow. Note here the focusing of the vorticity near $r = 0$.

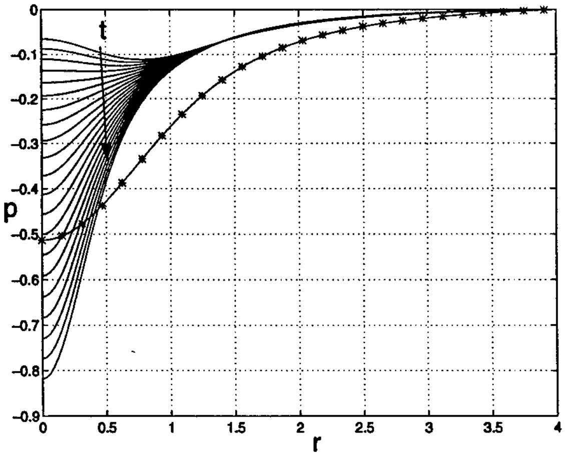

Figure 5.14: Pressure distribution on the wall for vortex-jet flow with axial flow directed away from the wall for $\Gamma = 5$. Time ranges from 0.0 to 1.1 in increments of 0.05 increasing in direction of arrow. The (*) denotes the pressure at $t = 0^-$.

time $t = 0^-$ and the pressure instantaneously jumps from this condition to its unsteady value.

From the results presented here, the vortex contracts locally near the wall as is seen in experiments. Coincident with the contraction of the swirl velocity the suction peak grows in magnitude monotonically with increasing time. This result is a likely explanation for the lingering suction peak seen in experiments on the retreating side of the airframe (see Figure 1.4). Note that for larger times, because of the rapid variation in the flow near $r = 0$, the numerical scheme becomes unstable and the solution breaks down. In practice, this will not occur because viscosity becomes important when fluid from the boundary layer is sucked into the vortex core thereby stemming the radial shrinking of the core.

5.7 The Influence of Circulation

In this section, the influence of the value of the circulation on the results for the case where the axial velocity in the vortex is directed toward the wall is discussed. In general, at small values of the circulation the flow behaves more like a jet, while at the larger values, the flow is dominated by the properties associated with a vortex, results which are to be expected.

Figure 5.15 shows the swirl velocity on the wall as a function of time for the three values of the circulation indicated. Note that the scales of the three figures are the same and the maximum azimuthal velocity rises linearly with circulation. Moreover, the rapid decrease in the azimuthal velocity occurs only very near the wall as shown on Figure 5.16 for $\Gamma = 2.5$.

Figure 5.17 shows the axial vorticity on the wall. For each value of the circulation, the axial vorticity on the wall decreases near $r = 0$ as time increases, and spreads radially outward with time. It can be seen that the axial vorticity at the smaller values of the circulation first decreases at small r, but later increases as a shell of large vorticity is formed. The results of Figure 5.17(c) appear to be tending toward similar behavior.

Figure 5.18 shows the pressure on the wall for each value of the circulation; again, the starred curve indicates the pressure at time $t = 0^-$ which is due to swirl only. For $\Gamma = 2.5$ the pressure actually rises above zero; that is, there is no suction peak associated with the pressure for this rather weak vortex. The results for the other values of the circulation are similar to that for $\Gamma = 5$. Note that for both $\Gamma = 7.5$ and 10, the pressure seems to approach

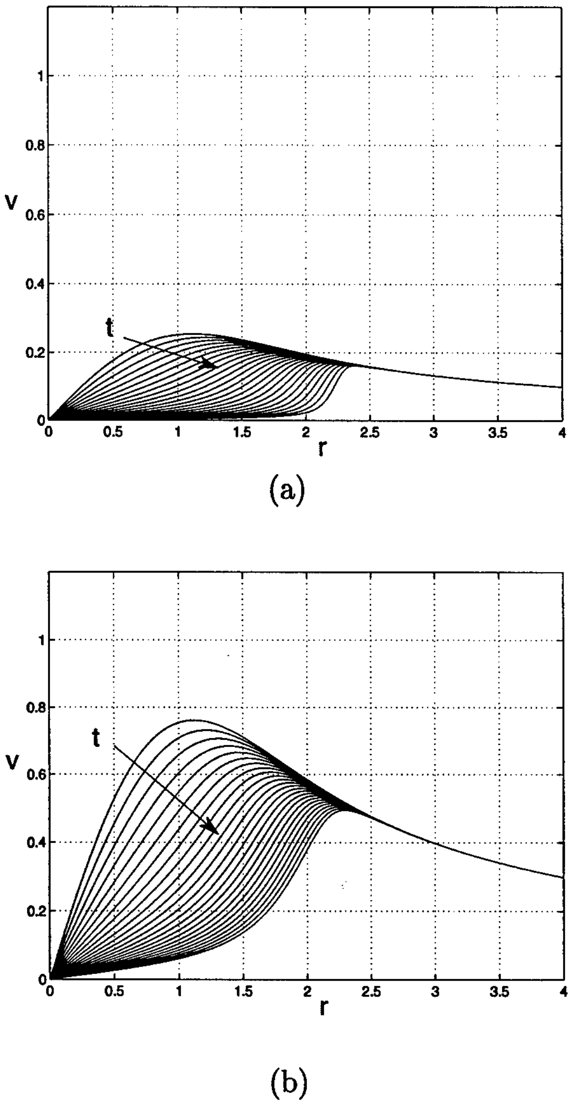

Figure 5.15(a,b)

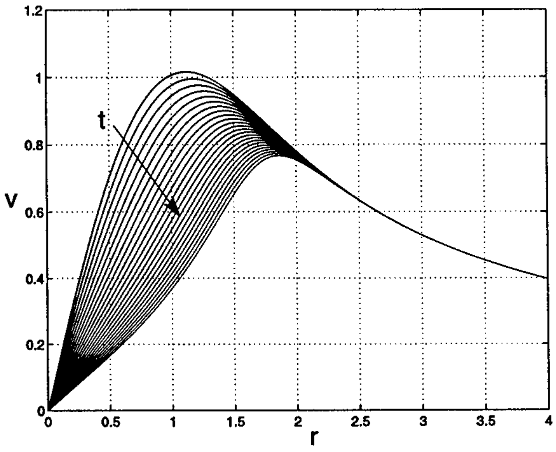

(c)

Figure 5.15: Swirl velocity on the wall for the vortex-jet flow with axial flow directed toward the wall for three values of Γ. (a) $\Gamma = 2.5$ for time ranging from 0.0 to 2.5 in increments of 0.1. in increments of 0.1. (b) $\Gamma = 7.5$ with time ranging from 0.0 to 2.5 in increments of 0.1. (c) $\Gamma = 10$ with time ranging from 0.0 to 1.2 in increments of 0.05. In each case time is increasing in the direction of the arrow.

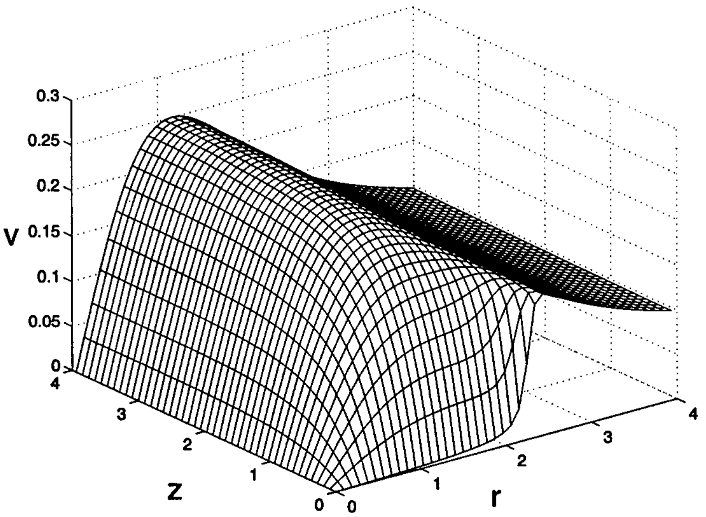

Figure 5.16: Swirl velocity field for the vortex-jet with axial flow directed toward the wall for $\Gamma = 2.5$ at time $t = 2.5$. Every third point is plotted.

a steady value near $r = 0$, as indicated by the clustering of curves at later times.

The azimuthal vorticity for each value of the circulation is shown on Figure 5.19. For ease of comparison, the scale of the figure is chosen to be the same as the pure jet case, Figure 5.6(a). Note that the azimuthal vorticity decreases substantially as the circulation increases. However, for the case of $\Gamma = 2.5$ the azimuthal vorticity is increasing in magnitude, as for $\Gamma = 0$ whereas for the other values, it is decreasing. The radial velocity (Figure 5.20) shows similar trends.

Finally, it is of interest to examine the streamline patterns and compare those for the vortex-jet to those of the pure jet. Figure 5.21(a) presents the streamlines for the jet case at $t = 2.5$; the corresponding streamlines for the case of $\Gamma = 2.5$ at the same time are shown on Figure 5.21(b). Note the similarity in the streamlines, which is perhaps to be expected since the flow is assumed to be axisymmetric. On the other hand, it is surprising that they are so similar, although the streamlines near the wall persist closer to the axis for the vortex-jet. The streamlines are not substantially different at the higher values of the circulation.

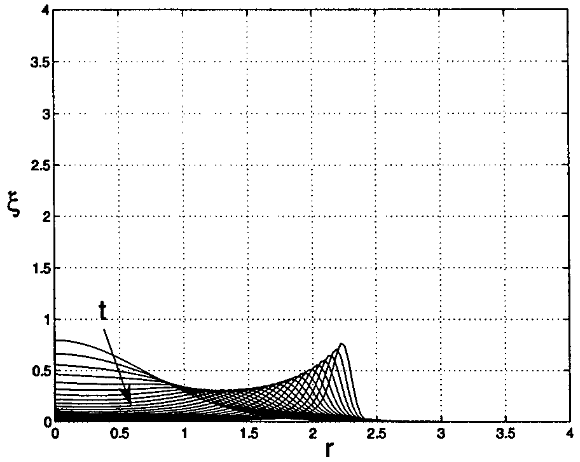

(a)

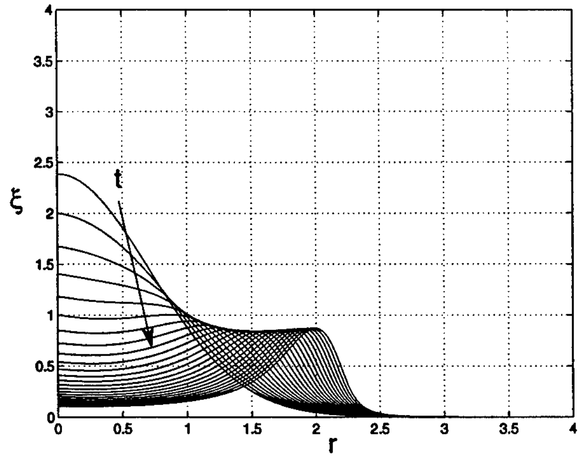

(b)

Figure 5.17(a,b)

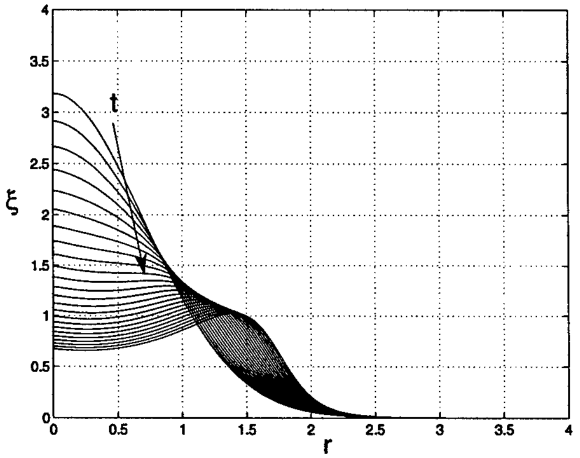

(c)

Figure 5.17: Axial vorticity on the wall for vortex-jet flow with axial flow directed toward the wall for three values of Γ. (a) Γ = 2.5 for time ranging from 0.0 to 2.5 in increments of 0.1. (b) Γ = 7.5 with time ranging from 0.0 to 2.5 in increments of 0.1. (c) Γ = 10 with time ranging from 0.0 to 1.2 in increments of 0.05. In each case time is increasing in the direction of the arrow. Note the rapid decrease in the axial vorticity in the original core of the vortex.

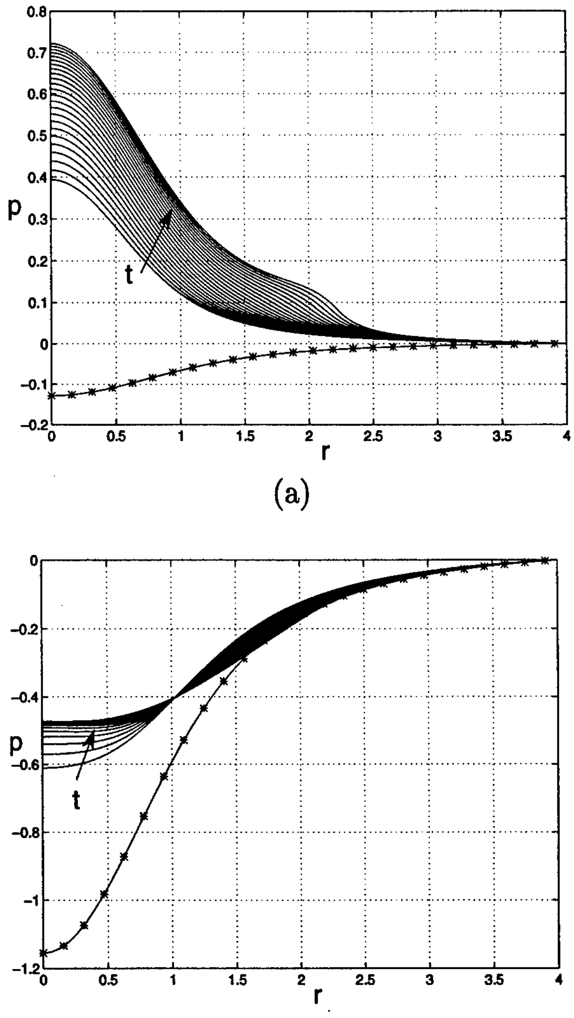

(a)

(b)

Figure 5.18(a,b)

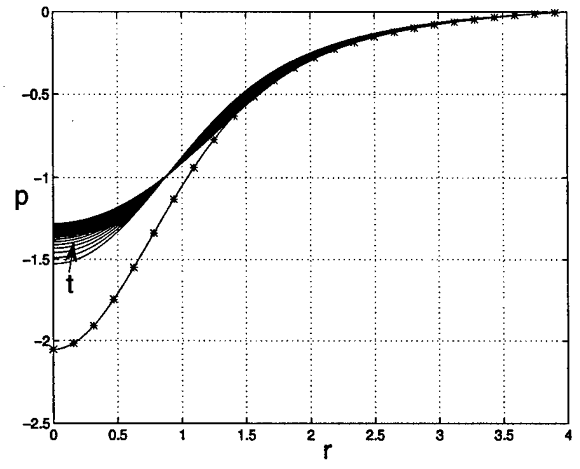

(c)

Figure 5.18: Pressure on the wall for the vortex-jet flow with axial flow directed toward the wall for three values of Γ. (a) $\Gamma = 2.5$ for time ranging from 0.0 to 2.5 in increments of 0.1. in increments of 0.1. (b) $\Gamma = 7.5$ with time ranging from 0.0 to 2.5 in increments of 0.1. (c) $\Gamma = 10$ with time ranging from 0.0 to 1.2 in increments of 0.05. In each case time is increasing in the direction of the arrow. Note the rapid decrease in the pressure in the original core of the vortex. The (*) indicates the initial condition, $t = 0^-$.

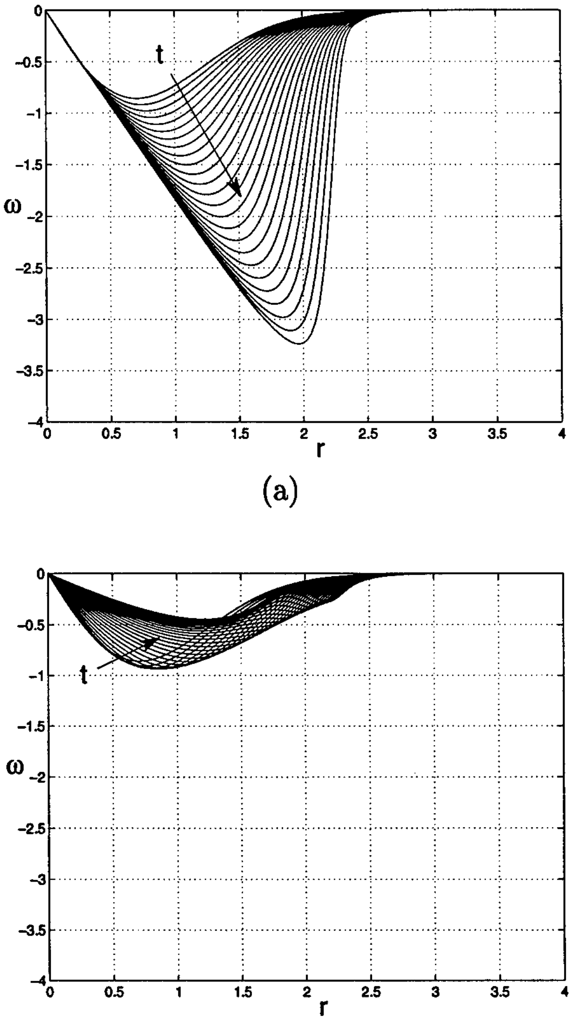

(a)

(b)

Figure 5.19(a,b)

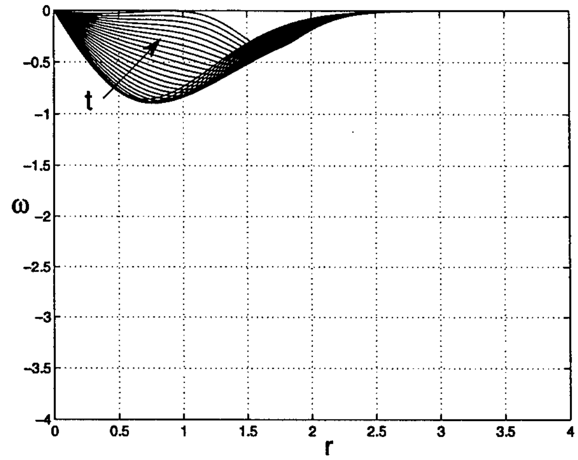

(c)

Figure 5.19: Azimuthal vorticity distribution on the wall for vortex-jet flow with axial flow directed toward the wall for three values of Γ. (a) $\Gamma = 2.5$ for time ranging from 0.0 to 2.5 in increments of 0.1. in increments of 0.1. (b) $\Gamma = 7.5$ with time ranging from 0.0 to 2.5 in increments of 0.1. (c) $\Gamma = 10$ with time ranging from 0.0 to 1.2 in increments of 0.05. In each case time is increasing in the direction of the arrow.

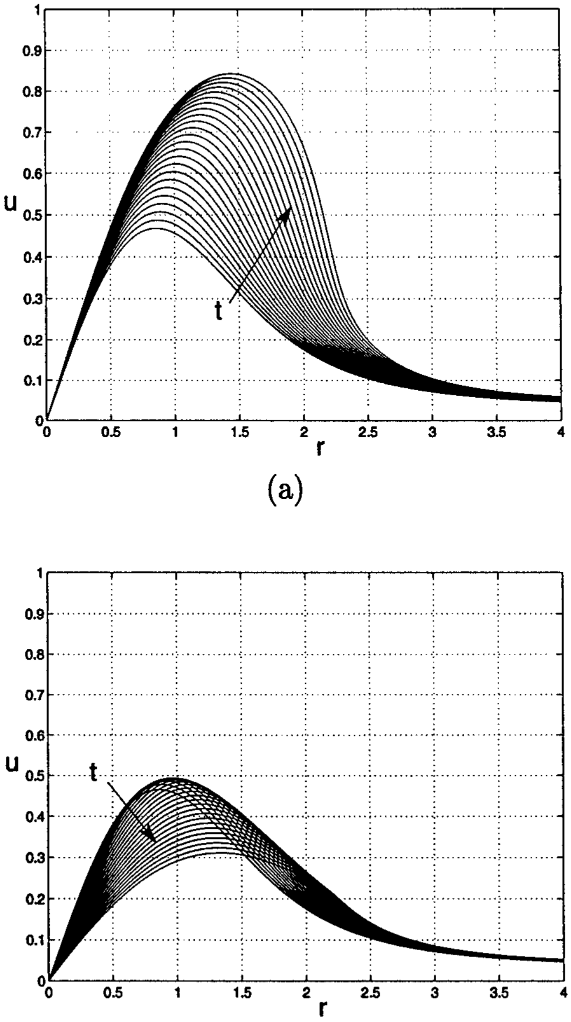

(a)

(b)

Figure 5.20(a,b)

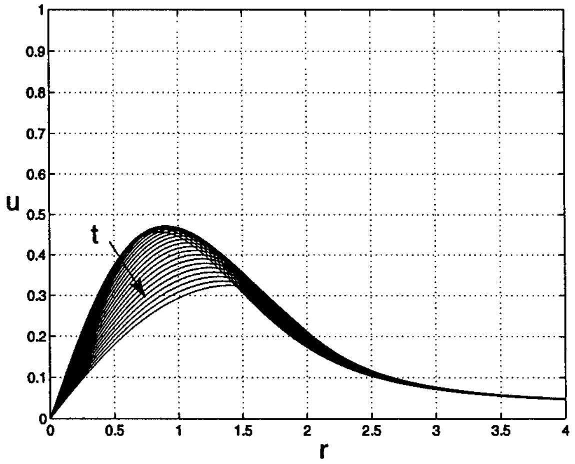

(c)

Figure 5.20: Radial velocity on the wall for vortex-jet flow with axial flow directed toward the wall for three values of Γ. (a) $\Gamma = 2.5$ for time ranging from 0.0 to 2.5 in increments of 0.1. in increments of 0.1. (b) $\Gamma = 7.5$ with time ranging from 0.0 to 2.5 in increments of 0.1. (c) $\Gamma = 10$ with time ranging from 0.0 to 1.2 in increments of 0.05. In each case time is increasing in the direction of the arrow.

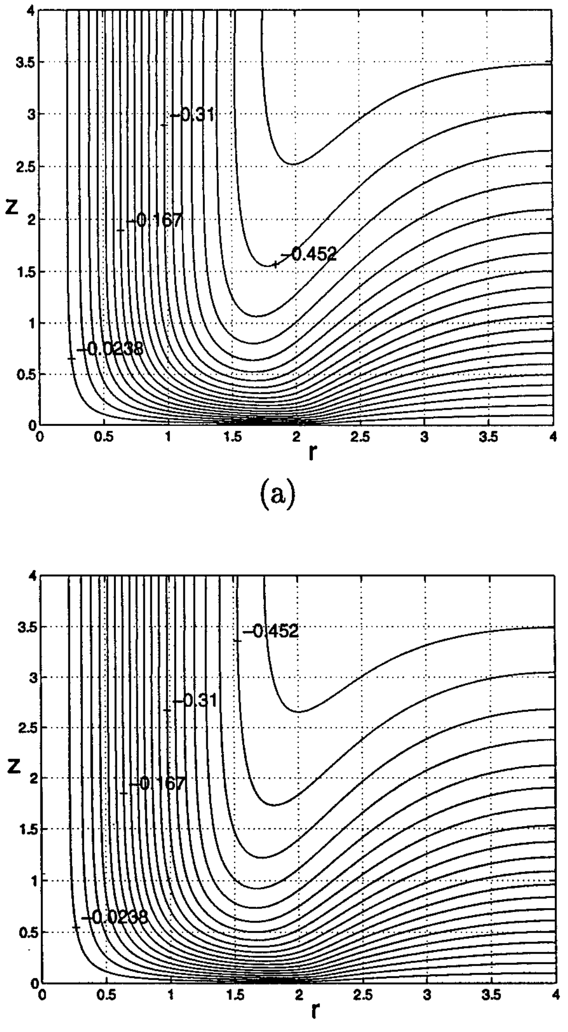

(a)

(b)

Figure 5.21: (a) Streamlines for jet flow at $t = 2.5$. (b) Streamlines for the vortex-jet with axial flow directed toward the wall ($\Gamma = 2.5$) at the same time. Note the similarity in the two plots.

For the larger values of the circulation (i.e. for $\Gamma = 7.5, 10$) and on the retreating side for $\Gamma = 2$ (and at the larger times), the computations were stopped when the radial velocity began to reverse direction near the plate. This "separation" is believed to be a result of accumulated numerical error. In this region, the streamfunction values are of the order of the discretization error in the equations; for all of the cases computed, reduction of the time step and the grid sizes considerably reduces the streamfunction values. Another form of truncation error-induced reversed flow can easily occur in the steady flow problem if not enough terms are taken in the series solution presented in the Appendix. The absence of reversed flow in the present work is counter to the conclusions of Marshall and Krishnamoorthy(1997) who show multiple eddies in their inviscid computation of a similar problem.

5.8 Comparison with Experiment

While the present problem is an idealization of the situation where a tip-vortex shed from a helicopter rotor blade strikes a circular cylinder, qualitative comparisons of the time scale of the interaction may be made. From the nondimensionalization in Section 5.2, we can calculate the dimensional parameters in order to compare with experiments conducted by Kim and Komerath(1995). It is known from Kim and Komerath(1995) and a very recent communication by Mahalingam(1996) that the nominal dimensional core radius is $a_v \sim 0.2in - 0.4in$. The best estimates from experiment suggest that the maximum dimensional core velocity is $w_0 \sim 25\frac{m}{s}$ at a rotor speed of 2100 rpm (Section 4.3.4). Using a median value for the core radius of $0.3in$ and $\Gamma^* \sim 1.5\frac{m^2}{sec}$ at $2100rpm$ (Affes et al 1993) we have $\Gamma \sim 8$ for an axial flow of $25\frac{m}{sec}$.

From the numerical results presented for $\Gamma = 5$ in Figure 5.8 it is seen that by the time $t = 2.0$, the swirl velocity in the core of the original vortex($r \leq 1$) is reduced by more than one order of magnitude. This corresponds to a dimensional time of $t^* \sim 0.63ms$. For $\Gamma = 7.5$ the results are similar. This is the same order of magnitude as the time frame for the reduction of the suction peak, as can be seen in Figure 5.11. Data from the experiments shows that the suction peak on the advancing blade side disappears in a time frame of $\Delta\psi \sim 12^o$, where ψ denotes rotor phase angle. For a rotor angular speed of $2100rpm$, this corresponds to $0.95ms$ which is near the calculated value of $0.63ms$. Of course, the problem is much more complex than is considered here and so it is not expected that these parameters will exactly represent what is happening in the experiments. Nevertheless the fact that the computational time scale of the interaction on the advancing blade side compares favorably with the time scale in the experiment is encouraging.

5.9 The Post-Collision Process

As shown by the results of this chapter, on the retreating side of the plate which corresponds to the case where the axial velocity in the core of the vortex is directed away from the plate, the boundary layer provides fluid that is ingested into the core and limits the reduction of the vortex core radius seen in Figure 5.12. The phenomenon of viscous limiting of vortex core thinning is suggested in studies by Burggraf and Stewartson (1971), and by Belcher, *et al.* (1972), who investigated the boundary layer induced by a potential vortex and a generalized vortex oriented normal to a coaxial disc respectively. These studies imply that the radial inflow in the boundary layer induced by the vortex will erupt from the wall at $r = 0$, continually feeding the core, and thereby halt the focusing of the swirl velocity seen in the present results.

As indicated previously in this chapter, the velocities in the vortex are $O(Re^{1/2})$ where Re is the local Reynolds number: $Re = \frac{\Gamma^*}{\nu}$, the ratio of the dimensional vortex circulation to the to the kinematic viscosity. For

$$\Gamma = \frac{\Gamma^*}{W_\infty a} = O(1)$$

the vortex Reynolds number is of the same order of magnitude as the Reynolds number based on the free stream velocity and the radius of the cylinder. Since the radius of the vortex core is of $O(Re^{-1/2})$ and the flow area is thus of $O(Re^{-1})$ the flux due to the axial flow in the vortex is $O(Re^{-1/2})$. Because the boundary layer provides a mass flux of the $O(Re^{-1/2})$ the balance of the flux can be provided by the boundary layer. This situation is depicted in Figure 5.22. It is expected that this structure is the asymptotic condition for the time dependent calculations and that the flow is effectively steady.

To complete the description of the flow on the retreating side, we note that there is an intermediate region connecting the boundary layer to the classical Lamb-type vortex far from the plate.[3] This region is inviscid in

---

[3] Burggraf, O. R., uunpublished notes 1976.

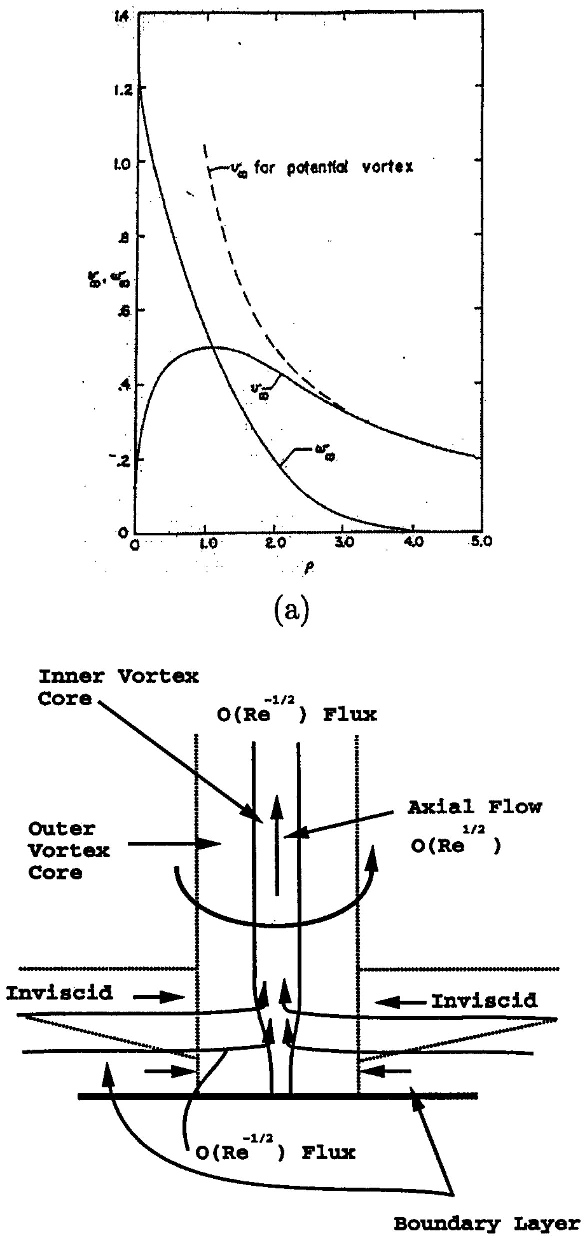

(a)

(b)

Figure 5.22: Wall layer structure for the retreating side case for the 90^o collision. (a) Swirl and axial velocity in the vortex as functions of r. (b) Basic structure.

character as noted on Figure 5.22 and all of the streamlines in this inviscid region provide the link from the boundary layer to the inner viscous core of the vortex. The governing equations are conservation of angular momentum along streamlines in the form

$$rv = \Delta\Psi = G_0(z), \tag{5.47}$$

where Ψ is the streamfunction and G_0 is known from the boundary layer flow; r is the radial coordinate originating at the center of the vortex and Δ is the Laplacian in cylindrical coordinates. The radial momentum equation is

$$\frac{dp}{dr} = \frac{v^2}{r}, \tag{5.48}$$

and continuity is

$$rw = \frac{d\Psi}{dr}, \tag{5.49}$$

where w is the velocity component in the inviscid region normal to the wall. We can integrate Bernoulli's equation along streamlines and recalling that the flow is assumed to be steady,

$$p + \frac{1}{2}\left(v^2 + w^2\right) = p_\infty, \tag{5.50}$$

where p_∞ is the total pressure in the outer potential flow field. Equations (5.47), (5.48), (5.49), and (5.50) are four equations in the four unknowns w, v, p, and Ψ subject to the appropriate boundary conditions. Combining equation (5.50) with (5.48), we obtain

$$\frac{d}{dr}(v^2 + w^2) + 2\frac{v^2}{r} = 0. \tag{5.51}$$

Then using the definition of the streamfunction, equation (5.51) becomes

$$r\frac{d}{dr}\left(\frac{1}{r}\frac{d\Psi}{dr}\right) = \frac{1}{2wr}\frac{d}{dr}\left(r^2v^2\right) = -\frac{1}{2}\frac{d}{d\Psi}\left(L^2(\Psi)\right) = fnc(\Psi). \tag{5.52}$$

Thus Ψ is defined by a non-homogenous second order differential equation from which the complete flow field can be determined. A plot of the velocities is shown on Figure 5.22(a) and the basic structure is depicted on Figure 5.22(b).

The situation is much different on the advancing side of the plate where the axial velocity is toward the wall, the core of the vortex is devoid of both swirl and axial vorticity as shown on Figures 5.8 and 5.9(a) for the dimensionless circulation $\Gamma = 5$. In this case the axial velocity in the core of the vortex opposes the suction-induced boundary layer flow. As the vorticity in the core of the vortex decreases to the magnitude of the boundary layer flow, boundary layer fluid and vortex fluid become indistinguishable. Note from Figure 5.11, that the radial pressure gradient is favorable and appears to be approaching steady state. Thus the boundary-layer flow also would be expected to be steady and unseparated, hence benign. On the other hand, there is still appreciable azimuthal vorticity. For this case we expect that there is an inviscid region near the wall of very low swirl, under which there is a viscous boundary layer whose function it is to bring the velocities to zero.

The picture is given on Figure 5.23. Eventually the vortex core radius is expected to bulge to an O(1) value, with the axial velocity decreasing to $O(Re^{-1/2})$ giving an $O(Re^{-1/2})$ mass flux as required far from the surface. Note that the axial velocity is the velocity component normal to the wall and is thus *required* to be $O(Re^{-1/2})$ by classical boundary layer theory. During this period of time that the vortex core bulges to O(1), it is expected that the radial pressure gradient would remain favorable countering the tendency of the vortex to ingest fluid from the surrounding boundary layer. This situation is depicted on Figure 5.23.

However, as indicated on Figure 5.9(a), there is a narrow band of appreciable axial vorticity which travels radially outward in time This is accompanied by a corresponding increase in the azimuthal vorticity as shown in Figure 5.9(b). This increase in the two vorticity components will lead to a non-traditional boundary layer structure; however, it is evident from Figure 5.11 that these components of vorticity have little effect on the pressure loading; note from Figure 5.11 that the pressure is near zero there.

5.10 Discussion

In this chapter we have calculated the inviscid response of a vortex to the presence of a wall and compared these results to the case of a jet. Initially, the wall is absent and is then suddenly inserted at time $t = 0$. This process is analogous to that which occurs in the impingement of a tip-vortex on a helicopter airframe. The evolution of the vortex for times $t > 0$ for initial

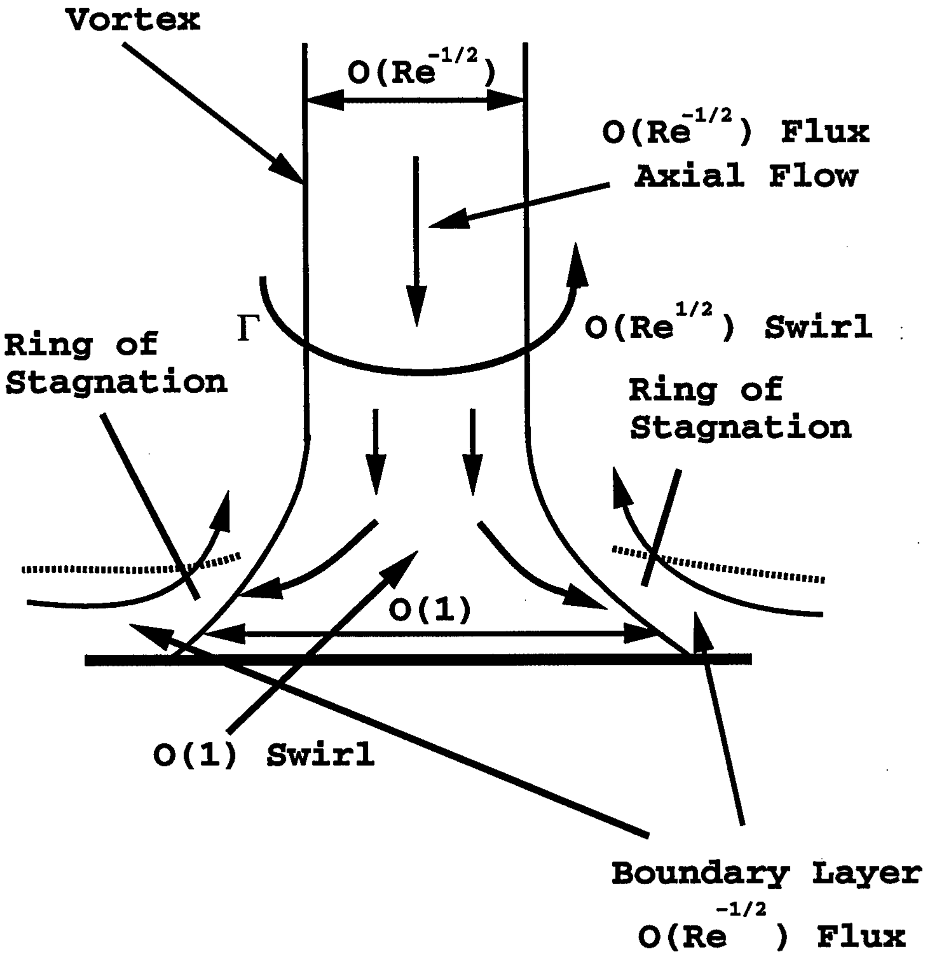

Figure 5.23: Wall layer structure for the advancing side case for the 90° collision.

conditions corresponding to a Lamb vortex has been calculated. For axial flow in the vortex directed toward the wall, the vortex core is seen to "bulge" as indicated by the radial convection of the point of maximum swirl velocity as depicted on Figure 5.8(a), for example. The swirl velocity decreases rapidly in the core of the vortex allowing the pressure distribution to return to its steady-state, mean value as observed in experiments. The time scale associated with the reduction of the pressure spike depends on the magnitude of the axial velocity in the core of the vortex and on the nominal vortex core radius. At the same time the axial vorticity near the axis decreases by an order of magnitude with a consequent increase at larger radii as the vorticity is carried outward by the induced radial velocity. A similar comment applies to the azimuthal vorticity.

For the case where the axial flow is directed away from the wall, the axial vorticity is redistributed inward and the vortex core radius shrinks. At the same time the suction peak increases in amplitude and focuses. The essential features of the process described here have been observed on the advancing side of the helicopter rotor in experiments(Kim and Komerath 1995). The present results suggest that as the vortex travels down the airframe, its profile will look something like that depicted previously on Figure 1.5. An analytical solution also was obtained for the swirl case and the results compare very well with the computational results(Figure 5.3).

What is surprising in the present work is that the jet produces similar trends with regard to the streamline patterns; i. e. the streamline patterns are qualitatively independent of swirl. The azimuthal vorticity, initially concentrated near the wall, is convected outward into the irrotational outer region, forming a wave front of vorticity which steepens as time increases. The numerical solution indicates a trough in the streamlines (Figure 5.21), which moves outward in time roughly at the same speed as the peak of the azimuthal vorticity. This trough corresponds to the change of sign of velocity normal to the wall that is predicted by the analytical solution for $t = 0^+$ (Appendix Section A.0.1). In the no-swirl case, the results of the time-marching computation tend toward the steady-state solution (Appendix Section A.0.2), for which azimuthal vorticity of the form $\omega = rH(\Psi)$ satisfies the conservation equation (5.11), where H is a function defined by the values of Ψ and ω at the inflow boundary. At the surface, this functional form produces vorticity whose magnitude grows linearly with r. This analytical solution, corresponding to conditions after the vorticity wave front has passed, predicts a layer of vorticity next to the surface which thins with increasing radius, thus concentrating the vorticity to ever greater levels.

A central suction peak is exhibited by the wall-pressure results for sufficiently large swirl. The magnitude of this suction peak diminishes rapidly at a rate depending on the value of circulation. The results indicate that the pressure approaches a steady-state distribution, and that an order-of-magnitude decrease in the amplitude of the pressure spike can occur very quickly for large values of circulation.

The fact that the dominant physics of the present problem is inviscid is not as surprising as it may seem. The induced pressure on the airframe is intimately related to the vorticity field through the local velocity field. Consider the situation where the ratio of the vortex core radius to the characteristic body length scale is small but finite and the case of a strong vortex in the sense that the dimensionless circulation based on free-stream variables $\Gamma = \frac{\Gamma^*}{W_\infty a}$, where a is the body length scale, is $O(1)$. Then the vortex Reynolds number, $Re_v = \frac{\Gamma^*}{\nu}$ is the same order of magnitude as the Reynolds number based on the body length scale and the external mean velocity, W_∞, $Re = \frac{W_\infty a}{\nu}$. Assuming that the scaled vortex radius in laminar flow is $O(Re^{-1/2})$, then from a simple Rankine vortex model the swirl velocity is $O(Re^{1/2})$. Since the axial vorticity is essentially the radial derivative of the swirl, it is easily seen that the axial vorticity within the vortex core is of magnitude $\xi \sim Re$ (see equation 5.6). If the axial velocity within the vortex is of the same order as the swirl, then similarly, the azimuthal vorticity is $\omega \sim O(Re)$. The vorticity magnitude within a classical laminar boundary layer on the body is $O(Re^{1/2})$ and so the vorticity within the vortex is much larger than that in the boundary layer. In particular, it is expected that in the collision process the magnitude of the vorticity field within the vortex will be reduced to the order of magnitude of the boundary layer vorticity, in which case distinguishing between boundary layer and vortex vorticity becomes impossible. This is the essence of the vorticity redistribution process; vorticity is not destroyed but merely redistributed in an inviscid way. As is well known, this is a major computational simplification: the dominant features of the collision process need not be modeled using the full Navier-Stokes equations. Coinciding with this redistribution of vorticity is the relaxation or focusing of the pressure suction peak associated with the original vortex. In this regard, it is useful to note that for small circulation when the boundary layer and vortex vorticity are of the same order (i.e. a weak vortex) the interaction between the vortex and the boundary layer is very weak. The same ideas may be applied to three-dimensional vortex sheets which in the present application are much weaker and thus much more benign in terms of impulsive loading on the airframe.

Viscous effects must become important in the case where the core axial velocity is away from the wall. The phenomenon of viscous limiting of vortex core thinning is suggested in studies by Burggraf and Stewartson (1971), who investigated the boundary layer induced by a potential vortex oriented normal to a coaxial disc respectively. Their results showed that the radial inflow in the boundary layer induced by the vortex will erupt from the wall at $r = 0$, continually feeding the core, and thereby halt the focusing of the swirl velocity seen in the present results. Incorporation of the boundary layer in the present vortex model may provide additional fluid so that the vortex can persist for a long period of time (Figure 1.4(b)); otherwise, it is evident from the present results that the swirl velocity focuses and this process cannot continue indefinitely in an inviscid fluid.

Chapter 6

The Three-Dimensional Vortex Airframe Collision

6.1 Introduction

Having demonstrated the collision process for a vortex cut by a plate at 90°, we now consider the collision of a tip-vortex with a cylindrical airframe. Previous results using a segmented, variable core radius rotor-tip vortex model to calculate vortex trajectory in the potential flow surrounding a cylindrical airframe (Affes and Conlisk 1993; Affes *et al.* 1993b; Xiao *et al.* 1994) indicate that when the vortex is more than one core radius away from the airframe, a simple model for the vortex core (Batchelor 1967; Widnall *et al.* 1971; Moore and Saffman 1972; equation (3.3)) is sufficient to predict the experimental vortex trajectory and the pressure on the top of the airframe with reasonable accuracy. During this time period the pressure distribution on the body is not substantially influenced by the local properties of the vortex, such as the core radius or the axial velocity in the core. As the vortex moves closer to and finally collides with the airframe, however, experimental data show that these factors become very important, as reflected in airframe pressure distribution measurements (Kim and Komerath 1995; Mahalingam *et al.* 1995. See the discussion of Figures 1.4 and 1.6 in Chapter 1.) that is not predicted by a simple model without axial flow.

In this chapter, results for the time frame where the vortex is within one core radius from the airframe in a stagnant medium are presented. These results extend those of Affes *et al.* (1993) into the collision phase of the motion.

Next, this model is extended to include axial flow in the vortex core. The vortex emanating from the rotor tip is helical in structure, representing the combined effects of the swirling and axial flow and in Section 6.3 we use a local coordinate system to develop a suitable model for the tip-vortex that automatically accounts for axial flow. Note that in this chapter the term "helical" refers to the helix of radius equal to the vortex core and not the helix of rotor blade radius shown on Figure 1.2. We approximate this helical vortex by continuous distribution of line vortices distributed around the vortex cylinder formed by the vortex core radius and ring vortices with a major radius equal to the vortex core radius distributed along the cylinder; we then consider the limit as core radius approaches zero. Results are presented for a stagnant medium, as well as for symmetric mean flow and asymmetric mean flow cases. We then compare these results with the experiments conducted at Georgia Tech. The primary deficiency of the circular vortex model which is associated with vorticity penetrating the airframe is then discussed and we address this issue by introducing the "box" vortex which allows the core of the vortex to change shape; an argument based on theoretical grounds supporting this concept is also given. The passage of the vortex along the sides of the airframe and possible reconnection of the vortex complete the present chapter.

6.2 The Vortex Without Axial Flow

The method of calculating the inviscid flow is similar to that described by Xiao, *et al.* (1994) and is summarized here. The inviscid flow is calculated using a panel technique originally due to Hess and Smith (1967). The airframe is represented by a finite-length circular cylinder which is approximated by $M \times N$ rectangular source panels, where M is the number of panels along the cylinder and N is the number of panels around the cylinder. Figure 3.2 shows a schematic of the cylinder panels and vortex segments with the global cartesian coordinates x, y and z. Details of the paneling method are given in Chapter 3 and in Radcliff *et al.* (1997) and only details pertinent to the present inviscid calculations are presented in this Chapter. The velocity field due to the vortex is represented via the Biot-Savart Law as in Chapter 3.

In the computations, the panel geometry used to compute the inviscid flow corresponds to $M = 81$ panels in the z direction and $N = 40$ in the azimuthal direction and the size of the panels is as described in Chapter 3. The minimum width of the panels is 0.0005, and the half length of the airframe cylinder is 5. Note these lengths are normalized to the airframe radius. The smallest panels are located directly under the vortex. The panel distribution in the azimuthal direction is also not uniform and is clustered near the symmetry plane at the top of the cylinder. The minimum panel width in the azimuthal direction is 1^o. The vortex is divided into 81 segments with a minimum spacing of 0.0005 and a half-length of 10.

An Adams-Moulton method is used to calculate the motion of the vortex. An additional difference in the present calculation from that of Affes *et al.* (1993) is that the vortex core is variable. The core radius for each vortex segment is evaluated by assuming that segment core volume is conserved as the vortex segment stretches. The numerical parameters such as the time step, the number of panels on the airframe, the half-length of the vortex and of the cylinder and the number of vortex segments have been tested for accuracy. A time step of 0.001 and cylinder mesh of $41, 81$, and 121 panels, airframe half-lengths of $5, 10$ and 100 and 161 vortex segments were tested. The parameters quoted above correspond to at least two figure accuracy in the vortex position at all times. Just before $t = 4.0$, however, vortex nodes begin to penetrate the airframe. This occurs because the panel representation of the airframe does not accurately enforce the zero normalvelocity boundary condition away from the panel centers; thus for a vortex node not coincident with a panel center there is a component of radial velocity which convects the node through the surface. This phenomenon is avoided in large-scale rotor codes which use vortex methods (Lorber and Egolf 1990) by establishing a fixed distance from the airframe which the vortex cannot penetrate; however, this heuristic model distorts the pressure distribution leading to inaccurate estimates of the load.

Results have been produced in the case of a stagnant medium for a vortex without axial flow to obtain the baseline behavior of the vortex as it approaches the airframe. The motion of the vortex is shown on Figure 6.1 for time $t = 0.1$ to $t = 3.9$ with an increment of 0.4 except for a final increment of 0.2. Note the time scale is nondimensionalized on the airframe radius and the circulation. In the absence of mean flow, the vortex center bends down towards the airframe surface and along the axis of the cylinder, stretching the vortex substantially. It should be noted that although the panels are translated to keep the point $z = 0$ directly below the vortex head to insure a dense concentration of panels there, the results presented on Figure

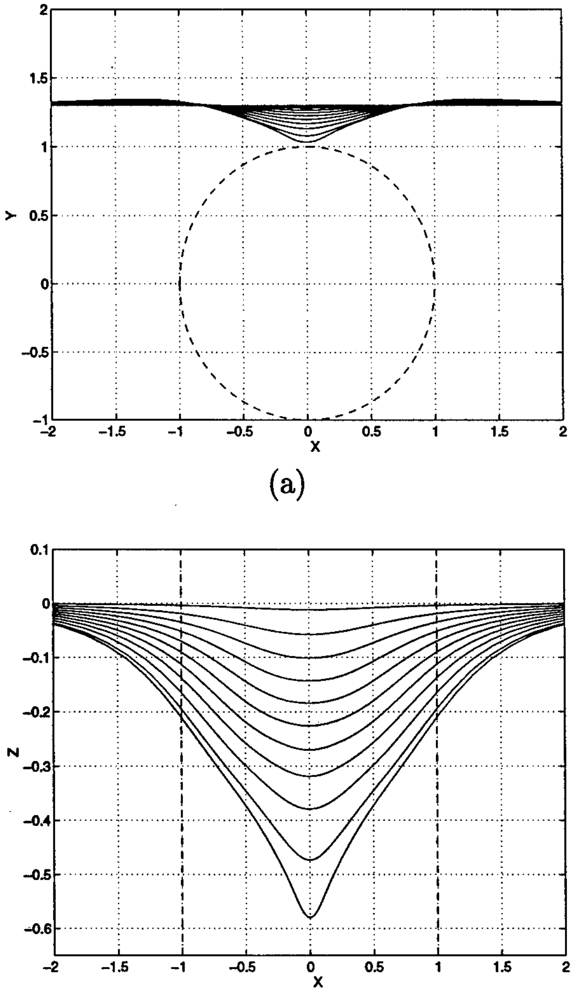

(a)

(b)

Figure 6.1(a,b)

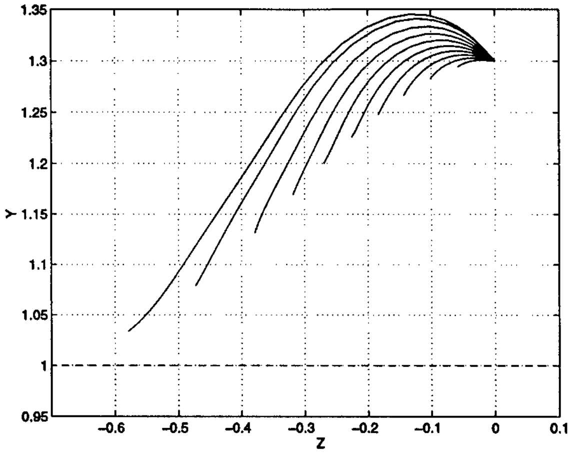

(c)

Figure 6.1: Motion of the line vortex toward the airframe in a stagnant medium; (a) x-y plane; (b) x-z plane; (c) z-y plane. The dashed lines indicate the airframe surface.

6.1 are plotted in physical coordinates. As it approaches the airframe, the vortex begins to assume the shape of the airframe due to the fact that the normal velocity on the airframe must vanish. We note the clear development of a horse-shoe shaped profile as time goes on. From Figure 6.1(b,c) it is clear that the legs of the vortex are significantly far from the airframe and the head is lying on the airframe. The vortex accelerates quite rapidly as the head approaches the airframe. Note the symmetry with respect to the centerline of the airframe in this case without axial flow.

The numerical parameters such as the number of panels on the airframe and the number of vortex segments have been tested for accuracy and the parameters quoted in the previous section correspond to at least two figure accuracy in the vortex position at all times. Just before $t = 4.0$, however, vortex nodes begin to penetrate the airframe. This occurs because the panel representation of the airframe does not accurately enforce the zero normal velocity boundary condition away from the panel centers; thus for an off-center vortex node not coincident with a panel center there is a component of radial velocity which convects the node through the surface. This phenomenon is avoided in large-scale rotor codes which use vortex methods (Lorber and Egolf 1990) by establishing a fixed distance from the airframe which the vortex cannot penetrate; however, this heuristic model distorts the pressure distribution leading to inaccurate estimates of the load.

The local behavior of the vortex core radius, which is always assumed to be circular, is depicted on Figure 6.2. As the vortex approaches the airframe, the radius decreases about 30% in a manner symmetric about $x = 0$. Noting the core radius in the last two time increments, Figure 6.1(c) shows that the outer portion of the vortex core has penetrated the surface at about $t = 3.5$. Clearly this is unphysical; on the other hand, this can be addressed by accounting for core deformation at the expense of a significant increase in computing time. This problem is addressed in a computationally efficient manner later in this chapter in Section 6.6 using the box vortex concept.

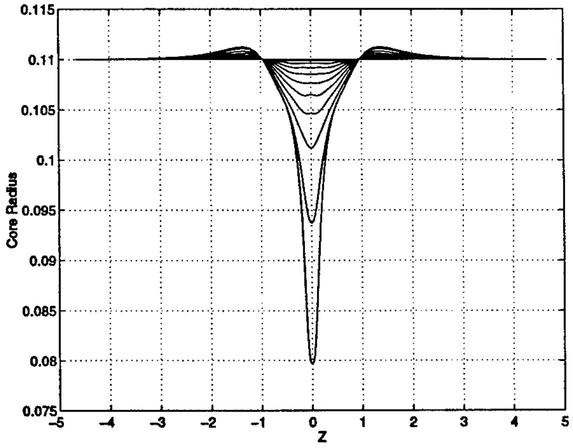

Figure 6.2: Line vortex core radius in a stagnant medium.

6.3 The Vortex With Axial Flow

To predict the airframe surface pressures as measured during experimental vortex-surface collisions, it is necessary to develop a model of the vortex-airframe velocity field and vortex movement when the vortex is in very close proximity to the surface. The model we have produced employs five components; a model for the vortex velocity field, a model to enforce the zero-normal-velocity boundary condition at the airframe surface which corresponds to the panel method presented in detail in Chapter 3, a representation of the mean flow surrounding the airframe, a means to propagate the vortex in space and a calculation of the surface pressure from the total velocity field. A picture of the vortex-airframe system is depicted on Figure 6.3. The individual model components are presented below.

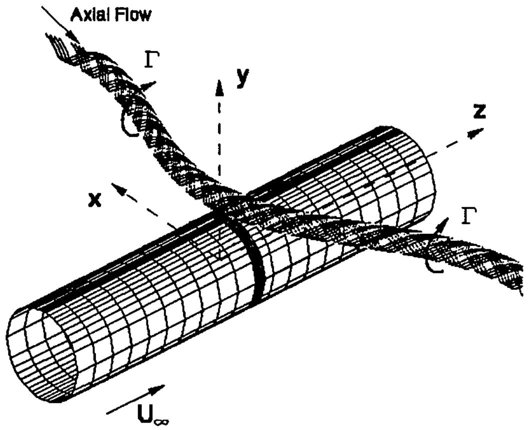

Figure 6.3: Panel airframe and helical vortex system representations with the global coordinate system used in the calculations.

6.3.1 The Classical Line Vortex with Axial Flow

A rotor-tip vortex occurs when vorticity on the loaded side of a rotor wraps up over the rotor tip and is shed as the rotor moves forward. This helico-cylindrical vortex sheet may be most simply represented by a uniform distribution of line vortices wrapped helically about the core radius of the tip vortex. Note that in this representation the line vortices have axial and azimuthal vorticity components and will generate a velocity field with components azimuthally about the tip vortex axis and along the axis, respectively. This velocity distribution may be produced by the superposition of axially-oriented line vortices distributed about the tip vortex core radius and azimuthally-oriented ring vortices with a radius equal to the tip vortex core radius distributed along the tip vortex axis. The line vortices will induce the azimuthal velocity component while the rings will induce radial and axial velocity. In this section, the velocity distributions induced by a semi-infinite tip vortex with line and ring components will be derived. A finite segment of such a vortex may then be created by superposition of two semi-infinite vortices of opposite sign.

A cylindrical-polar coordinate system with x the distance measured along the axis of the vortex cylinder, r the radius, and θ the azimuthal angle is defined. The origin is located in the end plane of the vortex cylinder as shown on Figure 6.4. We let a represent the radius of the cylindrical vortex sheet and Γ the total circulation of the flow around the vortex cylinder. Let γ_x be the circulation of the axial vortices per unit width of an axial strip along the cylinder, and γ_θ the circulation of the ring vortices per unit length along the cylinder. Then $\gamma_x = \Gamma/2\pi a$, and γ_θ depends on the advance ratio of the original helical vortices.

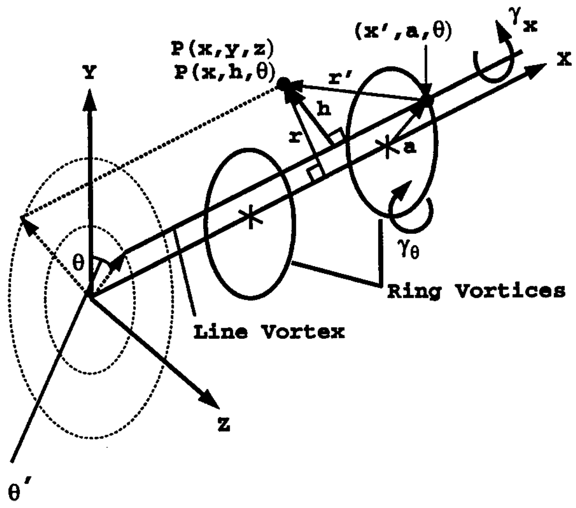

Figure 6.4: Configuration of the vortex cylinder and parameters for calculation of the velocity components for the helical vortex.

The Velocity Distribution due to the Line Vortices

We first consider the axial vorticity represented by the distribution of line vortices. For temporary convenience, we define a local Cartesian coordinate system for a semi-infinite vortex segment with origin at the center of the vortex cylinder and y and z axes in the endplane of the vortex cylinder, and local parallel y', z' coordinates relative to an elementary line vortex strip located on the core radius a, also shown in Figure 6.4. The circulation of such a strip is $\Gamma_x = \gamma_x \cdot a d\theta'$, where $d\theta'$ is the angular width of the strip. The velocity induced by the vortex strip at a point $P(x, y, z)$ is perpendicular to the meridian plane formed by the vortex line itself and the ray from the end of the vortex to the point P. Beginning with the basic Biot-Savart law

$$d\vec{v} = \frac{1}{4\pi}\frac{d\vec{\Gamma} \times \vec{r'}}{r'^3}, \tag{6.1}$$

where $\vec{v}$ is the induced velocity, $d\vec{\Gamma}$ is the circulation of the differential vortex element and r' is the distance from the vortex element to the object point, then the magnitude of the induced velocity at P is found by integrating from $x' = 0 \to \infty$, giving a well-known formula

$$v'_\theta = \frac{\Gamma_x}{4\pi h}\left(1 + \frac{x}{\sqrt{x^2 + h^2}}\right), \tag{6.2}$$

where h is the perpendicular distance from the vortex element to the point P. Denoting the angle measured around the vortex cylinder from the y axis to the vortex strip by θ', as depicted on Figure 6.4 we have

$$\begin{aligned} h &= \sqrt{(y - a\cos\theta')^2 + (z - a\sin\theta')^2}, \\ &= \sqrt{y^2 + z^2 + a^2 - 2a(y\cos\theta' + z\sin\theta')}, \\ &= \sqrt{r^2 + a^2 - 2ar\cos(\theta' - \theta)}, \end{aligned}$$

where r denotes the radius from the $x-$axis to the point P and θ is the angle from the $y-$axis to P. The velocity induced by the elementary vortex strip may now be resolved into Cartesian components, as

$$\begin{aligned} v'_y &= -v'_\theta \cdot (z - a\sin\theta')/h, \\ v'_z &= v'_\theta \cdot (y - a\cos\theta')/h. \end{aligned}$$

Summing the induced velocity of each such strip around the vortex cylinder yields the following integral formulas for the total induced velocity:

$$v_y = -\frac{\gamma_x a}{4\pi}\int_0^{2\pi} (1 + \frac{x}{\sqrt{x^2 + h^2}})\frac{z - a\sin\theta'}{h^2} d\theta', \tag{6.3}$$

$$v_z = \frac{\gamma_x a}{4\pi}\int_0^{2\pi} (1 + \frac{x}{\sqrt{x^2 + h^2}})\frac{y - a\cos\theta'}{h^2} d\theta'. \tag{6.4}$$

The radial and azimuthal components due to the line vortices in the cylindrical system of the tip vortex are then

$$v_r = v_y \cos\theta + v_z \sin\theta,$$

$$v_\theta = -v_y \sin\theta + v_z \cos\theta.$$

The integrand of v_r turns out to be an odd function of θ' and so the integral vanishes, leaving no net radial velocity. The last factor of the integrands in v_y and v_z, when combined into v_θ, may be simplified as follows:

$$\frac{1}{h^2}[(z - a\sin\theta')\sin\theta + (y - a\cos\theta')\cos\theta],$$

$$= \frac{1}{h^2}[z\sin\theta + y\cos\theta - a(\sin\theta\sin\theta' + \cos\theta\cos\theta')]$$

,

$$= \frac{r - a\cos(\theta' - \theta)}{r^2 + a^2 - 2ar\cos(\theta' - \theta)}.$$

Hence the integral for the azimuthal velocity component becomes

$$v_\theta = \frac{\gamma_x a}{4\pi}\int_0^{2\pi}\left[1 + \frac{x}{\sqrt{x^2 + r^2 + a^2 - 2ar\cos(\theta' - \theta)}}\right] \times$$

$$\left[\frac{r - a\cos(\theta' - \theta)}{r^2 + a^2 - 2ar\cos(\theta' - \theta)}\right] d\theta'. \qquad (6.5)$$

Nondimensionalizing with $\eta = r/a$ and $\xi = x/a$, we define the integrals

$$I_1(\eta) = \int_0^\pi \frac{\eta - \cos\phi}{1 + \eta^2 - 2\eta\cos\phi}\, d\phi \qquad (6.6)$$

and

$$I_2(\xi, \eta) = \int_0^\pi \frac{\eta - \cos\phi}{(1 + \eta^2 - 2\eta\cos\phi)} \times \qquad (6.7)$$

$$\left[\frac{1}{\sqrt{1 + \xi^2 + \eta^2 - 2\eta\cos\phi}}\right] d\phi, \qquad (6.8)$$

and the azimuthal velocity can be expressed as

$$v_\theta = \frac{\gamma_x}{2\pi}\left[I_1(\eta) + \xi \cdot I_2(\xi, \eta)\right].$$

The integrals I_1 and I_2 can be expressed in the form of elliptic functions. Recalling that $\gamma_x = \Gamma/2\pi a$, we obtain the final result

$$v_\theta = \frac{\Gamma}{4\pi r}\left\{\frac{1}{2}\left[1 + Sign(r-a)\right]\right.$$
$$\left. + \frac{1}{\pi}\frac{x}{\sqrt{x^2+(r+a)^2}}\left[K(k) + \frac{r-a}{r+a}\Pi(\sigma^2, k)\right]\right\}, \tag{6.9}$$

where $K(k)$ is the complete elliptic integral of the first kind and $\Pi(\sigma^2, k)$ is the complete elliptic integral of the third kind[1]. The moduli are defined as

$$k^2 = \frac{4ar}{x^2 + (r+a)^2}$$

and

$$\sigma^2 = \frac{4ar}{(r+a)^2}.$$

The Velocity Distribution Due to the Vortex Rings

The azimuthal vorticity component is represented by vortex rings distributed uniformly along the vortex cylinder. We proceed in the same manner as before, the only difference being the direction of the vortex segments. The starting point is again the basic Biot-Savart law, equation (6.1). Consider a differential element of the surface vorticity in the form of a rectangle with length dx' and width $ds = a\,d\theta'$, located at (x', a, θ') in the cylindrical-polar coordinate system of the vortex-cylinder. Then for an object point $P(x, r, \theta)$, the Biot-Savart law for this element of circulation has the vector form

$$d\vec{v'} = \frac{\gamma_\theta}{4\pi r'^3}\,dx'\,d\vec{s}\times\vec{r'},$$

where r' is the magnitude of $\vec{r'}$, the vector distance from the vortex element to the object point P, evaluated as

$$r' = [(x-x')^2 + r^2 + a^2 - 2ar\cos(\theta-\theta')]^{1/2}.$$

---

[1] The notation of Byrd and Friedman(1954) is used here, where σ^2 corresponds to the modulus n of Abramowitz and Stegun (1972).

The nonzero components are found to be

$$dv_r' = \frac{\gamma_\theta\, ds}{4\pi r'^3}\,(x - x')[cos(\theta - \theta')]\,dx',$$

$$dv_x' = \frac{\gamma_\theta\, ds}{4\pi r'^3}\,[a - r cos(\theta - \theta')]\,dx'.$$

The induced velocity of a semi-infinite strip of such lateral vortices is generated by integrating with respect to the surface element coordinate x' from 0 to ∞:

$$dv_r = \frac{\gamma_\theta\, ds}{4\pi}\int_0^\infty \frac{(x - x')[cos(\theta - \theta')]}{r'^3}\,dx',$$

$$dv_x = \frac{\gamma_\theta\, ds}{4\pi}\int_0^\infty \frac{a - r\cos(\theta - \theta')}{r'^3}\,dx',$$

Note that dv_r is parallel to the ray from the axis of the vortex cylinder through the strip. The result of the integration is

$$dv_r = -\frac{\gamma_\theta\, ds}{4\pi}\frac{cos(\theta - \theta')}{\sqrt{x^2 + r^2 + a^2 - 2ar cos(\theta - \theta')}}, \tag{6.10}$$

$$dv_x = \frac{\gamma_\theta\, ds}{4\pi}\frac{a - r\cos(\theta - \theta')}{r^2 + a^2 - 2ar\cos(\theta - \theta')} \times$$
$$\left[1 + \frac{x}{\sqrt{x^2 + r^2 + a^2 - 2ar\cos(\theta - \theta')}}\right]. \tag{6.11}$$

Now we set $ds = ad\theta'$ and integrate around the cylinder. Note that the azimuthal velocity component cancels out, since pairs of vortex strips at $\theta' = \theta + \Delta\theta$ and $\theta' = \theta - \Delta\theta$ produce the same radial velocity in the direction of their own radii. Hence the non-vanishing velocity components for the complete semi-infinite vortex cylinder due to the vortex rings are

$$v_r = \frac{\gamma_\theta\, a}{4\pi}\int_{\theta-\pi}^{\theta+\pi} \frac{\cos(\theta - \theta')}{\sqrt{x^2 + r^2 + a^2 - 2ar\cos(\theta - \theta')}}d\theta', \tag{6.12}$$

and

$$v_x = \frac{\gamma_\theta\, a}{4\pi}\int_{\theta-\pi}^{\theta+\pi} \frac{a - r\cos(\theta - \theta')}{r^2 + a^2 - 2ar\cos(\theta - \theta')} \times$$
$$\left[1 + \frac{x}{\sqrt{x^2 + r^2 + a^2 - 2ar\cos(\theta - \theta')}}\right] d\theta'. \tag{6.13}$$

Proceeding as before, these integrals can be expressed in terms of elliptic integrals. To evaluate v_r, we define the integral

$$I_0(\xi,\eta)=\int_0^{\pi}\frac{\cos\phi}{\sqrt{1+\xi^2+\eta^2-2\eta\cos\phi}}\,d\phi. \tag{6.14}$$

Using the (I_0, I_1, I_2)-notation these velocities become

$$v_r=-\frac{\gamma_\theta}{2\pi}\,\eta\,I_0(\xi,\eta),$$

and

$$v_x=\frac{\gamma_\theta}{2\pi}\,\eta\left[I_1(\eta)+\xi\,I_2(\xi,\eta)\right].$$

Evaluating the radial velocity component due to the rings gives

$$v_r=-\frac{\gamma_\theta a}{2\pi r}\sqrt{x^2+(a+r)^2}\left[F(x,r)K(k)-E(k)\right], \tag{6.15}$$

where

$$F(x,r)=\frac{x^2+a^2+r^2}{x^2+(a+r)^2},$$

while the axial component takes on a form similar to that of the azimuthal velocity component in equation (6.9):

$$v_x=\frac{\gamma_\theta}{4}\left\{[1+Sign(a-r)]\right.$$
$$\left.+\frac{2}{\pi}\frac{x}{\sqrt{x^2+(a+r)^2}}\left[K(k)-\frac{r-a}{r+a}\Pi(\sigma^2,k)\right]\right\}. \tag{6.16}$$

Finally the value of γ_θ for the vortex rings can be deduced from the helical-vortex distribution as follows. Consider a small triangular element of the surface of the vortex cylinder, for which the hypotenuse lies along the helically-wrapped vortex line and the base is parallel to the cylinder axis as shown on Figure 6.5. Denote by β the angle between the base and the hypotenuse; i.e., the advance ratio of the helix is $\tan(\beta)$. All of the vortex lines that pass through the base also pass through the height, and vice versa. Let the length of the base of the triangle be denoted by b and that of the height by s. Then if there are n vortex lines crossing the base, each of circulation Γ_1, the vortex density along the base is $n\Gamma_1/b$, and its perpendicular (azimuthal) component is $\gamma_\theta = (n\Gamma_1/b)\sin\beta$. Similarly for the height the axial component is $\gamma_x = (n\Gamma_1/s)\cos\beta$. The ratio is

$$\frac{\gamma_\theta}{\gamma_x} = \frac{s}{b}\tan\beta = \tan^2\beta.$$

But we have already noted that $\gamma_x = \Gamma/2\pi a$, where Γ is the total circulation of the vortex cylinder, so

$$\gamma_\theta = \frac{\Gamma}{2\pi a}\tan^2\beta.$$

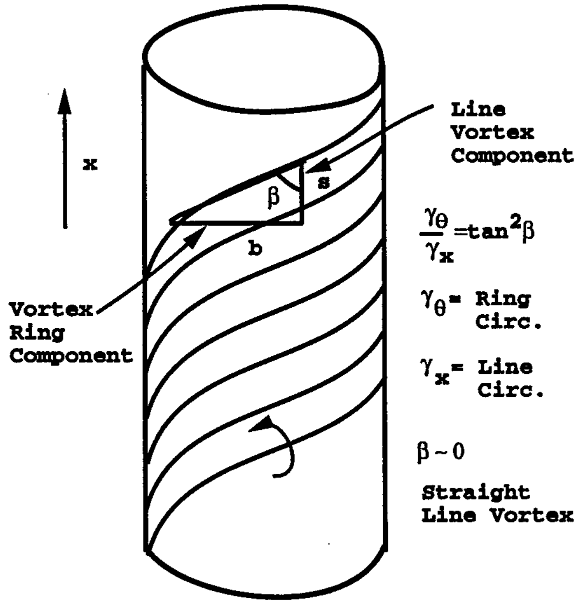

Figure 6.5: Relationship between the azimuthal and axial components of vorticity on the axial-flow vortex.

Now, equations (6.9), (6.15), and (6.16) give the three-dimensional velocity at a fixed point P induced by the semi-infinite helical vortex segment in terms of the total vortex circulation. The velocity field due to a finite vortex segment can be found by superposing semi-infinite segments with the desired end points having opposing circulation. Note that the velocity field is written in the local vortex segment coordinates and must therefore be transformed into the global coordinates of the airframe to sum the results for many segments.

6.3.2 Distributed Vorticity Model

Although the present formulation is perhaps the simplest representation of a three-dimensional rotor-tip vortex velocity field, the singularities associated with each line vortex and vortex ring at $r = a$ are not physical and make numerical computation of the motion of the tip-vortex much more difficult. A more physical model could be created by distributing the vorticity of the helico-cylindrical vortex sheet radially about the tip vortex radius. This refinement can be accomplished by smoothing the vorticity over the core radius using a cutoff parameter μ.

A μ-vortex is governed by the modified Biot-Savart law

$$d\vec{v} = \frac{\Gamma}{4\pi R^3}\, \vec{ds} \times \vec{R}, \tag{6.17}$$

where the magnitude of the vector $\vec{R}$ is

$$R = \sqrt{x^2 + y^2 + z^2 + \mu^2}.$$

For curved vortex filaments the cutoff parameter μ smooths vorticity over a finite core radius a and allows finite values for the self-induced velocity (Moore and Saffman 1972). Its value is usually chosen to match the correct propagation velocity of a vortex ring. In the present case, we already have the effect of a finite core by considering helical vortices distributed about a core radius. Applying a cutoff parameter to this helical vortex formulation will approximate a continuous distribution of line and ring vortex filaments through the core of the vortex cylinder, thus smoothing out discontinuities at the cylinder radius seen in the previous analysis. For a Rankine vortex

$$\mu = ae^{-\frac{3}{4}}.$$

The resulting velocity field may be derived following the same steps as before, but now beginning with the modified Biot-Savart law, equation (6.17).

The velocity components are found to be

$$v_\theta = \frac{\gamma_x a}{4\pi} \int_0^{2\pi} \left[1 + \frac{x}{\sqrt{x^2 + r^2 + a^2 + \mu^2 - 2ar\cos(\theta' - \theta)}}\right] \times \left[\frac{r - a\cos(\theta' - \theta)}{r^2 + a^2 + \mu^2 - 2ar\cos(\theta' - \theta)}\right] d\theta', \tag{6.18}$$

$$v_r = -\frac{\gamma_\theta\, a}{4\pi}\int_{\theta-\pi}^{\theta+\pi}\frac{\cos(\theta-\theta')}{\sqrt{x^2+r^2+a^2+\mu^2-2ar\cos(\theta-\theta')}}d\theta' \tag{6.19}$$

and

$$\begin{aligned} v_x = \frac{\gamma_\theta\, a}{4\pi}\int_{\theta-\pi}^{\theta+\pi}\frac{a-r\cos(\theta-\theta')}{r^2+a^2+\mu^2-2ar\cos(\theta-\theta')} \times \\ \left[1+\frac{x}{\sqrt{x^2+r^2+a^2+\mu^2-2ar\cos(\theta-\theta')}}\right]d\theta'. \end{aligned} \tag{6.20}$$

These integrals are evaluated using the method applied previously to give

$$\begin{aligned} v_\theta &= \frac{\Gamma}{4\pi r}\left\{\frac{1}{2}\left[1+\frac{r^2-a^2-\mu^2}{\sqrt{(r^2+a^2+\mu^2)^2-4a^2r^2}}\right]\right. \\ &+ \left.\frac{1}{\pi}\frac{x}{\sqrt{x^2+\mu^2+(r+a)^2}}\left[K(\bar{k})+\frac{r^2-a^2-\mu^2}{(r+a)^2+\mu^2}\Pi(\bar{\sigma}^2,\bar{k})\right]\right\}, \end{aligned} \tag{6.21}$$

$$v_r = -\frac{\gamma_\theta}{2\pi r}\sqrt{x^2+\mu^2+(a+r)^2}\left[\frac{x^2+r^2+a^2+\mu^2}{x^2+\mu^2+(a+r)^2}K(\bar{k})-E(\bar{k})\right] \tag{6.22}$$

and

$$\begin{aligned} v_x = \frac{\gamma_\theta}{4}\left\{\left[1+\frac{a^2-r^2-\mu^2}{\sqrt{(r^2+a^2+\mu^2)^2-4a^2r^2}}\right]\right. \\ \left.+\frac{2}{\pi}\frac{x}{\sqrt{x^2+\mu^2+(r+a)^2}}\left[K(\bar{k})+\frac{a^2-r^2-\mu^2}{(a+r)^2+\mu^2}\Pi(\bar{\sigma}^2,\bar{k})\right]\right\}. \end{aligned} \tag{6.23}$$

The elliptic-integral parameters defined for the μ-vortices are

$$\begin{aligned} \bar{k}^2 &= \frac{4ar}{x^2+(r+a)^2+\mu^2}, \\ \bar{\sigma}^2 &= \frac{4ar}{(r+a)^2+\mu^2}, \end{aligned}$$

and the relationships between the circulation Γ of the vortex cylinder and the vorticity components γ_x and γ_θ remain unchanged.

6.3.3 Distributed Vorticity - Zero Physical Radius

The application of the μ-vortex model to our helical vortex system introduces the possibility of a simplification. Initially, our model consisted of line and ring vortices distributed over the surface of a semi-infinite cylinder of radius a. Collapsing this structure to a physical radius of zero would give an azimuthal velocity component identical to a single line vortex, with infinite azimuthal velocity on the vortex axis. The component from the vortex rings would collapse to give infinite axial velocity on the vortex system axis.

Introduction of the cutoff parameter for both line and ring vortices allows the collapse of the helical vortex system into a meaningful three-dimensional velocity profile having a finite azimuthal velocity profile that peaks at an effective tip vortex core radius and a finite axial velocity profile that peaks at the tip vortex axis. This model, then, provides the detail we want without evaluating the elliptic integrals, a computational operation that is difficult to vectorize without resorting to tabular values.

The azimuthal velocity component for the zero-physical-radius model will be given by a single modified line vortex at the tip-vortex centerline with the aggregate circulation of the original cylindrical line vortex distribution. This velocity field, similar to that shown in equation (6.2), is

$$v_\theta = \frac{\Gamma_x}{4\pi\sqrt{r^2+\mu^2}}\left(1+\frac{x}{\sqrt{x^2+r^2+\mu^2}}\right), \tag{6.24}$$

where Γ_x is the total axial circulation of the helical vortices.

Several approaches are possible to derive the zero-radius limit case for the axial and radial velocity components:

1. Expand the μ-vortex ring elliptic integral formulas (equation 6.23) in power series;

2. Form the expression for a singular vortex ring ("ringlet") by expanding the well-known formula for a finite vortex ring (modified with a cutoff parameter) and then integrate it along the axis of the tip vortex cylinder; or

3. Expand the integrands of the μ-vortex given in equation (6.20) integrals prior to evaluating the elliptic integrals.

The third approach is the simplest and is followed here, though each of the three methods listed above were carried out, with identical results for each method.

Starting with the r and x velocities for the modified ring vortices expressed in terms of the I_0, I_1, and I_2 integrals presented in equations (6.6), (6.8) and (6.14), we may now expand the integrands in series of powers of η, keeping only the leading non-vanishing term in the integral, which turns out to be the O(η) term in each of the three integrals. Thus we have

$$\bar{I}_0(\xi,\eta,\mu) \sim \frac{1}{\sqrt{1+\xi^2+\mu^2}} \int_0^\pi \cos\phi \left\{1+\frac{\eta\cos\phi}{1+\xi^2+\mu^2}+\cdots\right\} d\phi,$$

and integrating term-by-term yields

$$\bar{I}_0(\xi,\eta,\mu) \sim \frac{\pi}{2}\frac{1}{(1+\xi^2+\mu^2)^{3/2}} \cdot \eta \,+\, O(\eta^3).$$

Similarly

$$\begin{aligned}\bar{I}_1(\eta,\mu) &\sim \frac{1}{1+\mu^2}\int_0^\pi \left\{-\cos\phi+\frac{1+\mu^2-2\cos^2\phi}{1+\mu^2}\cdot\eta+\cdots\right\} d\phi \\ &\sim \frac{\pi\mu^2}{(1+\mu^2)^2}\cdot\eta \,+\, O(\eta^3)\end{aligned}$$

and

$$\begin{aligned}\bar{I}_2(\xi,\eta,\mu) &\sim \frac{1}{(1+\mu^2)\sqrt{1+\xi^2+\mu^2}} \times \\ \int_0^\pi &\left\{-\cos\phi \,+\, \left[\frac{1+\mu^2-2\cos^2\phi}{1+\mu^2}-\frac{\cos^2\phi}{1+\xi^2+\mu^2}\right]\cdot\eta+\cdots\right\} d\phi \\ &\sim \frac{\pi}{2}\frac{(2\mu^2-1)(\mu^2+1)+2\mu^2\xi^2}{(1+\mu^2)^2(1+\xi^2+\mu^2)^{3/2}}\cdot\eta \,+\, O(\eta^3).\end{aligned}$$

Substituting these limit formulas for the integrals back into the expressions for the velocity components yields the results

$$v_r = -\frac{\gamma_\theta\, a^2}{4}\frac{r}{(x^2+r^2+\mu^2)^{3/2}},$$

and

$$v_x = \frac{\gamma_\theta\, a^2}{4}\left\{\frac{2\mu^2}{(r^2+\mu^2)^2}+x\,\cdot\,\frac{(2\mu^2-r^2)(r^2+\mu^2)+2\mu^2x^2}{(r^2+\mu^2)^2(x^2+r^2+\mu^2)^{3/2}}\right\}.$$

We term this the ringlet velocity distribution.

Note that these limit forms of the velocity field are useful provided the factors $\Gamma_x = \gamma_x 2\pi a$ and $\gamma_\theta a^2$ are held fixed, equal to their values for the original finite helical vortices. This interpretation is automatic for the axial vortices, but the ringlets may be interpreted more easily in terms of the axial volume flux induced by these vortices. It is convenient to consider the volume flux Q for a fully infinite vortex cylinder, which we obtain by evaluating the limit as $x \to \infty$ to find

$$v_x \longrightarrow \gamma_\theta \, a^2 \cdot \frac{\mu^2}{(r^2+\mu^2)^2}.$$

Then

$$Q = \int_0^\infty v_x \cdot 2\pi r \, dr = 2\pi\gamma_\theta \, a^2 \mu^2 \int_0^\infty \frac{r \, dr}{(r^2+\mu^2)^2} = \pi\gamma_\theta \, a^2. \tag{6.25}$$

Hence the former expressions for v_r and v_x may be rewritten in terms of Q, and the physical radius a is suppressed altogether:

$$v_r = -\frac{Q}{4\pi\mu^2} \cdot \frac{r/\mu}{(1+\frac{x^2}{\mu^2}+\frac{r^2}{\mu^2})^{3/2}}$$

$$v_x = \frac{Q}{4\pi\mu^2} \cdot \frac{1}{(1+\frac{r^2}{\mu^2})^2} \left\{ 2 + \frac{x}{\mu} \cdot \frac{(2-\frac{r^2}{\mu^2})(1+\frac{r^2}{\mu^2})+2\frac{x^2}{\mu^2}}{(1+\frac{x^2}{\mu^2}+\frac{r^2}{\mu^2})^{3/2}} \right\}$$

The parameter μ is now seen to be the effective radius of the ringlet vortices, in the sense that the axial velocity scale is obtained by dividing the volume flux Q by the cross-sectional area $\pi\mu^2$.

6.3.4 Mean Flow Model

The mean flow in the rotor downwash region occupied by the tip-vortex is very complex. Analysis of the vortex trajectory experimentally determined by Liou *et al.* (1990) suggests that the mean flow components in the rotor downwash near the airframe could be reasonably represented by a constant mean flow with a linear shear, as

$$W_\infty(x) = Ax + B$$

$$V_\infty(x) = Cx + D.$$

Affes *et al.* (1993) estimated the constants A,B,C and D from the experimental vortex trajectory at points at approximately five airframe radii from the airframe.

6.3.5 Vortex Propagation Model

To calculate the vortex trajectory, the velocity in the local vortex segment and panel coordinates are first transformed into the global vortex-airframe coordinates. The vortex segments are then advanced by solving the differential equation:

$$\frac{d\vec{x_v}}{dt} = \vec{u},$$

where $\vec{x_v}$ is the vortex position vector in the *global* coordinates, t is the time, and $\vec{u}$ is the velocity vector at a vortex segment due to other vortex segments, the presence of the cylindrical airframe and the mean flow. An Adams-Moulton method is used to calculate the motion of the vortex. As the vortex moves, the core radius for each vortex segment is evaluated by assuming that segment core volume is conserved as the vortex segment stretches or compresses. Vortex segment helical advance ratio and cutoff parameter, which are functions of the vortex core radius, are recalculated at each time step.

To properly calculate the trajectory for an axial-flow vortex, the transport algorithm was modified to regrid the vortex segments after each time step. This is necessary because points defining the vortex segment locations are convected axially along the vortex, causing the refined gridding at $x = 0$ to drift in a positive x direction. Regridding is accomplished by simply setting the grid points to their initial x location and then integrating the core volume along the axis to evaluate the new core radius and axial volume flux Q.

6.3.6 Pressure Calculation

Airframe pressure loading is calculated by integrating the Euler equations over the cylindrical surface. The nondimensional axial pressure gradient is given by

$$-\frac{\partial P}{\partial z} = \frac{\partial w}{\partial t} + (w - c)\frac{\partial w}{\partial z} + \frac{v}{r}\frac{\partial w}{\partial \theta}$$

where w and v are surface speeds in the axial and azimuthal directions, respectively, and c is the translational speed of the panel mesh. The Euler equation is integrated along z at constant θ; in particular, the axial derivative is integrated from $z = -L$ to z analytically to find

$$\int (w-c)\frac{\partial w}{\partial z} = \frac{1}{2}(w^2 - {w_{-L}}^2) - c(w - w_{-L}),$$

where

$$w_{-L} = w(\theta, -L)$$

and $2L$ is the length of the computational domain. The time and azimuthal derivatives are evaluated by central differencing and then integrated using the trapezoidal rule. In the results to follow, we call the instantaneous pressure *Cpinst*.

6.3.7 Results

Incorporating axial flow into the vortex model has significant effects on the vortex trajectory and particularly on the core radius. The initial axial volume flux was selected by iterating the value until the predicted axial velocity, normalized to the airframe radius and time scale, matched recent experimental values (Mahalingham 1996). The trajectory in global coordinates for a vortex initiated with axial velocity in a stagnant medium is depicted on Figure 6.6 from $t = 0.1$ to $t = 4.3$ in increments of 0.4 except for the final increment of 0.2.

As shown in Radcliff *et al.* (1997), the the axial-flow vortex advances less rapidly than the line vortex, but the qualitative features of the trajectory are similar. The clearest difference is twisting of the vortex about the cylinder axis, as shown in Figure 6.6(c). An offset of the trajectory in the positive x direction may also be discerned.

The difference in the core radius is much more obvious, as seen on Figure 6.7. As the outer radius of the vortex intersects the airframe, the vortex balloons by about 10% of the core radius locally on the surface of the advancing rotor side of the airframe, where axial core velocity is directed toward the surface. On the retreating blade side where axial flow is away from the airframe, the vortex thins strongly near the surface, with only slow recovery away from the surface. This behavior demonstrates qualitatively the relationship between the axial velocity and the core radius as given in equation (6.25), and also supports the predictions from the 90° vortex collision problem presented in Chapter 5.

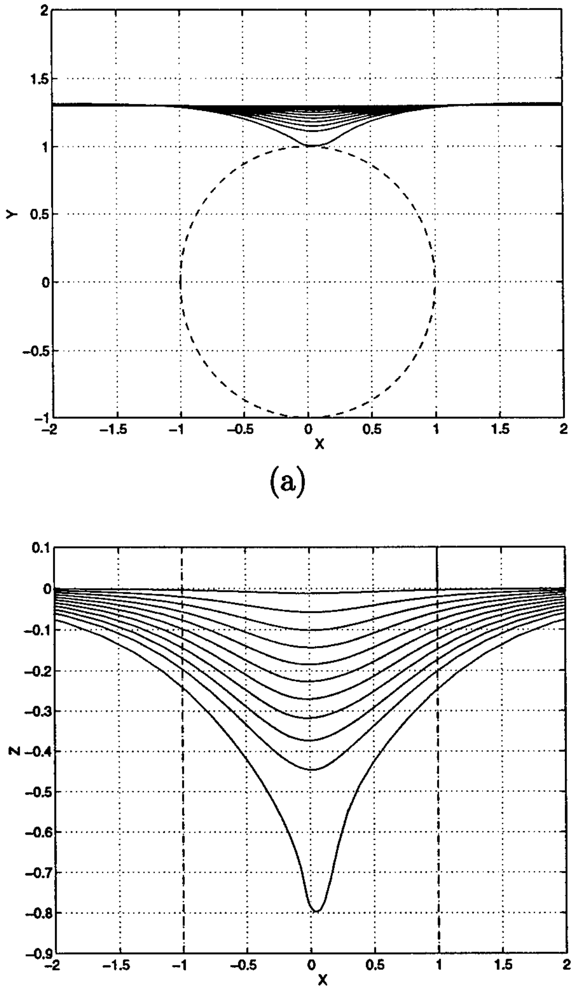

(a)

(b)

Figure 6.6(a,b)

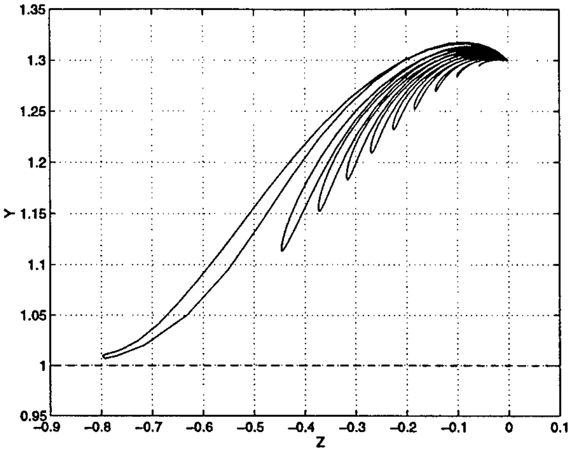

(c)

Figure 6.6: Motion of the axial-flow vortex toward the airframe in a stagnant medium; (a) x-y plane; (b) x-z plane; (c) z-y plane. The asymmetry in the spanwise direction is caused by the presence of axial flow in the vortex. Dashed lines indicate the airframe surface.

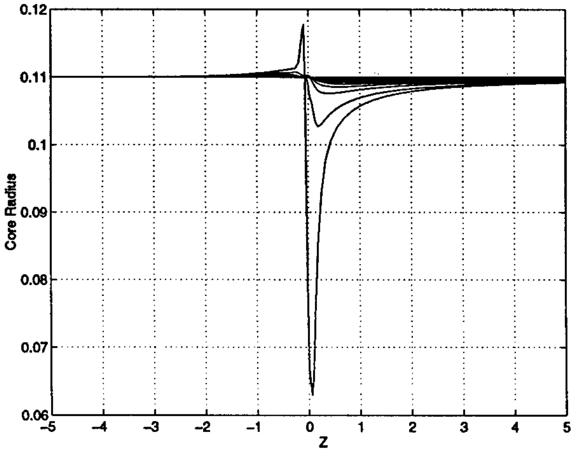

Figure 6.7: Axial-flow vortex core radius in a stagnant medium.

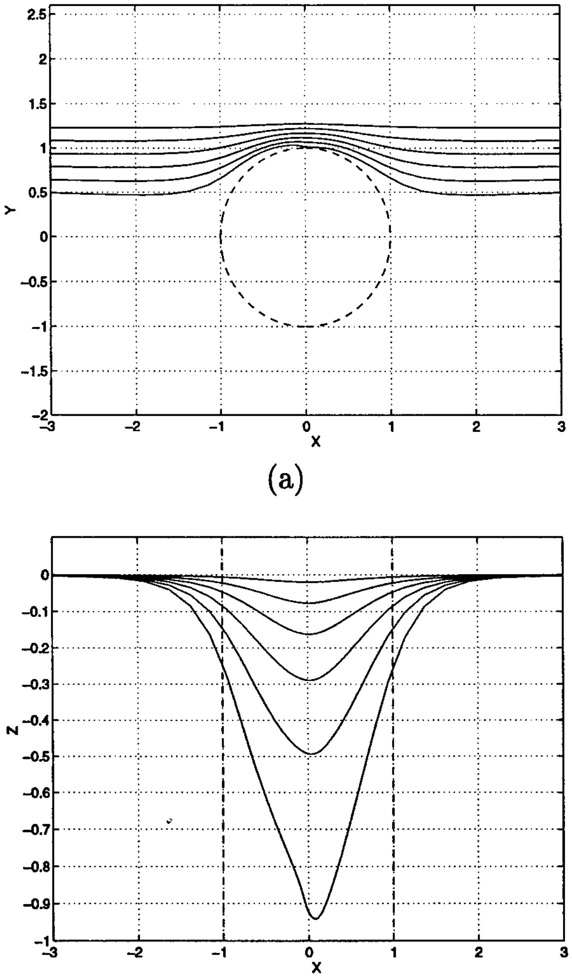

(a)

(b)

Figure 6.8(a,b)

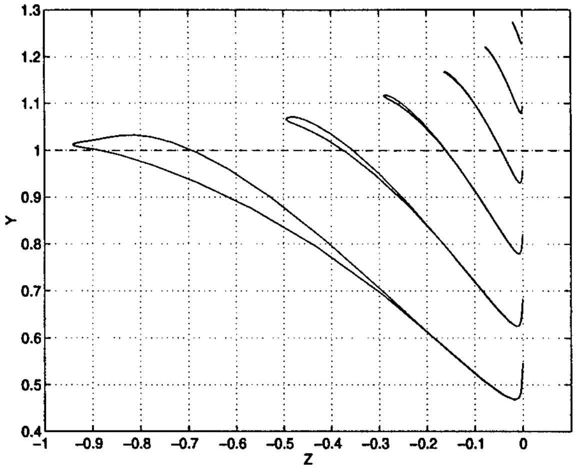

(c)

Figure 6.8: Motion of the axial-flow vortex toward the airframe in symmetric mean flow; (a) x-y plane; (b) x-z plane; (c) z-y plane. The dashed line indicates the airframe surface.

Adding a symmetric rotor downwash velocity brings us closer to the conditions represented by experimental and actual helicopter flow fields. For the following results, the dimensionless circulation is $\Gamma = 1.46$, and the dimensionless asymptotic downwash is 0.685. These two values correspond to the values for one of the tests run at Georgia Tech.

The results are depicted on Figure 6.8 from $t = 0.1$ to $t = 1.1$ in increments of 0.2. Here the strong y-velocity component sweeps the vortex over the airframe, producing the horseshoe vortex seen in Figure 6.8(a). The trajectory is nearly symmetric, but increasing axial velocity caused by vortex thinning does result in the vortex pulling closer to the airframe on the retreating rotor side of the airframe in the last time step. Twisting of the trajectory about the airframe axis is still evident.

The core radius, depicted on Figure 6.9, demonstrates the broadening and thinning seen in a stagnant medium, but there are some differences. Both effects now occur over more of the vortex length, an effect perhaps attributable to the larger airframe normal velocity components required to counter the faster advance of the vortex in the mean flow. Note that the point of minimum radius drifts in the positive x direction at first, but shifts

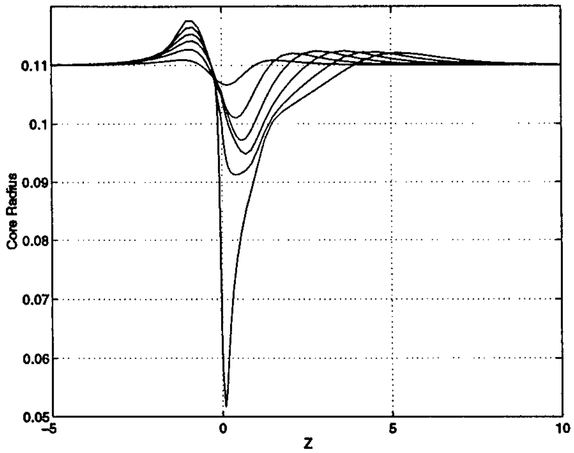

Figure 6.9: Axial-flow vortex core radius in a symmetric mean flow.

sharply back toward $x = 0$ as the vortex core radius intersects the airframe. In addition, a small increase in core radius now appears downstream of the thinned vortex on the retreating rotor side. The initial core radius minimum propagates down the side of the airframe on the RBS, but for the last two time steps shown, vortex thinning on the top of the airframe dominates the momentum thinning effect and the minimum radius moves back to the top of the airframe.

Finally, the effect of an asymmetric mean flow field is depicted on Figures 6.10 and 6.11. The time regime shown matches the previous case. Mean flow is input as a linear function of x to model the tilted downwash velocity typical of a helicopter rotor in the manner described by Affes *et al.* (1993b). This capability allows the transport model to predict the experimental vortex trajectory. Other than the obvious asymmetric transport noted in Figure 6.10(a), there is little difference in the vortex behavior compared to the symmetric mean flow case.

The major feature illustrated by these results is that axial velocity in the vortex core influences the behavior of the vortex motion as it comes within one core radius of the airframe. The presence of axial velocity is critical in explaining the results of measurements which are summarized in the sketch depicted on Figure 1.4. Without axial flow(Figure 6.2) the vortex core radius is symmetric with respect to $x = 0$ and thins the most at $x = 0$. This is because points on the vortex stretch apart as the vortex approaches the airframe. On the other hand, the presence of axial flow in the core of

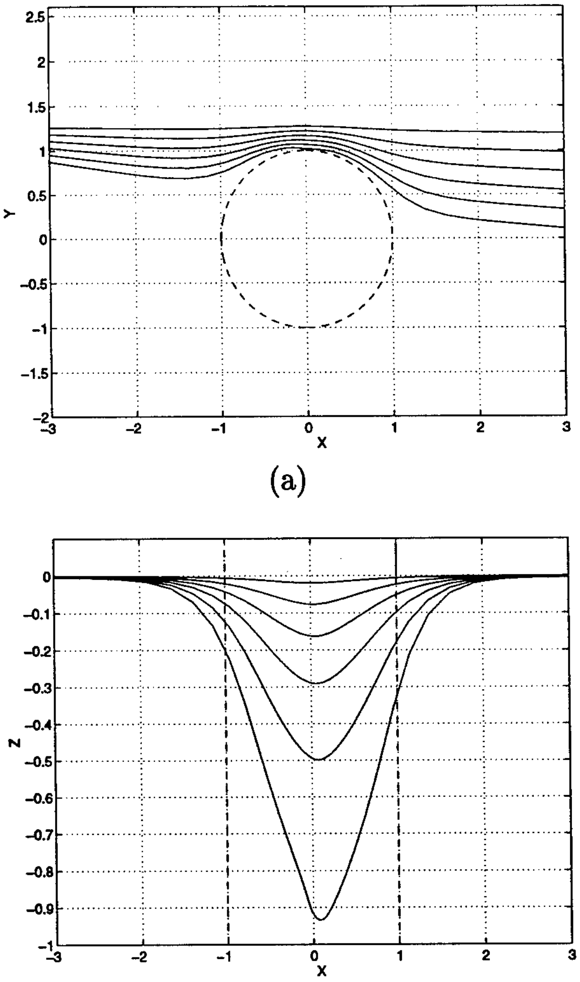

(a)

(b)

Figure 6.10(a,b)

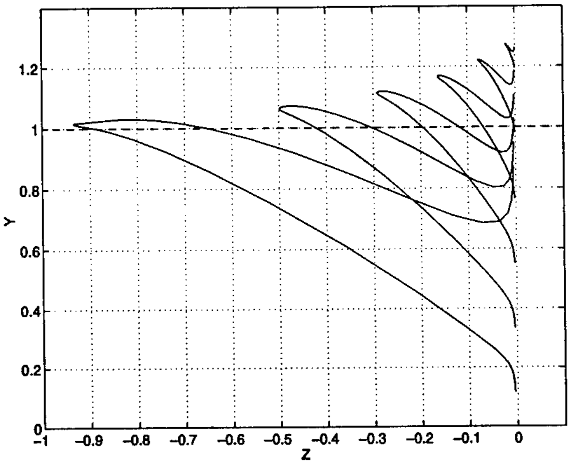

(c)

Figure 6.10: Motion of the axial-flow vortex toward the airframe in asymmetric mean flow; (a) x-y plane; (b) x-z plane; (c) z-y plane. The dashed line indicates the airframe surface.

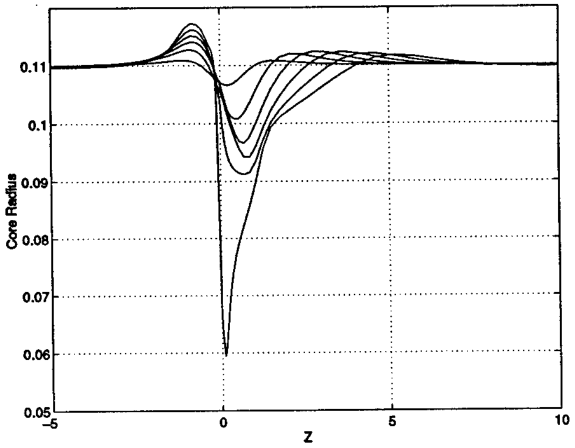

Figure 6.11: Axial-flow vortex core radius in asymmetric mean flow.

the vortex means that the velocity field is fundamentally asymmetric with respect to $x = 0$ and the vortex core is seen to bulge on the side of the airframe where the axial velocity is directed toward the airframe and thin on the side of the airframe where the axial velocity is directed away from the airframe(Figures 6.7 without mean flow and 6.9 with mean flow). Note from comparison of these results, the extent of this bulging and thinning along the vortex is much greater for the case of a mean downwash. This agrees with the experimental results of Figure 1.4, and the sketch of Figure 1.5(b).

The interpretation of the changes in vortex core radius in terms of the axial velocity component in the vortex core is clear from equation (6.25). For an arbitrary position along the vortex, the expression for the axial volume flowrate through the vortex requires that

$$Q \sim a_c^2 \gamma_\theta$$

This shows that the ring-vortex circulation density γ_θ is directly proportional to the axial velocity component within the vortex. Given a constant volume flowrate, a decrease in the vortex core radius corresponds to an increase in the axial velocity, as occurs on the retreating side of the rotor. On the other hand, when the vortex core radius increases, the axial velocity must decrease. Ultimately, this must result in the situation sketched on Figure 1.5 with the axial velocity in the core of the vortex stagnating under the vortex on the advancing side of the rotor as the vortex convects down the airframe. To the knowledge of the authors the influence of axial velocity within the core of the vortex has not been investigated in any previous computational studies of vortex-surface interaction.

Of course, it should be noted that the current results describe the behavior of the vortex in a limited time domain, corresponding to the initiation of the bulging and thinning depicted much later on Figure 1.5. In order for the entire range of the vortex collision process to be described the current computations should be extended to the point where the vortex fluid is indistinguishable from boundary layer fluid thus terminating the collision process. We now compare the computational results with those from the experiments.

6.4 Comparison With Experiment

The numerical model of the vortex and airframe has been applied to predict some of the experimental results from Georgia Tech. Vortex trajectory and airframe surface pressure are parameters available for comparison. To perform this comparison, the measured vortex position at rotor angle $\psi = 180^o$ was extracted from the experimental data of Liou *et al.* (1990) and used to initiate the computation. This places the vortex about four core radii away from the airframe, where detail of the vortex structure is relatively unimportant. To enforce the assumption of an infinitely long vortex, the finite vortex end points recorded in the experiments were extrapolated to produce semi-infinite ends. Measured values of vortex circulation, core radius and axial velocity were also incorporated into the initial conditions. For the computations presented here, experimental and computational parameters were non-dimensionalized on the airframe diameter of $0.137m$ and the mean flow velocity of $10m/s$ (advance ratio 0.1 at 2100 rpm) which results from a 0.1 advance ratio. This gives a dimensionless circulation of 2.24, an initial dimensionless core radius of 0.1, and a dimensionless axial velocity in the vortex core of 2.5.

The airframe is represented with 81 axial and 40 azimuthal panels. Once initiated, the vortex was allowed to propagate freely with a time step of 0.002985, corresponding to a rotor phase angle of 0.25^o. The computation was halted when one of the vortex centerline points, which define each vortex segment, crossed the airframe boundary in violation of the zero normal velocity boundary condition. The sensitivity of these results to number of panels and vortex segments, airframe and vortex length, and time increment has been tested. Doubling the number of panels or vortex segments, or increasing the airframe or vortex length, has little effect on the results. Four digit accuracy is obtained for vortex trajectory and two digit accuracy is obtained for pressure at the times presented. Time step size is chosen to ensure that vortex movement does not exceed the narrowest panel width in any interval, so time steps are typically shortened as the vortex approaches the airframe. Decreasing the time increment further has little effect other than providing finer resolution of the exact time at which the vortex is predicted to penetrate the airframe.

The predicted results for vortex trajectory are shown in Figure 6.12 from $\psi = 190^o$ to $\psi = 260^o$ in 10^o increments along with the measured trajectory from Liou *et al.* (1990) at $\psi = 210^o$ and $\psi = 240^o$. The trajectory matches well over 30^o of rotor advance but the experimental vortex moves toward the cylinder more rapidly than the modeled vortex over the next 30^o. These results also compare well with the with the results of Affes (1992) and Affes *et al.* (1993b) for the predicted vortex trajectories until $\psi = 240^o$. Affes

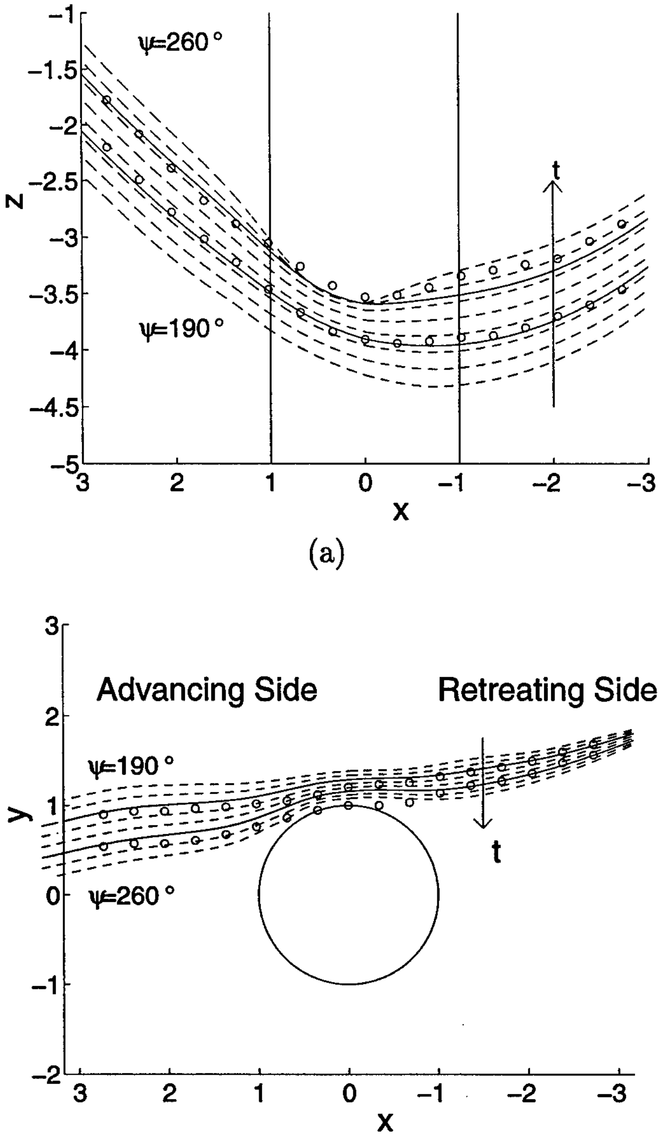

(a)

(b)

Figure 6.12: Vortex trajectory from $\psi = 190^o$ to $\psi = 260^o$. The solid lines denote the computed trajectories and the circles denote the the experimental data at the same times. Arrow denotes increasing ψ; that is, increasing time.

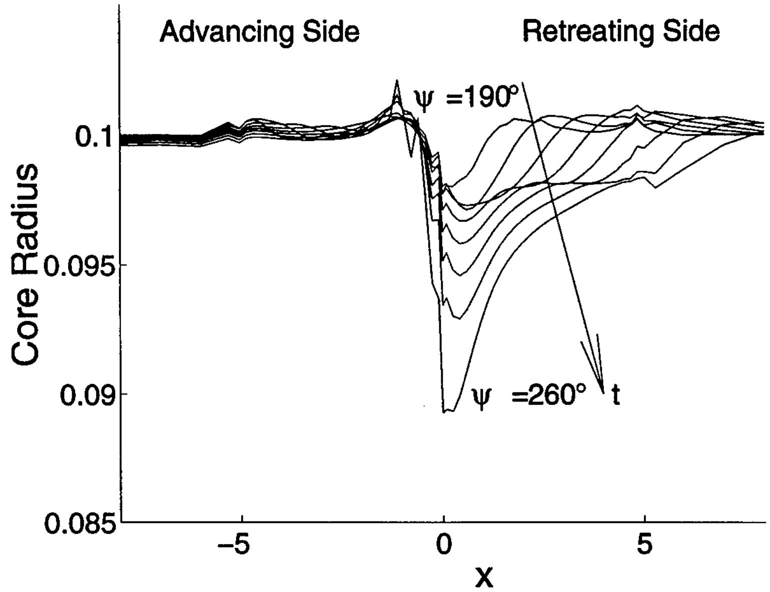

Figure 6.13: Vortex core radius from $\psi = 190^o$ to $\psi = 260^o$ for the conditions of the previous figure.

et al. (1993b) used a fixed core radius and no axial velocity. However the computation of Affes *et al.* (1993b) is much more computationally intensive than the current computation. Moreover, the present computations can be extended beyond those of Affes *et al.* (1993b); indeed, the results at $\psi = 250^o$ and $\psi = 260^o$ show that the advance of the vortex is halted. This has been seen in previous experiments (Kim and Komerath 1995, Liou *et al.* 1990) and in the current visualizations at about the same time as in the current computations.

The time variation in core radius at each vortex segment is shown in Figure 6.13. This figure shows that although the trajectory is similar to Affes *et al.* (1993b), axial momentum in the vortex core does cause the vortex to bulge slightly on the advancing-blade side (ABS) of the airframe and to thin substantially on the retreating-blade side (RBS). At the high value of axial velocity used here, the radius calculation can become numerically unstable. Very small mismatches in vortex segment radius tend to excite numerical oscillations and wave propagation, as seen in the figures. This tendency can be partially controlled by careful selection of the segment size, but it does not appear to drastically affect the overall trends of core radius.

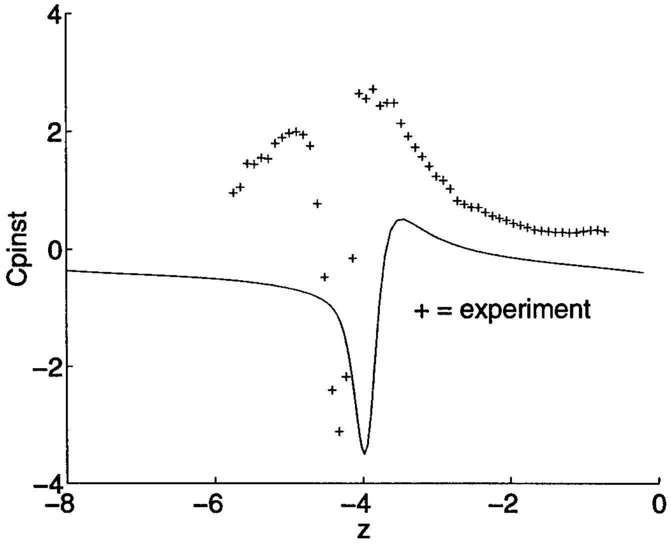

(a)

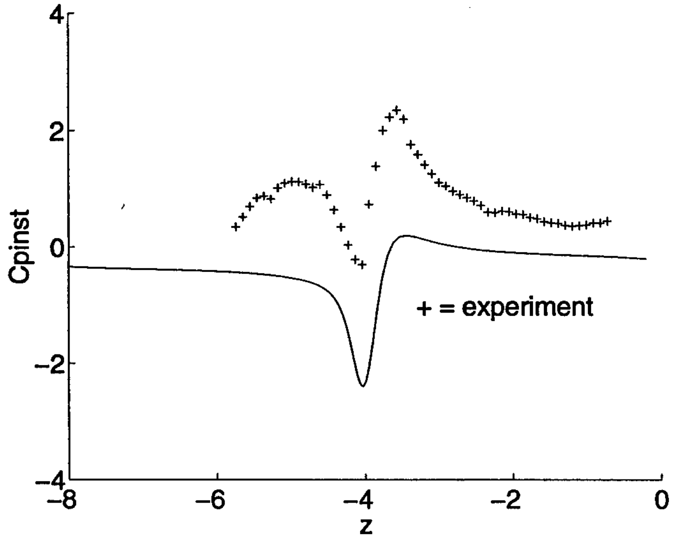

(b)

Figure 6.14(a,b)

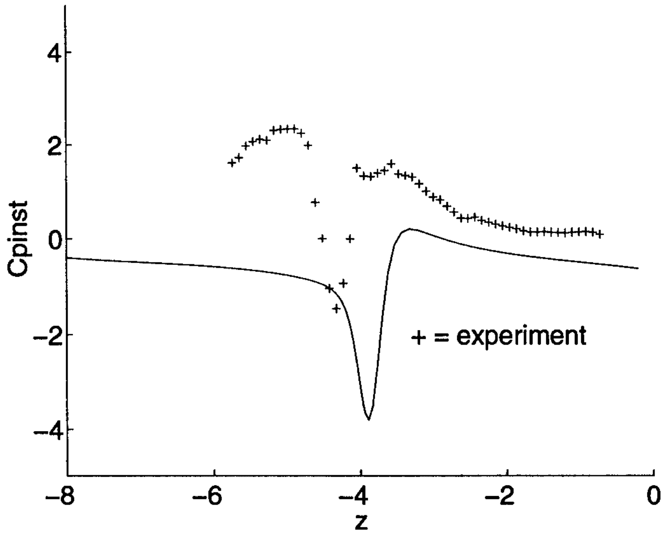

(c)

Figure 6.14: Instantaneous pressure at $\psi = 210^o$. (a) Top of the airframe; (b) 15^o to the advancing side; (c) 15^o to the retreating side.

Figures 6.14-6.16 illustrate the results for the pressure plotted as a function of distance along the airframe for several rotor phase angles at three locations around the cylinder azimuth near the top of the airframe. These locations are the top of the airframe and 15^o on either side. Note that for the first two rotor phase angles, the amplitude of the experimental suction peak is greater on the top than elsewhere; the amplitude on the advancing side is lower than that on the retreating side. However, at $\psi = 240^o$, the experimental suction peak on the top of the airframe is significantly reduced. The computational results are depicted as the solid lines. The computational results are in reasonable agreement with the experimental data (excluding bias from blade passage effects) except at the last rotor phase angle. Note that no adjustable parameters have been employed in these computations. At 240^o, the measured suction peaks on the top and retreating blade side of the airframe are considerably reduced from their values at 222^o while the computational suction peaks continue to deepen. This difference appears to have the same basis as the sharp reduction in core radius on the top of the airframe noted previously in Figure 6.13. As the vortex comes into very

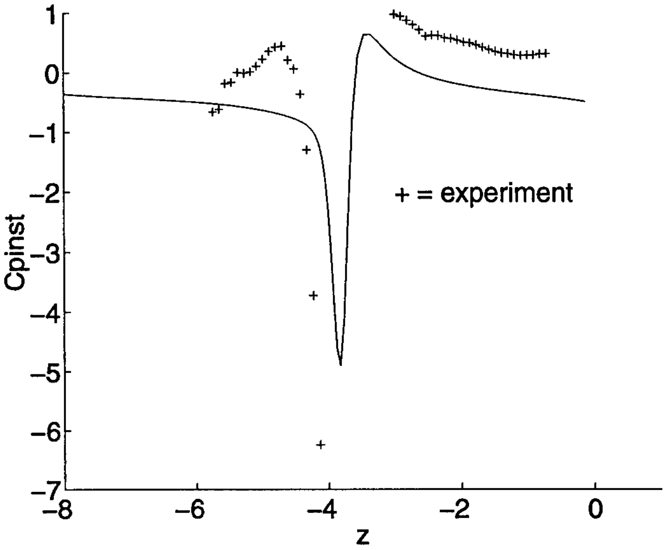

(a)

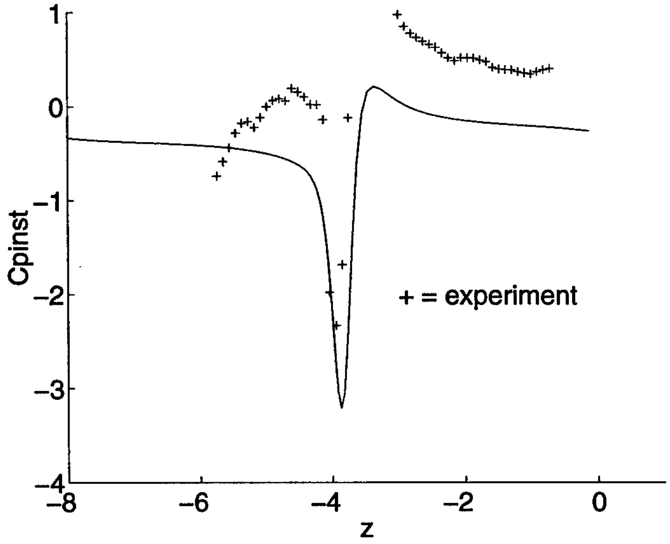

(b)

Figure 6.15(a,b)

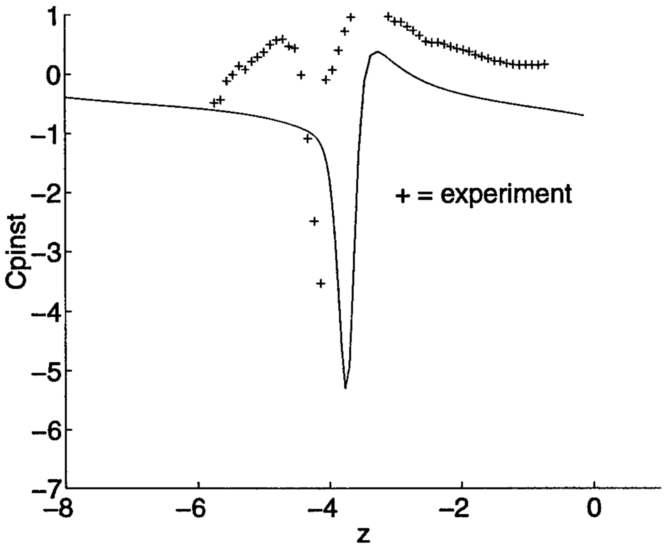

(c)

Figure 6.15: Instantaneous pressure at $\psi = 222^o$. (a) Top of the airframe; (b) 15^o to the advancing side; (c) 15^o to the retreating side.

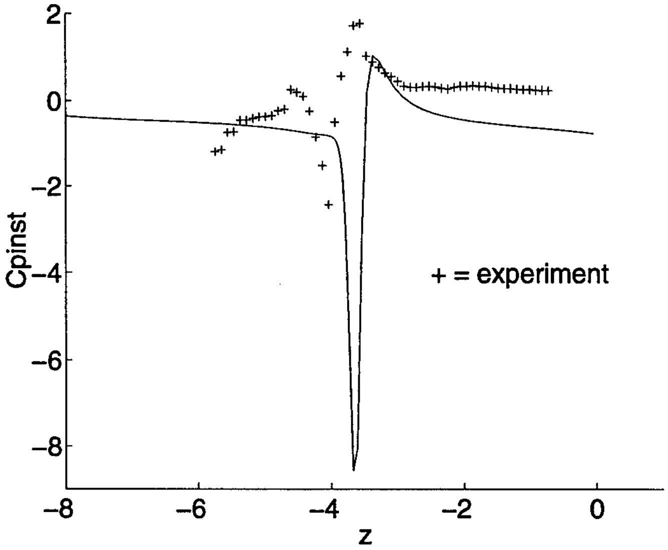

(a)

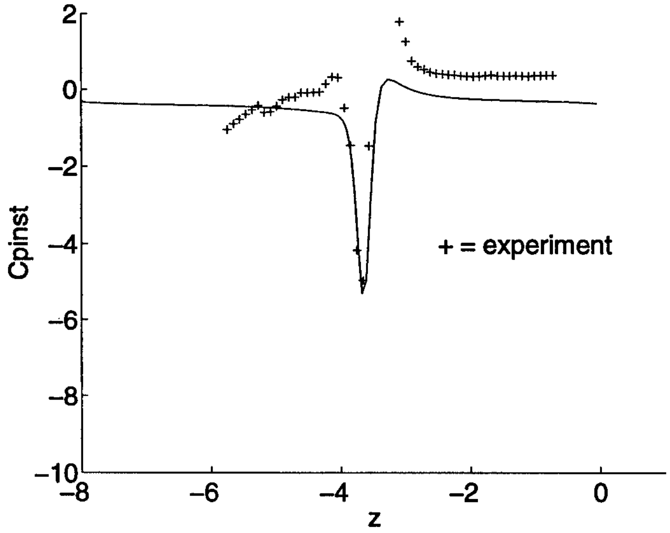

(b)

Figure 6.16(a,b)

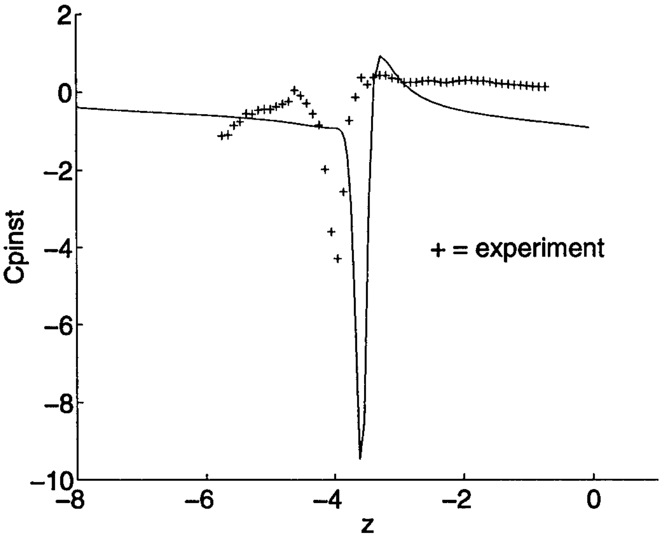

(c)

Figure 6.16: Instantaneous pressure at $\psi = 240^o$. (a) Top of the airframe; (b) 15^o to the advancing side; (c) 15^o to the retreating side.

close proximity of the airframe, the vortex stretches into a very long horseshoe shape. This reduces the core radius sharply, and core axial velocity even more sharply as this parameter scales with $(a/a_0)^6$. With low axial velocity on top of the airframe, then, the pressure-reducing mechanism of vorticity redistribution seen by Lee *et al.* (1995) is no longer present and the core radius collapses, swirl velocity sharpens and surface suction deepens relentlessly. It is interesting to note that the results of Affes *et al.* (1993b) predict that the suction peak on the top of the airframe at $\psi = 240^o$ is ~ -10 and so it would appear that the presence of the axial flow in the computation actually *reduces* the magnitude of the suction peak. Also, it is likely that the additional reduction is due to core deformation as seen in the experimental results on Figure 4.17. Comparison of the behavior of the numerical model to experimental visualizations shows that, upon close approach, the observed vortex first ovals then rapidly flattens into the boundary layer on the airframe. The next section describes a computational method designed to capture this observed behavior.

Note that in the perpendicular interaction described in Lee *et al.* (1995), a similar reduction in pressure occurs rapidly as a result of the presence of axial flow in the vortex. However, the present problem is more complex geometrically and the deformation of the vortex core is likely to play a significant role locally in time. This effect is iillustrated for the box vortex described in the next section.

6.5 The Box Vortex

The model for the vortex described in the previous sections of this chapter is not valid upon approach to within a core radius of the airframe for two reasons. The first is that the model does not predict the large reduction of the suction peak observed in experiments as discussed previously. The second reason is less obvious. In the axial-flow model, the helical vortex system is represented by a single line surrounded by distributed vorticity with the position of the vortex determined by the vortex axis. As the vortex approaches the airframe, the velocity field from the source panels representing the solid surface acts to prevent the centerline from penetrating but does nothing to prevent the distributed vorticity from unphysically overlapping the solid body. This results in a discontinuity in the pressure integration where the overlap occurs. To circumvent these problems, a model which maintains vorticity in a bounded region which cannot cross solid boundaries was formulated. Observation of experimental vortex-surface collisions also show an ovaling of the vortex core before the vortex merges into the boundary layer (Mahalingam 1996). The mathematics of bounded vorticity within an ellipse is quite complicated, however, so we have applied a rectangular, or "box" core formulation. As a first test of this concept we first consider the case of two-dimensional flow.

6.5.1 The Two-Dimensional Box Vortex

We first consider a simple box vortex in two dimensions above a plane wall. This simple problem will illustrate the fact that the pressure distribution will decrease as the vortex becomes flatter. As with the point vortex and the circular Rankine vortex, the centroid of the box vortex will also move at constant speed and remain at a constant distance from the wall. Thus, we consider only the frozen flow caused by a box vortex of specific aspect ratio at a fixed aspect ratio even though we know that the vortex will change shape, likely in a periodic manner as the time goes on. This situation is similar to that described by Tucker and Conlisk (1992) in their calculation of the motion of a finite-core vortex. The pressure distribution over the surface for the rectangular vortex is compared with the point vortex and with the Rankine vortex. In the situation such as the vortex-airframe collision, there is a strong downwash towards the surface which causes the vortex-surface collision. In this simple model problem, no downwash is included.

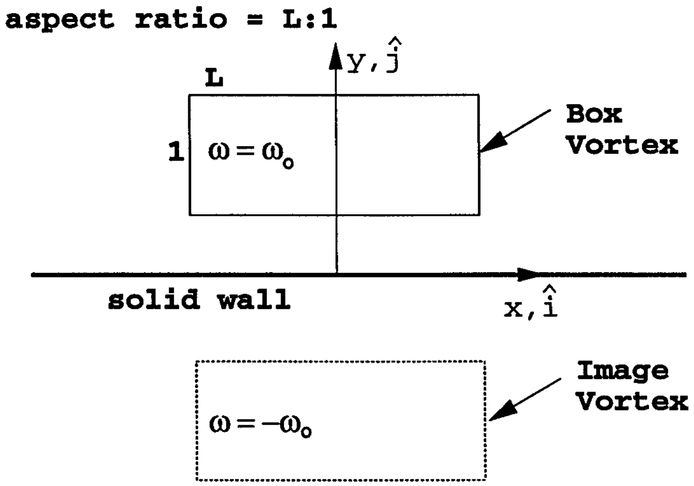

Figure 6.17: Sketch of a rectangular or "box vortex" in two dimensions.

A box vortex consists of a rectangular region of constant vorticity as depicted in Figure 6.17. The aspect ratio (L:1) is the ratio of the width to the height of the rectangle. The velocity distribution due to the vortex can be obtained analytically by integrating the Biot-Savart law for a fixed and constant vorticity inside the vortex and the velocity distribution may be obtained in closed form. Assuming a constant vorticity over a rectangle, the velocity distribution for the box vortex is given by:

$$\vec{u} = \frac{\omega_0}{2\pi} g(x, y, L, W)\hat{\imath} - \frac{\omega_0}{2\pi} g(y, x, W, L)\hat{\jmath}, \tag{6.26}$$

where,

$$g(x, y, L, W) \quad = \quad \frac{1}{2}(L - x) \ln \left\{ \frac{(W - y)^2 + (L - x)^2}{(W + y)^2 + (L - x)^2} \right\}$$

$$
\begin{aligned}
&+\frac{1}{2}(L+x)\ln\left\{\frac{(W-y)^2+(L+x)^2}{(W+y)^2+(L+x)^2}\right\} \\
&+(W-y)\tan^{-1}\left\{\frac{2L(W-y)}{(W-y)^2-L^2+x^2}\right\} \\
&+(W+y)\tan^{-1}\left\{\frac{2L(W+y)}{(W+y)^2-L^2+x^2}\right\},
\end{aligned}
$$

where ω_0 is the constant vorticity (Tucker and Conlisk 1992) and $W = 1$ in Figure 6.17 for simplicity.

To simulate the motion of a box vortex over a wall, the method of images is used. An image vortex of equal but opposite strength is introduced below the the solid surface such that the two vortices are equidistant from the wall (see Figure 6.17). The vortex above the wall is denoted as A and the image vortex is denoted as B. It can be easily shown that such a system of vortices satisfies the no-normal flow condition on the wall. Rewriting equation (6.26) for the coordinate system used in Figure 6.17 we get for the vortex A,

$$\vec{u}_A = \frac{\omega_o}{2\pi}g(x-x_v, y-y_v, L, W)\hat{\imath} - \frac{\omega_o}{2\pi}g(y-y_v, x-x_v, W, L)\hat{\jmath}, \tag{6.27}$$

Similarly for the vortex B, we get,

$$\vec{u}_B = \frac{\omega_o}{2\pi}g(x-x_v, y+y_v, L, W)\hat{\imath} - \frac{\omega_o}{2\pi}g(y+y_v, x-x_v, W, L)\hat{\jmath}, \tag{6.28}$$

Adding equations (6.27) and (6.28) we get the velocity distribution as,

$$
\begin{aligned}
\vec{u}_v \;=\; & \frac{\omega_o}{2\pi}\left(g(x-x_v, y-y_v, L, W) + g(x-x_v, y+y_v, L, W)\right)\hat{\imath} \\
& -\frac{\omega_o}{2\pi}\left(g(y-y_v, x-x_v, W, L) + g(y+y_v, x-x_v, W, L)\right)\hat{\jmath},
\end{aligned}
\tag{6.29}
$$

To determine the motion of the centroid of the box vortex we need to solve the evolution equations

$$\frac{dx_v}{dt} = u_{vx}, \tag{6.30}$$

$$\frac{dy_v}{dt} = v_{vy} = 0, \tag{6.31}$$

Here $\vec{u}_v$ is given by equation (6.29) evaluated at the vortex center(i.e. when $x = x_v$ and $y = y_v$) and x_v and y_v are the components of the position vector of the center of vortex A. The initial condition is:

$$x_v = 0, \quad y_v = 1.0 \;\; at \quad t = 0, \tag{6.32}$$

Since $u_{vy} = 0$, using the initial condition given by equation 6.32 for y_v, it follows that,

$$y_v(t) = 1.0 \; for \; t \geq 0,$$

Thus, only equation (6.30) is to be solved with the initial condition given by equation (6.32) for x_v. As with the point vortex, the box vortex travels at constant speed above the wall, although it may change shape (Tucker and Conlisk 1992). The numerical results indicate that the speed of the box vortex is constant and almost

$$u_{v0} = -\frac{1}{4\pi},$$

where the vorticity has been taken to be 1; there is a slight deviation from this value because the box vortex in these two-dimensional calculations is not permitted to deform.

Figures 6.18(a,b,c,d) show the pressure distribution on the surface for the various aspect ratios of the vortex. The results are compared with the circular vortex of a unit core radius (i. e., a Rankine vortex) and with a point vortex. Note that the core of the Rankine vortex is just touching the wall. It is observed that the peak reduces substantially and is spread out to a wider region on the wall as the ratio of the length to height of the box vortex becomes larger. For an aspect ratio of eight, the suction peak is almost five times smaller than that of the point vortex and the Rankine vortex. As a final test we consider a box vortex with an area 10 times that in Figure 6.18 while keeping the height of the box vortex the same as in Figure 6.18(d). Here we see additional reduction of the suction peak although the magnitude of the additional reduction is not large.

We can see from these results that the pressure peak reduces substantially as the aspect ratio of the box vortex is increased. This suggests that flattening of the vortex core has an important effect on the pressure distribution on the surface. We now consider the three-dimensional case.

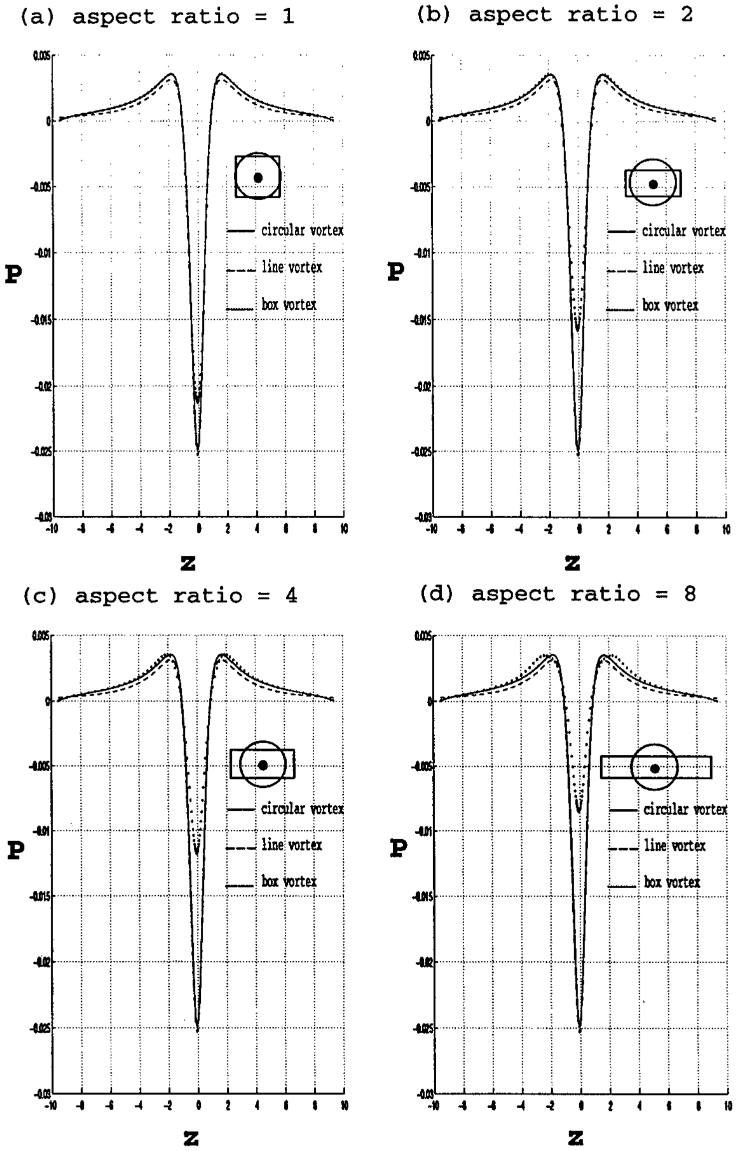

Figure 6.18: Pressure on the surface for various aspect ratios; here the area remains constant as the aspect ratio increases.

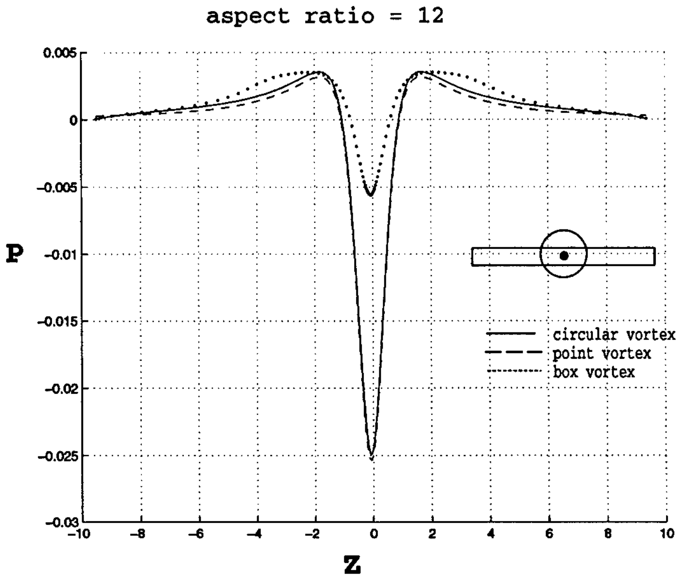

Figure 6.19: Pressure on the surface for the area 10 times that of Figure 6.18(d).

6.5.2 The Three-Dimensional Box Vortex

The two dimensional results suggest that the suction peak may be reduced substantially as the vortex is elongated or flattened by the presence of a wall. We now investigate this possibility in three dimensions and in a dynamic sense. In the three-dimensional box-vortex model, the axial vorticity is uniformly distributed throughout a rectangular volume while azimuthal vorticity is represented by a distribution of vortex "rings" comprised of finite line vortex segments wrapped about the periphery of the rectangular volume. The cutoff parameter applied previously is not incorporated here to ensure that vorticity is completely enclosed within the rectangular vortex structure. Variation of the aspect ratio of this box-vortex allows the vorticity to remain outside of the airframe on close approach while conserving the calculated vortex cross-sectional area. An illustration of the model configuration and the computational parameters is depicted on Figure 6.20.

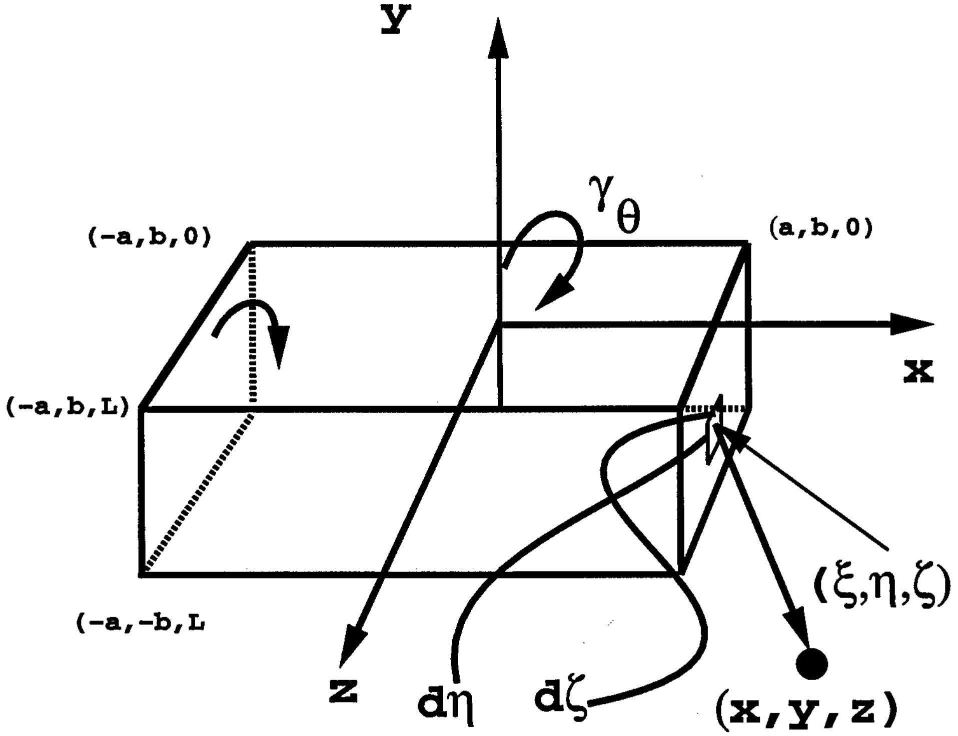

Figure 6.20: Box-vortex configuration in three dimensions.

6.5.3 Volume Distributed Vorticity

The azimuthal component of velocity for the box-vortex is modeled as a distribution of axial vorticity throughout the vortex volume. We begin as before with the Biot-Savart law for a vortex element, which is given as equation (6.1) Cartesian coordinates are oriented with the z-axis along the vortex element, which we locate at the point (ξ, η, ζ) within the box-vortex. Since our goal is to evaluate the velocity induced by vorticity ω uniformly distributed over a rectangular volume, we represent the circulation vector by $d\vec{\Gamma} = \vec{k}\,\omega\, d\xi\, d\eta\, d\zeta$ where $\vec{k}$ is the unit vector in the $z-$ direction of Figure 6.20. Thus the non-zero components of velocity are

$$u = -\frac{\omega\, d\xi d\eta\, d\zeta}{4\pi}\,\frac{y-\eta}{r^3}, \tag{6.33}$$

$$v = \frac{\omega\, d\xi d\eta\, d\zeta}{4\pi}\,\frac{x-\xi}{r^3}, \tag{6.34}$$

where

$$r = \sqrt{R^2 + (z-\zeta)^2},$$

and R is the perpendicular radius

$$R = \sqrt{(x-\xi)^2 + (y-\eta)^2}.$$

Extending the initial vortex element into a vortex line segment of finite length $z = 0$ to L, we find the x-component of velocity by integration with respect to ζ as

$$u = -\frac{\omega d\xi d\eta}{4\pi}(y-\eta)\int_0^L \frac{d\zeta}{[R^2 + (z-\zeta)^2]^{3/2}}.$$

Thus for the vortex segment

$$u = -\frac{\omega d\xi d\eta}{4\pi}\,\frac{y-\eta}{R^2}\left[\frac{z}{\sqrt{R^2+z^2}} - \frac{z-L}{\sqrt{R^2+(z-L)^2}}\right]. \tag{6.35}$$

Next we form a vortex sheet by integrating the segments with respect to η over the range $-b < \eta < b$ to find

$$u = -\frac{\omega d\xi}{4\pi}\left[z\int_{-b}^{b} \frac{(y-\eta)\, d\eta}{R^2\sqrt{R^2+z^2}} - (z-L)\int_{-b}^{b} \frac{(y-\eta)\, d\eta}{R^2\sqrt{R^2+(z-L)^2}}\right].$$

It is convenient to change variables

$$t = R^2 = (x-\xi)^2 + (y-\eta)^2,$$

so that the integrals in the above formula simplify to

$$u = \frac{\omega d\xi}{8\pi}\left[z\int_{\eta=-b}^{\eta=b}\frac{dt}{t\,\sqrt{t+z^2}} - (z-L)\int_{\eta=-b}^{\eta=b}\frac{dt}{t\,\sqrt{t+(z-L)^2}}\right].$$

The individual integrals have the form

$$\beta\int\frac{dt}{t\sqrt{t+\beta^2}} = 2\ln\left(\sqrt{t+\beta^2}-\beta\right) - \ln(t),$$

where the term $\ln(t)$ cancels out in the combination of the two integrals, leaving the result

$$u = \frac{\omega d\xi}{4\pi}\left[\ln\left(\frac{\sqrt{(\xi-x)^2+(b-y)^2+z^2}-z}{\sqrt{(\xi-x)^2+(b+y)^2+z^2}-z}\right)\right.$$
$$\left.-\ln\left(\frac{\sqrt{(\xi-x)^2+(b-y)^2+(z-L)^2}-(z-L)}{\sqrt{(\xi-x)^2+(b+y)^2+(z-L)^2}-(z-L)}\right)\right]. \qquad (6.36)$$

Now we form a rectangular volume of uniform vorticity by integrating the vortex sheet, located at $x=\xi$, over the range $-a<\xi<a$. Hence from Eqn. (6.36), we need to evaluate integrals of the form

$$I(s) = \int\ln\left(\sqrt{s^2+\alpha^2+\beta^2}-\beta\right)ds.$$

Integrating gives a logarithmic form plus a residual term

$$I(s) = s\,\ln\left(\sqrt{s^2+\alpha^2+\beta^2}-\beta\right) + f(s),$$

where the logarithm cancels in the result of differentiation, leaving

$$f'(s) = -\frac{s^2}{\sqrt{s^2+\alpha^2+\beta^2}\left(\sqrt{s^2+\alpha^2+\beta^2}-\beta\right)}.$$

The residual function $f(s)$ is found by integration of the above result. The process of integration may be simplified by use of the new variable

$$\sigma = \sqrt{s^2 + \alpha^2 + \beta^2} - \beta,$$

so that $f(s)$ becomes

$$f(s) = -\int \sqrt{\sigma^2 + 2\beta\sigma - \alpha^2}\ \frac{d\sigma}{\sigma} \cdot Sign(s).$$

The latter integral may be found in standard tables of integrals. Reverting to the original s-variable yields

$$\begin{aligned} I(s) &= s\ \ln\left(\sqrt{s^2+\alpha^2+\beta^2} - \beta\right) \\ &-s - \beta\, Sign(s)\ \ln\left(|s| + \sqrt{s^2+\alpha^2+\beta^2}\right) \\ &+ \alpha\ \arctan\left(\alpha s \Big/ \left[\alpha^2 + \beta^2 - \beta\sqrt{s^2+\alpha^2+\beta^2}\right]\right). \end{aligned}$$

The factor $Sign(s)$ jumps across $s = 0$, so special care is needed for evaluating the definite integral. We obtain

$$\int_{s_1}^{s_2} \ln\left(\sqrt{s^2+\alpha^2+\beta^2} - \beta\right)\ ds = s_2\ \ln\left(\sqrt{{s_2}^2+\alpha^2+\beta^2} - \beta\right)$$

$$-s_1 \ln\left(\sqrt{{s_1}^2+\alpha^2+\beta^2} - \beta\right) - (s_2 - s_1) - \beta Sign(s_2) \ln\left(|s_2| + \sqrt{{s_2}^2+\alpha^2+\beta^2}\right)$$

$$+\beta Sign(s_1) \ln\left(|s_1| + \sqrt{{s_1}^2+\alpha^2+\beta^2}\right) + \beta \ln\sqrt{\alpha^2+\beta^2}\,\left[Sign(s_2) - Sign(s_1)\right]$$

$$+ \alpha\ \arctan\left(\alpha s_2 \Big/ \left[\alpha^2+\beta^2 - \beta\sqrt{{s_2}^2+\alpha^2+\beta^2}\right]\right)$$

$$- \alpha\ \arctan\left(\alpha s_1 \Big/ \left[\alpha^2+\beta^2 - \beta\sqrt{{s_1}^2+\alpha^2+\beta^2}\right]\right). \qquad (6.37)$$

Reverting to the original x, y, z variables, an elemental integral in Eqn. (6.36) is evaluated as

$$\int_{-a}^{a} \ln\left(\sqrt{(\xi - x)^2 + (b+y)^2 + z^2} - z\right)\ d\xi =$$

$$(a - x) \ln\left(\sqrt{(a-x)^2 + (b+y)^2 + z^2} - z\right)$$

$$\begin{aligned}
&+ (a+x)\ln\left(\sqrt{(a+x)^2+(b+y)^2+z^2}-z\right) - 2a \\
&- z\,Sign(a-x)\ln\left(|a-x| + \sqrt{(a-x)^2+(b+y)^2+z^2}\right) \\
&- z\,Sign(a+x)\ln\left(|a+x| + \sqrt{(a+x)^2+(b+y)^2+z^2}\right) \\
&+ z\,\ln\sqrt{(b+y)^2+z^2}\,[Sign(a-x)+Sign(a+x)] \\
&+(b+y)\arctan\left((a-x)(b+y)\Big/\left[(b+y)^2+z^2-z\sqrt{(a-x)^2+(b+y)^2+z^2}\right]\right) \\
&+(b+y)\arctan\left((a+x)(b+y)\Big/\left[(b+y)^2+z^2-z\sqrt{(a+x)^2+(b+y)^2+z^2}\right]\right).
\end{aligned} \tag{6.38}$$

For brevity, we designate

$$\begin{aligned}
\mathcal{F}(x,y,z) = x\ln\left(\sqrt{x^2+y^2+z^2}-z\right) + y\arctan\left(\frac{xy}{y^2+z^2-z\sqrt{x^2+y^2+z^2}}\right) \\
- z\,Sign(x)\left[\ln\left(|x|+\sqrt{x^2+y^2+z^2}\right) - \ln\sqrt{y^2+z^2}\right].
\end{aligned} \tag{6.39}$$

Thus the elemental integrals of the log-factors in equation (6.36) may be written as

$$\begin{aligned}
\int_{-a}^{a} \ln\left(\sqrt{(\xi-x)^2+(b+y)^2+(z-L)^2}-(z-L)\right)\,d\xi = \\
\mathcal{F}(a-x,b+y,z-L) - \mathcal{F}(-a-x,b+y,z-L).
\end{aligned} \tag{6.40}$$

Adapting equation (6.40) to match the various log-factors in equation (6.36), the velocity induced by vorticity uniformly distributed throughout a rectangular volume is given by

$$\begin{aligned}
u = \frac{\omega}{4\pi}\,[\mathcal{F}(a-x,b-y,z) - \mathcal{F}(-a-x,b-y,z) \\
-\mathcal{F}(a-x,b+y,z) + \mathcal{F}(-a-x,b+y,z) - \mathcal{F}(a-x,b-y,z-L) \\
+\mathcal{F}(-a-x,b-y,z-L) + \mathcal{F}(a-x,b+y,z-L) - \mathcal{F}(-a-x,b+y,z-L)\,].
\end{aligned} \tag{6.41}$$

The y-component of velocity can now be obtained by group-theoretic arguments. Consider the new $(\bar{x},\bar{y})$ coordinates rotated through 90 degrees from the original (x,y) coordinates; then

$$\bar{x} = -y,\ \bar{y} = x, \text{and}\ \bar{v} = u.$$

Also the lengths of the rectangular volume are inverted, such that

$$\bar{a} = b, \bar{b} = a.$$

Hence if we denote

$$u = f(x, y, z; a, b, L),$$

then

$$v = -f(-y, x, z; b, a, L),$$

where the function $f(x, y, z; a, b, L)$ is given by equation (6.41).

6.5.4 Surface Distributed Vorticity

To provide the box-vortex with a component of axial velocity, surface vorticity oriented orthogonal to the box-vortex axis is formulated. To accomplish this, the vortex rings of the axial-flow formulation will be replaced with finite line-vortex segments around the periphery of the box-vortex surface. Integrating these line-vortex segments over the four vortex surfaces will give the desired result.

The method of solution is similar to the first two integrations performed in the previous section. Starting with a vortex element with $d\vec{\Gamma} = \hat{\jmath}\gamma_\theta d\eta d\zeta$ on the box-vortex $x = a$ surface at point (a, η, ζ) as shown on Figure 6.20, the Biot-Savart law gives nonzero components

$$du_a{}' = \frac{\omega_s d\eta}{4\pi} \frac{d\zeta(z-\zeta)}{[(x-a)^2 + (y-\eta)^2 + (z-\zeta)^2]^{\frac{3}{2}}} \tag{6.42}$$

and

$$dw_a{}' = -\frac{\omega_s d\eta}{4\pi} \frac{d\zeta(z-a)}{[(x-a)^2 + (y-\eta)^2 + (z-\zeta)^2]^{\frac{3}{2}}}. \tag{6.43}$$

We let $R^2 = (x-a)^2 + (y-\eta)^2$ and integrate the two velocity components with respect to ζ. Evaluating over the vortex length L gives the velocity from an axial strip of the vortex segments on the $+a$-face of the vortex as

$$du_a = \frac{\omega_s d\eta}{4\pi} \left[\frac{1}{\sqrt{R^2 + (z-L)^2}} - \frac{1}{\sqrt{R^2 + z^2}} \right] \tag{6.44}$$

and

$$dw_a = -\frac{\omega_s d\eta}{4\pi} \frac{x-a}{R^2} \left[\frac{z}{\sqrt{R^2 + z^2}} - \frac{z-L}{\sqrt{R^2 + (z-L)^2}} \right]. \tag{6.45}$$

Now integrating with respect to η and evaluating over the vortex height from $y = -b$ to b, the total velocity contributed by the vorticity on the box-vortex $+a$-surface over length L is

$$u_a = \frac{\omega_s}{4\pi}\left[\ln\left(\frac{(y-b)+\sqrt{(x-a)^2+(y-b)^2+z^2}}{(y+b)+\sqrt{(x-a)^2+(y+b)^2+z^2}}\right)\right.$$
$$\left.-\ln\left(\frac{(y-b)+\sqrt{(x-a)^2+(y-b)^2+(z-L)^2}}{(y+b)+\sqrt{(x-a)^2+(y+b)^2+(z-L)^2}}\right)\right] \tag{6.46}$$

and

$$w_a = \frac{\omega_s}{4\pi}\left[\arctan\left(\frac{z(y-b)}{(x-a)\sqrt{(x-a)^2+(y-b)^2+z^2}}\right)\right.$$
$$-\arctan\left(\frac{z(y+b)}{(x-a)\sqrt{(x-a)^2+(y+b)^2+z^2}}\right)$$
$$-\arctan\left(\frac{(z-L)(y-b)}{(x-a)\sqrt{(x-a)^2+(y-b)^2+(z-L)^2}}\right)$$
$$\left.+\arctan\left(\frac{(z-L)(y+b)}{(x-a)\sqrt{(x-a)^2+(y+b)^2+(z-L)^2}}\right)\right]. \tag{6.47}$$

The result for the $x = -a$ surface can be found from the same equations by reversing signs on a to account for the change of surface and on each term to account for the opposite sign of vorticity. Therefore if $v_a = f(x-a, z, z-L)$, then $v_{-a} = f(x+a, z-L, z)$.

Following the same procedure on the $y = b$ surface will give the velocity components as

$$v_b = \frac{\omega_s}{4\pi}\left[\ln\left(\frac{(x-a)+\sqrt{(x-a)^2+(y-b)^2+z^2}}{(x+a)+\sqrt{(x+a)^2+(y-b)^2+z^2}}\right)\right.$$
$$\left.-\ln\left(\frac{(x-a)+\sqrt{(x-a)^2+(y-b)^2+(z-L)^2}}{(x+a)+\sqrt{(x+a)^2+(y-b)^2+(z-L)^2}}\right)\right] \tag{6.48}$$

and

$$w_b = \frac{\omega_s}{4\pi}\left[\arctan\left(\frac{z(x-a)}{(y-b)\sqrt{(x-a)^2+(y-b)^2+z^2}}\right)\right.$$

$$
\begin{aligned}
&- \arctan\left(\frac{z(x+a)}{(y-b)\sqrt{(x+a)^2+(y-b)^2+z^2}}\right)\\
&- \arctan\left(\frac{(z-L)(x-a)}{(y-b)\sqrt{(x-a)^2+(y-b)^2+(z-L)^2}}\right)\\
&+ \arctan\left(\frac{(z-L)(x+a)}{(y-b)\sqrt{(x+a)^2+(y-b)^2+(z-L)^2}}\right)\Bigg]. \qquad (6.49)
\end{aligned}
$$

For the $y = -b$ surface, we again substitute. If $v_b = f(y-b, z, z-L)$, then $v_{-b} = f(y+b, z-L, z)$.

6.5.5 Three-Dimensional Box Vortex Results

The box vortex model was developed to accomplish two things: eliminate the unphysical model whereby vorticity can cross into the airframe and to provide a mechanism to model vortex deformation in the final stages of the vortex-body collision. This was accomplished by enclosing all vorticity in a vortex of rectangular cross-section that is allowed to increase in aspect ratio when the cross-section would otherwise overlap the airframe. Results are presented for several variations of this model. In all results, the time step is $\Delta t = 0.00298$, corresponding to $\Delta\psi = 0.25^o$ at a rotor speed of 2100 rpm.

To determine if the first objective could be met by the box-vortex model, pressure traces on the top of the airframe were found using both the helical vortex model of Section 6.3 and the box vortex model of Sections 6.5.3 and 6.5.4. To avoid complicating effects, the case of linear downwash and no axial velocity is considered in this section; the dimensionless circulation of the vortex is $\Gamma = 1.5$ which is somewhat less than the experimental value of 2.24 at 2100 *rpm*. These traces are compared in Figure 6.21. In the first plot (Figure 6.21(a)), the pressure on the top of the airframe for the helical vortex model is shown. The vorticity in this model is distributed between the vortex center and the core radius through the use of the cutoff parameter μ. As the vortex approaches within one core radius, the vorticity overlaps the airframe and a pressure defect is generated downstream of the center of the vortex. This defect is manifest in a very large deviation from the assumed value far downstream of $p = 0$. This defect starts small but increases rapidly: not only does the overlap area increase but also the vorticity in the overlap region increases exponentially with radius in this Lamb vortex. The appearance of this defect reduces the validity of the pressure prediction at all points.

In the second plot (Figure 6.21(b)), the box vortex formulation is applied but the aspect ratio, defined as vortex cross-section width divided by height, is fixed at unity. Now the pressure defect becomes visible only as the boundary of the vortex crosses the airframe. The onset of the defect is later and less gradual because overlap area increases faster for the intersection of a box and cylinder and because the vorticity is uniformly distributed in this model. The final plot (Figure 6.21(c)) shows the pressure trace due to a fully-deformable box vortex. In this case, no vorticity overlap or significant pressure defect is observed.

We may conclude, then, that the box vortex model should substantially improve our pressure prediction, but a different aspect of the model causes some difficulty. The axial vorticity in the model is distributed throughout the vortex, but the azimuthal vorticity is implemented through line vortices at the vortex periphery. This causes a sharp discontinuity in the axial velocity at the edges of the box. Because the vortex segments are curved, the axial velocity induced at a vortex segment by the surrounding segments changes in a discontinuous manner. This results in a discontinuity in the local axial velocity and subsequent oscillation in the core radius of the vortex segments.

For this reason, a hybrid model was introduced to try to improve the pressure prediction of the box vortex model along with the relative axial stability of the helical vortex model. In this model, axial vorticity is distributed over a rectangular cross-section as described in Section 6.5.3 while azimuthal vorticity is distributed using the ringlet model of Section 6.3.3. This vortex is referred to as the "boxlet" vortex. This model gives some pressure defect as the azimuthal vorticity is permitted to cross into the airframe but the effect is reduced significantly because axial vorticity is prevented from crossing the airframe. The axial stability is comparable to that of the helical vortex.

Using this model we have found that the effectiveness of the box vortex formulation in providing a mechanism for the suction peak to dissipate is intimately tied to the magnitude of the axial velocity and the observed pressure defect. A wide range of core axial velocities were studied. Qualitatively, when the axial velocity in the vortex core is low, the vortex will stretch substantially as it approaches the airframe and the core radius decreases substantially at the point closest to the airframe. This narrowing increases the swirl velocity in the vortex which then feeds back to further increase stretching as the vortex moves farther along the airframe. The result is an ever-increasing suction peak on the top of the airframe as shown in

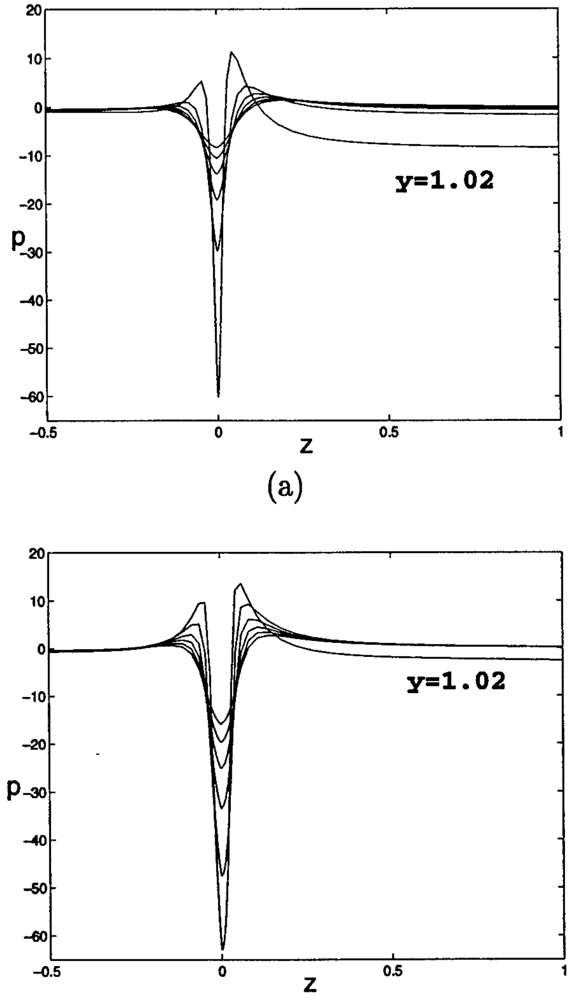

(a)

(b)

Figures 6.21(a,b)

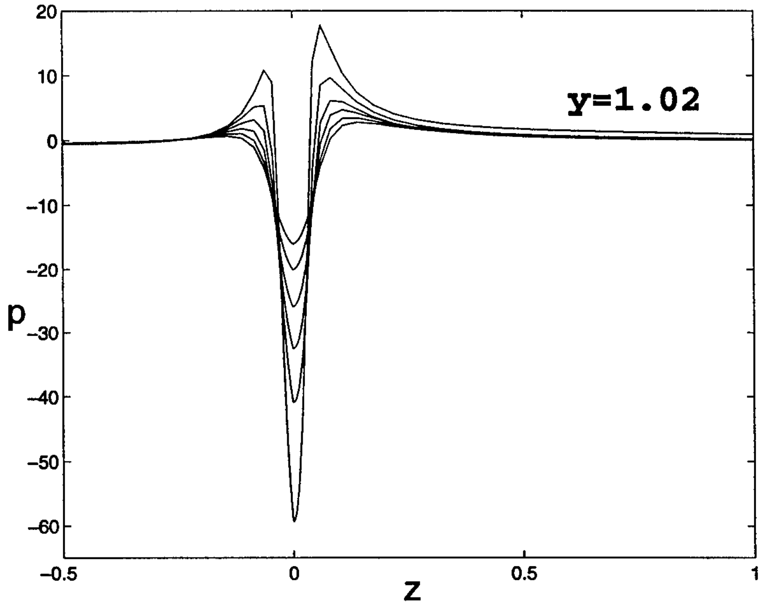

(c)

Figure 6.21: Pressure on the top of the airframe as the vortex approaches within one core radius of the airframe from approximately $y = 1.1$ to $y = 1.02$ in a uniform downwash of 0.557 with no axial velocity. The dimensionless circulation $\Gamma = 1.5$. (a) Helical vortex model; (b) box vortex model with unity aspect ratio; (c) box vortex model with unconstrained aspect ratio.

Figure 6.21(a,b), a prediction not supported by experiment. In some cases we find that the vortex core radius can decrease very quickly as the vortex approaches the airframe; in this case, vorticity does not overlap the airframe until the vortex center crosses the airframe surface. This result negates the advantage of the box vortex model since core deformation can occur only if the vortex overlaps the airframe.

If we now consider the case of high axial velocity in the vortex core, the scenario better matches the experimental observations. As a vortex approaches the airframe, it will begin to stretch along the airframe axis. The core radius begins to narrow, but this process is limited by the effect of axial velocity. As the vortex stretches, the alignment of the vorticity changes to increase the axial vorticity component at the expense of the azimuthal component. The axial velocity therefore decreases and the stagnation of this velocity component works to push the core radius radially outward in a manner described for the 90^o collision of Chapter 5. The net result can range from a reduction in the rate of vortex narrowing to an actual increase in core radius as the vortex approaches the airframe.

As the vortex approaches within a core radius of the airframe, the zero-normal velocity boundary condition on the surface will force momentum from the axial velocity stagnation to be directed predominantly in an azimuthal direction relative to the airframe. This causes an ovaling of the vortex that is approximated by increasing the aspect ratio of the box vortex model. In contrast to the low axial velocity case, the swirl velocity will not increase because core radius does not decrease. Rather, the vorticity will be distributed over a larger portion of the airframe surface and the negative pressure peak associated with the flattened portion of the vortex will dissipate rather than intensify. Note also that redistribution of the vorticity is particularly important here to avoid the pressure defect. A cylindrical vortex will cause severe vorticity overlap if the vortex does not narrow as in the low axial velocity case.

Figures 6.22 and 6.23 demonstrate this situation. The results presented are based on the experimental conditions described in Section 6.4 with the exceptions of the axial velocity value and the use of a dimensionless circulation of 1.5. The boxlet vortex model is used. On Figure 6.22, the axial velocity is 5 $\frac{m}{sec}$, perhaps one-fifth of the estimated experimental value. The vortex core radius is predicted to decrease sharply as the vortex approaches the airframe as shown in Figure 6.22(a). Although the distance between the vortex and the airframe decreases, the box vortex cross-section also decreases

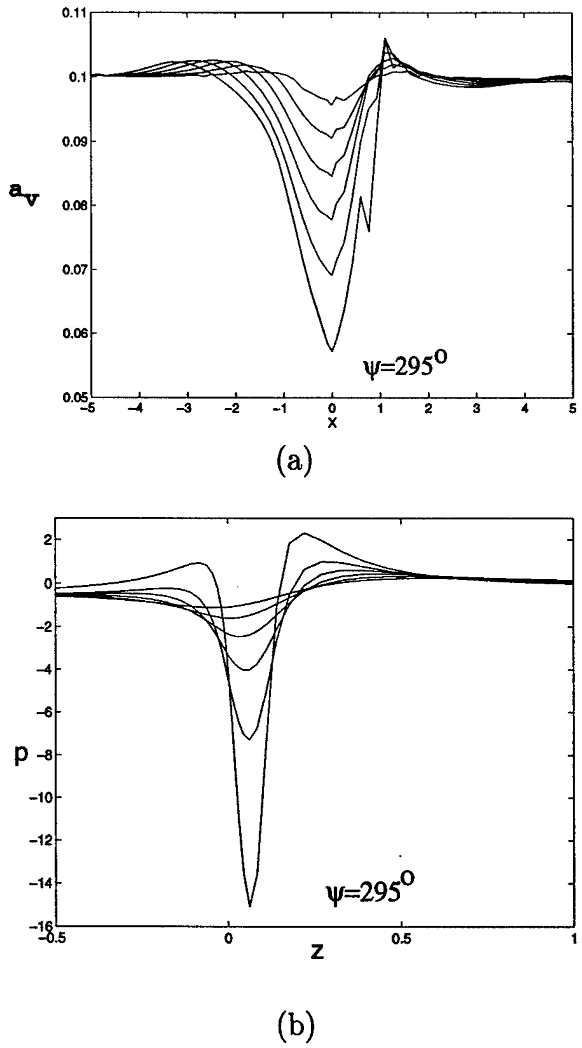

Figure 6.22: Vortex behavior from $\psi = 195^o$ to $\psi = 295^o$ with low core axial velocity of approximately $5\frac{m}{sec}$. The downwash velocity is 0.557 and the dimensionless circulation $\Gamma = 1.5$. (a) vortex segment radius; (b) pressure on the top of the airframe.

so the aspect ratio remains unchanged. The pressure predicted on the top of the airframe shows a suction peak that deepens at an ever-increasing rate. As we would expect, pressure defect is not observed in this case and the vortex aspect ratio remains unity throughout.

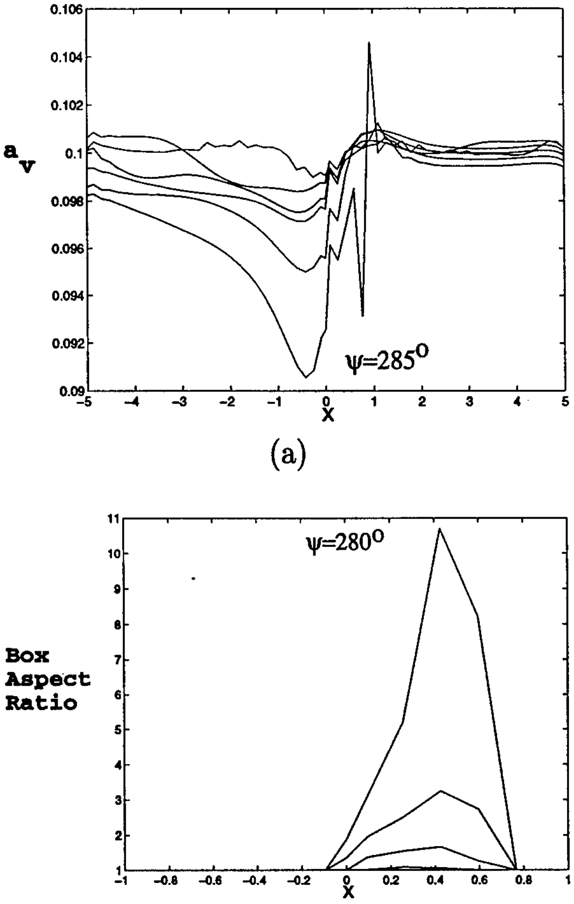

(a)

(b)

Figures 6.23(a,b)

When the axial velocity is increased to 30 $\frac{m}{sec}$, the predictions change dramatically. As on Figure 6.23, the core radius decreases by only a few percent as axial momentum is stagnated. As a result the box vortex aspect

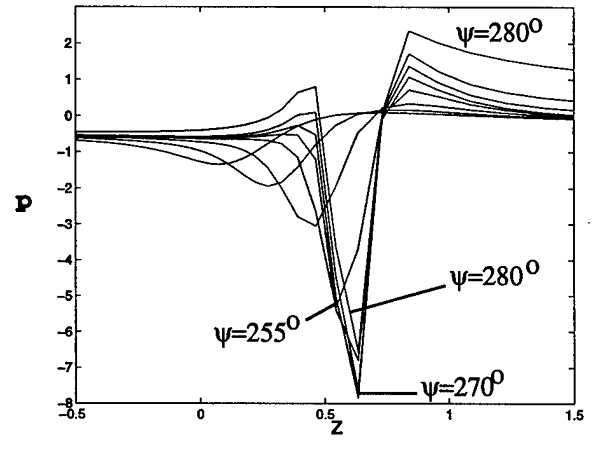

(c)

Figure 6.23: Vortex behavior from $\psi = 185^o$ to 285^o with high core axial velocity of approximately $30\frac{m}{sec}$. The downwash velocity is 0.557 and the dimensionless circulation $\Gamma = 1.5$. (a) Vortex segment radius from $\psi = 195^o$ to $\psi = 285^o$ in 20^o increments; (b) vortex segment aspect ratio from $\psi = 265^o$ to $\psi = 280^o$ in 5^o increments; (c) pressure on the top of the airframe from $\psi = 195^o$ to $\psi = 255^o$ in 20^o increments with additional detail from $\psi = 265^o$ to $\psi = 280^o$ in 5^o increments to show the decrease in the amplitude of the suction peak is pressure that begins at $\psi = 275^o$. The amplitude is ~ -6.5 after being almost -8 (the maximum) at $\psi = 270^o$.

ratio becomes very large upon close approach to the surface. The pressure trace shows that the suction peak is not only decreased by a factor of 2, but the deepening of the peak slows and even reverses as the vortex approaches the airframe. The actual reversal is somewhat ambiguous as some pressure defect shows up just as the peak is predicted to dissipate, but the trend is clear. The pressure defect seen here was initially thought to be the result of azimuthal vorticity overlap from the ringlet model, but later results suggest this is only partially true. In all of these cases, the calculation is terminated when the vortex centerline is predicted to violate the airframe surface.

Despite the improvements noted in the test cases, using the boxlet model to directly predict the experimental observations gives mixed results. Comparing the pressure prediction for the helical model from Section 6.4 with the boxlet vortex model as depicted on Figure 6.24 demonstrates little improvement in the prediction from rotor phase angles of $\psi = 190^o$ to $\psi = 240^o$. The notable difference occurs at later rotor azimuths where the boxlet model predicts pressure with less but not zero pressure defect. The vortex trajectory predicted by the boxlet vortex model is virtually identical to that predicted using the helical vortex model.

During this work, it was noted that although the intent in Section 6.4 was to set the vortex axial velocity to $25\frac{m}{sec}$ in the helical model, the axial velocity in that case was later found to be only $15\frac{m}{sec}$. To ascertain the effect of increasing axial velocity, the boxlet model was applied to predict the experimental data if an axial velocity of $30\frac{m}{sec}$ and dimensionless circulation of 2.24 were assumed. This result, depicted on Figure 6.25, shows the effect of axial velocity when compared to Figure 6.24b. We can see that increasing axial velocity reduces the peak pressure by one third. The time to peak pressure decreases significantly because the vortex radius is supported by the increased axial velocity and core deformation begins 10^o earlier.

Another parameter that has been studied is vortex circulation. In the experiment, the tip vortex is generated by a real rotor in forward flight, so the vortex circulation changes significantly as a function of phase angle. Up to now we have applied a circulation of 2.24 to predict the experimental results. This value is representative of the measured circulation at the onset of the experimental vortex collision. If circulation is averaged over the time frame of the collision this value drops to around 1.5. The effect of increasing circulation can be seen by comparing Figure 6.25 to Figure 6.23c. Increasing the circulation increases the peak pressure by a factor of 2 as we might expect. The vortex is also transported at higher speed when circulation is increased,

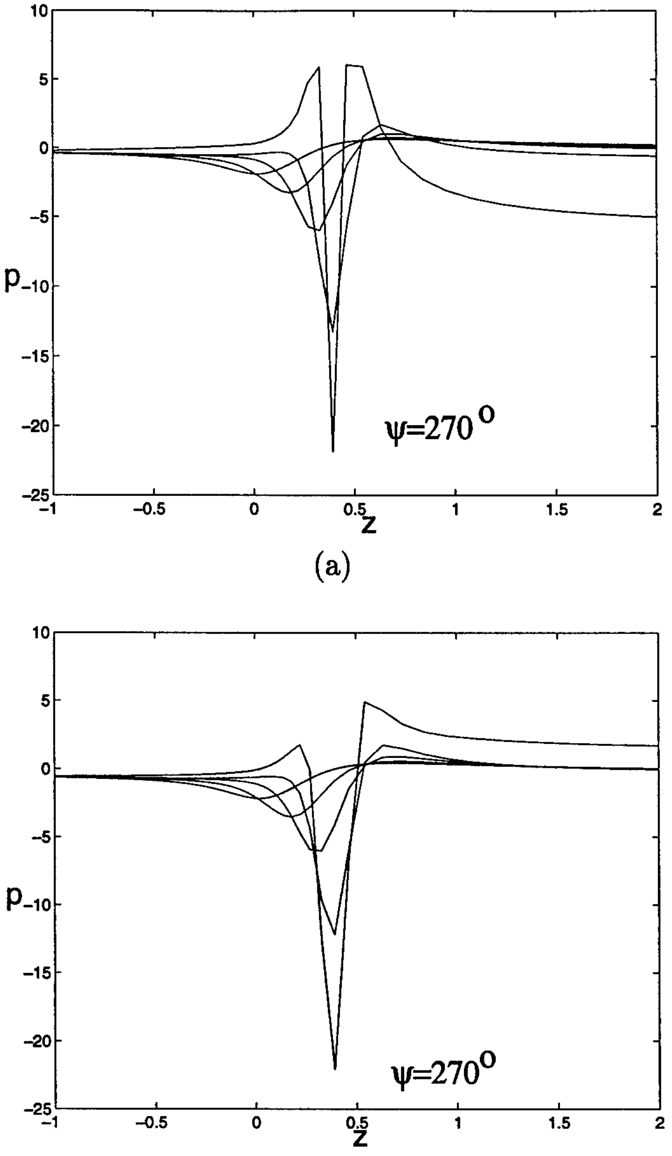

(b)

Figure 6.24: Comparison of pressure predictions from $\psi = 190^o$ to $\psi = 270^o$ using the helical and boxlet vortex models. The axial velocity is about 15 m/s and dimensionless circulation is $\Gamma = 2.24$ in both cases. (a) Helical vortex model (as in Section 6.4); (b) boxlet vortex model.

so the peak pressure occurs 15^o earlier.

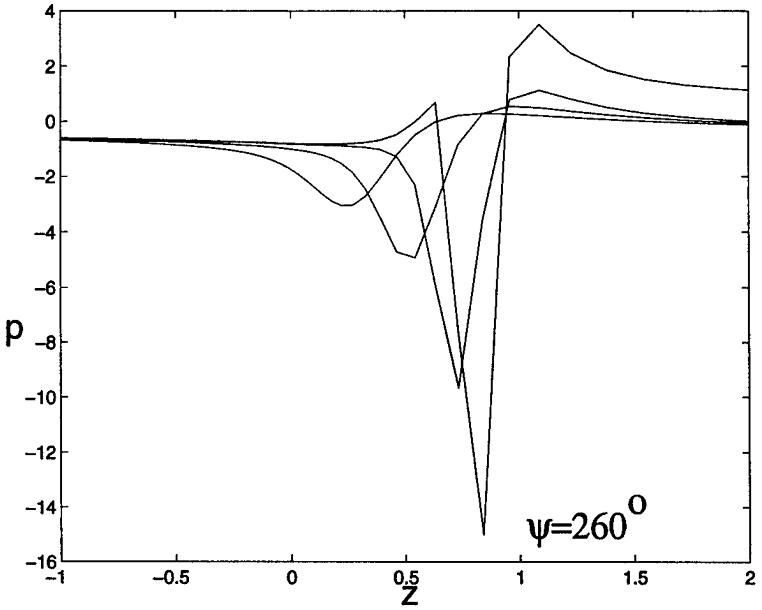

Figure 6.25: Pressure prediction using the boxlet model from $\psi = 200^o$ to $\psi = 260^o$. The core axial velocity is 30 $\frac{m}{sec}$ and the dimensionless circulation is $\Gamma = 2.24$.

The final study using the boxlet model addresses rotor downwash velocity. We have observed that the boxlet model predicts pressure reversal as seen in the experiments. The magnitude of the predicted pressure peak is very near the experimental value when circulation is 1.5 as in Figure 6.23c, but the peak occurs about 50^o late in rotor phase angle. Increased circulation causes the peak to occur earlier in time, but the pressure becomes substantially higher than that observed in the experiments. The numerical model uses a linearly sheared rotor downwash velocity determined from the experimental vortex trajectory at the limit of the measurements about five airframe radii from the airframe surface by Affes *et al.* (1993b). This velocity has not been measured directly and the magnitude and distribution is not well known. Sensitivity to this parameter was tested by simply increasing the mean velocity from 0.557 to 0.757. This change had little effect on the magnitude of the pressure predictions, so this result is not shown here, but the vortex transport velocity and therefore time to collision was accelerated by about 15^o in rotor phase angle.

Finally, to remove the vorticity overlap caused by the radially distributed vorticity of the ringlet axial flow model while avoiding the instability of the original box vortex model, the vortex formulation was modified to distribute the azimuthal vorticity throughout the box vortex volume rather than representing it on the surface as in Section 6.5.4. The resulting expression for axial velocity is composed of variations of the F-function given in equation (6.39). This model change causes significant flattening of the axial velocity distribution compared to the ringlet distribution, so the actual advance angle used to define the strength of the azimuthal vorticity must be increased significantly to achieve the same axial velocity prediction at the vortex centerline. Vortex segment stability is improved greatly because this model gives a continuous axial velocity as a function of radius unlike the original box vortex model.

The pressure trace on the top of the airframe with an axial velocity of $30\frac{m}{sec}$ and Γ of 1.5 is depicted on Figure 6.26. The differences between this result and the previous comparable result of Figure 6.23c are a 12% lower pressure peak that occurs 5^o earlier in time and a much more pronounced pressure peak dissipation. Unfortunately some pressure defect is still apparent. This is now thought to be caused by the fact that the box vortex is formulated to deform along the *global* x-axis rather than orthogonal to the surface of the airframe where vortex-surface contact occurs. The current model may allow vorticity overlap as the corner of the box can intrude on airframe space when the vortex closely approaches the airframe side rather than the top.

This analysis shows substantial improvement in predicting experimental vortex behavior compared to previous models. It is clear that the magnitude and timing of the pressures observed in the experiments depend on the axial vortex velocity, the vortex circulation and the downwash velocity from the rotor. It would appear that a combination of these values, still within experimental uncertainty, could be found that would reasonably predict the measured pressures. That exercise has not been performed as we believe the current vortex-surface interaction model demonstrates all of the physics necessary to predict the experimental data given appropriate initial conditions.

Several changes could allow improved prediction of the experimental data. Refinement of experimental parameters used as input to the model could be useful. If available, spatially-varying circulation and axial velocity initial conditions could be applied in the current model with little revision. Also, the linear shear representation of rotor downwash velocity is simplistic considering the level of detail available from the rest of the model. The only

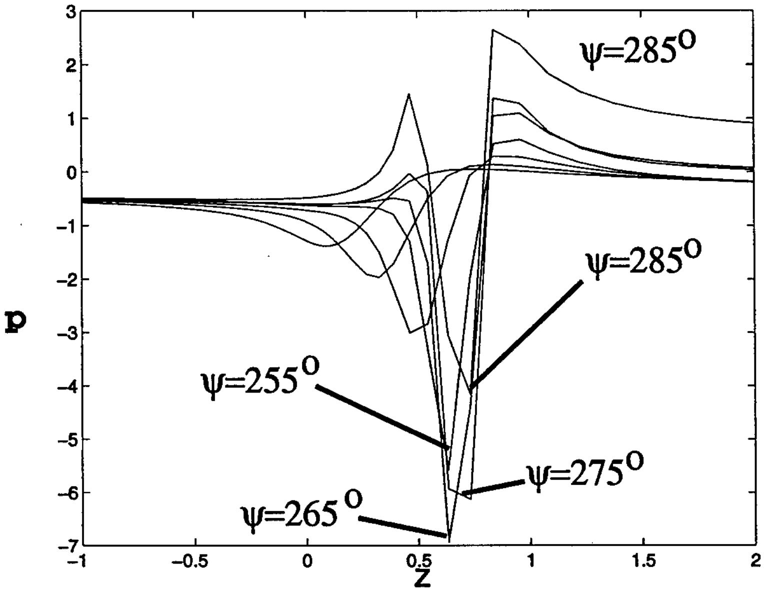

Figure 6.26: Pressure prediction using the box vortex model with fully-distributed vorticity from $\psi = 195^o$ to $\psi = 255^o$ in increments of 20^o and $\psi = 265^o$ to $\psi = 285^o$ in increments of 10^o. The core axial velocity is $30\frac{m}{sec}$ and the dimensionless circulation is $\Gamma = 1.5$.

revision recommended for the box vortex model is the tangential deformation modification just discussed. The principal remaining limitation on the current model is the inability of the panel representation of the airframe to enforce the zero-normal velocity boundary condition on the airframe surface as the strong vortex approaches. Better panel methods, such as interpolation methods discussed by Terzi and Chiu (1997) or adaptive panel gridding would allow study of the collision to extend further in time.

6.6 Beyond The Initial Collision: Passage of the Vortex Down the Sides of the Airframe

6.6.1 Introduction

In this section we discuss the nature of the flow locally around the tip-vortex after it has collided at the top of the airframe and the vortex proceeds to convect down the sides of the airframe. In particular, we discuss the case where the collision is symmetric with respect to the $y-$axis of Figure 1.3; note that for symmetry to hold, the initial vortex position must be symmetric and the axial flow in the vortex must vanish. Next we discuss the situation where the flow is non-symmetric and the axial flow in the core of the vortex is significant. Finally the reconnection process at the bottom of the airframe is discussed.

6.6.2 The Symmetrical Collision: Tip-Vortex, Airframe Interaction

In the symmetric case discussed here we assume that the vortex is initially straight and parallel to the $x-$axis of Figure 1.3. Further to preserve symmetry, the axial flow in the vortex is assumed to vanish.

As the vortex approaches the surface of the cylinder, the influence of the image becomes stronger and the vortex elongates into a tongue, approaching the shape of a horse-shoe. This tongue continually lengthens and lies closer and closer to the cylinder, with its side-arms becoming nearly parallel to the generators of the cylinder. During this period, the vortex core radius decreases because it is being stretched by the mean flow. In the limit, the vortex core radius approaches zero and the axial vorticity in the vortex core thus must approach infinity so the circulation remains constant. Clearly, in this situation, vortex fluid can never merge with the fluid in the boundary layer because the vorticity in the vortex is much larger. Moreover, the pressure on the top of the airframe will continue to grow and the suction peak grow narrow as the core radius decreases. Thus, the influence of the vortex on the top of the airframe will allways be significant, counter to the experimental results. Consequently, either axial flow in the vortex must be included or the vortex cross-section must be permitted to deform.

If the cross-section deforms, analysis (see the next section) indicates that it must flatten out, at first into an oval shape, and later in the extreme stage of flattening, into a near rectangular cross-section (wrapping around the cylinder, of course). This phase of the motion is much like the asymmetric case discussed in the next section (see, for example, Figure 6.27). Hence the vortex cross-section thins and elongates in the direction of the cylinder axis. In the limit, the motion of the base of the tongue will be independent of the main part of the vortex, responding only to the essentially infinitely long horse-shoe vortex elements and their images. This discussion suggests that the influence of the head region of the vortex on the rest of the vortex can be neglected and computations of the subsequent vortex motion may consider the vortex to end at the surface of the airframe.

6.6.3 The Oblique Collision: Tip-Vortex, Airframe Interaction

The discussion of the vortex core deformation is illustrated in detail for the oblique(i.e. non-symmetric) collision on Figure 6.27 which is a sketch of the top view of the interaction just after the collision on the top of the airframe has occurred. To accomodate the airframe and because the vortex centerline becomes approximately parallel to the airframe surface locally near the top, the vortex has abruptly flattened to a sheet of width of the order of the airframe radius and height $O(Re^{-1/2})$. This occurs when the vortex is within one core radius from the airframe. Here the axial velocity is the component parallel to the wall and so at this stage must reduce to $O(1)$ in order to preserve the $O(Re^{-1/2})$ mass flux through the vortex. The swirl and radial velocities must abruptly decrease locally to accomodate the presence of the surface. Note that the swirl now becomes the velocity locally normal to the surface and the radial velocity within the vortex becomes aligned with the streamwise direction. To fit within the boundary layer approximation the swirl must be $O(Re^{-1/2})$. When this occurs, vortex fluid is indistinguishable from boundary layer fluid.

In order to preserve the magnitude of the circulation, the cross-sectional area of the vortex must increase to $O(Re^{-1/2})$ from $O(Re^{-1})$. This is seen from the definition of the circulation in the form

$$\Gamma = \int\int \omega dA$$

where ω is the axial component of vorticity within the vortex. To fit within the boundary layer approximation $\omega = O(Re^{1/2})$ and so $A = O(Re^{-1/2})$ so that $\Gamma = O(1)$ as it was before the interaction. Locally, the pressure loading on the airframe is now small since the large suction peak caused by the original vortex is gone.

As time goes on, the region where the vortex flattens has increased substantially in size as the vortex travels down the airframe. This situation is depicted on Figure 6.28. Here the region where the vortex flattens into a sheet spans the entire width of the airframe as more and more vortex fluid "merges" with the boundary layer. Local bulging and thinning of the vortex is still seen during this period on the sides of the airframe.

As the vortex travels down the airframe, the axial velocity in the tip-vortex on the RBS is still high since it is attached to the rotor blade. A region of strong rotation devoid of seed particle deficit is seen on the RBS in the experiment, presumably due to the core tightening and drawing fluid from the boundary layer. On the ABS however, once the axial velocity stagnates the filament is not longer atteched to the rotor-blade, thus the effect of stagnation due to the axial velocity persists for only a short period of time. The local pressure distribution on the retreating side where the vortex thins has a strong suction peak whereas on the advancing side the pressure loading is benign.

Eventually, on the RBS, the flow is expected to approach a steady balance whereby boundary layer fluid is ingested into the vortex preserving its structure near the airframe and limiting the core radius decrease seen in the current computations. The phenomenon of viscous limiting of vortex core thinning is suggested in studies by Burggraf and Stewartson (1971), and by Belcher, *et al.* (1972), who investigated the boundary layer induced by a potential vortex and a generalized vortex oriented normal to a coaxial disc

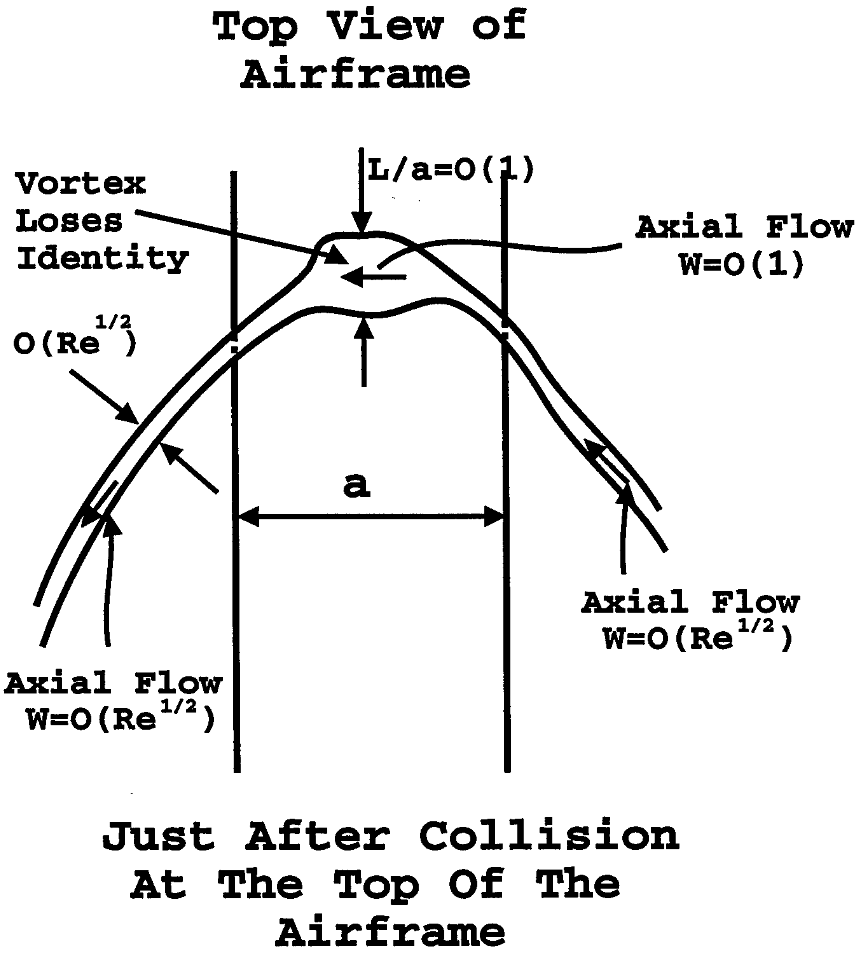

Figure 6.27: Top view of the interaction just after collision has occurred on the top of the airframe. *a* is the radius of the airframe.

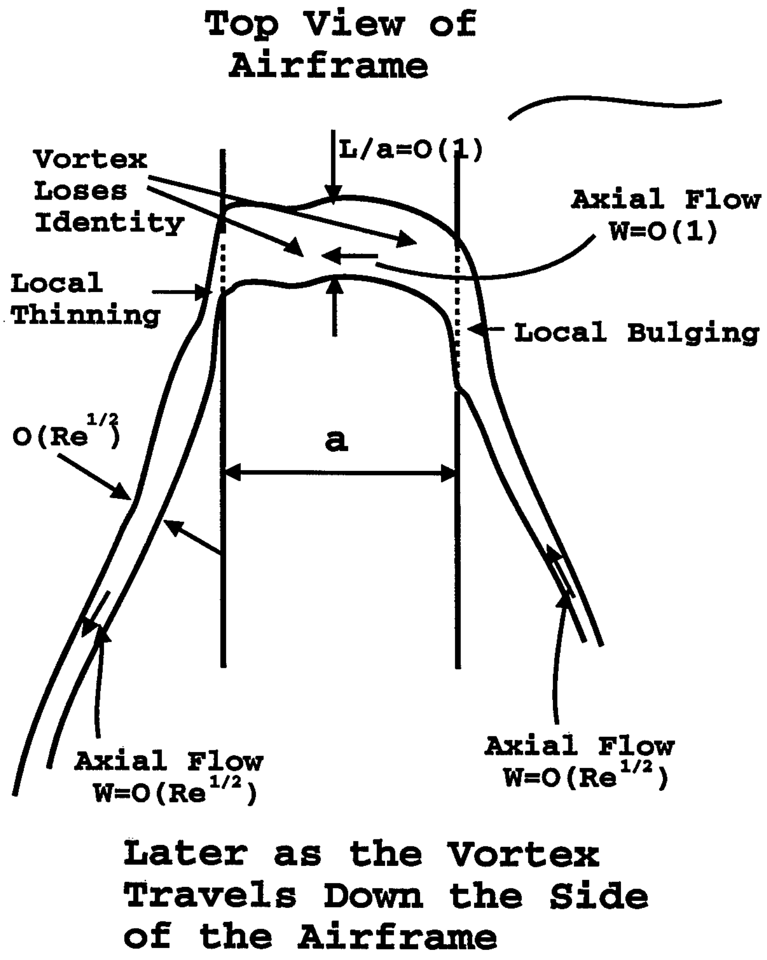

Figure 6.28: Top view of the interaction long after collision has occurred and the vortex is passing down the sides of the airframe.

respectively. These studies imply that the radial inflow in the boundary layer induced by the vortex will erupt from the wall at $r = 0$, continually feeding the core, and thereby halt the focusing of the swirl velocity seen in the present results. In this scenario, the suction peak will level off at a fixed value and persist even as the vortex approaches the trailing edge of the airframe. It is likely that the local flow is steady and so the vortex can be viewed as ending at the airframe with the magnitude of the axial flow determined by continuity between the boundary layer and the flow in the vortex far from the airframe. Evidence for the steady nature of the pressure distribution is given by Kim (1993) who shows carpet plots of the pressure distribution around the airframe. On the retreating side of the airframe, the plots show a suction peak of substantially constant amplitude as the vortex has travelled a distance over halfway down the airframe.

On the advancing blade side, the situation is expected to be similar to that seen for the 90^o collision in Figure 5.23. On this side of the airframe the vortex can be assumed to be pinned at the airframe boundary. Since the vortex is no longer fed by fluid from the rotor blade from which it came, the axial flow within the vortex can be set equal to zero. On this side of the airframe then, the vortex can be modeled by a classical line vortex. Moreover, there is evidence that the flow also approaches a steady state as seen in Figure 5.11 and in the carpet plots of Kim (1993). The fact that on both sides of the airframe the flow appears to be locally steady greatly simplifies the modelling of the process.

6.6.4 Reconnection

As can be seen in the previous two figures the tip-vortex successively loses its head as it passes down the airframe. Moreover, since the vortex cannot end in the fluid the tip-vortex tube must end at the airframe boundary within the boundary layer. As the vortex travels down the sides of the airframe, it eventually will be exposed to a separated flow field around $\phi = 100^o$, where ϕ measures angle around the airframe from the top. The separated shear layer in the present configuration has the primary vorticity in the streamwise direction which is approximately perpendicular to the primary vorticity component in the tip-vortex. Near the bottom of the airframe, the ends of the vortex get progressively closer together. There will be very little interaction with the locally separated flow since the largest vorticity components in the two flows are approximately at right angles to each other. At the bottom of the airframe, since the vortex tube cannot end in the fluid, the vortex ends must merge locally and reconnect. This must occur since the vorticity distributions along the axis of the vortex are of the same order of magnitude. This must be true even if the two ends of the vortex reach the bottom of the airframe at different times.

Chapter 7

Summary

In this work, we have defined and analyzed the collision of a rotor tip vortex with a simplified helicopter airframe. The distinguishing feature of this problem, which falls within the general class of vortex-surface interactions is that the vortex-core flow is modified by the presence of the airframe. This is in contrast to the vast majority of the work on vortex-surface interactions in which the problem is essentially two-dimensional, or the vortex trajectory is substantially parallel to the body surface. The primary conclusion of this work is that the collision process may be described to a first approximation using inviscid flow theory. This is an important conclusion which has significant implications for future computations of rotor wakes.

Specifically, we have considered the impingement of a tip-vortex shed from a rotary wing on a cylindrical airframe. Tip-vortices shed from wings are known to possess a significant velocity component directed along their axes (Batchelor 1964) and we have indicated how this component has a major effect on the interaction of the vortex with a downstream body. The primary objective of this work has been to describe the interaction when the vortex "collides" directly with the airframe. The pressure field caused by the collision has also been described. In the present work we have considered the case where the scale of the vortex is much smaller than the body scale although this is not essential.

The primary results and major accomplishments of this work are

- The dominant physics of the collision process may be described by inviscid flow theory because the vorticity associated with the vortex is much larger than that associated with the surrounding fluid which includes the boundary layer.

- The collision is induced in large part by the presence of a significant velocity component oriented along the vortex centerline and directed back toward the blade tip at which the vortex is formed.
- Experiments indicate that this "axial flow" component can exceed the local swirl velocity component.
- The presence of axial flow causes the vortex core to bulge on the advancing side and to thin on the retreating side of the airframe. This phenomenon has been seen in the experiments and is predicted in the computations.
- The presence of axial flow along with entrainment of boundary layer fluid is responsible for the persistence of a suction peak on the retreating side of the airframe seen in previous experiments and as predicted in the analysis and computations.
- The experiments indicate and the analysis and computations also predict that the suction peak on the advancing side of the airframe is reduced substantially in a very short period of time, due primarily to the stagnation of the axial velocity in the core of the vortex.
- Just prior to the completion of the collision process, the vortex core flattens enabling the vorticity level to be reduced to the level of the surrounding boundary layer.
- The final stages of the collision may be modeled using a "box" vortex which allows the suction peak to decrease as seen in the experiments.

During the course of this work a new model for the tip-vortex which includes the presence of axial flow has been developed. This model views the vortex as a superposition of a set of axially-oriented line vortices along a cylinder simulating the finite-radius core of the vortex (the vortex cylinder) and vortex rings with major radius coinciding with the radius of the vortex cylinder. The vortex rings induce axial flow along the centerline of the vortex automatically. In addition, to model the flattening process and to prevent vorticity from crossing the airframe boundary, the tip-vortex has been modeled as a "box" having one side parallel to the airframe boundary.

The current problem is approached from a fundamental point of view with targeted computations supported by appropriately directed experiments. A modular approach to the problem has been taken because as noted in Chapter 1, the present computational environment does not support an approach in which the Navier-Stokes equations can be solved accurately over the entire domain. This is because the small length and time scales which naturally arise cannot be resolved.

At this point it is useful to summarize the picture of the vortex-surface collision based on the results described in the body of this report. As the tip-vortex approaches the airframe, a suction peak develops on and near the top of the airframe which grows in time as the vortex approaches. As long as the vortex is more than one vortex-core radius from the airframe, a model for the structure of the vortex based on the Biot-Savart Law with a classical model for the vortex core flow is sufficient to describe with good accuracy the trajectory of the vortex (Figure 6.12). At this point the dynamics of the core flow become important and three other factors must be incorporated.

First, the core radius must be permitted to vary because the vortex is exposed to a straining field due to the presence of the airframe. In Sections 6.2-6.4 we have assumed that the core remains circular and the variation of the core is calculated based on volume conservation. The variation of the vortex core does not affect the trajectory of the vortex substantially, but it does affect the pressure distribution on the airframe. Second, upon interaction with the surface, the axial velocity undergoes stagnation on the advancing side of the rotor and suction on the retreating side. After the vortex collides at the top of the airframe, a segment of the vortex is disconnected from the rotor. Indications gleaned from the experiments are that the disconnected segment(on the retreating side) survives as a strong vortex at least until the ends reach below the airframe in this configuration. This is supported by the theory described in Chapters 5 and 6. Third, the vortex core begins to change shape and elongate in the primary flow direction as shown on Figure 4.17. This, along with the redistribution of vorticity described in Chapter 5 causes the suction peak to decrease substantially in a time frame very close to $\psi = 12^o$ which is the time scale for decay of the suction peak for an advance ratio of $\mu = 0.1$ and rotor speed $2100rpm$ seen in the experiments. As the vortex proceeds farther down the airframe, the suction peak is no longer present on the advancing side of the airframe since the axial velocity directed toward the surface opposes the entrainment of boundary layer fluid and a relatively low speed flow region persists indefinitely.

On the other hand, because the vortex core radius decreases on the retreating side (the axial flow in the vortex is directed away from the airframe), the suction peak focuses eventually reaching a maximum value which is limited by entrainment of fluid from the boundary layer. This is clearly shown in the experimental results depicted on Figure 1.4(b). The phenomenon of viscous limiting of vortex core thinning is suggested in studies by Burggraf and Stewartson (1971), and by Belcher, *et al.* (1972), who investigated the boundary layer induced by a potential vortex and a generalized vortex oriented normal to a coaxial disc respectively. These studies showed that the radial inflow in the boundary layer induced by the vortex will erupt from the wall at $r = 0$, continually feeding the core, and thereby halt the focusing of the swirl velocity seen in the present results. It is important to note that these three aspects of the vortex-surface collision process are not normally included in rotor wake models.

As the tip-vortex approaches the bottom of the airframe, it appear to end in the disturbed flow in the wake of the cylinder. Under the advancing -blade side, the axial flow drives the region of rotation across the vertical plane of geometric symmetry. Under the retreating blade side, the suction trace on the surface decreases as the vortex sinks below the horizontal diameter of the cylinder. The wake of the cylinder rolls up into a quasi-steady Foppl-type structure, skewed towards the retreating blade side. The tip vortex loses definition in the region between this rolled-up structure and the undisturbed portion of the vortex segment, which moves tangentially away from the airframe.

We have mentioned that the critical features of the collision process may be described by inviscid flow theory. This is indicated in Chapter 3 where we have shown that to leading order the effect of the boundary layer flow on the collision process is negligible provided that the main vortex is sufficiently strong. Thus it is shown in the summary of Chapter 3 that while the velocities in the erupting part of the boundary layer are large on the boundary layer scale, they are still small compared to the maximum velocity in the vortex core and thus the mass flux in the erupting region is small compared to that in the vortex core. For this reason we expect that the dominant aspects of the collision process may be described by inviscid (but rotational) flow theory. The present calculations assume that the dimensionless circulation $\Gamma = O(1)$, which means that the dimensional circulation $\Gamma^* \sim U_\infty L$ where U_∞ and L are the appropriate velocity and length scales. Thus the collision of weaker vortices with a solid boundary may be significantly affected by the eruption of the boundary layer. As indicated in other portions of this report, the tip-vortex shed from a rotor blade is a very strong vortex. This result, that the collision process is dominated by inviscid processes for a sufficiently strong vortex makes the computation of such collision flows much simpler since it implies that the Navier Stokes equations need not be solved.

Several issues concerning tip-vortex surface interaction with an airframe should be clarified by the current work. First, in the present configuration, the vortex collidies with the airframe and the vorticity originally in the vortex core is redistributed outward. Concurrently, the local pressure load is reduced rapidly within milliseconds. On the other hand, Bagai and Leishman (1992) report considerable stretching of the vortex as it slides along the airframe. During this time it undergoes continued stretching with the vortex core apparently continuing to decrease in size. This must lead to the increase of axial vorticity within the vortex because circulation must be conserved. The suction peak continues to grow until the vortex reraches the trailing edge of the airframe. The difference in the two scenarios, as pointed out by Kim and Komerath (1995) is likely due to the fact that relative to the airframe, the vortex in the current work has clockwise rotation when viewed from the side and the Bagai and Leishman (1992) work has a counter-clockwise rotation. This allows the tip-vortex to slide along the airframe on the top while bending around the sides. Quite distinct from this scenario, it has been shown by Soell (1994) that vortices of smaller strength are more likely to wrap around the cylinder, whereas stronger vortices collide.

In addition, the methods employed by Lorber and Egolf (1990) to avoid the complexities of the collision process, namely requiring the tip-vortex to remain a fixed distance above the airframe, will likely to lead to over-prediction of the actual loads because destruction of the vortex core is not incorporated into the analysis. On the other hand, they also suggested setting the circulation locally around the collision point equal to zero, forshadowing the collision process. This procedure yields considerably different results for the fuselage lift than for the fixed offset. While their work was the first to address the basic computational problem of what to do when the tip-vortex approaches to within a core radius of the airframe, their results depend the value of the fixed offset distance and they cannot resolve the fine time-scale behavior of the suction peak when compared with experiments(Brand *et al.* 1989). Finally, methods which permit part of the vortex core to overlap the airframe inevitably lead to considerable numerical error as pointed out earlier in Section 6.5.5.

7.1 Application to Blade-Vortex Interactions

It is well-known that blade-vortex interactions (BVI) are a serious problem in rotorcraft from an acoustics point of view. The fluid dynamics problem is extremely complicated involving 3D and unsteady interactions between the tip-vortex shed from a rotor blade and the following blade(s). The interaction is particularly acute when the vortex passes very close to the blade or cuts directly into a blade; in this case, the axial flow in the vortex has a significant effect on the interaction as well. Moreover, a number of interactions may occur in a relatively short period of time as measured by rotor-phase angle. When the vortex is very close to the surface, a similar picture of the vortex surface collision process emerges.

It is generally acknowledged that three types of interactions between the rotor blade and the tip vortex are most common. These interactions are

- almost parallel interactions(Figure 7.1(a));
- almost perpendicular interactions(Figure 7.1(b));
- direct collisions in which the core of the vortex is locally destroyed (Lee *et al.* 1995; Figure 7.1(c)) .

The direct collision case is similar to that described here. and it has been noted in the literature both explicitly (Hassan *et al.* 19) and implicitly by use of a standard rotor design code which uses an inviscid-based approach to calculate the wake (Burley and Tadghighi 19) that the problem seems to be inviscid in character.

Moreover, BVI calculations are generally made with a coupling of a CFD or some other rotor wake code to a comprehensive rotor design code in which the trim conditions and aeroelastic properties of the rotor blades are prescribed. While it is generally acknowledged that BVI is a local event, a comprehensive rotor design code requires resolution of the entire rotor wake. This requires that a single aerodynamic module accurately represent in both space and time, the generation of the tip-vortex, its motion, its interaction with one or more blades, and interactions with other tip-vortices and the inboard sheet. Clearly, because of the complexity of the rotor wake, these requirements are overly optimistic and it is perhaps not surprising that comprehensive aerodynamic modules miss many of the critical features of BVI.

The situation is illustrated by a simple dimensional analysis. A major limitation in the calculation of the flow field leading to the prediction of the

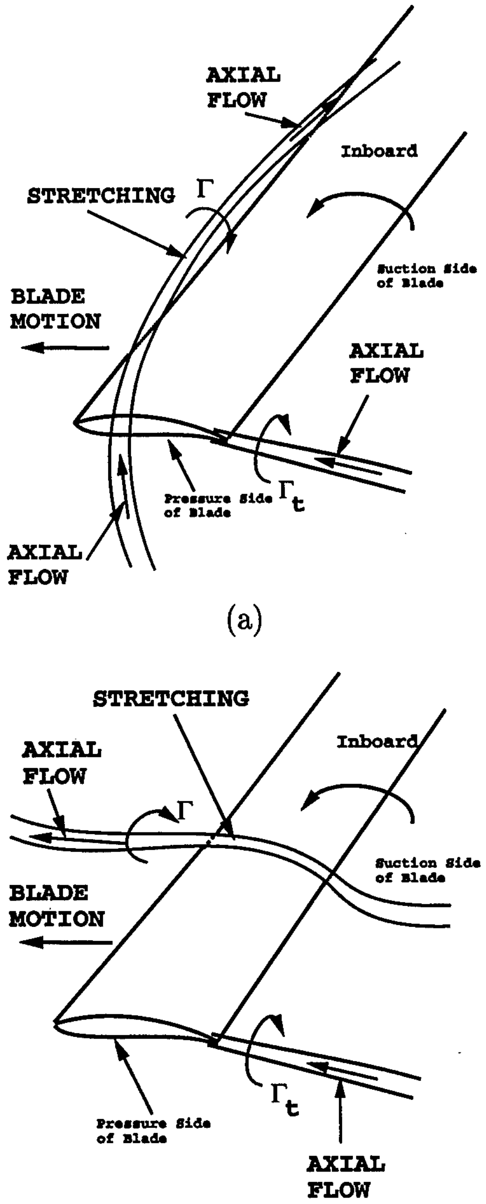

(a)

(b)

Figure 7.1(a,b)

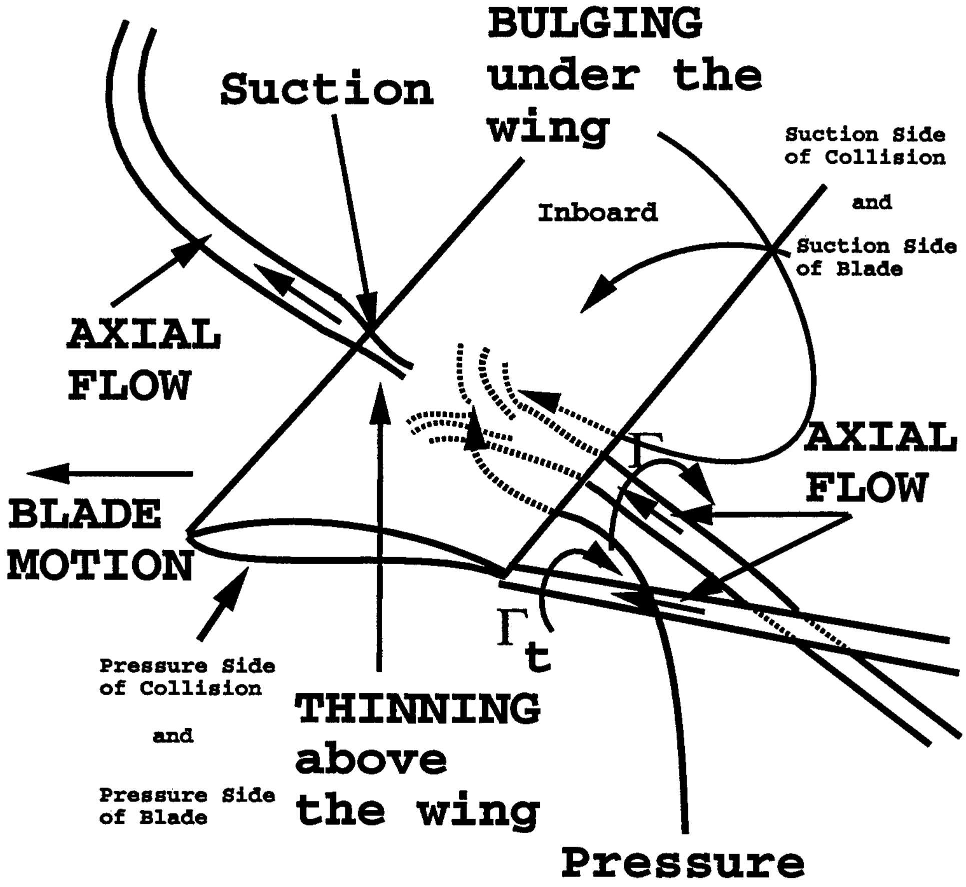

(c)

Figure 7.1: Sketch of the most common BVI events. (a) Almost parallel interactions. (b) Almost perpendicular interactions; and (c) oblique collision. A sketch of the tip-vortex shed from the interacting blade is also shown.

blade pressure distribution using a rotor design code is that the minimum time step which can be resolved is 10^o in rotor phase angle. Consider the almost-parallel situation and suppose the rotor speed is 1000rpm, and the advance ratio is 0.15. At room temperature this corresponds to a tip Mach number $M \sim 0.6$ for a rotor radius of 2m and a forward flight speed of about 31 $\frac{m}{sec}$. The time scale of passage of the vortex over or under a blade will vary over the rotor span but near the tip on the advancing side, the time scale for passage past a blade having a chord of about $c = 120mm$ is

$$t \sim \frac{c}{W} \sim \frac{.120m}{180\frac{m}{sec}} = 6.7 \times 10^{-4} sec$$

On the other hand, at this rotational speed, $\psi = 10^o = 5 \times 10^{-4} sec$ and so this rotor phase increment is of the same order as the overall time scale of the interaction. Thus it is not surprising that an analysis of the BVI phenomena which are modeled using classical rotor design codes can likely miss many of the short-time scale phenomena which occur during BVI events. The situation is even more acute if the local length scale of the flow which is the vortex core radius and not the chord of the airfoil is used in the scaling. Indeed in order to match experimental data, Hassan *et al.*(1992) had to use a much weaker vortex than that indicated by experiments in their computations using CAMRAD and an Euler solver and discrepancies were still present. They attribute some of the discrepancies to the assumed invariance of the vortex core structure. Thus the present modular approach is suitable for application to the BVI problem as well. Indeed, the importance of axial flow in the vortex core and vortex core radius variation in the BVI problem seem clear. The above is a clear argument for the modular approach taken in the present work.

7.2 Implications for Wake Modeling

There are a number of implications for wake modeling that are contained in the results of this work. From the results of the experiments, it is clear that the trajectory of the tip-vortex is repeatable from cycle to cycle, and there are no random fluctuations until the vortex reaches within one core diameter of the surface. The motion of the tip-vortex as it approaches the airframe agrees with the results of the potential flow calculation indicating the accuracy of vortex methods for wake modeling. However, the effects of the inboard vortex sheet are clearly shown in the interaction. These effects no doubt have an effect on the precise trajectory of the tip vortex.

The strong axial flow in the core implies that there must be substantial movement of vortex features along the core axis. This should have interesting effects on the spatial periodicity of the vortex, along the core axis. For example, the variations in strength expected as the blade goes around the tip path, should now be seen with some phase shift as the effects are convected along the core. These changes should also be spread out along the core, since the core axial velocity appears to have a sharply-peaked profile.

The length and time scales of the collision process described here are based on vortex parameters and thus these scales are small. We have indicated that this is the case for the BVI problem as well. Recent experiments (Caradonna *et al.* and Komerath *et al.* 1997) suggest that this will also be the case in near-wake modeling in general and the modular approach using vortex methods described in this work may have wider application.

Moreover, as the vortex travels down the sides of the airframe, each piece of the vortex may be treated as if it were pinned at the airframe boundary. On the retreating side of the rotor, the vortex draws fluid from the boundary layer in an amount required to satisfy continuity and preserve the magnitude of the axial velocity far from the airframe. Note that on this side of the airframe, the vortex is still attached to the rotor blade from which it came. On this side of the rotor the full full helical model of the vortex is appropriate.

On the other hand, on the advancing blade side, the axial flow can be assumed to stagnate at the boundary, and since the magnitude of axial flow will not affect the motion of the vortex as shown in Section 6.4, the simple line vortex model should be used. These modifications of the model for the tip-vortex can be easily incorporated into the appropriate rotor-body interaction code.

Another issue which has implications for the accurate computation of rotor wakes has arisen recently. Experiments by Caradonna *et al.* and Komerath *et al.* (1997) have suggested that interactions between adjacent tip-vortices may be important in wake computations and even dominate within one or two rotor revolutions. This vortex-vortex interaction is also expected to take place on the scale of the vortex core and so very fine scale numerical computations which resolve time scales on the order of 1^o in rotor phase angle may be required. Similar to the current work on vortex-airframe collisions, the computation of this interaction requires a very accurate time integrator and resolution of length scales on the order of the vortex core.

This is especially true because the vortex will not diffuse for a very long time.

Because the Lamb vortex and other simple models have been shown to be accurate models for the tip-vortex we can demonstrate the long time scale of the viscous diffusion process very simply. Suppose the age of the vortex is identified by

$$t_0 = \frac{a_{v0}^2}{5\nu},$$

where a_{v0} is the initial core radius and ν is the kinematic viscosity of air. Then we seek to determine how long it would take for the core radius to increase by a factor of 2. This time is given by

$$t_D = \frac{4a_{v0}^2}{5\nu} - t_0 = 3t_0.$$

A typical data set from the experiments of Caradonna *et al.* and Komerath *et al.* (1997) is rotor radius, $R = 1.04m$, average dimensionless downwash scaled by ΩR $\lambda = 0.04$, rotor tip speed: 1800 rpm, and initial tip vortex core radius, $a_v = 0.0122R = 0.0127m$. For this data set:

$$t_0 = \frac{a_{v0}^2}{5\nu} = 2.8sec,$$

$$t_D = 3 \times t_0 = 8.4sec,$$

and so the number of rotor revolutions is

$$Revolutions = \frac{\Omega}{2\pi} \times t_D \sim 250.$$

Thus the length scale associated with the vortex core is expected to remain small throughout the duration of the calculation of the rotor wake. Consequently, very fine time steps such as those used in the current work will be required for the near wake calculation, especially in light of the expected vortex-vortex interactions identified by Caradonna *et al.* and Komerath *et al.* (1997). Such vortex-vortex interactions will be especially intense in descent.

Appendix A

Appendix: Analytical Solutions for a Gaussian Jet

In this appendix we present analytical solutions for the initial and terminal states of flow for the Gaussian jet, defined in equation (5.42). The analysis below makes use of normalized variables, so that r implies r/a, w implies w/w_0, etc. For axi-symmetric incompressible flow, the stream function ψ must satisfy equation (5.9). The difference in the two limit cases is the form that the vorticity must take.

A.0.1 Starting Solution: $t = 0^+$

Initially the vorticity is that of the undisturbed jet, given by equation (5.46) for the Gaussian jet. The stream function is governed by equation (5.9), which for this case may be expressed in the form

$$4\rho\frac{\partial^2\psi}{\partial\rho^2} + \frac{\partial^2\psi}{\partial z^2} = 2\rho e^{-\rho}$$

where we have utilized the variable $\rho = r^2$. The stream function distribution for the undisturbed jet provides a particular solution of this equation

$$\psi^{(0)} = -\frac{1}{2}\left(1 - e^{-r^2}\right) \tag{A.1}$$

A complementary function, satisfying the homogeneous equation, must be added to satisfy the boundary condition $w = 0$ at the surface $z = 0$. Omitting the details, we observe that the complementary function can be expressed as a Fourier-Bessel integral, so that the complete solution has the form

$$\psi = \frac{1}{2}\left\{-\left(1-e^{-r^2}\right) + r\int_0^\infty J_1(\lambda r)e^{-\lambda z-\lambda^2/4}d\lambda\right\} \tag{A.2}$$

The velocity components can now be evaluated from the partial derivatives of ψ. In particular the surface velocity has the form

$$u(r,0) = \frac{1}{2}\int_0^\infty \lambda J_1(\lambda r)e^{-\lambda^2/4}d\lambda$$

This integral has been evaluated in terms of the modified Bessel functions.[1] There results

$$u(r,0) = \frac{\sqrt{\pi}}{2}re^{-r^2/2}\left[I_0(r^2/2) - I_1(r^2/2)\right] \tag{A.3}$$

An interesting feature of the flow is the sign of the axial velocity near the wall. From the continuity equation, the derivative $\partial w/\partial z$ also can be evaluated in terms of modified Bessel functions:

$$\left.\frac{\partial w}{\partial z}\right|_{z=0} = -\left.\frac{1}{r}\frac{\partial(ur)}{\partial r}\right|_{z=0} = -\sqrt{\pi}e^{-r^2/2}\left[(1-r^2)I_0(r^2/2) + r^2 I_1(r^2/2)\right] \tag{A.4}$$

This expression has a zero at the radius $r^* = 1.256963\cdots$, so that the flow is toward the wall for $r < r^*$ and away from the wall for $r > r^*$.

A.0.2 Steady State: $t \to \infty$

We now consider the terminal state of steady flow. The conservation laws for axisymmetric flow require ω/r to be constant on streamlines, so that we can write

$$\omega = rH(\psi) \tag{A.5}$$

The stream function ψ still satisfies equation (5.9), which now takes the special form

$$D^2\psi = -r^2H(\psi) \tag{A.6}$$

---

[1] Erdelyi et al, *Tables of Integral Transforms*, Vol. II, p. 29, McGraw-Hill Book Co., 1954

The azimuthal vorticity in the undisturbed jet at upstream infinity is given by equation(33). Making use of equation (A.1), we find that the function $H(\psi)$ has the form

$$H(\psi) = -2\,(1 + 2\psi) \tag{A.7}$$

$H(\psi)$ is invariant throughout the flow field. Hence equation (A.6) simplifies to a linear partial differential equation:

$$D^2\psi - 4r^2\psi = 2r^2 \tag{A.8}$$

A particular solution of this equation is given by equation (A.1). The homogeneous equation can be solved readily by the method of separation of variables, leading to the complete solution in the form of a series of associated Laguerre polynomials, as

$$\psi = -\frac{1}{2}\left(1 - e^{-r^2}\right) + r^2 e^{-r^2} \sum_{n=0}^{\infty} c_n \; L_n^1(2r^2)\; e^{-\sqrt{8(n+1)}z} \tag{A.9}$$

The exponentially growing solution has been suppressed, so that the flow predicted by equation (A.9) approaches that of equation (A.1) as $z \to \infty$. Also ψ automatically vanishes for $r = 0$ and $r \to \infty$, leaving only the boundary condition at the wall, $z = 0$, to be satisfied. Set $z = 0$ in equation (A.9), and multiply through by $e^{-r^2} L_m^1(2r^2)$. Then integrating from $z = 0$ to ∞, the orthogonality of the Laguerre polynomials leads to the following set of equations for the coefficients:

$$c_n = \frac{4}{n+1}\int_0^{\infty} e^{-r^2}(1 - e^{-r^2})\; L_n^1(2r^2)\; r dr$$

These integrals may be evaluated using the generating function for L_n^1, yielding the simple result

$$c_n = \frac{(-1)^n}{n+1}$$

Owing to the exponential factor, the series in equation (A.9) converges fairly rapidly except near $z = 0$. On $z = 0$, the terms decay like $(-1)^n n^{-1/2}$ for large n, except at $r = 0$, where even slower convergence occurs. However, if one evaluates the Laguerre polynomials successively using their recurrence relation, term-by-term summation on a desk-top computer requires only a few seconds for a given point located near both wall and axis.

The velocity components u and w (radial and axial) are obtained as derivatives of the stream function, as

$$u = -\frac{1}{r}\frac{\partial\psi}{\partial z}, \qquad w = \frac{1}{r}\frac{\partial\psi}{\partial r}$$

Thus we find for the surface velocity

$$u(r,0) = re^{-r^2}\sum_{n=0}^{\infty} c_n \sqrt{8(n+1)}\; L_n^1(2r^2)$$

and for the axial velocity

$$w(0,z) = -1 + 2\sum_{n=0}^{\infty} c_n \; L_n^1(0)\; e^{-\sqrt{8(n+1)}z}$$

The axial velocity series for $w(0,z)$ converges except at the wall, $z = 0$. However, we know that w must vanish on $z = 0$, since the stream function does. Above the surface the radial velocity series converges owing to the exponential factor, although we have not written down its explicit form. The surface velocity series, however, is an oscillatory (though not alternating) series converging slowly with terms decaying as $n^{-1/4}, r > 0$. Note that the Euler transformation can be used to dramatically accelerate convergence of the axial-velocity series, even at the wall, but this technique is not successful for the surface velocity.

The azimuthal vorticity takes an especially simple form on the wall. From equations (A.5) and (A.7), we find

$$\omega = rH(0) = -2r$$

so that the magnitude of the vorticity simply increases linearly with radius. It is interesting that this result is obtained *ab initio*, without resort to the solution of the differential equation.

We also note that the solution may be expanded in terms of the similarity variable $\eta = rz$. There results for the radial velocity, for example,

$$u(r,z) \sim e^{-2\eta} + \frac{1}{6r^4}\eta^2(2\eta - 3)e^{-2\eta}$$

Hence the velocity decays exponentially to zero for any positive fixed value of z, except within a layer of order $z \sim 1/r$ next to the wall.

A.0.3 Results

The flow speed at the surface is plotted in Figure A.1 for the starting solution, $t = 0^+$, and for the terminal steady flow, $t \to \infty$. For the starting solution, the surface speed peaks at the value 0.44582 at the radius $r = 0.84423$; i.e., 45% of the peak speed in the undisturbed jet at 84% of the characteristic radius of the jet. For large radii, $u(r, 0)$ decays as $1/2r^2$.

For the steady-flow case, the series for ψ, equation (A.9), was summed at discrete points above the wall. Forward differences were applied to the resulting numerical data to obtain the z-derivative needed for the radial velocity. The results were deemed sufficiently accurate when values obtained from difference formulas of both third-order and fourth-order accuracy agreed to five significant figures. This test corresponded to six-place accuracy in the stream-function sums. The results are also shown in Figure A.1. The surface flow speed for steady flow increases monotonically with radius, rapidly approaching the maximum speed of the original undisturbed jet, as required by conservation of total pressure on the central streamline.

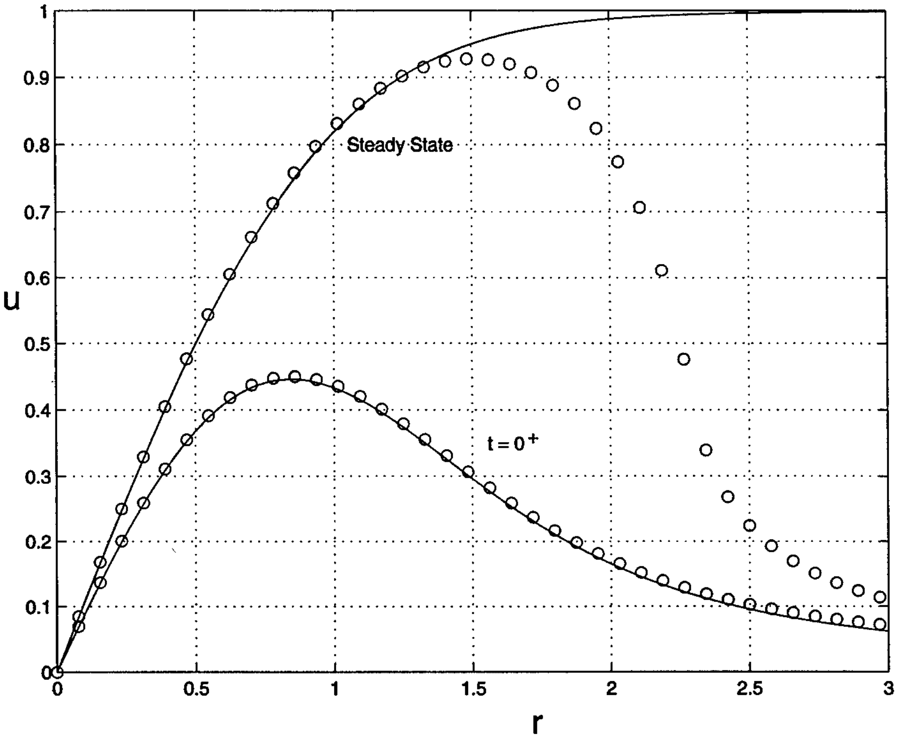

Figure A.1: Radial velocity on the surface for the starting solution, $t = 0^+$, and for the terminal steady flow, $t \to \infty$. On this figure, the open circles are the numerical solution, with the solid line being the analytical solution. The numerical solution is evaluated at $t = 2.5$ and at $t = \Delta t = 0.005$. The numerical solution for times in between is given in Figure 5.5.

Appendix B

Honors, Papers, Presentations, and Degrees Awarded

This is a listing of the honors and awards, papers, presentations and degrees awarded since the inception of the grant in 1993.

Honors

J. M. Kim, Georgia Tech Sigma Xi Best PhD Thesis Award, June 1994

N. M. Komerath, Georgia Tech Outstanding PhD Advisor Award for the period 1992-1996, June 1997.

A. T. Conlisk, Ohio State University, College of Engineering 1997 Lumley Research Award

Archival Papers

Kim, J. M. and Komerath, N. M. "Summary of the Interaction of a Rotor Wake with a Circular Cylinder", AIAA paper 93-3084, 1993; also *AIAA J.* , Vol. 33, no. 3, pp. 470-478, 1995.

Z. Xiao, E. C. Adams, and A. T. Conlisk, "Terminal Structure of Unsteady Classical and Interacting Boundary Layers", *Physics of Fluids*, **8**, no. 6, pp. 1397-1407, 1996. Partial support.

Z. Xiao and O. R. Burggraf, and A. T. Conlisk, "The Interacting Boundary Layer Due to a Vortex Outside a Cylinder", *J. Fluid Mech.*, **346**, Sept. 10, pp.319-346, 1997.

J. A. Lee, O. R. Burggraf, and A. T. Conlisk, "On the Impulsive Blocking of a Vortex-Jet", accepted *J. Fluid Mech.*

T. D. Radcliff, O. R. Burggraf, and A. T. Conlisk, "Axial Core Flow Effects on the Interaction of a Rotor-Tip Vortex with an Airframe", in preparation.

Conference Papers

Each of these papers had a presentation.

J. Lee, Z. Xiao, O. R. Burggraf, A. T. Conlisk, and N. M. Komerath, "An Inviscid Approach to Vortex-Surface Collisions", paper 95-2237, 26th AIAA Fluid Dynamics Meeting, San Diego, June 1995.

R. Mahalingam, K. Peterson, R. B. Funk, N. M. Komerath, and A. T. Conlisk, "Recent Experiments on Vortex Collision with a Cylinder", paper 95-2236, 26th AIAA Fluid Dynamics Meeting, San Diego, June 1995.

R. Mahalingam and N. M. Komerath "Rotor Tip-Vortex/Airframe Collision Features", paper 96-2013, 27th AIAA Fluid Dynamics Conference, June 18-20, 1996, New Orleans, LA.

R. Mahalingam, R. B. Funk, and N. M. Komerath "Flow Visualization of Perpendicular Vortex Airfoil Interaction", paper 96-2387, 14th AIAA Applied Aerodynamics Conference, June 18-20, 1996, New Orleans, LA.

T. D. Radcliff, O. R. Burggraf, and A. T. Conlisk, "Axial Core Flow Effects on the Interaction of a Rotor-Tip Vortex with an Airframe", paper 97-0658, 35th AIAA Aerospace Sciences Meeting, Reno, Nev., January 1997.

R. Mahalingam, R. B. Funk, N. M. Komerath, "Low Speed Canard-Tip-Vortex Airfoil Interaction", SAE Paper no. 971469, GCRAM 97', April 1997, KS.

R. Mahalingam, N. Komerath, T. Radcliff, O. R. Burggraf, and A. T. Conlisk

"Vortex-Surface Collision: 3-Dimensional Core Flow", paper 97-2061, 28th AIAA Fluid Dynamics Conference, Snowmass, Col., June 1997.

Degrees Awarded

John Lynn, MSAE, June 1994, GT

Z. Xiao, PhDME, December 1995, OSU.

R. Mahalingam, MSAE, September 1995, GT.

Jeff Lee, MSME, August 1996, OSU.

Appendix C

Technology Transfer Events

In May of 1995, the PI travelled to NASA Ames to give a presentation to the Aeroflightdynamics Directorate; Dr. Chee Tung hosted my visit. In this presentation the basic theory behind the results in the paper by Lee *et al* were described. The PI also discussed the analytical/computational work with Dr. John Berry of NASA Langley in April.

In May of 1996, the Professors Conlisk and Komerath travelled to NASA Ames to give a presentation to the Aeroflightdynamics Directorate; Dr. Chee Tung hosted the visit. In this presentation recent experimental and analytical/computational results were presented and this is leading to to discussions of Hart data and wake measurements at NASA-Ames.

Professor Komerath presented the latest experimental results at United Technologies Research Center in December 1996 to UTRC and Sikorsky researchers.

On August 1, 1997 Professor Conlisk travelled to UTRC to present the latest results of the work to Alan Egolf and Peter Lorber. Others including Brian Wake and Jack Landgrebe also attended the seminar.

Currently, an effort to introduce the model for the vortex described in this work into 2GChas and to the Scully wake code is underway.

Bibliography

[1] Abramowitz, M. and Stegun, I. A. (1964) *Handbook of Mathematical Functions*, National Bureau of Standards.

[2] Adams, E. C., Conlisk, A. T., and Smith, F. T. (1995) "Adaptive Grid Scheme Vortex-Induced Boundary Layers", *AIAA J*, Vol. 33, No. 5, May.

[3] Affes, H. (1992) "Tip-Vortex/Airframe Interaction", Ph.D Thesis, The Ohio- State University.

[4] Affes, H. and Conlisk, A. T. (1993a) "A Model for Rotor Tip Vortex-Airframe Interaction, Part 1: Theory", *AIAA J.*, Vol. 31, no. 12, pp. 2263-2273.

[5] Affes, H., Conlisk, A. T., Kim, J. M. and Komerath, N. M. (1993b), "A Model for Rotor Tip Vortex-Airframe Interaction, Part 2: Comparison with Experiment", *AIAA J.*, Vol. 31, no. 12, pp. 2274-2282.

[6] Affes, H., Xiao, Z., Conlisk, A. T., Kim, J. M. and Komerath, N. M. (1993c), "The Three-Dimensional Boundary-Layer Flow due to a Rotor-Tip Vortex", *AIAA 93-3081*, AIAA 24th Fluid Dynamics Conference, July 6-9. Also *AIAA J.*, Vol. 36, no. 2, pp. 409-415, February 1998.

[7] Affes, H., Xiao, Z. and Conlisk, A. T. (1994), "The Boundary-Layer Flow due to a Vortex Approaching a Cylinder", *J. of Fluid Mech.*, Vol. 275, pp. 33-57.

[8] Bagai, A. and Leishman, J. G. (1992), "Experimental Study of Rotor/Wake Interactions in Hover", *J. Am. Hel. Soc.*, Vol. 37, no. 4, pp. 48-57.

[9] Batchelor, G.K. (1967), *Introduction to Fluid Dynamics*, Cambridge University Press, Cambridge.

[10] Batchelor, G. K. (1964), "Axial Flow in Trailing Line Vortices", *J. Fluid Mech*, Vol. 20, part 4, pp. 645-658.

[11] Beam, R. M. and Warming, R. F. (1978), "An Implicit Factored Scheme for the Compressible Navier-Stokes Equations", *AIAA J.*, Vol. 16, pp.393-402.

[12] Belcher, R., Burggraf, O. R. and Stewartson, K. (1972), "On Generalized-Vortex Boundary Layers", *J. Fluid Mech.*, Vol. 52, part 4, pp. 753-780.

[13] Betzina, M. D. and Smith, C. A. (1983), "Rotor/Body Aerodynamic Interactions", NASA TM 85844, October.

[14] Bi, N. P., Leishman, J. G. and Crouse, G. C. (1993), "Investigation of Rotor Tip Vortex Interactions with a Body", *J. Aircraft*, Vol. 30, No. 6.

[15] Brand, A. G., McMahon, H. M. and Komerath, N. M. (1989), "Surface Pressure Measurements on a Body Subject to Vortex Wake Interaction", *AIAA J.*, Vol. 27, May, pp. 569-574.

[16] Briggs, W. L. (1987), *A Multigrid Tutorial.*

[17] Burggraf, O. R. (1995), Private Communication.

[18] Burggraf, O. R., Stewartson, K. and Belcher, R. (1971), "Boundary Layer Induced by a Potential Vortex", *Phys. of Fluids*, Vol. 14, No. 9, September.

[19] Burley, Casey L. and Tadghighi, H. (1994), "Importance of High Accuracy Blade Motion and Airloads Prediction for Acoustic Analysis", *American Helicopter Society 50th Annual Forum*, May 11-13.

[20] Byrd, Paul F. and Friedman, Morris D.i (1954), *Handbook of Elliptic Integrals for Engineers and Physicists*, Springer-Verlag.

[21] Caradonna, F. X. (1992), "The Application of CFD to Rotary Wing Flow Problems", NASA TM 102803, March.

[22] Caradonna, F. X. *et al.* and Komerath, N. M. *et al.* (1997), "An Experimental Study of a Rotor in Axial Flight", AHS Technical Specialists meeting for Rotorcraft Acoustics and Aerodynamics, Williamsburg, VA, October 28-30, 1997.

[23] Cebeci, T., Chen, L. T. and Chang, K. C. (1986), "An Interactive Scheme for Three-Dimensional Transonic Flows", *Numerical and Physical Aspects of Aerodynamic Flows*, ed. T. Cebeci, pp. 412-431.

[24] Chen, Z. L. and Wu, J. M. (1984), "Approximate Viscous/Inviscid Interacting Method for Laminar and Turbulent Flows", *AIAA Paper 84-0267.*

[25] Conlisk, A. T. (1989), "The Pressure Field in Intense Vortex-Boundary Interaction", *27th Aerospace Sciences Meeting*, Reno, Nev, AIAA paper 89-0293.

[26] Conlisk, A. T., Adams, E. C. and Xiao, Z. (1996), "Novel Computational Techniques for Boundary Layers", Final Report ARO-29768.2-EG-AAF, US Army Research Office. Available on request.

[27] Conlisk, A. T. (1997), "Modern Helicopter Aerodynamics", *Ann. Rev. Fluid Mech*, Vol. 27, pp. 515-567.

[28] Cutler, A.D., and Bradshaw, P. (1993), "Strong Vortex/Boundary Layer Interactions", Experiments in Fluids, Vol.14, ,pg. 321-332.

[29] Doligalski, T. L., Smith, C. R., and Walker, J. D. A. (1994), " Vortex Interactions with Walls", Annual Review of Fluid Mechanics, Vol. 26, pgs. 573-616.

[30] Duck, P. W. (1990), "Triple-Deck Flow over Unsteady Surface Disturbances: The Three-Dimensional Development of Tollmein-Schlichting Waves", *Computers and Fluids*, vol. 18, no. 1, pp. 1-34.

[31] Duck, P. W. and Burggraf, O. R. (1986), "Spectral Solutions for the Three-Dimensional Triple-Deck Flow over Surface Topography", *J. Fluid Mech.*, vol. 162, pp.1-22.

[32] Edwards, D. E. (1986), "Analysis of Three-dimensional Separated Flow Using Interacting Boundary Layer Theory", in *IUTAM Symposium*, London, ed. F.T. Smith and S.N. Brown, pp. 297-308.

[33] Egolf, T. A. and Lorber, R. F. (1987), "An Unsteady Rotor/Fuselage Interaction Method", Proc. International Specialists Meeting on Aerodynamics and Astroacoustics, Arlington, Texas, February.

[34] Elliott, J. W., Cowley, S. J. and Smith, F. T. (1983), "Breakdown of Boundary Layers: (1) On Moving Surfaces; (ii) Self-similar Unsteady Flow; (iii) in Fully Unsteady Flow", *Geophy. Astrophys. Fluid Dynamics*, Vol. 25, pp.77-138.

[35] Flegg, G. C. (1974), "From Geometry to Topology", Crane, Russak & Co. Inc., New York.

[36] Freeman, C. E. (1980), "Development and Validation of a Combined Rotor-Fuselage Induced Flow Field Computational Method", NASA TP 1656.

[37] Gray, R. B. (1956), "An Aerodynamic Analysis of a Single-Bladed Rotor in Hovering and Low-Speed Forward Flight as Determined from Smoke Studies of the Vorticity of the Ground", *AIAA J.*, Vol. 9, pp. 1659-1660.

[38] Harvey, J. K. and Perry, Fi J. (1971), "Flow Field Produced by Trailing Vortices in the Vicinity of the Ground", *AIAA J.*, Vol. 9, pp. 1659-1660.

[39] Hassan, A. A., Tung, C., and Sankar, L. N. (1992), "Euler Solutions for Self-generated Rotor Blade-Vortex Interactions, *Int. J. Num. Meth. Fluids*, vol. 15, pp. 427-451.

[40] Hassan, A. A., Charles, B. D., Tadghighi, H., and Burley, Casey L. (1993), "A Consistent Approach for Modelling the Aerodynamics of Self-Generated Rotor Blade-Vortex Interactions", *American Helicopter Society 49th Annual Forum*, May 19-21.

[41] Hess, J. L. and Smith, A. M. O. (1967), "Calculation of Potential Flow about Arbitrary Bodies", *Progress in Aeronautical Sciences*, Vol. 8, pp. 1-138.

[42] Hoyle, J. M. and Smith, F. T. (1994), "On Finite-time Breakup in Three-Dimensional Unsteady Interacting Boundary Layers", *Proc. Roy. Soc. A*, Vol. 447, pp. 467-492.

[43] Johnson, W. and Yamauchi, G. K. (1984), "Applications of an Analysis of Asymmetric Body Effects on Rotor Performance and Loads", Proc. 10th European Rotorcraft Forum, August.

[44] Kalkhoran, I. M.,Wilson, D. R., and Seath, D. S. (1992), "Experimental Investigation of the Perpendicular Rotor Blade-Vortex Interaction at Transonic Speeds", AIAA Journal, Vol. 30, No. 3, March, pgs. 747-755.

[45] Kim, J. M. and Komerath, N. M. (1995), "Summary of the Interaction of a Rotor Wake with a Circular Cylinder", *AIAA J.*, Vol. 33, No. 3, pp. 470-477.

[46] Kim, J. M. (1993), "An Experimental Study of the Interaction Between a Rotor Wake and an Airframe With and Without Flow Separation", PhD Thesis, Georgia Institute of Technology, May 1993.

[47] Lamb, H. (1945), *Hydrodynamics*, 6th Edition, p. 592, Dover, New York.

[48] Landgrebe, A. J. (1994), "New Directions in Rotorcraft Computational Aerodynamics Research in the U.S.", Proc. AGARD Conference on Aerodynamics and Aeroacoustics of Rotorcraft, Berlin, GE.

[49] Landgrebe, A. J., Moffitt, R. C. and Clark, D. R. (1977), "Aerodynamic Technology for Advanced Rotorcraft", *J. Amer. Hel. Soc.*, Vol. 22, No.2 and 3, April and July.

[50] Lee, J.,Burggraf, O. R., Conlisk, A. T. (1997), "On the Impulsive Blocking of a Vortex Jet", submitted to *J. Fluid Mech.* .

[51] Lee, J., Xiao, Z., Burggraf, O. R., Conlisk, A. T. and Komerath, N. M. (1995), "An Inviscid Analysis of Vortex/Surface Collisions", *AIAA 95-2237, 26th AIAA Fluid Dynamics Conference*, June 19-22.

[52] Liou, S. G., Komerath, N. M. and McMahon, N. M. (1990), "Measurement of the Interaction Between a Rotor Tip Vortex and a Cylinder", *AIAA J.*, Vol. 28, No. 6, pp. 975-981.

[53] Lombardi, G. (1995), "Canard Tip Vortex Splitting in a Canard-Wing Configuration:Experimental Observation", Journal of Aircraft, vol. 32, no. 4, pgs.875-877, July-Aug.

[54] Lorber, R. F. and Egolf, T. A. (1990), "An Unsteady Rotor-Fuselage Interaction Analysis", *J. Am. Hel. Soc.*, Vol. 35, No. 7, pp. 32-42; also NASA CR-4178, August 1988.

[55] Mahalingam, R., Peterson, K., Frank, R. B. Komerath, N. K. and Conlisk, A. T. (1995), "Recent Experiments on Vortex Collision with a Cylinder", paper 95-2236, *26th AIAA Fluid Dynamics Conference*, June 18-21, San Diego.

[56] Mahalingam, R., Funk. R. B., and Komerath, N. M. (1996), "Flow Visualization of Low Speed Perpendicular Vortex-Airfoil Interaction", AIAA 14th Applied Aerodynamics Conference, AIAA paper 96-2387, New Orleans, LA.

[57] Mahalingam, R. (1996), Private communication.

[58] Mahalingam, R., Funk. R. B., and Komerath, N. M. (1997), "Low Speed Canard-Tip-Vortex Airfoil Interaction", SAE paper 971469, GCRAM 97', Wichita, KS.

[59] Marshall, J.S. and Krishnamoorthy, S., (1997), "On the Instantaneous Cutting of a Columnar Vortex with Non-zero Axial Flow", *J. Fluid Mech.*, Vol. 351, pp. 41-74.

[60] McCroskey, W. J. (1995), "Vortex Wakes of Rotorcraft", *AIAA 95-0530. 33rd Aerospace Sciences Meeting and Exhibit*, January 9-12, Reno, NV

[61] Moore, F. K. (1952), "Displacement Effect of a Three-Dimensional Boundary Layer", *NACA report 1124*, pp.367-371.

[62] Moore, F. K. (1958), "On the Separation of the Unsteady Laminar Boundary Layer", Boundary-Layer Research, Ed. Gortler, H.G., pp. 296-310, Springer, Berlin.

[63] Moore, D. W. (1972) "Finite Amplitude Waves on Aircraft Trailing Vortices", *Aero. Quart.*, Vol. 23, pp. 307-314.

[64] Moore, D. W. and Saffman, P. G. (1972), "The Motion of a Vortex Filament with Axial Flow", *Philosophical Transactions of the Royal Society*, Vol. 272, pp. 403-429.

[65] Patel, M.H., Hancock, G.J. (1974), "Some Experimental Results of the Effect of a Streamwise Vortex on a Two-Dimensional Wing", Aeronautical Journal, April, pgs.151-155.

[66] Peridier, V., Smith, F. T. and Walker, J. D. A. (1991), "Vortex-Induced Boundary Layer Separation, Part 1: $Re \to \infty$, Part 2, Unsteady Interacting Boundary Layer Theory", *J. Fluid Mech.*, Vol. 232, pp. 99-165.

[67] Radcliff, T. D., Burggraf, O. R. and Conlisk, A. T. (1997), "Axial Core Flow Effects on the Interaction of a Rotor-Tip Vortex with an Airframe", paper 97-0658, 35^{th} AIAA Aerospace Sciences Meeting, Reno, Nev., January.

[68] Rockwell, D. (1983), "Oscillations of Impinging Shear Layers", *AIAA J.*, Vol. 21, pp. 645-664.

[69] Rockwell, D. and Naudascher, E. (1979), "Self-sustained Oscillation of Impinging Shear Layers", *Ann. Rev. Fluid Mech.*, Vol. 11, pp. 67-94.

[70] Rockwell, D. (1998), "Vortex-Body Interactions", *Ann. Rev. Fluid Mech.*, Vol. 28.

[71] Saffman, P. G. and Baker, G. R. (1979), "Vortex Interactions", *Ann. Rev. Fluid Mech.*, Vol. 11, pp. 95-122.

[72] Sarpkaya, T. (1989), "Computational Methods with Vortices- The 1988 Freeman Scholar Lecture", *J. Fluids Engineering*, Vol. 111, no. 3, pp. 5-52.

[73] Seath, D. D., Wilson, D. R. (1986), "Vortex-Airfoil Interaction Tests", AIAA 24th Aerospace Sciences Meeting, AIAA Paper 86-0354, Reno, NV, USA.

[74] Sheridan, P. F. and Smith, R. F. (1980), "Interactional Aerodynamics- A New Challenge to Helicopter Technology", *J. Amer. Hel. Soc.*, Vol. 25, No. 1, January.

[75] Smith, C. A. (1979), "Some Effects of Wake Distortion Due to Fuselage Flow Field on Rotor Thrust Limits", ARO Workshop on Rotor Wake Technology, Raleigh, NC, April.

[76] Smith, F. T. (1986), "Steady and Unsteady Boundary Layer Separation", *Annual Review of Fluid Mechanics*, Vol. 18, pp. 197-220.

[77] Smith, F. T. (1988), "Finite time breakup can occur in any unsteady interacting Boundary layer", *Mathematika*, vol. 35, pp. 256-273.

[78] Smith, F.T. (1991), "Steady and Unsteady Interactive Boundary Layers", *Computers and Fluids*, Vol. 20 no. 3, pp. 243-268.

[79] Soell, Julian (1994), "A Panel Method Formulation for Inviscid Vortex/Body Interaction Problems", MSc Thesis, The Ohio State University, May 1994.

[80] Terzi, A. and Chiu, T. (1997), "Modern Panel Method Techniques for Modeling Wake-Body Interference", 28th AIAA Fluid Dynamics Conference, AIAA paper 97-1829, Snowmass Village CO, July.

[81] Thompson, J. (1985), "A Survey of Dynamically Adaptive Grids in the Numerical Solution of Partial Differential Equations", *Appl. Numer. Math.*, Vol. 1, pp. 3-27.

[82] Tucker, Bryan and Conlisk, A. T. (1992), "Massive Vortex Motion in the Presence of Solid Boundaries", *Physics of Fluids* 4, no. 2, pp. 290-305.

[83] Tung, C. and Yu, Y. H., Low, S. L. (1996), "Aerodynamic Aspects of BVI ", AIAA 27th Fluid Dynamics Conference, AIAA paper 96-2010, New Orleans, LA, June.

[84] Van Dommelen (1991), "Lagrangian Description of Unsteady Separation", *Lectures in Applied Math.*, Vol. 28.

[85] Van Dommelen and Cowley, S. J. (1990), "On the Lagrangian Description of Unsteady Boundary-Layer Separation. Part 1. General Theory", *J. Fluid Mech.*, Vol. 210, pp.593-626.

[86] Van Dommelen and Shen, S. F. (1981), "The Spontaneous Generation of the Singularity in a Separating Laminar Boundary Layer", *J. Comp. Phys.*, Vol. 25, pp.125-140.

[87] Walker, J. D. A. (1978), "The Boundary Layer Due to a Rectilinear Vortex", *Proc. Roy. Soc. A*, Vol. 359, pp. 167-188.

[88] Widnall, S., Bliss, D. and Zalay, A. (1971), "Theoretical and Experimental Study of the Stability of a Vortex Pair", in *Aircraft Wake Turbulence and its Detection*, New York: Plenum Press.

[89] Wilson, J. C. and Mineck, R. E. (1975), "Wind-Tunnel Investigation of Helicopter Rotor Wake Effects on Three Helicopter Fuselage Models", NASA TM X-3185, March.

[90] Wittmer, K. S., and Devenport, W. J., (1994), "Interaction of a Streamwise Vortex with a Full-span Blade", AIAA paper 95-2214, June.

[91] Wittmer, K. S., and Devenport, W. J. (1995), "Perpendicular Blade Vortex Interaction", AIAA Journal, Vol 33, No. 9,September, pg. 1667-1674.

[92] Wittmer, K. S., and Devenport, W. J. (1996), "Turbulence Structure resulting from a Perpendicular Airfoil-Vortex Interaction", AIAA paper 96-2014, 27th AIAA Fluid Dynamics Conference, June.

[93] Wong, O., Gialloreto, V. B. , Hendricks, T. (1997) "Wing-wing interaction experiment test manual". Final report in AE4010 Advanced Flow Diagnostics, School of Aerospace Engineering, Georgia Institute of Technology, Atlanta, GA, Winter.

[94] Xiao, Z. H., Burggraf, O. R. and Conlisk, A. T. (1994), "The Three Dimensional Interacting Boundary-Layer Flow Induced by a Vortex on a Circular Cylinder", *25th AIAA Fluid Dynamics Conference*, June 20-23, Colorado Springs, CO.

[95] Xiao, Z., Adams, E. C., and Conlisk, A. T. (1996), "Terminal Structure of Unsteady Classical and Interacting Boundary Layers", *Physics of Fluids* 8, no. 6, pp. 1397-1407.

[96] Yahiaoui, M. (1993), "A Numerical Study of Boundary Layer Stability", Phd Thesis, The Ohio State University.

[97] Yu, Y. H. (1995), "Rotor Blade-Vortex Interaction Noise: Generating Mechanisms and Control Concepts", Proceedings of the AHS 2nd International Aeromechanics Specialists' Conference, Bridgeport, CT, Vol. 1, October, pgs. 3.1-3.12.